Density Functional Theory augmented Multiplet Ligand Field Theory Applied to X-ray Spectroscopy of $3d$ Transition Metals

Charles Cardot

A dissertation

submitted in partial fulfillment of the

requirements for the degree of

Doctor of Philosophy

University of Washington

2025

Reading Committee:

Gerald T. Seidler, Chair

Josh J. Kas

John J. Rehr

Program Authorized to Offer Degree:

Physics

University of Washington

Abstract

Density Functional Theory Augmented Multiplet Ligand Field Theory Applied to X-ray Spectroscopy of $3d$ Transition Metals

Charles Cardot

Chair of the Supervisory Committee:

Gerald T. Seidler

Physics

The usual flow of new information within science is such that experiments are used to refine our understanding of the world, with theory playing a supporting or interpretive role. The rarer occurrence comes from when theory is used to motivate new directions for scientific exploration. The difficulty of course comes from the need for a theory that can provide predictions for novel phenomena that are sufficiently accurate and precise enough to merit experimental efforts. Here I explore methods for improving the standard multiplet ligand field theory (MLFT) model of x-ray spectroscopy with density functional theory (DFT), with the goal of making it more *ab-initio* so that it can be used for predictive applications instead of just interpretive. The main improvements come from reducing the number of free parameters that are used when fitting an MLFT calculated spectra to experiment, namely the Slater-Condon scaling, crystal field, and ligand hopping parameters.

First, I apply the DFT + MLFT framework to core-to-core X-ray emission spectroscopy (CtC-XES), exploring how the charge transfer dynamics are affected by the core-hole in the intermediate and final states. In this work, I surveyed 8 different $3d$ transition metal systems across the periodic table and analyze how calculated spectra reproduce trends across peak width, spin state, and integral intensity to conclusively demonstrate the accuracy of this approach. Next, I utilized this framework to explore a resonant shake effect that manifests in $3d^0$ materials when the bonding-antibonding splitting matches the $2p$ spin-orbit splitting. Through this resonance I was able to predict and later experimentally verify a new spectral feature within the Kα XES of PbCrO$_4$, which too my knowledge is the first ever example of multiplet theory being used to inform new experiment. Finally, I switched focus to studying how the linear polarization x-ray emission of single crystal systems varies depending on local geometry and chemistry. I compared the information contained both a core-to-core level where the local anisotropy was transmitted through Coulomb coupling between the core and valence states, with valence-to-core x-ray emission spectroscopy (VtC-XES) where the occupied density of states directly reflects the local anisotropy. This project was also extended to a study of how the anisotropy in polarized VtC-XES could be reproduced through supervised machine learning applied to a large dataset of crystal structures. This model highlights correlations between key chemical and geometric indicators such as the normalized quadrupole moment, and provides a continuous, quantitative method for characterizing spectral anisotropy.

Table of Contents

Acknowledgements

Thank you to my advisors, Professor John Rehr and Professor Jerry Seidler, who helped me develop as both a theorist and experimentalist when I always found myself somewhere in the middle. They have both demonstrated amazing mentorship and encouragement throughout my academic career. They have also been incredibly giving outside of the lab, and have provided me with more support and opportunities to develop professionally than I ever expected. They have been teachers not just in physics but in life, and I am eternally grateful for their guidance throughout my degree. I also would like to specially thank Professor Josh Kas, who has spent countless hours with me almost every week of the last four years. He has helped me get 'unstuck' so many times that without him, it is no exaggeration to say that this PhD would never have happened. I've shared my gratitude with him many times throughout this journey, but I want to express it once more here, for the record: thank you, Josh.

I would also like to acknowledge the other amazing undergraduate and graduate students from both groups for all their support: Dr. Samantha Tetef, Dr. Diwash Dhakal, Dr. Jared Abramson, Dr. Tun Sheng Tan, Helen Chen, Anthony Gironda, Fiona Mclary, John Tichenor, and Seth Shjandemaar. You have helped me stay entertained during long days in the lab and have been amazing sources of laughter, comfort, and support throughout the last four years. I'd like to highlight Sam in particular for taking me under her wing in my first year at UW. She showed me not just how to be a better programmer and how to make nicer plots, but also how to be a better scientist.

Thank you to my collaborators and mentors, especially Professor Maurits Haverkort, Dr. Simon Heinze, and Dr. Martin Bras who helped introduce me to the world of multiplet physics

List of Acronyms

XES – X-ray Emission Spectroscopy

XAS – X-ray Absorption Spectroscopy

XPS – X-ray Photoemission Spectroscopy

RIXS – Resonant Inelastic X-ray Scattering

XANES – X-ray Absorption Near Edge Structure

EXAFS – Extended X-ray Absorption Fine Structure

XMCD – X-ray Magnetic Circular Dichroism

XLD – X-ray Linear Dichroism

DFT – Density Functional Theory

MLFT – Multiplet Ligand Field Theory

TM – Transition Metal

SC – Slater-Condon

DOS – Density of States

Introduction

Motivation

Theoretical physics seeks to explain physical phenomenon through mathematical models which can be evaluated against experiments. To be successful, these models must rely on fundamental assumptions which can be interpreted and adjusted based on observations. The outcome of a successful theoretical model is twofold: 1) it provides a reliable method of reproducing experimental results, and 2) it provides a framework for interpreting new experiments through a model of the underlying physics. As experimental capabilities have grown over the last 120 years, the need for more accurate quantitative theoretical models has also grown. However, solving the ground state of a Coulombic Hamiltonian for an n-electron system quickly becomes an impossible problem, even with the massive development in computational power that has accompanied the quantum revolution. This can be demonstrated using a simple cluster of Hydrogen atoms. The Hilbert space for this cluster is given by $\binom{n}{k} = n!/(k!\,(n-k)!)$, which for 20 Hydrogen atoms, each with a single electron, is $\binom{40}{20} = 1.37 * 10^{11}$ configurations. This exponential wall emerges even for relatively small systems and makes exact calculations of full crystals or molecules unachievable on classical computing infrastructure. Therefore, theoretical models that tackle these quantum systems must strive to find sufficiently accurate approximations that are still numerically reasonable to compute.

One of the most powerful tools for studying quantum many-body systems in modern science is spectroscopy. The interaction of light with matter directly probes the behavior of fundamental particles (ex: x-rays for absorption, radio waves for nuclear magnetic resonance, infrared light for vibrational modes) and provides an ideal testbed for the evaluation of theoretical models. The

main focus of this thesis is on improving theoretical descriptions of locally perturbed atomic systems as probed by x-ray spectroscopy. These systems often exhibit strong electronic correlations, where the assumptions of independent-electron theories break down and many-body effects play a dominant role in shaping the observed spectra. To address this, the work emphasizes computational approaches that go beyond mean-field approximations, aiming to retain physical interpretability while reducing reliance on empirical parameter fitting. These improvements directly impact experimental design by enhancing the predictive power of commonly used theoretical models and offer a stronger foundation for future theoretical interpretation.

Thesis Organization

This thesis is organized into 7 chapters as follows:

- Chapter 1: Introduction and background on x-ray spectroscopy including a brief review of experimental and theoretical techniques.

- Chapter 2: Introduction to Multiplet Ligand Field Theory and the perturbed atomic system, with examples and discussion of modern software.

- Chapter 3: The development of the DFT augment calculation method for the multiplet model, which allows for *ab-initio* determination of most free parameters.

- Chapter 4: Application of DFT + MLFT to the core-to-core x-ray emission of a range of $3d$ transition metal systems, evaluating the augmented multiplet model for a previously unexplored spectroscopy

- Chapter 5: A deep dive using the augmented multiplet model into the behavior of nominally $3d^0$ systems and the resonant shake effects they can exhibit in the presence of a $2p$ core-hole

- Chapter 6: Exploration of the polarization dependence for core-to-core and valence-to-core x-ray emission of highly anisotropic single crystal systems.

- Chapter 7: Conclusion and future directions

Chapter 1 Background on X-ray Spectroscopy

X-ray spectroscopy is a general term which refers to a family of techniques that are used for studying materials based on how light in the x-ray regime (energies roughly between 100 eV to 100,000 eV) interacts with matter. The origins of x-ray spectroscopy can be approximately traced through the first 30 years of the Nobel prize in physics, starting with Wilhelm Röntgen in 1901 for the discovery of x-rays [1]. The father son pair William Henry Bragg and Lawrence Bragg and Maurice de Broglie independently observed the first absorption lines in 1913 while studying x-ray diffraction in crystals [2, 3], and the Braggs went on to win a Nobel prize (specifically for their work in explaining diffraction patterns) in 1915. Finally in 1924, Manne Siegbahn won the prize for providing an almost complete description of the electronic shell by studying the characteristic transitions between energy levels via x-ray spectroscopy [4], and it's from him that we get the modern K-, L-, M-edge notation for describing electron transitions. For more information about the scientific history of x-ray spectroscopy, see the work by Farrel Lytle, *The EXAFS family tree: a personal history of the development of extended X-ray absorption fine structure* [5].

1.1   X-ray Absorption Spectroscopy

The first order process known as x-ray absorption, involves the photoelectric effect [6] where a photon is absorbed by a given electron and (assuming the energy of the photon was greater than binding energy) kicks the electron out of the atom. This is shown diagrammatically on the left side of Figure 1.1. The attenuation of x-rays as they pass through a medium is described by the Beer-Lambert law [7] in Eq. 1.1.

$$I(E) = I_0(E)e^{-\mu(E)d} \quad (\textbf{Eq. 1.1})$$

The intensity as a function of photon energy $I(E)$ is exponentially attenuated from its baseline level $I_0(E)$, where $\mu(E)$ is the absorption coefficient as a function of energy and d is the distance through the medium that the beam travels. For most of the x-ray energy regime $\mu(E) \propto Z^4/E^3$ [8], but near the binding energy of electrons in the medium the absorption coefficient spikes up, creating 'absorption edges' such as the ones shown in Figure 1.2 (a). Each edge is labeled based on the occupied quantum state associated with an excitation, with principal quantum number n = 1, 2, 3 corresponding to K, L, and M edges. Within each principal quantum number, they are further broken down numerically according to the angular momentum (l) and total angular momentum (J) quantum numbers. For example, the L_1, L_2, and L_3 edges correspond to the $2s$, $2p_{1/2}$, $2p_{3/2}$ energy levels respectively, where the 1/2 and 3/2 notation is used to denote the spin orbit split $2p$ states. These discontinuities in absorption (specifically the fine structure near the edge) hold information about many electronic and chemical properties such as spin, oxidation state, coordination number, and bond length.
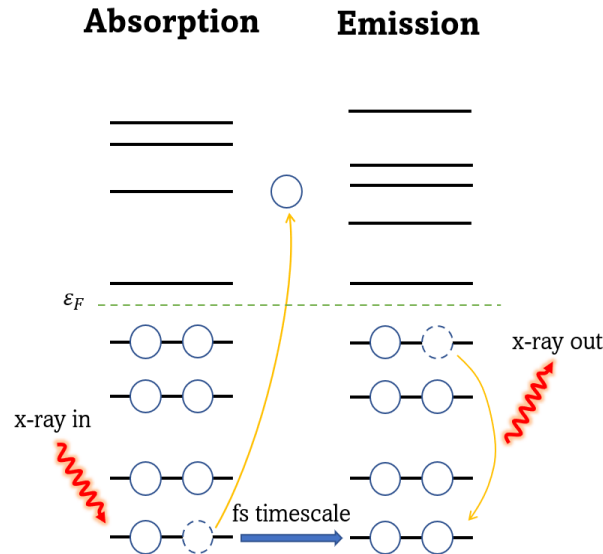
Figure 1.1: Schematic of the x-ray absorption and non-resonant x-ray fluorescence process. Going from left to right, an x-ray (red wiggling line) is absorbed by a core electron (solid blue

circle), which is subsequently ejected from the system into the continuum. A short time later a less tightly bound electron decays into the hole (dashed blue circle) left behind by the deep core electron, emitting an x-ray to preserve energy.

The transition probability per unit time (in the limit of $t \rightarrow \infty$) $\Gamma_{i \rightarrow f}$ from second order perturbation theory between an initial and final state ($|i\rangle$ and $|f\rangle$) is given by Eq. 2 [9, 10]. The δ function is responsible for energy conservation between the initial and final states by enforcing that their difference is equal to the photon energy $\hbar\omega$.

$$\Gamma_{i \rightarrow f} = \frac{2\pi}{\hbar} |\langle f|\widehat{H}|i\rangle|^2 \delta(E_f - E_i - \hbar\omega) \quad \textbf{(Eq. 1.2)}$$

The perturbation, $\widehat{H}$, comes from the interaction of the electromagnetic field with the electronic system and is proportional to $\exp(-i\boldsymbol{k} \cdot \boldsymbol{r}) \, \hat{\boldsymbol{\epsilon}} \cdot \boldsymbol{r}$, where $\boldsymbol{k} = 2\pi/\lambda$ is the wavenumber of the photon, $\hat{\boldsymbol{\epsilon}}$ is the polarization vector of the photon, $\boldsymbol{r}$ is a position vector in real space [11]. The $\exp(-i\boldsymbol{k} \cdot \boldsymbol{r}) \, \hat{\boldsymbol{\epsilon}} \cdot \boldsymbol{r}$ term can be approximated using a Taylor expansion on the basis that the wavelength of the light is much larger than the size of the 1s shell, $\lambda \gg |\boldsymbol{r_{1s}}|$ meaning $\exp(-i\boldsymbol{k} \cdot \boldsymbol{r})\hat{\boldsymbol{\epsilon}} \cdot \boldsymbol{r} \approx (1 - i\boldsymbol{k} \cdot \boldsymbol{r} + (\boldsymbol{k} \cdot \boldsymbol{r})^2/2 + \ldots)\hat{\boldsymbol{\epsilon}} \cdot \boldsymbol{r}$. Keeping the first term, $\widehat{H} \approx (1)\hat{\boldsymbol{\epsilon}} \cdot \boldsymbol{r}$, provides the dipole approximation commonly used in x-ray spectroscopy, and other higher order terms in the expansion give quadrupole, octupole, etc contributions. The relative strength of the different transitions in the expansion will change with the atomic number Z of the element, and therefore the size of the orbitals involved. However, for transition metals (which are the focus of this thesis) the quadrupole transitions are approximately 1/20 the strength of dipole transitions [11] and will be ignored unless otherwise specified.

The observable spectrum $I(\omega)$ is shown in Eq. 1.3 and is known as Fermi's Golden rule (see Sakurai, Chapter 2) [10]. Taking K-edge absorption as an example, the sum over final states

in Eq 1.3 leads to the golden rule formula $I(\omega) \propto 2\pi/\hbar \left| \langle p | \hat{H} | i \rangle \right|^2 \rho_p (E_i + \hbar\omega)$ where ρ_p is the

angular momentum projected density of states (p denoting some degenerate set of states) in the

presence of a core-hole in the final state.

$$I(\omega) \propto \sum_f \left| \langle f | \hat{H} | i \rangle \right|^2 \delta \left(E_f - E_i - \hbar\omega \right) \quad \textbf{(Eq. 1.3)}$$

Zooming in on a single K-edge, a more complex 'fine' structure is observed such as in

Figure 1.2 (c). This absorption edge shows the spectrum from every allowed excitation of an

electron from a 1s shell. For K-edge spectra, the region near the beginning of the discontinuity is

known as the X-ray Absorption Near Edge Structure (XANES) and is usually denoted as

extending from any pre-edge features out to ~30 eV past the edge. The pre-edge region includes

localized transitions of the photoelectron between semi-localized orbitals, while above the edge

the photoelectron is being excited into the continuum [12]. Beyond this, the K-edge spectra ~30

eV up to 500-2000 eV (depending on atomic number) past the edge is known as the Extended X-

ray Absorption Fine Structure (EXAFS). The exact cutoff between XANES and EXAFS is

system dependent but is determined by the onset of plasmon excitations which limits the mean

free path of the photoelectron [13]. The behavior in the region is well understood through the

EXAFS equation [14] given in Eq. 1.4, where N_j is the number of equivalent atoms at radial

distance r_j, $\lambda(k)$ is the mean free path of the photoelectron, σ_j is the Debye-Waller term which

accounts for thermal vibrations, $\delta_j(k)$ is an element dependent phase shift to the scattered

photoelectron, $f_j(k)$ is the scattering factor, and S_0^2 is a term related to the intrinsic losses that

come from the relaxation of other electrons in the excited atom.

$$\chi(k) = \sum_j \frac{S_0^2 N_j f_j(k)}{k r_j^2} \exp\left[-2k^2\sigma_j^2\right] \exp\left[-\frac{2r_j}{\lambda(k)}\right] \sin\left[2kr_j + \delta_j(k)\right] \quad \textbf{(Eq. 1.4)}$$
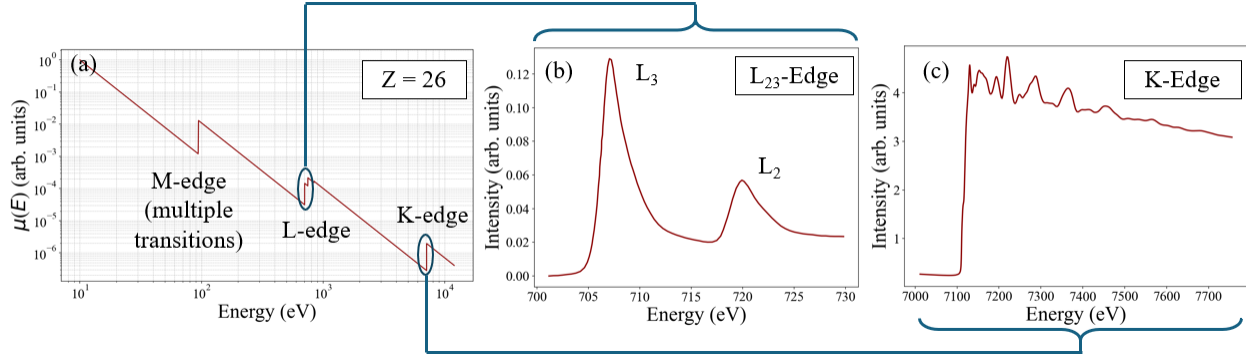
Figure 1.2: (a) Absorption edges for Z=26, (b) zoomed in L$_{23}$-edge to show fine structure (c) zoomed in K-edge to XANES and EXAFS structure.

While the absorption K-edge is likely the most well studied transition line, the L-edge and M-edges can hold additional information, especially when considering that they include dipole allowed transitions to the valence level for a wider range of elements. An example of this is given in Figure 1.2 (b) which shows the $2p$, or L$_{2,3}$, XAS. The spectrum is split into two main peaks which correspond to the spin orbit split $2p_{3/2}$ (L$_3$) and $2p_{1/2}$ (L$_2$) peaks, with each peak further split by many-body interactions coupled to the local environment. This spin orbit splitting is an important feature that allows for additional spin and angular momentum information to be extracted via x-ray magnetic circular dichroism (XMCD), a technique which exploits the difference in absorption from x-rays of left and right helicity [15]. When a magnetic field is applied, the spin-up and spin-down DOS become split, and using light of a certain allows them to be probed independently. A similar technique which uses linearly polarized light is known as x-ray magnetic linear dichroism (XMLD) and is used to study magnetic ordering in materials [16, 17]. Linear dichroism that is present even without a magnetic origin comes from the local

crystallographic anisotropy of a material and is called x-ray natural linear dichroism (XNLD) or just simple x-ray linear dichroism (XLD) [18]. It can be used to learn about the local symmetry of the ligands around an absorbing atom.

1.2 X-ray Photoemission Spectroscopy

While x-ray absorption studies a material by counting the number of photons absorbed at a specific energy, x-ray photoemission spectroscopy (XPS) studies the kinetic energy of the ejected photoelectrons [19]. The measured energy of the emitted electron is the difference between the incoming photon energy (E_{in}) and the binding energy (E_b), $E_k = E_{in} - E_b - \phi$, where ϕ is the work function the describes the energy required for an electron to move from the Fermi surface to vacuum (material surface). Electrons have a much high inelastic scattering cross section compared to photons, which means that many of the photoelectrons that make it out of a material will come from very near the surface. This makes XPS much more surface sensitive compared to other x-ray spectroscopy techniques, with a penetration depth on the order of 10 nm for most materials.

The transition rate for XPS uses the same Fermi's golden rule as in Eq. 1.2, where the final states enforce that the photoelectron gets excited into the continuum so that it can eventually be detected. The states $|s\rangle$ and $\langle f|$ are many-body wavefunctions, and the core-hole left behind by the photoelectron can lead to strong many-body effects known as shake excitations. This is best understood through the sudden approximation which is the basis of modern XPS analysis [20]. This is an extension of the 'final state rule' which states that the experimentally observed dynamics of a transition are dominated by the final state configuration [21]. The sudden approximation uses the fact that the timescale of the photoelectron leaving the atom is much faster than the orbital relaxation time, to approximate the creation of the core-hole

as 'instantaneous'. The ionized ground state wave function is not an eigenstate of the ionized atom's Hamiltonian, leading to many-body shake-up or shake-off processes. These in turn are observed in the XPS spectra, meaning that the binding energy of the photoelectron reflects that of the excited final state configuration.

1.3   X-ray Emission Spectroscopy

The relaxation which follows the creation of a core-hole can happen in two ways: radiatively (x-ray emission) or non-radiatively (Auger process) [22]. In both cases energy is conserved such that the emitted photon or electron carries an energy equal to the difference between the initial and final states of the electron that decays into the core-hole ($E_{emitted} = E_i - E_f$). For this thesis I will focus exclusively on the x-ray emission process (also sometimes called x-ray fluorescence). The full process of core-to-core (CTC) XES involves a core electron absorbing a high energy photon, leaving behind a deep core-hole. After a few fs, the core-hole is filled by a less tightly bound (shallower) electron, and a photon is emitted, leaving the system in a final state with either a semi-core or valence level hole (right side of Figure 1.1).

A diagram showing the initial, intermediate, and final states for a few common transition metal (TM) emission lines is shown in Figure 1.3, reproduced from Glatzel and Bergmann [23]. When studied with modest energy resolution, the resulting x-ray fluorescence is commonly used for elemental identification [24], but when studied with an energy resolution that is comparable to the intrinsic lifetime broadening it can provide more detailed information about electronic, chemical, and material properties [25, 26]. For this thesis, I am particularly interested in studying the K-shell fluorescence lines, where the intermediate core-hole is in the $1s$ orbital. The strongest of these is Kα, which comes from the $2p$ to $1s$ transition. Roughly 20x weaker is Kβ, which

comes from $3p$ to $1s$, and finally about 100x weaker are the transitions from the valence level to the $1s$, often called valence-to-core (VtC) XES.
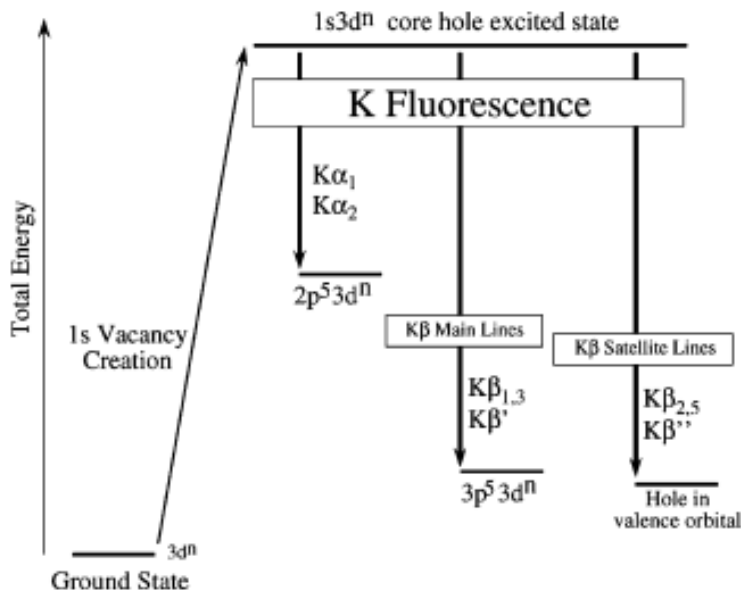
Figure 1.3: "Simplified energy scheme for K florescence emission. The different radiative decay channels of the $1s$ vacancy give rise to the K fluorescence spectrum. The continuum electron that occurs after $1s$ photoionization is neglected in the intermediate and final states. Atomic configurations are used for simplicity." Figure and caption reproduced from Glatzel and Bergmann [23].

For $3d$ transition metals the CTC XES mainly provides information about the spin state of the emitting atom. Kα lines show a spin dependence in the full-width half-maximum of the Kα_1 peak, and Kβ lines show a spin dependence in the strength of in the Kβ' satellite [23]. The physical reasoning behind this will be discussed in Chapter 2, but fundamentally this relationship is a product of the Coulomb interaction between the final state core-hole and the valence orbital.

The K-shell VtC XES comes mainly from metal and ligand hybridized orbitals that contain p-character and can be used for ligand identification. VtC transitions are the weakest, but because they come from the valence shell they tend to hold the largest amount of information about the local environment around the atom. Examples of CtC and VtC XES for multiple transition metals is provided in Figure 1.4, reproduced from Gironda *et al.* [27]. Studying the polarization of emitted light in the VtC XES range of a single crystal can provide information about the local symmetry, as I will explore in Chapter 6.
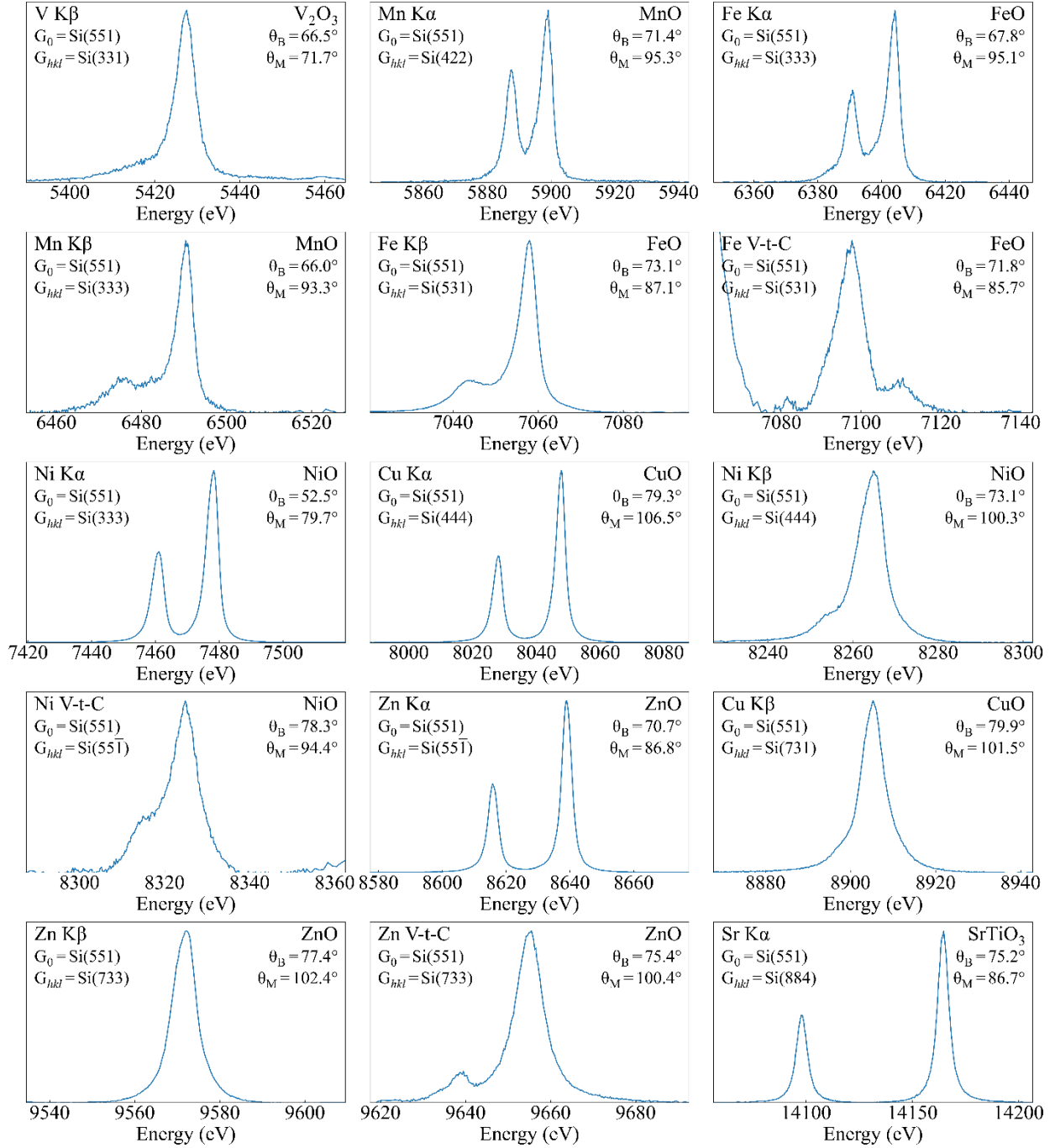
Figure 1.4: Emission lines measured asymmetrically with a Si(551) analyzer, arranged in order of ascending energy, presented with no background subtraction. Figure reproduced from Gironda *et al.* [27].

Sufficient overlap between core and valence levels leads to many-body electronic correlations. These are called multiplet effects and they mean that much of the fine structure in spectra with deep core-hole final states comes from strong Coulombic electron-electron interactions. For $3d$ TMs, the highly localized nature of the $3d$ shell means that multiplet effects become important even at the $2p$-$3d$ level. Properly calculating the multiplet effects will be an important part of this thesis, with the exception of VtC XES. Even in 3d TMs, the valence level electrons tend to expand and delocalize enough when bonding with neighboring atoms (often called ligands) that multiplet effects can be ignored when considering valence to $1s$ core-hole transitions. Functionally, this means that the effect of a hole in the valence shell can be more accurately approximated by a mean-field approach, which I will discuss in more detail in section 1.5.

1.3.1 One Step Versus Two Step Process

The resonant inelastic x-ray scattering (RIXS) of a photon is described by the Kramers-Heisenberg formula [28] shown in Eq. 1.5, where $|I\rangle, |M\rangle, |F\rangle$ are initial, intermediate, and final N-electron many-body states, with corresponding energies E_I, E_M, E_F. The broadenings Γ_M, Γ_F, are due to the lifetimes of the intermediate and final states (not to be confused with the transition rates from Eq. 1.2), respectively, and $\hat{T}_1, \hat{T}_2$, are dipole transition operators. The terms ω_1 and ω_2 are the energies of the incoming and outgoing photons, respectively, making $\omega_1 - \omega_2$ the energy transferred to the system. For a given initial state, every intermediate and final state that can be accessed via the dipole selection rules are summed over. For isotropic spectra, it is also necessary to sum over x, y, and z polarizations of the two dipole operators for a total of 9 combinations. The energy denominator within the absolute value squared enforces energy conservation between the initial and intermediate states, while the Lorentzian profile (the rightmost fraction) enforces

energy conservation between the initial and final states. This representation is slightly different than other modern forms of the Kramers-Heisenberg equation [29], but all that I've done is expand the usual Dirac delta, $\delta(E_I - E_F + \omega_1 - \omega_2)$, into a Lorentzian with the same center to account for the broadening that comes from the lifetime of the final state.

$$\frac{d^2\sigma(\omega_1, \omega_2)}{d\omega_1 d\omega_2} \propto \sum_F \left| \sum_M \frac{\langle F|\hat{T}_2|M\rangle\langle M|\hat{T}_1|I\rangle}{E_I + \omega_1 - E_M + i\Gamma_M/2} \right|^2 \frac{(\Gamma_F/2\pi)}{(E_I - E_F + \omega_1 - \omega_2)^2 + \Gamma_F^2/4} \quad (\textbf{Eq. 1.5})$$

It should be noted that there is an important distinction between the resonant and non-resonant emission processes (sometimes called NXES). In the resonant case, the energy of the incoming photon is set, and the measured emission spectrum is constrained by the intermediate states that can be reached from the incident photon's energy. This is the case described in Eq. 1.5, where the cross section varies as a function of both incident and emission energy.

For non-resonant XES, the emission spectrum comes from a sample that has been excited by a polychromatic incident beam, in which most of incoming photon energy is well above the binding energy of the core electron. This means the photoelectron is excited into a high energy continuum and can be neglected, making it independent in our intermediate and final state wavefunctions. By approximating the continuum density of states and the dipole transition amplitude as constant, the incident energy ω_1 can be integrated out. A full derivation of these steps is provided in Chapter 8, pages 340-341, of de Groot and Kotani's *Core Level Spectroscopy of Solids* [29], but the resulting form is shown in Eq. 5. The states $|m\rangle, |f\rangle$ are N - 1 electron many-body states which do not include the photoelectron, and Γ_m is assumed to be constant. The transition operators are specific to the emission line being studied. However, for K-shell, the intermediate core-hole is always in the $1s$ orbital ($\hat{T}_1 = 1s$), and the polarization term is neglected

because the continuum final state of the photoelectron is no longer relevant. The expression in Eq. 1.6 only holds for ω_1 well above the x-ray absorption threshold, similar to the way that we distinguish the pre-edge from the main-line region in XANES.

$$\frac{d\sigma_{XES}(\omega_2)}{d\omega_2} \propto \sum_f \left| \sum_m \frac{\langle f|\hat{T}_2|m\rangle\langle m|\hat{T}_1|I\rangle}{E_f - E_m - \omega_2 + i(\Gamma_m + \Gamma_f)/2} \right|^2 (\Gamma_m + \Gamma_f)/2\pi \quad (\textbf{Eq. 1. 6})$$

While Eq. 1.6 simplifies the final form of the non-resonant XES, from a practical perspective it still requires calculating the full ω_1, ω_2 plane of RIXS only to then integrate over on of your axes, which I refer to as the 'two-step' process. It is possible to make a further approximation by utilizing the ground state in the presence of the intermediate deep core-hole instead of calculating every accessible intermediate state. By assuming that the non-resonant XES is dominated by emission from this intermediate state Eq. 1.6 can be simplified to the form shown in Eq. 1.7,

$$\frac{d\sigma_{XES}(\omega_2)}{d\omega_2} \propto \sum_f \left| \frac{\langle f|\hat{T}_2|i'\rangle}{E_f - E_{i'} - \omega_2 + i(\Gamma_m + \Gamma_f)/2} \right|^2 (\Gamma_m + \Gamma_f)/2\pi \quad (\textbf{Eq. 1. 7})$$

where the relaxed intermediate state is given by $|i'\rangle$, which I refer to as the 'one-step' process. The physical justification behind this approximation comes from the fact that the valence orbital relaxation time (for $3d$ transition metals) is at least an order of magnitude faster than the deep core-hole lifetime, with the relaxation times of the core orbitals being even faster. The orbital relaxation times and core-hole lifetimes are nearly linear as a function of atomic number and are shown in Figure 1.5. This means that as the valence electrons have plenty of time to re-arrange themselves and relax in the presence of the core-hole potential, and it's reasonable to assume that many of the intermediate states that are directly accessed via absorption are *not* the state that an

ionized atom is in immediately before emission occurs. To perfectly model this process,

additional relaxation channels like plasmon and phonon processes that carry energy away from

the excited atom [30] would need to be considered. However, this relaxed intermediate

approximation is already successfully applied [31, 32] by the spectroscopy community, and I will

demonstrate in Chapter 3 its validity for K-shell emission of $3d$ transition metal systems.
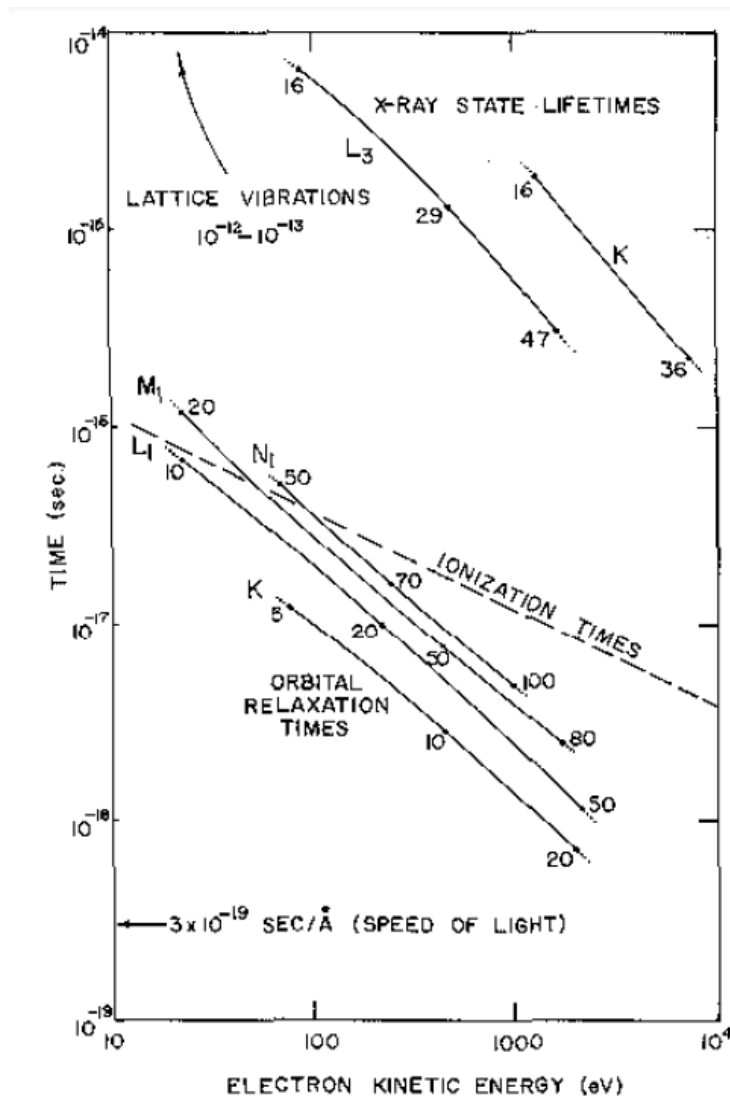
Figure 1.5: "Ionization, relaxation, and x-ray excited-state times for the atomic numbers and shells indicated. The ionization time is taken to be the time required for an electron with the indicated kinetic energy to travel two angstroms. Relaxation times and lifetimes are plotted against the kinetic energy of the electron in the atomic orbitals indicated". Figure and Caption reproduced from Nagel's *Interpretation of Valence Band X-ray Spectra* [33].

1.4   Experimental Instrumentation

This thesis is primarily focused on the study of methods for calculating x-ray emission spectra, and for comparison, many compounds were experimentally measured in a lab-based setting. While this setup differs somewhat from the traditional synchrotron setup, the fundamental principles are still the same [34]. All spectra presented in this thesis were measured by either myself or my collaborators at the University of Washington and easyXAFS LLC, unless otherwise mentioned. Extensive details of the instrument used can be found in Jahrman, *et al.* [35], but I will briefly summarize it here.

To get a high-resolution spectrum of the transition metal K-shell fluorescence, the emission was measured using a crystal analyzer arranged in a Rowland circle geometry, shown in figure 1.6. The sample is illuminated with a conventional x-ray tube (Varex VF80, Pd-Anode) operated at 100 W electron beam power (35 kV, 2 mA). The sample and detector are arranged in the Rowland plane allowing for point-to-point focusing, limited only by the size of the entrance slit [36]. This is a Johann type spectrometer, the focal properties of which have already been well studied in previous work [37, 38]. By scanning the sample and detector through θ, the energy of the focused beam that reaches the detector is changed according to Bragg's law in Eq. 1.8 [39].

$$2d \sin\theta = n\lambda \quad (\textbf{Eq. 1.8})$$

The Bragg angle θ is the angle the incident x-rays make with the crystal plane, d is the spacing of the crystal planes, and λ is the wavelength of the x-rays. Bragg's law assumes only a single scattering event, and multiple scattering diffraction can lead to broadening of the reflected x-rays [40]. However, this effect is relatively small compared to the other sources of experimental broadening (on the order of 0.1 eV) [23], and I will neglect it for the purposes of determining the appropriate experimental broadening. By using a suite of high-quality silicon and germanium crystals to create the spherically bent crystal analyzer (SBCA), it's possible to measure x-rays at a wide range of relevant energy for transition metal systems, from roughly 1 keV to 10 keV [27].
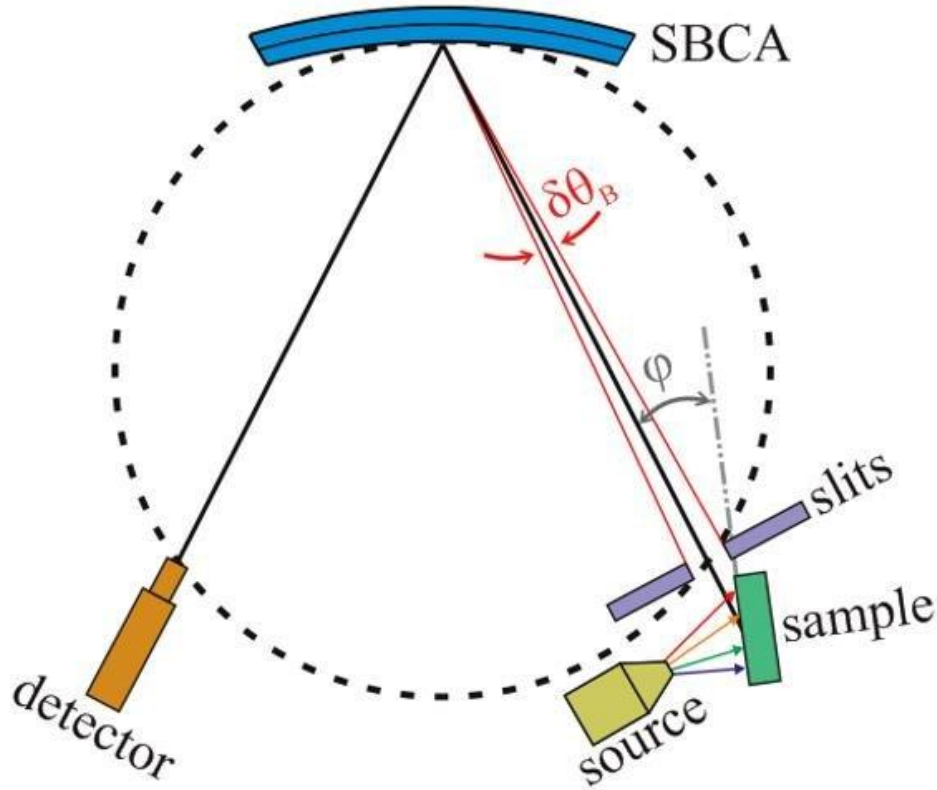
Figure 1.6: The lab-based Rowland-circle spectrometer. The slit in front of the sample provides a finite sized source with angular width of $\delta\theta_B$, assuming the illuminated portion of the sample is

large enough to completely fill the slit. The sample is slightly rotated (φ) to allow improved line-of-sight to the SBCA. Reproduced from Mortensen *et al*, 2016 [41]

1.4.1 Source Size Broadening

The experimental broadening can be separated into 2 main sources: source size and Johann broadening, both of which are geometric. Source size broadening comes from the finite sized entrance slit, which cannot be approximated as a perfect point source. The amount of source size broadening depends on the x-ray energy (E_0), radius of the Rowland circle (r), slit width (d_s) and Bragg angle (θ_B) of the specific experimental setup. A derivation of the source size broadening is shown in Figure 1.7, where in (a) the center of the source slit lies on the Rowland circle at (s_x, s_y) and the vector $\vec{\rho}$ defines the chord from the top of the Rowland circle to the source slit. For convenience, ϕ_B is defined to be 90° minus the Bragg angle θ_B. (b) The source slit has some finite width d_s. The vectors $\vec{s}_L$ and $\vec{s}_R$ define the line from the top of the Rowland circle to the left and right edges of the slit respectively. The range of energies allowed in by the slit is shown in (c). The Bragg condition is $E = E_o/Sin(\theta)$ where E_o depends on the specific crystal plane and analyzer. Using the minimum $(90° - \phi_L)$ and maximum $(90° - \phi_R)$ Bragg angles the energy window ΔE associated with the finite source size can be calculated. For simplicity, the source slit can be approximated to be much smaller than the radius of the Rowland circle, $d_s \ll r$, which gives a much simpler expression. Subplot (d) shows a plot of the energy window ΔE for various Bragg angles with an E_o of 8000 eV, slit width of 1 millimeter, and Rowland circle radius of 1 meter. Notice how ΔE approaches zero at backscatter. Subplot (e) shows a plot with the same E_o and Rowland circle radius as (d) but this time the Bragg angle is set to 75° and the slit width is allowed to vary. Here the slit width is sufficiently smaller than the Rowland circle radius, causing ΔE to be linearly related to d_s in agreement with the final

equation from (c). The approximate form of ΔE shown in (c) breaks down when approaching

backscatter ($\phi_B \rightarrow 90°$). The source size broadening rapidly approaches zero, demonstrating why

there is often much effort put in to operating near backscatter whenever possible [42].

a)

$\phi_B = 90° - \theta_B$
$|\vec{\rho}| = r\,Cos(\phi_B)$
$s_x = r\,Cos(\phi_B)\,Sin(\phi_B)$
$s_y = -r\,Cos(\phi_B)\,Cos(\phi_B)$

b)

$\vec{s}_L = \left(s_x - \frac{d_s}{2}Cos(\phi_B)\right)\hat{\imath} - \left(s_y + \frac{d_s}{2}Sin(\phi_B)\right)\hat{\jmath}$

$\vec{s}_R = \left(s_x + \frac{d_s}{2}Cos(\phi_B)\right)\hat{\imath} + \left(\frac{d_s}{2}Sin(\phi_B) - s_y\right)\hat{\jmath}$

c)

$$\phi_R = Cos^{-1}\left(\frac{-\hat{\jmath}\cdot\vec{s}_R}{|\vec{s}_R|}\right) \quad \phi_L = Cos^{-1}\left(\frac{-\hat{\jmath}\cdot\vec{s}_L}{|\vec{s}_L|}\right)$$

$$\Delta E = E_o\left(\frac{1}{Sin(90° - \phi_R)} - \frac{1}{Sin(90° - \phi_L)}\right)$$

$$Sin(90° - x) = Cos(x), \quad \Delta E = E_o\left(\frac{|\vec{s}_R|}{-\hat{\jmath}\cdot\vec{s}_R} - \frac{|\vec{s}_L|}{-\hat{\jmath}\cdot\vec{s}_L}\right)$$

$$\Delta E = \frac{2d_s E_o\,Sin(\phi_B)\sqrt{d_s^2 + 2r^2(1 + Cos(2\phi_B))}}{4r^2 Cos(\phi_B)^4 - d_s^2 Sin(\phi_B)^2}$$

$$\lim_{d_s \ll r} \Delta E \approx \frac{d_s E_o\,Sin(\phi_B)}{r\,Cos(\phi_B)^3}$$
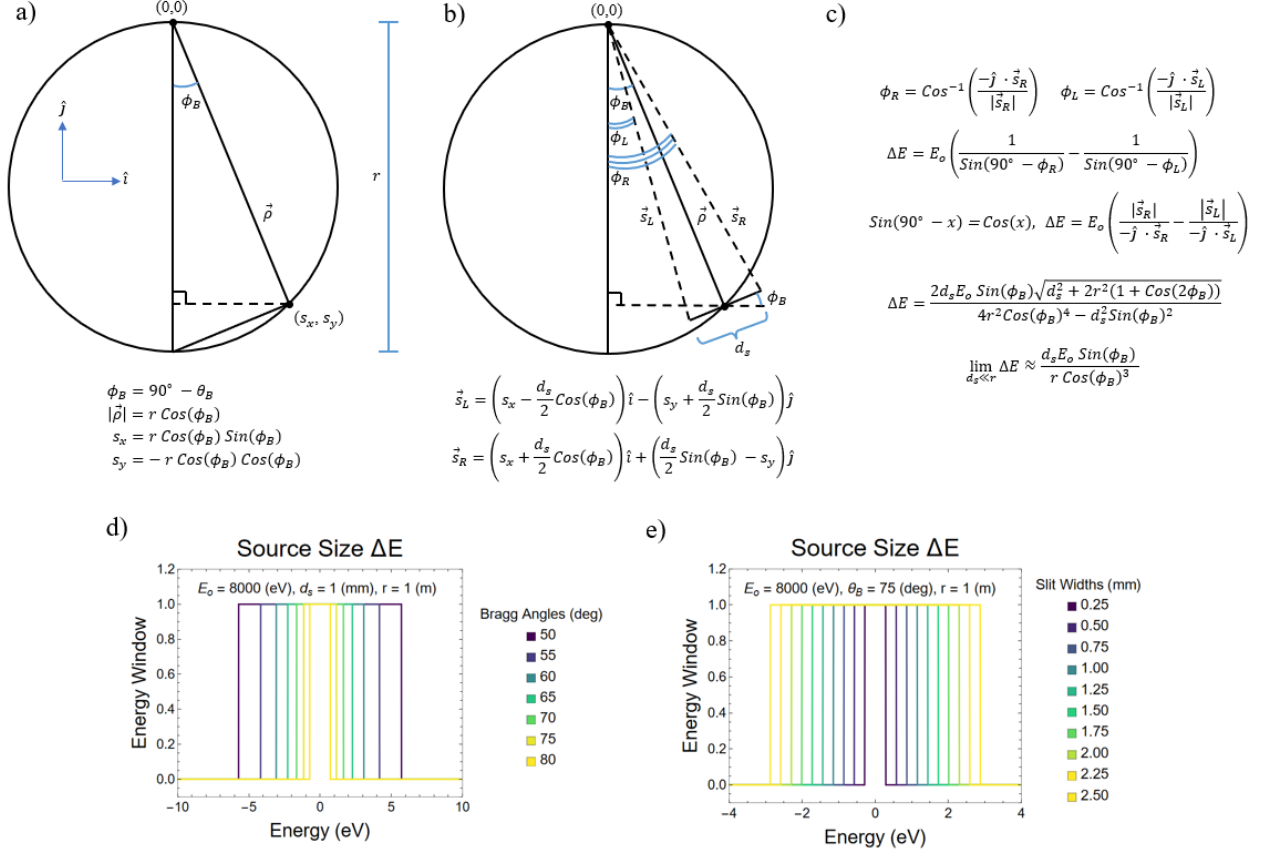
Figure 1.7: Derivation of the broadening ΔE that comes from a finite source size. Subplots (a)

and (b) give a diagram of the 2-dimensional slit with width d_s, centered at (s_x, s_y), and oriented

to be perpendicular to the cord running from the top of the Rowland circle to the slit center $\vec{\rho}$. (c)

Steps for deriving the broadening ΔE given the angular width of the slit as $\phi_R - \phi_L$ and Bragg's

law in Eq 7. (d) and (e) show the source size broadening for a given experimental setup for

variable Bragg angles and slit widths respectively.
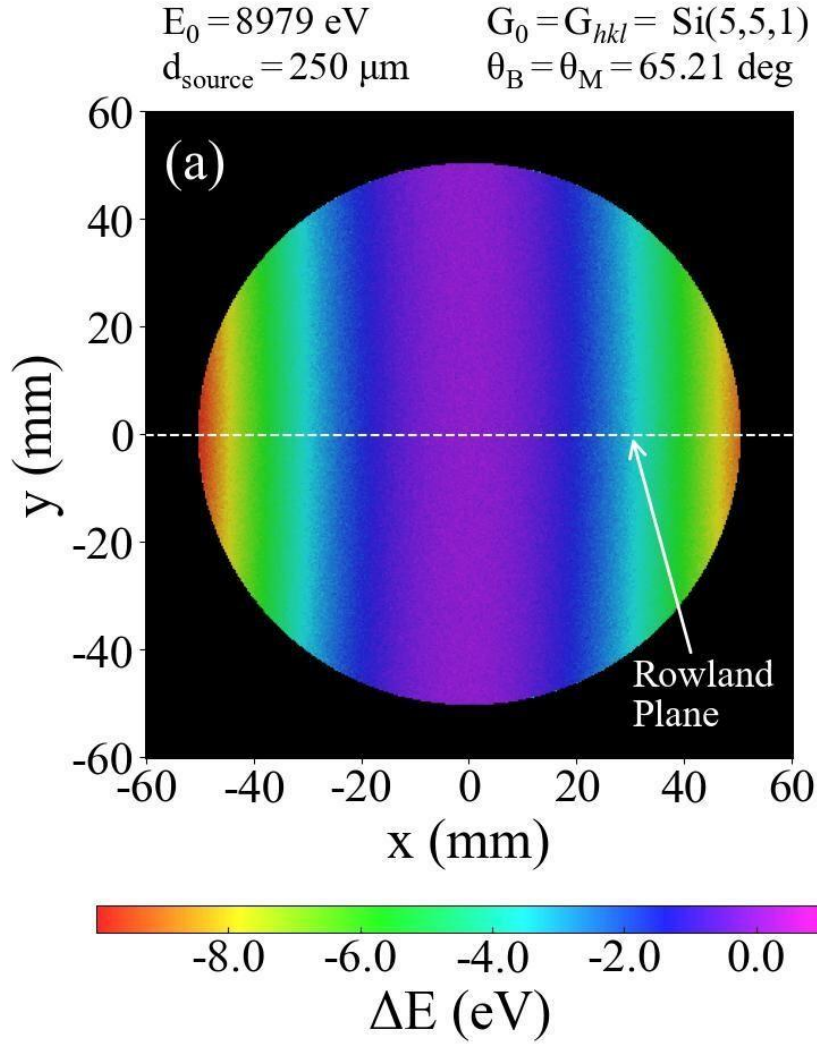
Figure 1.8: "XRT ray traced simulation of a Si(551) operated symmetrically far from backscatter, demonstrating Johann error as lower diffracted energies on the left and right sides of the crystal" Figure and caption reproduced from Gironda *et al*. [27].

1.4.2 Johann Broadening

Johann broadening is a result of the how the spherically bent crystal analyzer (SBCA) is experimentally implemented within the Rowland circle geometry of an x-ray spectrometer [43], shown in Figure 1.9. For perfect point to point refocusing the Bragg condition from equation Eq. 1.8 must be the same at every point on the analyzer, but this can only be achieved by bending the

analyzer to have twice the radius of the Rowland circle and then grinding it down so that the face of the analyzer matches the curvature of the circle. This is known as the Johannson geometry [44], and while it provides the most ideal experimental operating conditions, the economics and practical difficulty of manufacturing such crystal analyzers means that most x-ray spectrometers operate using the conventional Johann geometries. The error introduced by a Johann configuration is an asymmetric broadening in energy which gets worse when further away from backscatter, as demonstrated with ray tracing in Chen *et al* [45]. An example of this is shown in Figure 1.8 where the x-rays reflected from the center of the analyzer (dark purple) have no energy shift, but moving towards the edge of the analyzer the source to detector Bragg condition requires a larger Bragg angle and energy of the reflected rays decreases in energy ($E \propto 1/\sin(\theta)$). The exact form of this asymmetric broadening depends on the Bragg angle, energy of radiation, and source size but it can be mitigated by operating at a high Bragg angle as much as possible.
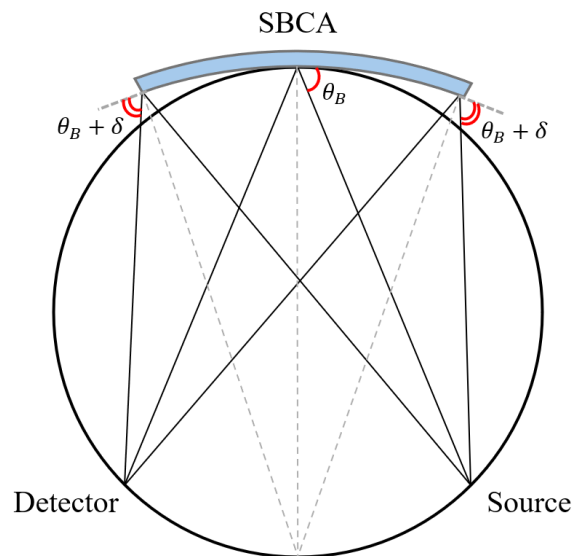
Figure 1.9: Rowland circle diagram with a crystal analyzer in the Johann configuration. The analyzer is bent to a radius of twice the Rowland circle, but gaps between the circle and the analyzer get larger away from the center and give a different Bragg condition $(\theta_B + \delta)$ for the source to detector refocusing.

The experimental XES presented in this thesis were taken with a spectrometer configuration optimized for high Bragg angles and small source sizes (0.5 mm for data taken at UW and 0.25 mm for data taken at easyXAFS). The two experimental broadening sources I have mentioned so far are important for ruling out sources of error for later sections where I will directly compare theory and experiment. However, I have found that it is sufficient to approximate the line shape of the experimental broadening as a simple Gaussian with width between 0.5 and 1.0 eV depending on the experiment [11]. This, in combination with lifetime broadening provides a good, if somewhat simplified, method for broadening raw theoretical spectra for comparison with experiment, as I will demonstrate in Chapter 4.

1.5   Theoretical Methods in X-ray Spectroscopy

Depending on the system and spectroscopy in question, different levels of theory and approximation are required for accurately calculating these wavefunctions. The focus of this thesis will be on multiplet methods specifically for $3d$ transition metals, which I will discuss in extensive detail in Chapter 2. Here though I will provide brief context as to other common approaches to determining the electronic structure of a material for calculating spectra. The following is by no means an exhaustive list, but a brief overview of techniques that are connected to work in this thesis.

1.5.1 Density Functional Theory

Density Functional Theory (DFT) is perhaps the most well-known method in computational condensed matter and quantum chemistry. While on its own it is strictly a ground-state method, it is often used in conjunction with other techniques to provide a starting point for spectroscopy calculations. DFT is used for that exact reason in this thesis, and so I will cover it in detail here.

DFT has its origins in early work on the statistics of electron gases done by Thomas and Fermi [46], modern DFT is rests on the work of Hohenberg, Kohn, and Sham. The Hohenberg-Kohn theorems form the theoretical foundation for DFT by asserting that (1) the ground-state energy of a system is unique functional of the electron density $\rho(r)$, Eq. 1.9, and (2) the ground-state energy corresponds to an electron density that minimizes this energy functional [47]. Functionally, this provides a massive simplification over wavefunction based approaches given an N electron problem can be reformulated into a functional of the electron density with only 3 spatial degrees of freedom. The density can be used to determine all terms within the Hamiltonian (up to a constant), meaning that there is a one-to-one mapping between the electron density and the wavefunctions of an N-electron system.

$$\rho(r) = N \int \Psi^*(r, r_i, \dots, r_N) \Psi(r, r_i, \dots, r_N) dr_i \dots dr_N \quad \textbf{(Eq. 1.9)}$$

A method for putting these theorems into practice comes through the use of a non-interacting reference system as demonstrated by Kohn and Sham [48]. The classical Coulomb ($J[\rho(r)]$, sometimes called the 'Hartree' term) and exchange-correlation ($E_{XC}[\rho(r)]$) are separated out from the kinetic ($T_s[\rho(r)]$) and nuclear potential ($V_N(r)$) terms of the density functional as shown in equation Eq. 1.10.

$$E[\rho(r)] = T_s[\rho(r)] + J[\rho(r)] + E_{XC}[\rho(r)] + \int V_N(r)\rho(r)dr \quad \textbf{(Eq. 1.10)}$$

Kohn and Sham use the variational principle to demonstrate that a corresponding system with no electron-electron interactions but the same density $\rho(r)$ from an external potential $V_{eff}(r)$ is equivalent to the interacting case if $V_{eff}(r) = e^2/(4\pi\epsilon_0) \int \rho(r)/(r-r')dr' + V_{XC}(r) + V_N(r)$, where $V_{XC}(r) = \delta E_{XC}/\delta\rho(r)$. The important takeaway is that by using an effective potential the solutions to the Schrödinger equation (Eq. 1.11) provide a single-particle description of a many-electron system. The eigenfunctions of Eq. 1.11 are known as the Kohn-Sham orbitals and they provide a basis for determining the density from Eq. 1.8, assuming some temperature dependent occupation [46]. This can then be used to recalculate the effective potential $V_{eff}(r)$ in a self-consistent loop, providing the energy and density of the ground state.

$$\left[\frac{\nabla^2}{2} + V_{eff}(r)\right]\psi_i(r) = \epsilon_i\psi_i(r) \quad \textbf{(Eq. 1.11)}$$

This method conveniently brushes the combinatoric complexity of large N-electron systems into the exchange-correlation (XC) functional $E_{XC}[\rho(r)]$. Many different functionals exist with two of the most common being the local-density approximation (LDA) and generalized gradient approximation (GGA). These are both derived from a reference system (the homogenous electron gas), which assumes that the electron density $\rho(r)$ is constant throughout space. As their names suggest, these XC functionals are only semi-local approximations and they fail to fully cancel the self-interaction introduced from the Hartree term. This leads to electrons interacting with their own density and causing an over delocalization of the electron density. More advanced hybrid functionals can include a fraction of the Hartree-Fock exchange to try to compensate for this, and there are entire families of functionals dedicated to better approximating the exchange-correlation for different systems [49, 50]. However, DFT generally fails when

dealing with highly correlated systems with more localized electrons, which is a large focus of the work in this thesis. There are many systems though the electrons near the Fermi level are already relatively delocalized compared to atomic systems, and DFT can do a good job at predicting the density of states, band structures, optimized molecular structures, and other ground state properties for these materials.

While DFT is designed for ground-state calculations, it has seen extensive application to valence level spectroscopies such as for calculating the pre-edge in XAS or VtC-XES [51, 52]. By solving a time-dependent version of the Kohn-Sham equations [53] a modified version of DFT, known as time-dependent DFT (TD-DFT) can determine the response of the density to an external time-dependent potential. This approach was built off a 1984 paper by Runge and Gross [54], who showed that a time dependent single-particle potential will uniquely determine a time dependent density much the same was as Hohenberg and Kohn did for static DFT. This approach is relatively widespread and implemented in electronic structure codes such as `NWChem` [55] and `ORCA` [56].

1.5.2   Real Space Green's Function Methods

The single particle Green's function $G(r, r'; E)$ is defined in Eq. 1.12 and gives the relative probability amplitude for an electron to propagate from r to r' at energy E for a given effective one-electron Hamiltonian H. The term Γ is a small positive number that helps enforce physical solutions. Codes like `FEFF` have been used for efficiently calculating XANES, EXAFS, XES, XMCD, and non-resonant inelastic x-ray scattering (NIXS) via within the real-space multiple-scattering Green's function formalism [57]. The Green's function itself can be used to efficiently describe how electrons scatter from nearby atoms in aperiodic systems, while the imaginary part is related to the local density of states. Spectroscopic quantities can be calculated

from the Green's function in much the same way as Eq. 1.3 and Eq. 1.4 (this will be addressed in more detail in the supplemental info of Chapter 4).

$$G(r, r'; E) = \langle r | (E - H + i\Gamma)^{-1} | r' \rangle \quad (\textbf{Eq. 1.12})$$

The one-electron nature of the Green's function is treated by the exchange-correlation effects with an LDA functional. This means that it has the same sort of limitations when it comes to core-level spectroscopies in highly correlated systems as TDDFT has. Regardless of this, the full multiple scattering approach is critical for reproducing the photoelectron's behavior in XANES and EXAFS, and codes like `FEFF` have been massively successful at interpreting experimental results [58-60] and creating machine learning datasets [61-63].

1.5.3 Multireference Wavefunctions

Multireference methods represent many body states using a linear combination of Slater determinants to explicitly describe the different excited state configurations [64]. The energy of the states is solved by simultaneously optimizing the coefficients on the Slater determinants and the molecular orbitals in a self-consistent manner. When this is done for a certain subset of partially filled orbitals it is known as Complete Active Space Self-Consistent Field (CASSCF). While this method is one of the most sophisticated ways to treat electronic structure, in practice it is very computationally expensive, and it only applicable to small particle number (n) systems. Restricted Active Space Self-Consistent Field (RASSCF) is more suitable for treating larger systems by placing restrictions on the number of excitations in the subset of orbitals. For x-ray spectroscopy of singly excited core-states, this is ideal, but for highly correlated $3d$ systems a more complete treatment of the allowed excitations is often necessary. While this approach has been implemented in many codes [56, 65, 66], it has only recently been applied to core-level

spectroscopies [67]. The choice of the active space is incredibly important as the type of allowed excitations, e.g. spin-flip, shake-up, charger transfer, will depend on which orbitals are included. This method also allows the ligand electrons to be treated directly within the molecular orbital framework. Active space methods which include the metal $3d$, metal core-hole, and ligand electrons correspond to a self-consistent treatment of the electrostatic and charge transfer effects that I will discuss in Chapter 2.

Other methods include configuration interaction (CI), which uses the Hartree-Fock states as single-particle orbitals and constructs excited configurations as linear combinations of the Hartree-Fock ground states [68]. Full CI includes all possible configurations with the correct symmetry for a given system, but often the CI space is truncated by limiting the number of allowed excitations to reduce computational cost. CI naturally captures multiplet effects in partially filled shells, as the mixing of determinants with different spin and orbital occupations reproduces the energy splittings observed in strongly correlated systems. Finally, a related but distinct method called coupled cluster (CC) builds the wavefunction using an exponential ansatz of excitation operators acting on a single reference determinant [69]. Unlike CI, which uses a linear combination of determinants, CC captures dynamic correlation in a size-extensive and highly accurate manner [70].

Chapter 2 Multiplet Ligand Field Theory

2.1   History and Background

I will begin by clarifying some of the terms used in MLFT. The term "multiplet" is generally used to describe a grouping of electrons, and "multiplet interactions" or "multiplet splittings" are a result of the electron-electron Coulomb interactions within that electron group. Both "multiplet states" and "multiplet configurations" refer to the specific arrangement of electrons in terms of spin-orbital occupation. I will use the term "state" to describe a specific arrangement of electrons, and "orbitals" to describe which fermionic modes (ex: p_x spin-up, d_{xy} spin-down) are being occupied. Naturally multiplets only become important when describing partially filled shells, as the contribution of the Coulomb interaction to the total energy changes depending on the state of the system. Close shell systems (ex: Ne $1s^2 2s^2 2p^6$) can only be described by a single configuration and multiplet effects become moot. Phenomena such as Hund's rule [71] which govern how electrons fill the atomic shells are a product of multiplet effects, which penalize certain electron configurations (e.g. two electrons occupying the same orbital) with an energy cost. The term "crystal field" and "ligand field" are used somewhat interchangeably in literature [29, 72], but both refer to the perturbation on the valence level orbital from a static charge model of nearby ligands. I will use the term "crystal field" exclusively to address this perturbation.

Multiplets play a critical role in core-level spectroscopy because they treat the many-body electron-electron interaction between the partially filled core and valence levels. Practically, the energies of these configurations are framed through the Slater-Condon terms, which I will address in the next section. The multiplet combinatorics of even medium sized

systems quickly becomes difficult to deal with. For example, a single Mn atom has a partially

occupied $3d$ shell, with 5 d electrons and 5 holes. The total number of unique configurations is

10 choose 5, or $\frac{10!}{2*5!} = \mathbf{252}$. On its own this isn't too bad, but to model a system of just 2 Mn

atoms all interacting with each other (such as a solid), that would be $\frac{20!}{2*10!} = \mathbf{184756}$

configurations. The number of configurations goes up another 3 orders of magnitude when you

add the next Mn atom. This exponential scaling is part of what makes mean field approaches so

attractive, because they don't have to deal with an explicit treatment of the electron behavior. It

is for this reason that multiplet approaches tend to treat systems as perturbed atomic clusters,

where we focus only on the local effects around the atom of interest.

In purely atomic systems, many configurations are degenerate in energy and it's not until

we start to add in crystal field (section 2.3) and charge transfer (2.4) effects that this degeneracy

begins to be broken down. The strength of these local perturbations, as well as how the energies

of the atomic multiplets change due to valence level bonding, are all parameterized as a part of

MLFT. This means that for any system, the model can be adapted to match the specific local

bonding environment to produce a good agreement with any physical observables (e.g. x-ray

spectra). This has contributed broadly to the popularity of MLFT, and it is one of the most widely

used theory methods for treating core-level spectroscopies of highly correlated systems [31, 67,

73].

However, MLFT has two main drawbacks. 1) The popularity of the technique is partially

because the many parameters allow for the calculated spectra to be fit to the spectra. These fits

generally agree well with experiment, but the large parameter space means that it can be difficult

to confidently determine the "best" combination of parameters. This means that there are many

potential pitfalls, where small changes in broadening, alignment shifts, or even the choice of starting local geometry can lead to different fitting parameters being published for the exact same material and spectra. An example of this is shown in Figure 2.1 where for the Ni $L_{2,3}$ XAS, 3 different spectra are shown, each one corresponding to a calculation done assuming a different local geometry around the Ni atom. The same broadening (1 eV FWHM Lorentzian broadening) and alignment shift (main L_3 peak shifted to 0 eV) are applied to every spectrum. I have explicitly chosen parameters which demonstrate just how similar MLFT calculated spectra can be, even for systems for which the local geometry is very different. In this specific example only atomic and crystal field perturbations are considered, but only 2 to 4 free parameters is enough to produce theoretical spectra which are barely experimentally resolvable. These spectra, along with all other core-to-core spectra presented in this thesis were calculated using the many-body scripting code `Quanty` [74], unless otherwise mentioned. The key point here is that it is remarkably easy for two people to obtain essentially the same spectrum using different parameters when both are working within the MLFT framework. This has led to incorrect physical interpretation of spectra in past work [75, 76].
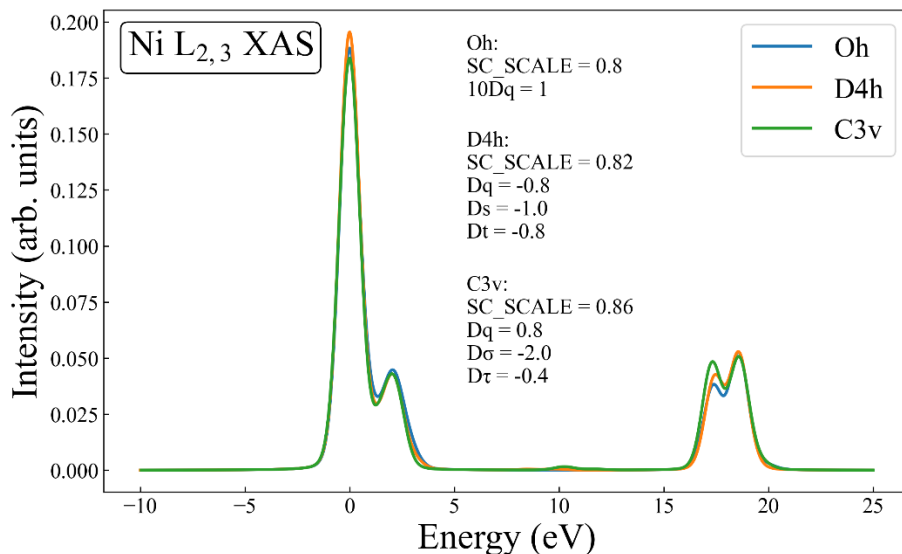
Figure 2.1: Calculated Ni $L_{2,3}$ x-ray absorption for 3 different local geometries (O_h, D_{4h}, C_{3v}). The Slater-Condon scaling parameter and crystal field splittings for each system are reported in the plot.

2) The second main drawback comes from the fact that MLFT relies on parameters at all. This dramatically limits the application of the theory to being restricted to interpretive tasks instead of predictive ones. While not exclusively, many x-ray spectroscopy methods rely on expensive and state-of-the-art facilities to collect data. Given the limited access to this technique, having a reliable method of predicting spectra is imperative to informing new experimental directions, as good theory can help confirm novel results, highlight experimental issues, and even predict potential systems of interest. Groups from any discipline that are interested in studying core-level spectroscopy of highly correlated materials can't rely on MLFT until after they've already gone through the work of measuring a spectrum, and then they must trust that whatever fit they get to their data provides a reliable interpretation of the underlying physics. For good reason, these two issues limit the widespread adoption of this theory, and this is why there is a need for new development of a more reliable and more *ab-initio* version of MLFT. The details of that new development will be discussed in section 3.

2.2 Atomic Beginnings

The Hamiltonian which describes an atomic system in the Born-Oppenheimer approximation is given in equation Eq 2.1, where the first term denotes the kinetic energy of electron i, the second term is the nuclear potential, the third term is the electron-electron Coulomb term between every pair of electrons ij, and the last term is the spin-orbit coupling [77]. The prefactor $\zeta(r_i)$ is an element and orbital specific constant, but it changes very little with changes in bonding environment and therefore can be treated as a constant. The terms

which dominate the fine-structure of any core spectroscopy are the Coulomb and spin-orbit coupling, with the single-particle kinetic and nuclear potential only contributing and overall shift to the energy of the system. Most of the interesting physics that dominates multiplet theory comes from the treatment of the Coulomb term, which thanks to the work of Slater in 1929 [78] and Condon in 1930 [79] this term can be broken up into angular and radial components for efficient evaluation.

$$H = \sum_i \frac{p_i^2}{2m} - \sum_i \frac{Ze^2}{r_i} + \frac{1}{2} \sum_{i \neq j} \frac{e^2}{|r_i - r_j|} + \sum_i \zeta(r_i) l_i \cdot s_i \quad (\textbf{Eq. 2. 1})$$

The Coulomb term can be rewritten in second quantization to have the form shown in equations Eq. 2.2 and 2.3, where $\tau_i = n_i l_i m_i \sigma_i$ labels a set of quantum numbers. By expanding the $1/|r_i - r_j|$ term in spherical harmonics, the angular and radial integrals can be separated. The angular component is just a product of two Gaunt coefficients [80], which are straightforward to calculate and well tabulated. The radial term can be further separated into the direct (F) and exchange (G) Slater integrals [77, 81] which are shown in equations Eq. 2.4 and 2.5. Within an orbital, there are only direct terms with Slater integrals $F^{(k)}$ where k goes from 0 to $2l$ in steps of 2 (ex: for a $3d$ orbital, the Slater integrals are F^0, F^2, and F^4). Between orbitals the direct Slater integrals are counted going from to 0 to $Min[2l_1, 2l_2]$ in steps of 2, and the indirect Slater integrals, $G^{(k)}$, go from $|l_1 - l_2|$ to $|l_1 + l_2|$ in steps of 2 (ex: there are four Slater integrals between a $2p$ and $3d$ orbitals; F^0, G^1, F^2, G^3).

$$H = \frac{1}{2} \sum_{i \neq j} \frac{e^2}{|r_i - r_j|} = \sum_{\tau_1 \tau_2 \tau_3 \tau_4} U_{\tau_1 \tau_2 \tau_3 \tau_4} \hat{a}_{\tau_1}^\dagger \hat{a}_{\tau_2}^\dagger \hat{a}_{\tau_3} \hat{a}_{\tau_4} \quad (\textbf{Eq. 2. 2})$$

$$U_{\tau_1\tau_2\tau_3\tau_4} = -\frac{1}{2}\delta_{\sigma_1,\sigma_3}\delta_{\sigma_2,\sigma_4}\sum_{k}^{\infty}\frac{4\pi}{2k+1}\langle Y_{m_1}^{l_1}|Y_{m_1-m_3}^{k}|Y_{m_3}^{l_3}\rangle\langle Y_{m_4}^{l_4}|Y_{m_4-m_2}^{k}|Y_{m_2}^{l_2}\rangle$$

$$\times R^k[\tau_1\tau_2\tau_3\tau_4] \quad (\text{Eq. 2.3})$$

$$R_{direct}^{k} = F^{(k)} = e^2\int_0^{\infty}\int_0^{\infty}\frac{Min[r_i,r_j]^k}{Max[r_i,r_j]^{k+1}}R_1[r_i]^2R_2[r_j]^2dr_idr_j \quad (\text{Eq. 2.4})$$

$$R_{exchange}^{k} = G^{(k)} = e^2\int_0^{\infty}\int_0^{\infty}\frac{Min[r_i,r_j]^k}{Max[r_i,r_j]^{k+1}}R_1[r_i]R_1[r_j]R_2[r_i]R_2[r_j]dr_idr_j \quad (\text{Eq. 2.5})$$

The radial wave function can be solved for with a self-consistent Hartree-Fock approach using Cowan's code [82], which gives decent agreement between theory and experiment for atomic spectra [83]. However, in solids the radial wavefunctions will change due to bonding, leading to less overlap in what is known as the nephelauxetic effect. The electron-electron repulsion is effectively screened by the delocalization of electrons and states that are not explicitly included in this model. The average screened electron-electron interaction can be written as $U_{dd} = F^0 - \frac{2}{63}(F^2 + F^4)$ [81]. However, this screening primarily affects the monopole component of the Coulomb interaction, F^0, which can go from ~20 eV for a free atom to ~5 eV in a solid [84]. The F^2 and F^4 multiplet terms change much less and are frequently modeled as being reduced by some constant scalar from their atomic values. Often the Slater-Condon scaling parameter is taken factor is taken to be ~0.8, but in practice it is a parameter that can tweaked when fitting to experiment [31, 85, 86]. An example of how varying this parameter affects a spectrum is shown in Figure 2.2 for the 2p-XAS of Ni in NiO. At low scaling (0.2) the spectra is comprised entirely of the spin-orbit coupling within the 2p shell, and when the scaling factor is closer to atomic values the fine structure that comes from the interaction between the 2p

core-hole and the $3d$ shell causes features to emerge. The atomic scaling factor for the multiplet interaction works reasonably well for charge neutral spectroscopies (ex: $2p$ to $3d$ XAS), but once charge begins transferring too and from the metal ion, the screened average Coulomb term U_{dd} becomes much more important, as will be addressed in section 2.4.
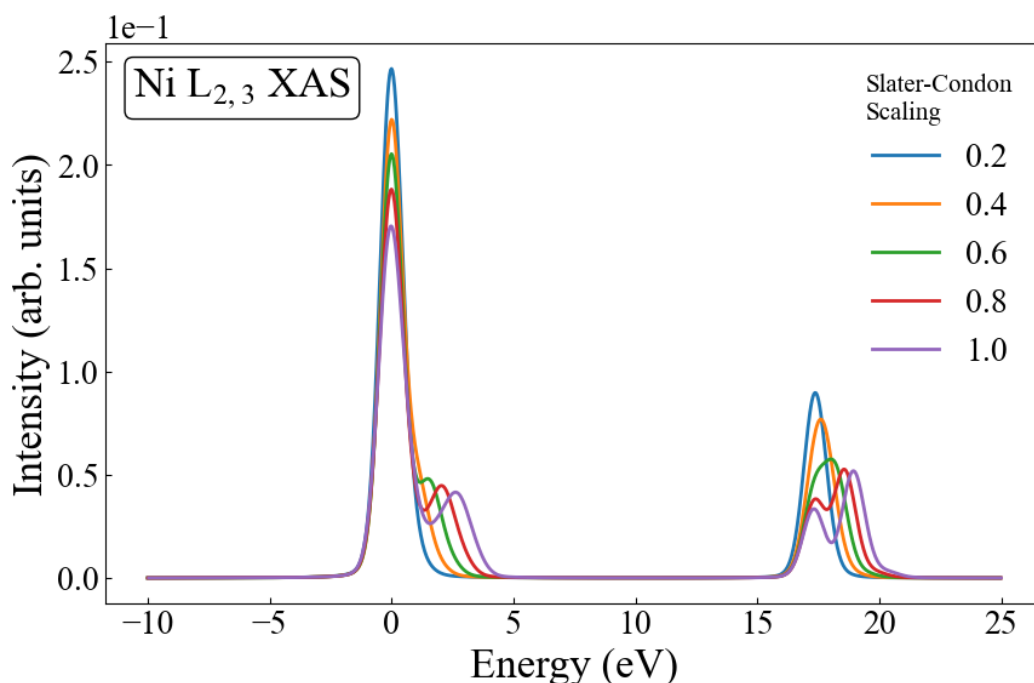
Figure 2.2: The Ni L$_{2,3}$ XAS for different strengths of multiplet coupling relative to atomic calculations.

The different effects on the L-edge spectrum are illustrated in Figure 2.3. No onsite/single particle energies are included for the p and d orbitals, but I have shifted each spectrum so the peak intensity lies at 0 eV. In subplot (a), all Slater-Condon integrals, spin-orbit, and crystal field interactions are turned off. This leads to the trivial result of only one transition at 0 eV. Once spin-orbit coupling within the $2p$ shell is turned on in subplot (b), this peak separates into $2p_{3/2}$

(L$_3$) and 2$p_{1/2}$ (L$_2$) contributions, but the peaks remain perfectly symmetric. In subplots (c) and

(d) the (2p, 3d) and (3d, 3d) Slater-Condon interactions are turned on and the peaks separate into

different multiplet contributions, generally described as "fine-structure". 2p core level

spectroscopies of 3d transition metal systems are generally dominated by the large spin-orbit

splitting, but at the 3p level the spin-orbit contribution is much weaker (roughly 10% that of the

2p term for the same element) and the large Coulomb exchange between the 3p and 3d orbitals

instead dominates the spectra [85]. The 3d spin-orbit coupling is omitted from this example

because it is not experimentally resolvable (on the order of 0.05 eV), but in practice should be

included in any full multiplet calculation for the sake of completeness. Finally in subplot (e) the

crystal-field is turned on which splits 3d orbitals into e$_g$ and t$_{2g}$ levels for the O$_h$ coordinated

NiO. This is a single-particle contribution and has the weakest overall effect on the spectra

compared to the multiplet terms, but it is still necessary to include when fitting to experimental

spectra with different local symmetries.
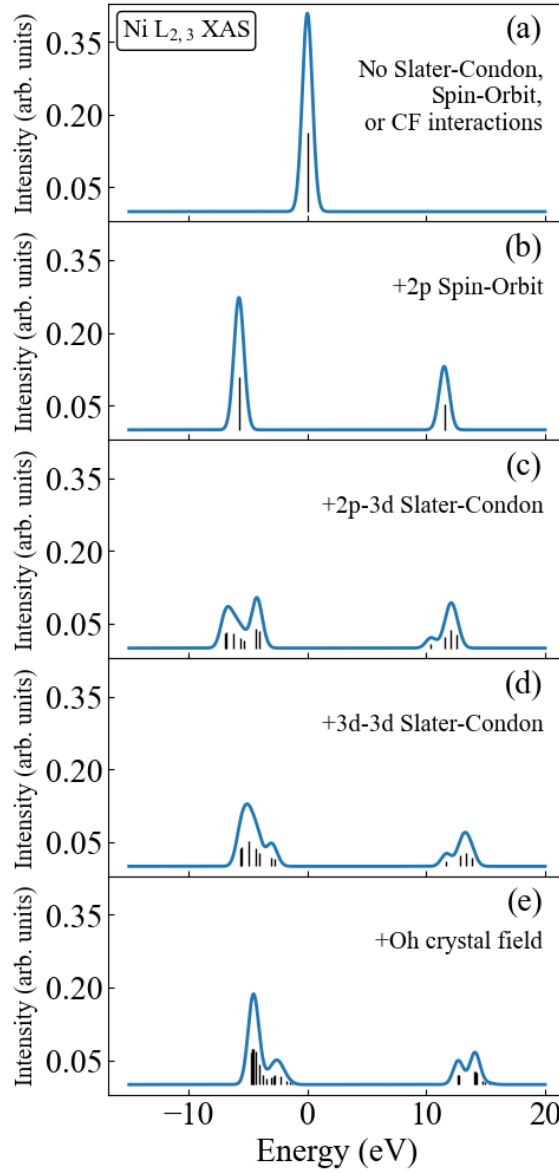
Figure 2.3: Ni $L_{2,3}$ XAS based on atomic multiplet and crystal field theory. (a) All interactions are turned off and the spectrum is comprised of a single peak. (b) $2p$ spin-orbit coupling leads to two transitions which make up the L_2 and L_3 main peaks. (c, d) the ($2p$, $3d$) and ($3d$, $3d$) integrals from Eq. 2.3 are set to 80% their atomic values, leading to the emergence of fine structure. (e) The O_h crystal field parameter 10Dq is set to 1 eV to incorporate the local electrostatic environment of NiO.

2.3   Crystal Field Theory
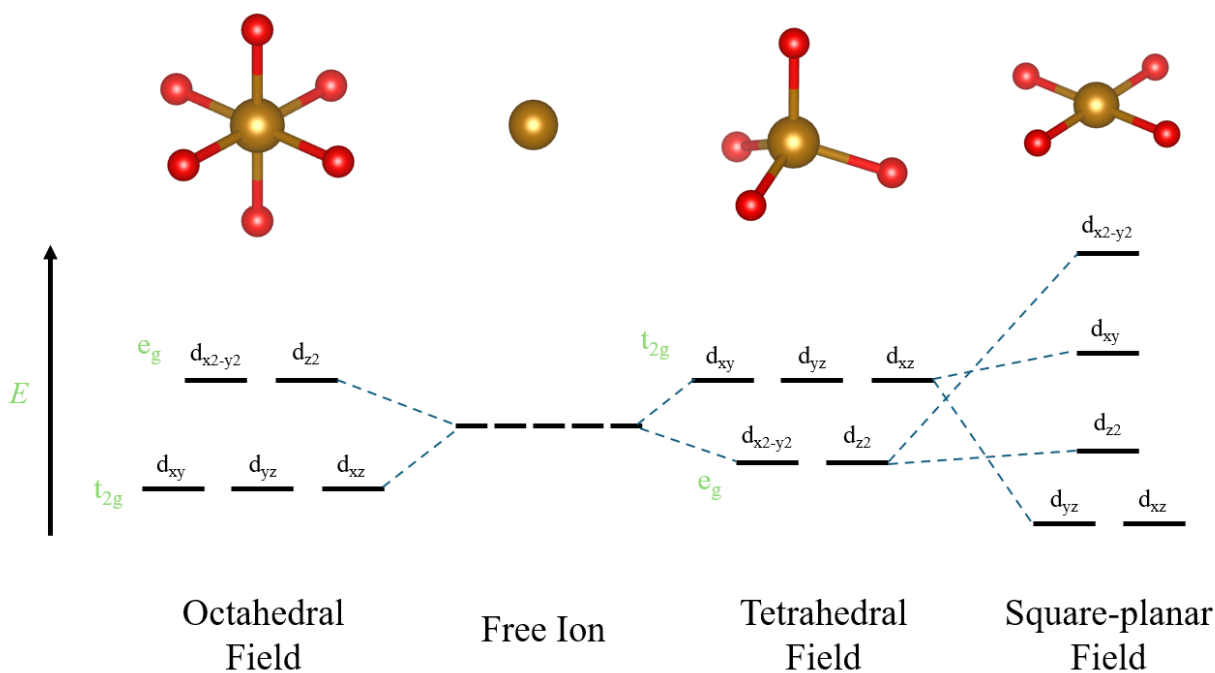
Figure 2.4: Crystal field energy diagram for Octahedral (O_h), free ion, Tetrahedral (T_d), and Square-planar (D_{4h}) point group symmetries.

Crystal field theory was first developed by Hans Bethe in 1929 [87], and it described the electric field made up of point charges in place of the ligands which surround an atom. For most transition metal compounds, the ligands are negatively charged and the effect of the crystal field on the spectra comes from the symmetry of the ligands and the strength of their effective fields. An example of this is shown in Figure 2.4 where crystal field split d-orbitals are shown for different local geometries, often denoted by point groups [88]. In general, the more symmetry operators which a cluster obeys, the fewer individual levels the d-orbitals are split up into, with

O_h and T_d being examples of relatively high symmetry and D_{4h} and C_{3v} being examples of relatively low symmetry clusters.

$$H_{CF} = \sum_{\tau_1,\tau_2} \sum_{k,m} A_{k,m} \langle Y_{l_1,m_1} | C_{k,m} | Y_{l_2,m_2} \rangle \hat{a}^{\dagger}_{\tau_1} \hat{a}_{\tau_2} \quad (\textbf{Eq. 2.4})$$

The crystal field Hamiltonian is given in equation Eq. 2.4, where the $A_{k,m}$ are related to the effective potential created by the ligand point charges and are taken as fitting parameters when calculating spectra. In practice, the strength of the crystal field is on the order of 0.1 to 2.0 eV, where a strong crystal field can lead to larger splittings between the different d-orbitals, enough to even violate Hund's rule [71]. An example of this, and the effect it has on a hypothetical Mn(2+) Kβ x-ray emission spectra is shown in Figure 2.5. In the case of O_h symmetry, the d-orbitals split into 2 e_g and 3 t_{2g} orbitals, and if the crystal field effect is large enough the electrons will preferentially fill the 3 t_{2g} orbitals first. This is because the energy cost of putting an electron into the e_g orbital is higher than the Coulomb repulsion energy cost from having two electrons occupy the same magnetic angular momentum orbital, leading to a low-spin configuration. Conversely, in the high-spin case, the crystal field splitting is weak enough that Coulomb repulsion still determines the configuration. This high-spin and low-spin behavior gets "communicated" to the core orbitals via the Coulomb exchange coupling. In the case of $3p$-XES, the overlap between the $3p$ and $3d$ states is quite strong (Slater-Condon terms on the order of 15 eV). This leads to a large splitting between the configurations where, in the final state, the unpaired $3p$ electron is spin-aligned versus spin-opposed to the net spin of the valence level [31], and results in a distinct satellite feature known as the Kβ' [89]. In general, the stronger the Kβ' feature, the higher the spin of the system being probed.
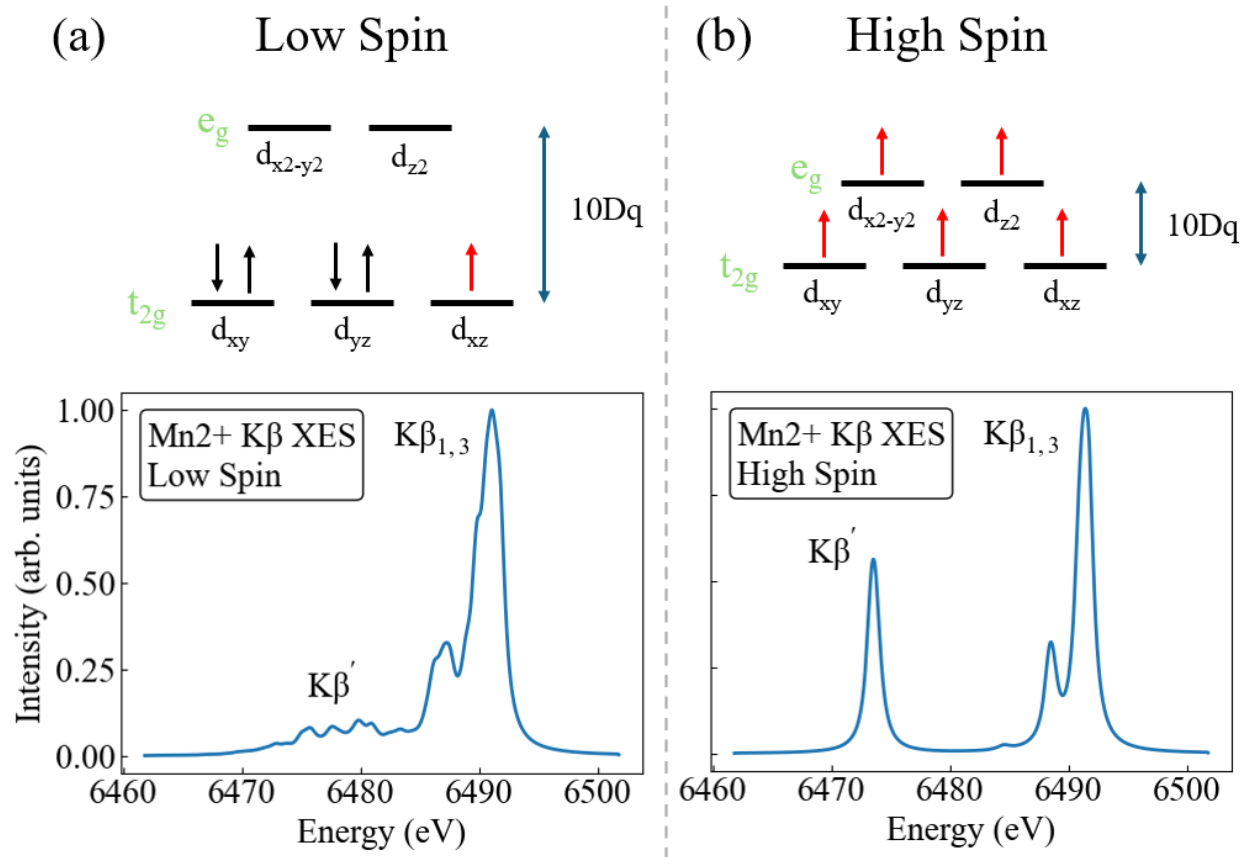
Figure 2.5: Kβ XES from a Mn(2+) systems ($n_d = 5$) for a large crystal field splitting, low spin (a) and small crystal field splitting, high spin (b).

Using just a treatment of the transition metal with multiplet and crystal field effects, good agreement between theory and experiment for charge-neutral spectroscopies such as $L_{2,3}$-edge XAS can already be achieved [90]. With local environmental perturbations being included, additional spectral information can be extracted by taking advantage of the dipole selection rules. So far, I have focused exclusively on isotropic spectra, but photons can exhibit linear and circular polarizations, and the fine structure of polarized spectra can provide magnetic angular momentum resolved information about the occupied and unoccupied DOS [15]. The simplest dichroism comes from a non-cubic (ex: D_{4h}, C_{3v}) crystal field that causes an anisotropy in orbital

occupation. In L-edge absorption, the valence $3d$-orbital is directly probed through the $2p$ to $3d$ dipole transitions. Ignoring multiplet excitations, the absorption spectrum is a mirror of the single particle unoccupied DOS, with electrons only transitioning into valence magnetic angular momentum orbitals which have holes to accept them.

There are 3 p-orbitals (p_x, p_y, and p_z) which can be excited to 5 d-orbitals (d_{xy}, d_{yz}, d_{z2}, d_{xz}, d_{x2y2}), and 3 different linearly polarizations which correspond to the x, y, and z polarizations of light. This comes out to a total of $3 \times 5 \times 3 = 45$ total matrix element. Which ones contribute to the spectrum can be determined by the selection rules that emerge from the Clebsch-Gordan coefficients in the Wigner-Eckart theorem [10]. The Wigner-Eckart theorem states that the matrix elements of tensor operators with respect to angular-momentum eigenstates must satisfy Eq 2.5, where $|jm\rangle$ is an eigenstate of the total angular momentum operator J^2, $T_q^{(k)}$ is the q-th component of the spherical tensor operator $T^{(k)}$, $\langle jk|j'm'kq\rangle$ is the Clebsch-Gordan coefficient, and the final term with the $||$ is the reduced matrix element which does not depend on m, m', or q.

$$\left\langle j'm'\left|T_q^{(k)}\right|jm\right\rangle = \langle jk|j'm'kq\rangle \frac{\left\langle j'\,||T_q^{(k)}||\,j\right\rangle}{\sqrt{2j+1}} \quad (\textbf{Eq. 2.5})$$

The Clebsch-Gordon coefficients must obey the triangular condition, $|j - k| \leq j' \leq j + k$ which determines the allowed values for the rank j'. This enforces the dipole selection rules, given that the dipole transition operator is rank $k = 1$ ($\Delta l = \pm 1$), and the transition must be between orbitals that are related by $\Delta m = m' - m = q = 0, \pm 1$. For transitions between spherical harmonics, the Gaunt coefficients are well tabulated [80], but when considering tesseral harmonics (sometimes called cubic harmonics) [91] cross terms must also be considered. For

example, the dipole transition from p_y to d_{x2y2} is only non-zero for a y-polarized dipole operator, as shown in equation Eq. 2.6, where the notation Y_l^m refers to a spherical harmonic and $Y_{l,m}$ refers to a tesseral harmonic. A table of which dipole operators appropriately couple tesseral harmonics is provided in Appendix A.

$$\langle Y_{1,-1}|y|Y_{2,2}\rangle = \sqrt{\frac{\pi}{6}}\langle Y_1^{-1} + Y_1^1|Y_1^{-1} + Y_1^1|Y_2^{-2} + Y_2^2\rangle$$

$$= \sqrt{\frac{\pi}{6}}(\langle Y_1^{-1}|Y_1^{-1}|Y_2^{-2}\rangle + \langle Y_1^{-1}|Y_1^{-1}|Y_2^2\rangle + \langle Y_1^{-1}|Y_1^1|Y_2^{-2}\rangle + \langle Y_1^{-1}|Y_1^1|Y_2^2\rangle$$

$$+ \langle Y_1^1|Y_1^{-1}|Y_2^{-2}\rangle + \langle Y_1^1|Y_1^{-1}|Y_2^2\rangle + \langle Y_1^1|Y_1^1|Y_2^{-2}\rangle + \langle Y_1^1|Y_1^1|Y_2^2\rangle$$

$$= 0 + 0 - \frac{1}{2\sqrt{5}} + 0 + 0 - \frac{1}{2\sqrt{5}} + 0 + 0 = -\frac{1}{\sqrt{5}} \qquad (\textbf{Eq. 2. 6})$$

By combining the selection rules with the orbital occupation, a picture of the unoccupied DOS can be extracted. An example of this behavior is demonstrated for a square-planar system in Figure 2.6. For a Mn2+ system, $n_d = 5$, and assuming that the crystal field splitting is large enough to dominate over the $3d$-$3d$ Coulomb repulsion, the electrons will arrange themselves as is shown in subplot (a). The energy ordering of the valence orbitals for a general configuration can be determined by molecular orbital theory [88]. When the metal bonds to ligands, the ligands become negatively charged and repel the electrons left on the metal atom. Therefore, the d-orbitals oriented along the bonds have the highest energy (d_{x2y2}) and the orbitals with no weight along the bonds have the lowest energy (d_{xz} and d_{yz}). Orbitals like d_{z2} are mostly oriented with two nodes perpendicular to the xy-plane but have some weight in the plane and therefore are of intermediate energy. The absorption is shown in subplot (b), where the z-polarized spectra is shifted to lower energy compared to the x and y-polarized spectra. This is because the d_{z2} orbital

is partially occupied and lower in energy than the unoccupied d_{xy} and d_{x2y2} orbitals, and the

$\langle p_z|z|d_{z2}\rangle$ matrix element is twice as large as x or y dipole terms. It should be noted however

that for most of the absorption spectrum all three polarizations have non-zero contributions.

Looking at the table provided in Appendix A this is not unexpected, but there is less variation in

the intensity than would be expected from directly evaluating the matrix elements. This is due to

two main caveats, 1) Coulomb coupling in the valence level distorts the single particle

occupation depicted in (a), degrading some of the anisotropy enforced by the crystal field, and 2)

we are not actually probing the unoccupied DOS of the ground state, as the DOS of a system

with an electron promoted into the valence level (which includes effects from the $2p$ core-hole) is

not equivalent to the ground state system. Despite this, we can observe large shifts in the

polarized spectrum and use them to form a more complete interpretation of any absorption

spectra from a non-cubic system.

This is not necessarily the case with x-ray emission, however. In subplot (c) we show the

same system with polarization separated emission. The effects of the polarization are much

weaker, not even experimentally resolvable. The reasoning for this difference between absorption

and emission comes from the orbitals which each transition is directly probing. If all of the

environmental information is being contained in the $3d$ shell, absorption will be much more

sensitive to it as it involves a transition directly from $2p$ to $3d$. Conversely, core-to-core emission

like Kα is only sensitive to the valence shell through the Coulomb coupling between the $2p$ core-

hole. The $1s$ core-hole is also coupled to the valence shell, but much more weakly than the $2p$.

The strength of the polarization effects on the CtC-XES is proportional to the strength of the

Coulomb coupling, but for VtC-XES (which involves emission from the environmentally

41

sensitive valence orbitals) the effect is much stronger. The concept will be explored further in Chapter 6, discussing polarized XES.
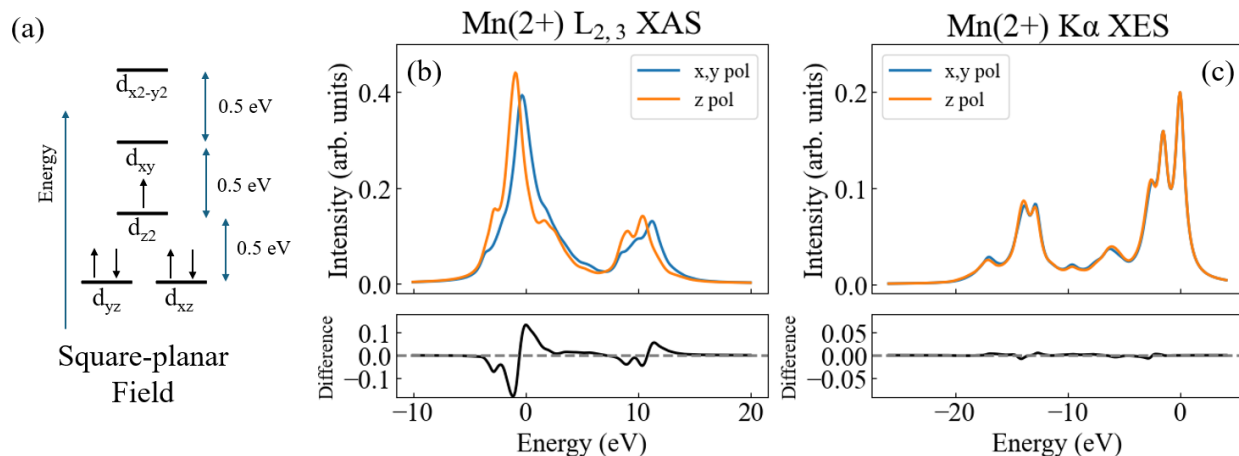
Figure 2.6: Core-level spectra for a Mn(2+) oxidized system with a square-planar (D_{4h}) crystal field. (a) Energy diagram for the crystal field split d-orbitals, each irreducible representation is split by 0.5 eV. (b) 2p-XAS separated by the polarization of the dipole transition operator. The symmetry of the system is such that the x and y polarized spectra are equivalent. (c) The 2p-XES, also separated by polarization. 1 eV of Lorentzian broadening is applied to both absorption and emission.

2.4   Charge Transfer Effects

The final perturbation to consider in the MLFT model comes from modeling how the ligands hybridize and share electrons with the central metal ion. This is essential for modeling how charge transfer occurs in XPS or XES where the atom is in a charged state following x-ray absorption. Up until now, the Hamiltonian has been comprised of 10 crystal field split d-orbitals coupled through Coulomb interactions to either 6 core p-orbitals or 2 core s-orbitals, as depicted in subplot (a) of Figure 2.7. Adding in the Ligand orbitals increases the basis by at least another

10 fermionic modes which couple to the 10 $3d$ orbitals (b), and the particle number of electrons in the 3d shell is no longer constrained to n_d. The sharing of electrons between the d and Ligand orbitals can lead to non-integer occupation of both orbitals for a general many-body wavefunction and spectrally will lead to a large increase in the number of satellite peaks.
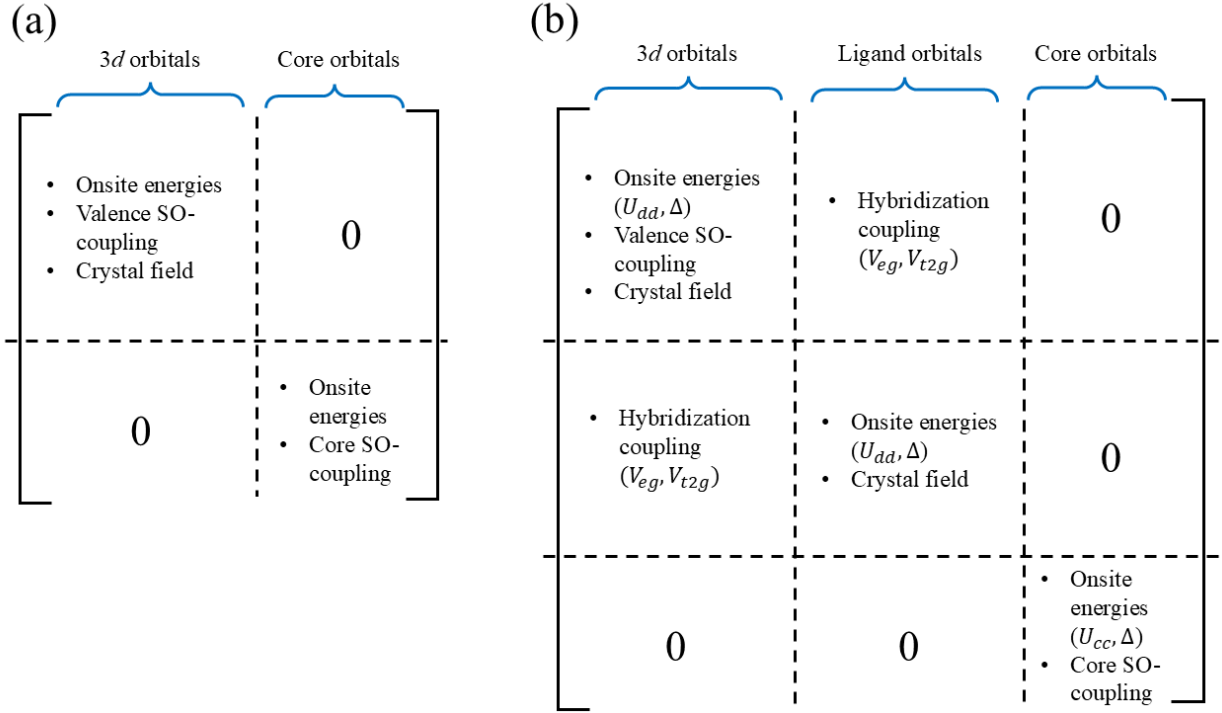
Figure 2.7: Examples of single particle Hamiltonians in MLFT with ligand charge-transfer coupling (b) and without (a). The onsite energies do not affect the fine structure of spectra when the number of d electrons n_d and core electrons n_c are constant. However, once charge transfer between the d and Ligand orbitals becomes allowed though hybridization coupling, the different multielectron configurations that become possible will produce new multiplets and therefore more allowed states that contribute to the spectra. The single-particle energies of these multielectron configurations will be affected by the onsite energies of all orbitals, and they will be parameterized in terms of U_{dd} (U_{cc} for the core orbitals) and Δ.

The dynamics of the different configuration energies are parameterized through the screened many-body Coulomb term U_{ij}, and the charge transfer energy Δ. For clarity this parameter scheme is the same as the one laid out in J. Zaanen, G. A. Sawatsky, and J. W. Allen [92], but the exact definitions of the U_{ij} and Δ parameters comes from equations defined in Bocquet et. al [93, 94]. The larger the charge transfer energy, the harder it is to transfer an electron from the ligand to the metal and will depend on the bonding properties (ex: more covalent or more ionic) compound. The number of $3d$ electrons, n_d, is determined by the free atom and the oxidation state. For example, a free Mn atom has an electron configuration of $4s^2 3d^5$ so Mn3+ will have a $n_d = 4$, with electrons always being taken from the $4s$ orbital first. A higher Δ indicates that a system's ground state configuration is dominated by the nominal n_d configuration because of the high energy penalty, while lower Δ indicates a ground state with is more strongly mixed.

Kα XES Energy Configurations
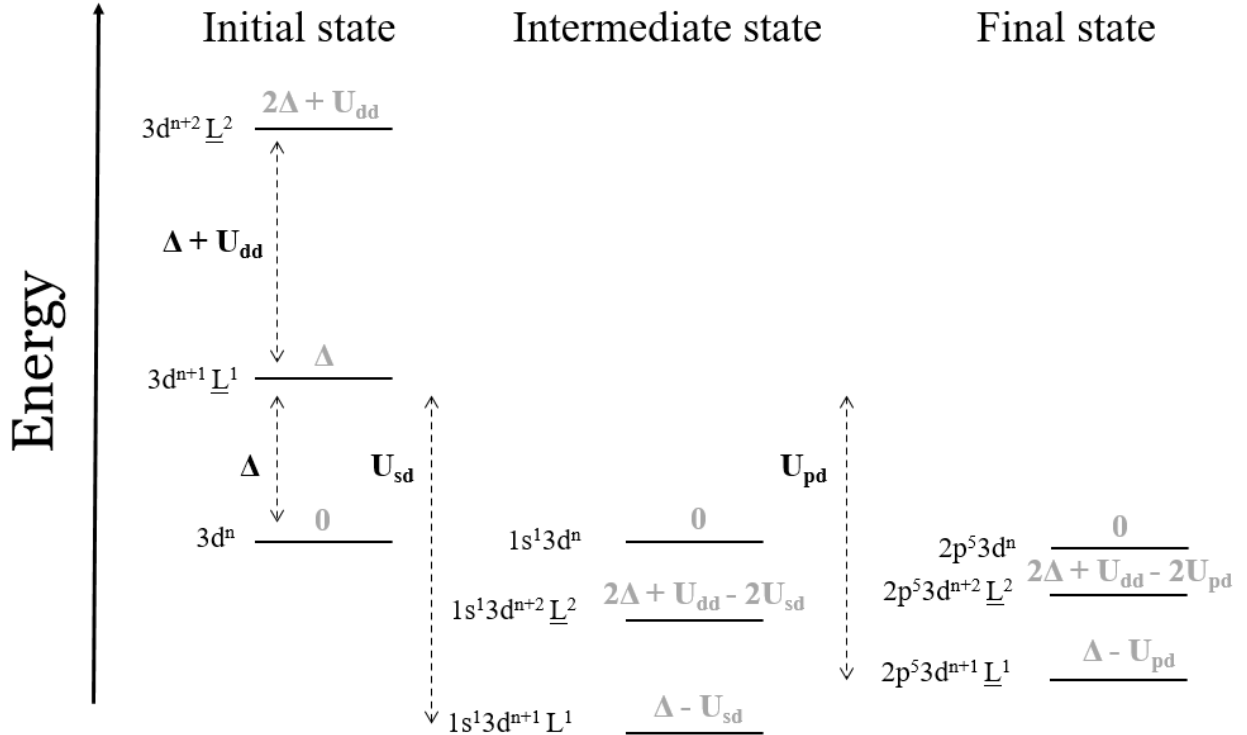
Figure 2.8: Energies of different configurations for the initial, intermediate, and final states of the Kα XES emission process in terms of U_{ij} and Δ.

As addressed in section 2.2, the U_{dd} term is related to the Slater integrals by $U_{dd} = F_{dd}^0 - \frac{2}{63}(F_{dd}^2 + F_{dd}^4)$, and the value for U_{dd} within a solid is greatly reduced from the Hartree-Fock derived value for a single atom. U_{dd} is related to but not the same as the Hubbard U_{eff}, defined by $U_{eff}(n_d) = E(n_d + 1) + E(n_d - 1) - 2E(n_d)$, which gives the energy minimum required to move an electron from one metal ion site to another [95]. The Hubbard U_{eff} (sometimes called E_{gap}) in this case involves only the lowest energy multiplet states for each electron configuration n_d while the U_{dd} term is the average screened Coulomb interaction for all multiplet states of a given configuration. One way of interpreting this that U_{dd} and Δ define the

centroids of the valence and conduction bands [92]. For more information about the distinction, please refer to the thesis of Maurits Haverkort [83] and Simon Heinze [96], and for examples of parameters extracted from fits to experimental data please refer to [93].

Together, the two parameters (U_{dd} and Δ) can be used to define the onsite energies of different states. An example of this is provided for the Kα XES emission process in Figure 2.8, which shows the energies of the n_d, n_{d+1}, and n_{d+2} configurations for the initial (no core-hole, Eq 2.7 to Eq. 2.9),

$$n_L \varepsilon_L + n_d \varepsilon_d + n_d (n_d - 1) \frac{U_{dd}}{2} = 0 \quad \textbf{(Eq. 2.7)}$$

$$(n_L - 1)\varepsilon_L + (n_d + 1)\varepsilon_d + (n_d + 1)n_d \frac{U_{dd}}{2} = \Delta \quad \textbf{(Eq. 2.8)}$$

$$(n_L - 2)\varepsilon_L + (n_d + 2)\varepsilon_d + (n_d + 2)(n_d + 1)\frac{U_{dd}}{2} = 2\Delta + U_{dd} \quad \textbf{(Eq. 2.9)}$$

intermediate (1s core-hole, Eq 2.10 to Eq. 2.15),

$$2\varepsilon_s + n_L \varepsilon_L + n_d \varepsilon_d + n_d (n_d - 1)\frac{U_{dd}}{2} + 2n_d U_{sd} = 0 \quad \textbf{(Eq. 2.10)}$$

$$2\varepsilon_s + (n_L - 1)\varepsilon_L + (n_d + 1)\varepsilon_d + (n_d + 1)n_d \frac{U_{dd}}{2} + 2(n_d + 1)U_{sd} = \Delta \quad \textbf{(Eq. 2.11)}$$

$$2\varepsilon_s + (n_L - 2)\varepsilon_L + (n_d + 2)\varepsilon_d + (n_d + 2)(n_d + 1)\frac{U_{dd}}{2} + 2(n_d + 2)U_{sd}$$
$$= 2\Delta + U_{dd} \quad \textbf{(Eq. 2.12)}$$

$$\varepsilon_s + n_L \varepsilon_L + n_d \varepsilon_d + n_d (n_d - 1)\frac{U_{dd}}{2} + n_d U_{sd} = 0 \quad \textbf{(Eq. 2.13)}$$

$$\varepsilon_s + (n_L - 1)\varepsilon_L + (n_d + 1)\varepsilon_d + (n_d + 1)n_d \frac{U_{dd}}{2} + (n_d + 1)U_{sd} = \Delta - U_{sd} \quad \textbf{(Eq. 2.14)}$$

$$\varepsilon_s + (n_L - 2)\varepsilon_L + (n_d + 2)\varepsilon_d + (n_d + 2)(n_d + 1)\frac{U_{dd}}{2} + (n_d + 2)U_{sd}$$

$$= 2\Delta + U_{dd} - 2U_{sd} \quad \textbf{(Eq. 2.15)}$$

and final ($2p$ core-hole, Eq 2.16 to Eq. 2.21) states.

$$6\varepsilon_p + n_L\varepsilon_L + n_d\varepsilon_d + n_d(n_d - 1)\frac{U_{dd}}{2} + 6n_d U_{pd} = 0 \quad \textbf{(Eq. 2.16)}$$

$$6\varepsilon_p + (n_L - 1)\varepsilon_L + (n_d + 1)\varepsilon_d + (n_d + 1)n_d\frac{U_{dd}}{2} + 6(n_d + 1)U_{pd} = \Delta \quad \textbf{(Eq. 2.17)}$$

$$6\varepsilon_p + (n_L - 2)\varepsilon_L + (n_d + 2)\varepsilon_d + (n_d + 2)(n_d + 1)\frac{U_{dd}}{2} + 6(n_d + 2)U_{pd}$$

$$= 2\Delta + U_{dd} \quad \textbf{(Eq. 2.18)}$$

$$5\varepsilon_p + n_L\varepsilon_L + n_d\varepsilon_d + n_d(n_d - 1)\frac{U_{dd}}{2} + 5n_d U_{pd} = 0 \quad \textbf{(Eq. 2.19)}$$

$$5\varepsilon_p + (n_L - 1)\varepsilon_L + (n_d + 1)\varepsilon_d + (n_d + 1)n_d\frac{U_{dd}}{2} + 5(n_d + 1)U_{pd} = \Delta - U_{pd} \quad \textbf{(Eq. 2.20)}$$

$$5\varepsilon_p + (n_L - 2)\varepsilon_L + (n_d + 2)\varepsilon_d + (n_d + 2)(n_d + 1)\frac{U_{dd}}{2} + 5(n_d + 2)U_{pd}$$

$$= 2\Delta + U_{dd} - 2U_{pd} \quad \textbf{(Eq. 2.21)}$$

The system of equations Eq. 2.7 to Eq. 2.21 are over defined and missing an overall shift in the intermediate and final state equations that should come from the lack of a core electron. However, this shift does not affect the fine structure of the spectra, and the standard multiplet formulation already omits many static energy contributions, so we gladly ignore this fact and focus instead on the multiconfigurational character of the solutions to the now hybridized Hamiltonian. This is determined by solving the charge-transfer equations for the onsite energies

$\varepsilon_d, \varepsilon_L, \varepsilon_p$, and ε_s. These are then used to set the centroid of each block (dd, LL, $\alpha\alpha$, etc) in the Hamiltonian using equation Eq. 2.22, where there are n fermionic modes in orbital α.

$$\varepsilon_\alpha = \sum_{i \in \alpha_{basis}} \frac{H_{ii}}{n} \quad (\textbf{Eq. 2.22})$$

All of this helps to explain the energies of the various configurations, but what is the character of the hybridized wavefunctions that are produced from the metal-ligand coupling? This can be answered through traditional ligand field theory [88], where orbitals of the same symmetry end up mixing together to produce linear combinations of metal and ligand atomic orbitals. This behavior is shown in Figure 2.9 for a metal ($3d$) ligand ($2p$) complex that is O_h coordinated, reproduced from Xiao Cheng's thesis [72]. The d_{z2} and d_{x2y2} bonds that make up the e_g crystal field level lie along the x, y, z axes and form σ bonds with the ligand p orbitals that are also oriented along axis. Conversely the d_{xy}, d_{yz}, and d_{xz} orbitals have their lobes oriented $45°$ degrees relative to any axis and thus hybridize with the ligand p orbitals that are perpendicular to the axis connected them to the metal ion to form π bonds. When any two orbitals hybridize, they will always produce a higher and lower energy pair of mixed states, which are denoted as bonding (no *) and antibonding (*) orbitals.
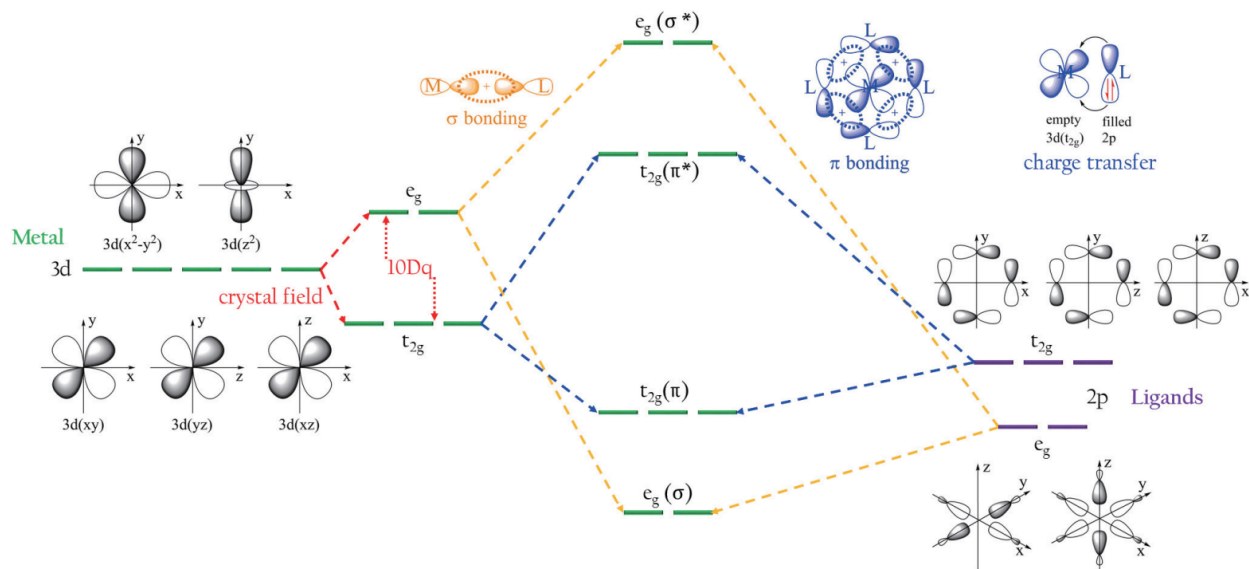
Figure 2.9: Molecular orbital bonding scheme considering crystal field, ligand field, and charge transfer effects in O_h symmetry. Figure taken from Xiao Cheng's thesis [72].

2.4.1 Approximations and Parameter Dependence

While U_{dd} and Δ are generally taken as free parameters to be fit to experiment, the screened average Coulomb interaction between the core and valence levels (U_{cd}) are in principle related to the strength of the valence – valence term. The more localized the valence electrons are, the more their wavefunctions will overlap both within the valence shell and with the core electrons. Often the U_{cd} terms are found to be within 0.5 eV to 2.0 eV larger than U_{dd} [97], and are frequently approximated as having a fixed ratio between U_{cd} and U_{dd} [98]. This ratio is often around $U_{cd}/U_{dd} \approx 1.2$ with the ratio getting larger the more localized the core level is. This approximation is important because it reduces the number of free parameters that are involved when fitting a spectrum to experiment. While fits over a full parameter space sweep can result in

$\pm 10\%$ from this ratio for different compounds, it is a good rule of thumb that constrained the U_{cd} parameters to physically reasonable values. The range of physically reasonable values for U_{dd} and Δ are generally taken to be between 1.0 and 9.0 eV [99]. However, in highly covalent materials, the charge transfer energy can become very small or even negative [100, 101]. The energy of charge-transfer satellites is strongly dependent on these parameters, as well as the strength of the hybridization coupling (usually around 0.5 eV to 4.0 eV).
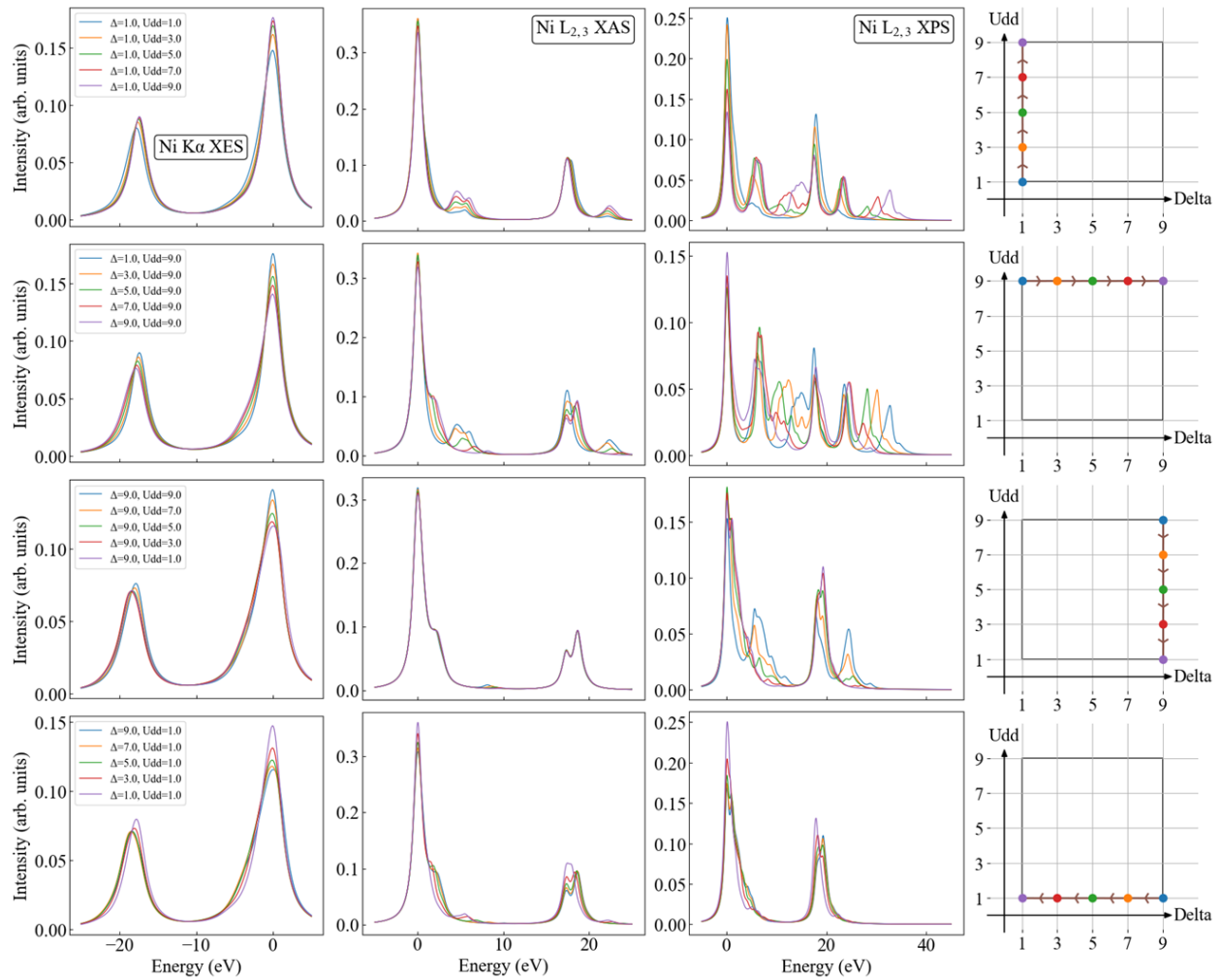
Figure 2.10: Demonstration of how different various spectroscopies (XES, XAS, XPS in the first, second, and third columns respectively) vary for different charge transfer parameters U_{dd}

and Δ. Each row corresponds to a different path through the charge transfer phase space, as shown in the rightmost column.

An example of how the spectra can vary for different charge transfer parameters is shown in Figure 2.10. Each row shows the XES, XAS, and XPS spectra for a Ni(2+) ion from NiO for variable U_{dd} and Δ. The spectra are calculated using an O_h crystal field with 10Dq = 0.6 eV, a Slater-Condon scaling of 0.8, hybridization coupling of V_{eg} = 2.12 eV and V_{t2g} = 1.214 eV, ligand crystal field of 10Dq-L = 1.5 eV, and a ratio of U_{sd}/U_{dd} = 1.2 and U_{pd}/U_{dd} = 1.15, with 1.0 eV of constant Lorentzian broadening applied for visualization purposes. In XES the spectra are moderately sensitive to the charge-transfer parameters, which comes from the indirect sensitivity to the valence shell and that the spectrum only involves transitions between core orbitals. The XAS shows a mixture of sensitivity strengths, with some regions of the phase space diagram producing large changes in the spectrum for relatively small changes in the parameters. This is not uncommon and is generally related to the fact that the x-ray absorption is a direct probe of the $3d$ valence level and can thus be highly sensitive to the character unoccupied valence orbitals. Finally, the XPS shows the largest variability with charge-transfer parameters. In general, charge-transfer effects are most prevalent in spectroscopies where the final state experiences a dramatic change in screening [102]. This leads to strong shake satellites, the energies of which are highly sensitive to the charge transfer parameters.

2.5 Computational Methods

2.5.1 Multiplet Software
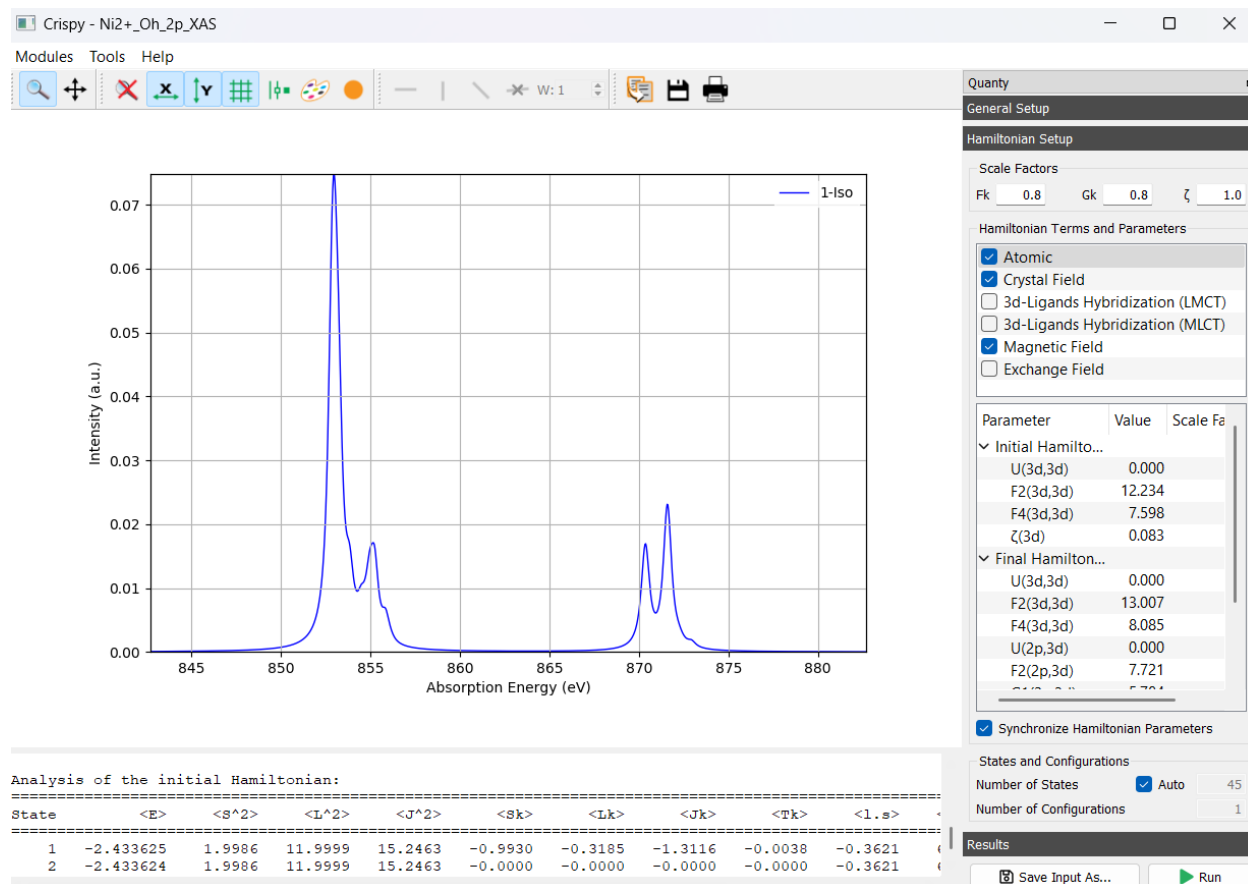
Figure 2.11: Screenshot of the Crispy GUI software for running Quanty. Shown is an example calculation of Ni(2+) $L_{2,3}$ XAS using default parameters.

Most modern multiplet software relies on the initial development work of Robert D. Cowan [82] which computes the Slater-Condon Coulomb parameters and spin-orbit splitting parameters for an arbitrary configuration, with up to five open subshells. Many updates and iterations have been applied to it since it's development in the late 1960's, but the original scripts are preserved in the NIST public data repository [103]. On top of Cowan's code, packages such as the THOLE [104] and TANAKA (also known as XTLS) [83] codes have been built for calculating various

spectra and other properties from the multiplet + perturbation model. Further on top of these, certain graphical user interface (GUI) have been developed such as the `CTM4XAS` [105], `CRISPY` [106], and `MISSING` [107] that make it easier for new users to get started with multiplet software. Screenshot examples of the `CRISPY` and `MISSING` GUI interfaces are provided in Figures 2.11 and 2.12, respectively. The development of these GUIs and more capable multiplet codes over the last 30 years has led to an increase in their application to machine learning tasks [62, 108-111]. Examples of extensive studies using these codes and a complete review of all multiplet codes and their capabilities is available in de Groot *et al.* [67].
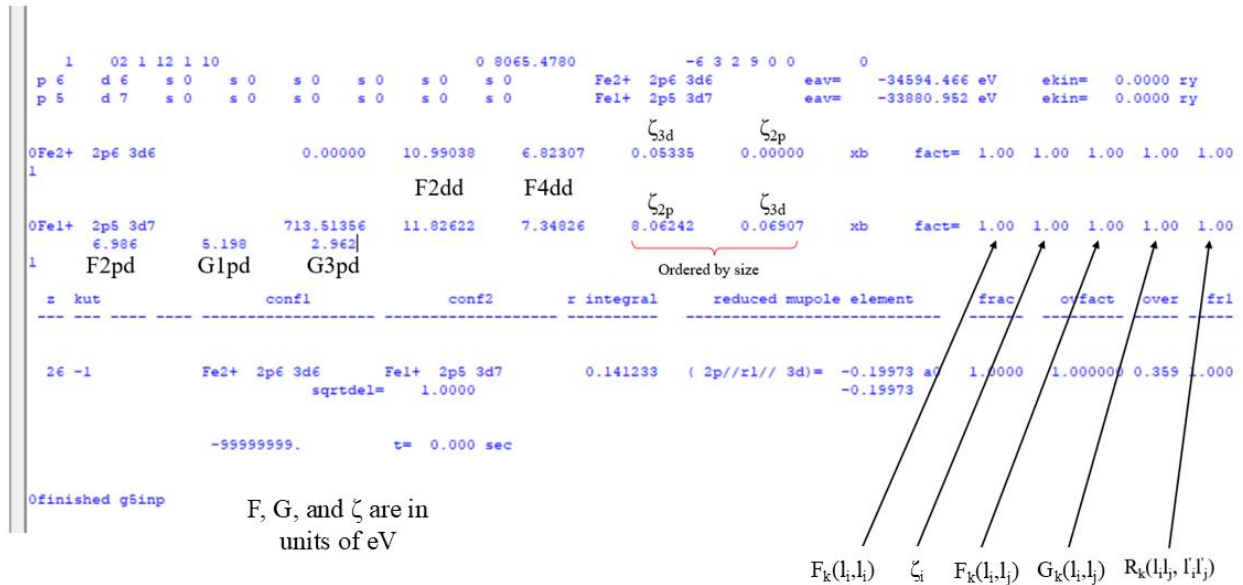
Figure 2.12: Screenshot of output from the MISSING code showing the Hartree-Fock calculated Slater-Condon and spin-orbit coupling parameters from the `RCN2` module for two different configurations of an Fe2+ atom (2*p*6 3*d*6 and 2*p*5 3*d*7). No scaling has been applied to the atomic values.

2.5.2 Real Space Multiple Scattering

One of the most widely used real space multiple scattering codes is FEFF (which also happens to be the once most relevant this work), which implements a self-consistent scattering framework to compute observables in x-ray spectroscopy (ex: XANES, x-ray Raman spectroscopy, Compton scattering) [13]. In FEFF, the scattering problem is solved by partitioning the system into atomic scattering centers and representing the photoelectron's propagation as a sum over all possible sequences of scattering events, considered up to a given order or within a finite cluster size. Convergence in FEFF is primarily controlled by a few key parameters. First, the self-consistent field (SCF) radius, which determines the cluster surrounding the absorbing atom over which the charge density is self-consistently determined. Second, the full multiple scattering (FMS) radius, which defines the set of atoms over which the multiple scattering solution (all paths) is determined. A core approximation made within the FEFF code is the use of a muffin-tin approximation [112], where the total potential is described by a sum of spherically symmetric potentials centered around in each, with interstitial potentials between spheres. This helps make the multiple scattering formalism tractable but can be problematic for systems with strongly aspherical charge densities.

2.5.3 Lifetime Broadening

The final state in x-ray spectroscopy often involves a core-hole and is inherently unstable. An atom in this state will eventually relax either radiatively (x-ray emission) or non-radiatively (Auger [22]). All relaxation processes contribute to the finite core-hole lifetime, and this effects the spectra through the energy-time uncertainty principle, $(\Delta E)(\Delta t) \geq \hbar$ [10]. Functionally this leads to broadening of the spectra proportional to the energy uncertainty associated with the core-hole lifetime. This is the origin of the Γ terms in Eqs. 1.4 to 1.6. The deeper a core-hole is

the shorter its lifetime will be and consequently the larger its energy broadening effect will be on the x-ray spectrum. This is because a deep core-hole has more available orbitals with electrons that can decay down in energy to fill it, compared to a valence level hole which can only be filled by other, more weakly bound, valence electrons.

This process generally exists outside of the MLFT model, as it can be difficult to treat all possible decay pathways for a given state. The output of most MLFT codes is a list of energies and intensities which are then convolved with Lorentzian and Gaussian line shapes to treat lifetime and instrumental broadening effects respectively. Therefore, we usually rely on tabulated values from different experimental techniques to determine the appropriate broadening [113]. In general, every final state in a spectrum will have a different lifetime [114], but we will often treat the broadening with an approximate constant or linear energy dependence to approximate the true lifetime effects. An example of this for Kα and Kβ emission is provided in Figure 2.13, but it should be noted that there is not general accepted method for approximating the energy dependent broadening. Due to the commutative nature of convolutions, the order in Gaussian and Lorentzian broadening is applied does not matter. An example of how the spectra changes from a set of energies and intensities to a final spectrum that can be compared to experiment is provided in Figure 2.14.
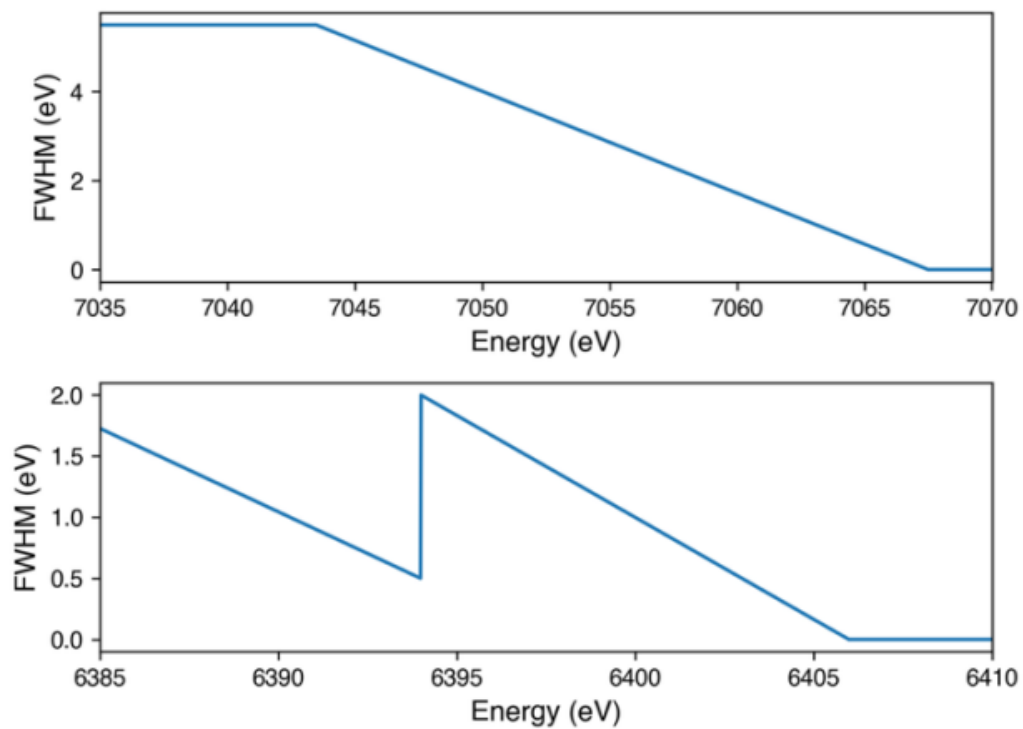
Figure 2.13: Energy dependent Lorentzian broadening use to convolve calculated Kβ (upper panel) and Kα (lower panel) emission spectra. Figure reproduced from the supplemental information of Lafuerza *et al.* [31].

MnF$_2$
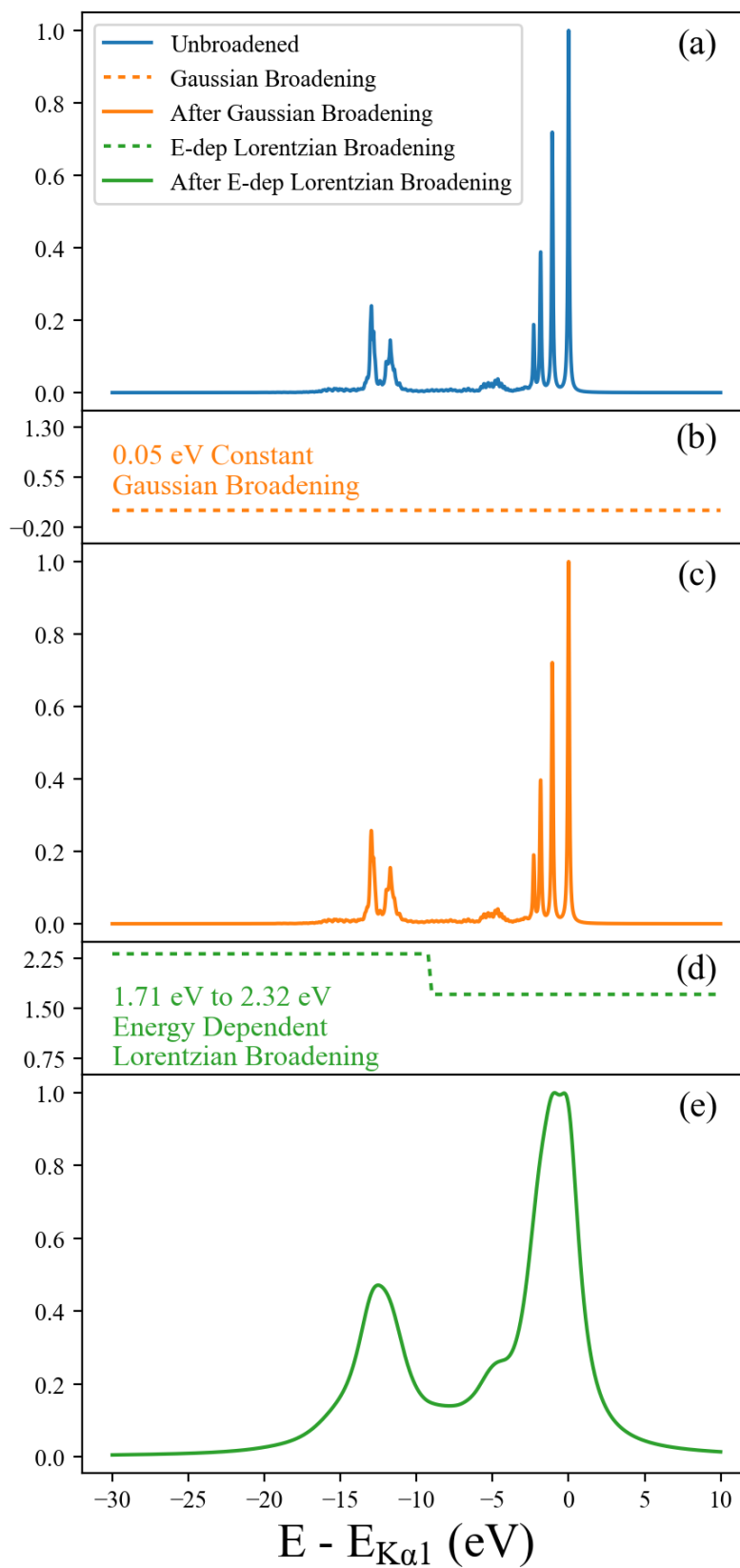
Figure 2.14: Depiction of the how the experimental and lifetime broadenings were applied for MnF_2. (a) The spectrum with a weak constant 0.1 eV Lorentzian broadening across the entire energy range, referred to as the "unbroadened" spectrum. (b) The Gaussian experimental broadening as a function of energy. (c) The resulting spectrum after constant Gaussian broadening is applied. (d) The Lorentzian lifetime broadening as a function of energy. The lifetime broadenings are constant near the centroids of the peaks, but roughly halfway in between they quickly vary from one value to the other. (e) The final spectrum after all broadening has been applied. Figure reproduced from Cardot *et al.* [101].

Chapter 3 DFT + MLFT

As addressed in Chapter 1, there are many levels of theoretical methods for treating the multiplet and strong correlation effects that are intrinsic to the core-level spectroscopy of most transition metal systems [72. They face major detractors in terms of accuracy, computational efficiency, or limited range of applicability, all except for MLFT. The semi-empirical perturbed cluster model is widely successful and achieves excellent agreement compared with experiment given its relatively cheap computational cost. As of writing, it is still actively used for treating XAS, XES, XPS, and RIXS research {Amorese, 2019 #115, 115, 116] and multiplet spectral calculation software still receive regular updates [74, 105]. However, the main advantage of MLFT is also its greatest disadvantage, with its semi-empirical nature limiting its utility.

To combat this notorious problem serious research has been put towards shaving off and eliminating certain free parameters. While DFT fails to capture many-body effects in strongly correlated systems, it can still reproduce reliable values for crystal field effects and hopping parameters. Earlier work demonstrated how molecular orbitals formed from LDA calculations could be used to reproduce some MLFT parameters [117, 118], but it wasn't until 2012 when Haverkort *et al.* [97] demonstrated a complete first-principles pipeline for extracting the vast majority of the MLFT parameters. They accomplished this through extracting a tight-binding Hamiltonian built from symmetry-adjusted Wannier functions (WFs), which provides a localized single-particle basis onto which the multiplet and charge-transfer effects can added onto. This idea is the critical foundation behind all of the core-level spectra that will be presented in this thesis after this point.

3.1   Tight-Binding Hamiltonian from Wannier Functions

The DFT + MLFT pipeline originally developed by Haverkort relied on the linear augmented plane wave basis code `Wien2K` [119], which treats all electrons explicitly including the core states. In this work we use the `QUANTY` interface with the DFT code `FPLO` [120], "Full Potential Local Orbital", which can treat both infinite crystals and individual molecules, and provides a similar all-electron treatment to accurately capture the physics of core electrons. More details about the basis functions and capabilities of the `FPLO` code can be found in its manual, but critically the output of its Wannier downfolding and radial functions for the basis orbitals can be read in and processed by `Quanty`. The tight-binding calculation procedure begins with a standard DFT calculation using an LDA functional and a dense k-grid to get well converged Kohn-Sham wavefunctions and band structure. The Kohn-Sham wavefunctions can be Fourier transformed into WFs that are localized in space, as defined in Eq. 3.1.

$$W_{R\mu} = \frac{V}{(2\pi)^3} \int dk\, e^{-ikR} \sum_n \Psi_n^k U_{n\mu}^k \quad (\textbf{Eq. 3.1})$$

The Wannier function $W_{R\mu}$ is defined by lattice vector R and type μ which denotes the center of the WF and its symmetry (ex: WF for Ni d_{xy}) [121]. The Fourier transform (transforming from k-space to real-space), is over a sum of Bloch waves Ψ_n^k each transformed by an arbitrary k-dependent unitary matrix $U_{n\mu}^k$ that mixes the Bloch wavefunctions at each k point. This $U_{n\mu}^k$ has no unique definition, and different choices can be made to achieve different Wannier functions from the same Bloch wavefunctions. Often the approach is to minimize the gauge variant part of the total spread to achieve maximally localized Wannier functions [122]. However, the minimization procedure we use enforces a constraint that the Wannier functions

have the same symmetry as the atomic derived `FPLO` basis used to construct them [123]. This is not necessarily a global minimum in the spread function, but it is critical for later use in symmetry analysis (e.g. polarized spectra) of the perturbed multiplet model.

In the present approach, the band structure and projected density of states are calculated using the LDA functional on a 20x20x20 Monkhorst-Pack k-mesh with a density convergence parameter of 10^{-10} Å^{-3}. All materials were carefully checked for convergence before moving on to the Wannier downfolding. The Perdue Wang 92 functional was used to perform the LDA calculation [124], and no spin was included in the DFT step. All spin state effects observed in the calculated spectra are the results of terms included in the MLFT step. The unit cells used to create the input files for `FPLO` were taken from the crystallographic open database [125, 126]. The bulk of the calculations were performed using FPLO version 14.00-49-x86_64, however some materials were recalculated with FPLO version 21.00-61_x86_64 for real space visualizations of the Wannier orbitals. For the systems and properties calculated numerical differences between the outputs are negligible.

The band structure and density of states are used as a guide to define and energy window around the Fermi energy. It is within this window that all physically relevant processes for the valence shell will take place (eg. crystal field splitting, hybridization). This is similar in scope to defining an 'active space' in CASSCF techniques, where only basis orbitals within the energy window are considered for constructing the Wannier orbitals. This result of this procedure (known as 'downfolding' within `FPLO`) is shown for Cr_2O_3 in Figure 3.1, where the bands built from the localized Wannier orbitals for Cr-3d (red) and O-2p (blue) coincide exactly with the full DFT band structure. From the LDOS we clearly see that while the bands have primarily d and Ligand character, they have some hybridization which will lead to off diagonal coupling between

61

the *d* and Ligand blocks in the tight binding Hamiltonian. In the case of well-isolated bands the accuracy and degree of localization is generally quite good, but band disentangling is sometimes needed [121, 127]. The presence of bands from other atoms that are not included in the tight binding Hamiltonian (ex: Pb in $PbCrO_4$) can also complicate the downfolding procedure. It is good practice to always check the agreement of the Wannier bands with the true DFT band structure, and to adjust the energy window and orbitals included in the downfolding before moving on.
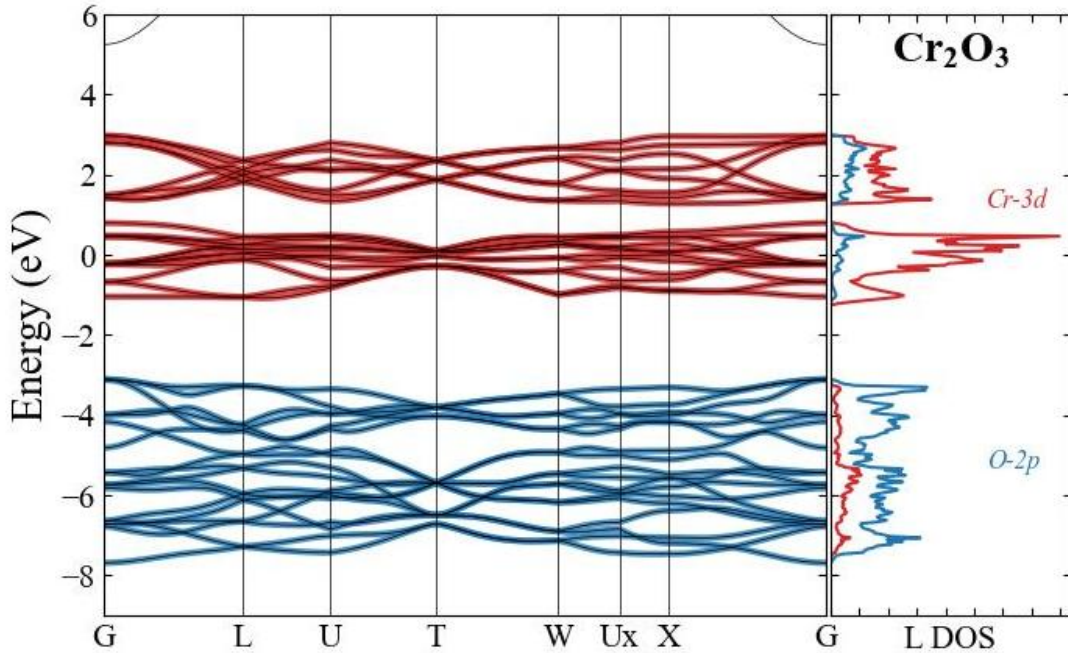
Figure 3.1: (left) The DFT calculated band structure for Cr_2O_3 (black) with the Wannier bands for the Cr-3*d* and O-2*p* projected orbitals shown in red and blue respectively. (right) the l-projected density of states separated into the Cr-3*d* and O-2*p* contributions.

A real-space visualization of the Wannier orbitals is shown in Figure 3.2 for a projection onto the Ni 3*d* and O 2*p* of NiO. The symmetry adapted Wannier functions are similar in shape

to the atomic orbitals, but some of the weight of the wave functions is shared with the

neighboring atoms.
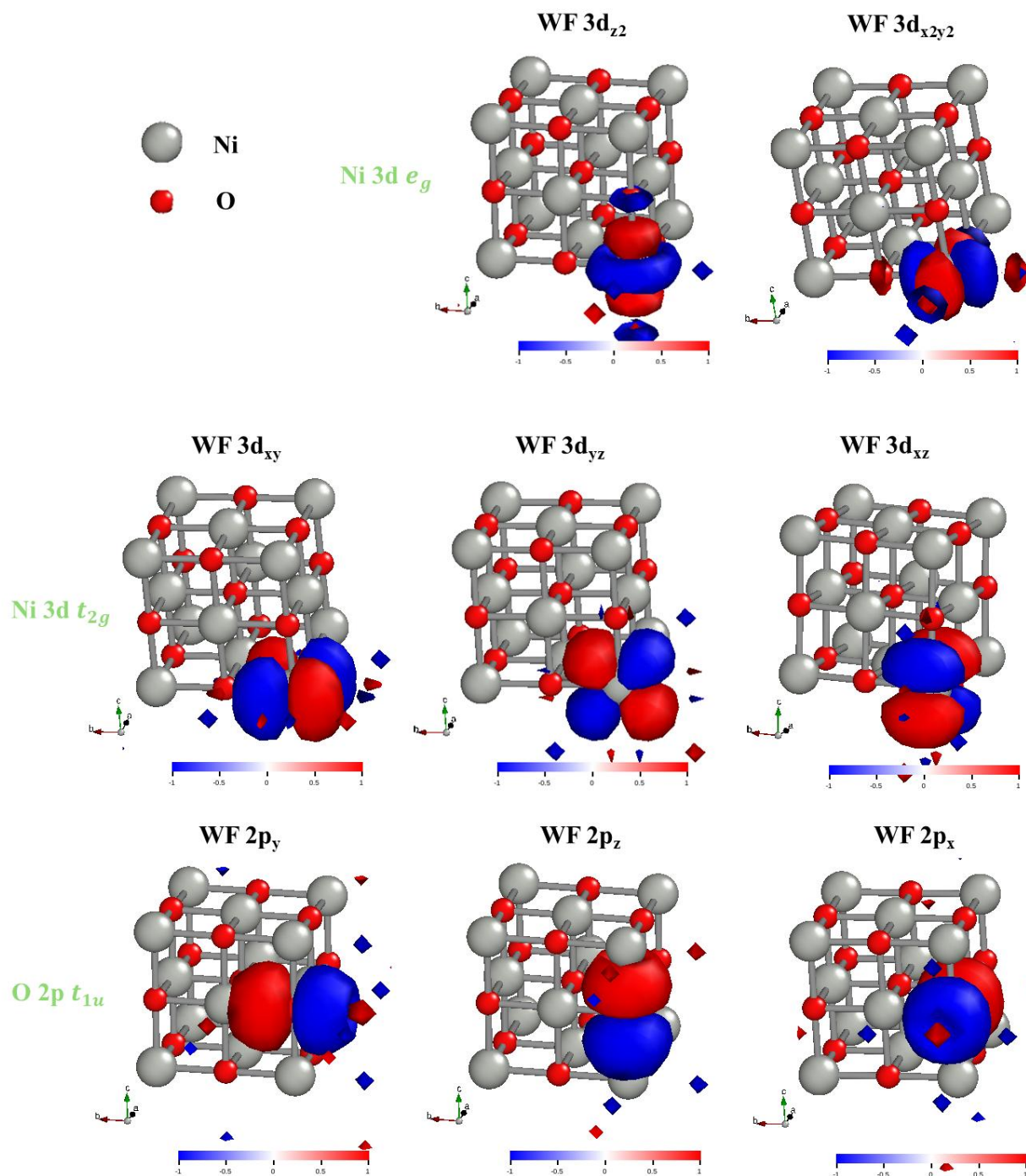
Figure 3.2: Symmetry adapted Wannier functions for atomic Ni $3d$ and O $2p$ orbitals calculated and visualized using `FPLO` version 21.
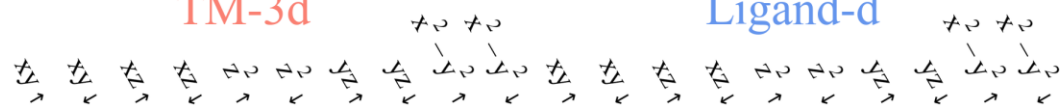
Once the downfolding is complete, they overlap between every Wannier band with every other Wannier band is output from `FPLO` into a massive list of matrix elements which are used to create H_{DFT} defined in Eq. 3.2. The onsite energy ε_d and ε_L are the same that are addressed in equations 2.7 to 2.21 but will have to be shifted according to the charge transfer parameters. The index γ goes over both the d and L basis encapsulates the single particle crystal field and hybridization coupling from the Wannier orbitals.

$$H_{DFT} = \varepsilon_d \sum_d \hat{c}_d^\dagger \hat{c}_d + \varepsilon_L \sum_L \hat{c}_L^\dagger \hat{c}_L + \sum_{\gamma\gamma'} V_{\gamma\gamma'}^{LF} \hat{c}_\gamma^\dagger \hat{c}_{\gamma'} \quad \textbf{(Eq. 3.2)}$$

The size of the basis for an arbitrary cluster will depend on the number of Ligands and how many fermionic modes are in their open shells. The ligand orbitals are much more delocalized than the TM $3d$ orbitals, and the size of the Hilbert space can be greatly reduced by treating them as uncorrelated and taking linear combinations of the Ligand orbitals. In the one-electron basis, an O_h cluster with $n_d = 5$ would have $5 + 6 \times 6 = 41$ electrons which in turn gives 46 choose 41, $\binom{46}{41} \sim 10^6$ possible states. By using a linear combination of Ligand orbitals, the matrix can be tridiagonalized [128], and the Ligand-d block immediately adjacent to the TM-$3d$ block is comprised of a basis of Ligand orbitals that are most strongly coupled to the transition metal orbitals. An example of one of these matrices for just the TM-$3d$ and Ligand-d blocks is shown in Figure 3.3. The advantage of this is two-fold, 1) the tridiagonalization procedure also helps make the matrix sparser which makes it easier to treat numerically and 2) The basis can generally be reduced to only the transition metal block and first ligand block without significant loss of information [97].

Figure 3.3: The single particle tight binding Hamiltonian created from the Wannier downfolded orbitals for NiO. The transition metal *3d* block is shown in red, the ligand *d* block is shown in blue, and the coupling terms between them are shown in pink. Note that because spin is not included in the DFT calculation there is no coupling between the spin up and spin down orbitals within the Hamiltonian.

|	$xy\uparrow$	$xy\downarrow$	$xz\uparrow$	$xz\downarrow$	$z^2\uparrow$	$z^2\downarrow$	$yz\uparrow$	$yz\downarrow$	$x^2{-}y^2\uparrow$	$x^2{-}y^2\downarrow$	$xy\uparrow$	$xy\downarrow$	$xz\uparrow$	$xz\downarrow$	$z^2\uparrow$	$z^2\downarrow$	$yz\uparrow$	$yz\downarrow$	$x^2{-}y^2\uparrow$	$x^2{-}y^2\downarrow$
$xy\uparrow$	-1.341	0	0	0	0	0	0	0	0	0	1.214	0	0	0	0	0	0	0	0	0
$xy\downarrow$	0	-1.341	0	0	0	0	0	0	0	0	0	1.214	0	0	0	0	0	0	0	0
$xz\uparrow$	0	0	-1.341	0	0	0	0	0	0	0	0	0	1.214	0	0	0	0	0	0	0
$xz\downarrow$	0	0	0	-1.341	0	0	0	0	0	0	0	0	0	1.214	0	0	0	0	0	0
$z^2\uparrow$	0	0	0	0	-1.130	0	0	0	0	0	0	0	0	0	2.118	0	0	0	0	0
$z^2\downarrow$	0	0	0	0	0	-1.130	0	0	0	0	0	0	0	0	0	2.118	0	0	0	0
$yz\uparrow$	0	0	0	0	0	0	-1.341	0	0	0	0	0	0	0	0	0	1.214	0	0	0
$yz\downarrow$	0	0	0	0	0	0	0	-1.341	0	0	0	0	0	0	0	0	0	1.214	0	0
$x^2{-}y^2\uparrow$	0	0	0	0	0	0	0	0	-1.130	0	0	0	0	0	0	0	0	0	2.118	0
$x^2{-}y^2\downarrow$	0	0	0	0	0	0	0	0	0	-1.130	0	0	0	0	0	0	0	0	0	2.118
$xy\uparrow$	1.214	0	0	0	0	0	0	0	0	0	-5.404	0	0	0	0	0	0	0	0	0
$xy\downarrow$	0	1.214	0	0	0	0	0	0	0	0	0	-5.404	0	0	0	0	0	0	0	0
$xz\uparrow$	0	0	1.214	0	0	0	0	0	0	0	0	0	-5.404	0	0	0	0	0	0	0
$xz\downarrow$	0	0	0	1.214	0	0	0	0	0	0	0	0	0	-5.404	0	0	0	0	0	0
$z^2\uparrow$	0	0	0	0	2.118	0	0	0	0	0	0	0	0	0	-3.909	0	0	0	0	0
$z^2\downarrow$	0	0	0	0	0	2.118	0	0	0	0	0	0	0	0	0	-3.909	0	0	0	0
$yz\uparrow$	0	0	0	0	0	0	1.214	0	0	0	0	0	0	0	0	0	-5.404	0	0	0
$yz\downarrow$	0	0	0	0	0	0	0	1.214	0	0	0	0	0	0	0	0	0	-5.404	0	0
$x^2{-}y^2\uparrow$	0	0	0	0	0	0	0	0	2.118	0	0	0	0	0	0	0	0	0	-3.909	0
$x^2{-}y^2\downarrow$	0	0	0	0	0	0	0	0	0	2.118	0	0	0	0	0	0	0	0	0	-3.909

3.2   DFT + MLFT Calculations

The DFT calculation uses an LDA functional to treat the exchange interaction between electrons, which is similarly included from the atomic terms in the MLFT calculation. Therefore, steps need to be taken to ensure that we avoid double counting of this interaction. The monopole component and the on-site energies are dealt with through fitting U_{dd} and Δ to experiment, but

the multipole components will still be shifted. The original method for treating the double-counting is addressed in appendix C of Haverkort *et. al* [97], but the method we use here is to simply remove the mean field component of every multipole term from the H_{DFT} before adding in the explicit Slater-Condon terms. Any two-particle operator can be represented as a one-particle operator using the Hartree-Fock approximation [129]as shown in Eq. 3.3.

$$\hat{a}_i^\dagger \hat{a}_j^\dagger \hat{a}_k \hat{a}_l = \hat{a}_i^\dagger \hat{a}_l \langle \hat{a}_j^\dagger \hat{a}_k \rangle + \hat{a}_j^\dagger \hat{a}_k \langle \hat{a}_i^\dagger \hat{a}_l \rangle + \langle \hat{a}_i^\dagger \hat{a}_k \rangle \langle \hat{a}_j^\dagger \hat{a}_l \rangle - \hat{a}_i^\dagger \hat{a}_k \langle \hat{a}_j^\dagger \hat{a}_l \rangle - \hat{a}_j^\dagger \hat{a}_l \langle \hat{a}_i^\dagger \hat{a}_k \rangle$$
$$- \langle \hat{a}_i^\dagger \hat{a}_l \rangle \langle \hat{a}_j^\dagger \hat{a}_k \rangle \quad (\mathbf{Eq.\,3.3})$$

$$DFT_{Self\ Interaction} = \sum_{m,n} U \left(\langle \hat{a}_m^\dagger \hat{a}_n \rangle \right)^T \hat{a}_m^\dagger \hat{a}_n \quad (\mathbf{Eq.\,3.4})$$

$$U = \frac{2}{(N_F(N_F - 1))} \sum_{m,n} (U_{m,n,n,m} - U_{m,n,m,n}) \quad (\mathbf{Eq.\,3.5})$$

The DFT self-interaction as defined in equation Eq. 3.4, where U is the average electron-electron interaction energy for a system of N_F fermions (Eq. 3.5). For the F_{dd}^0, F_{dd}^2, and F_{dd}^4 operators, they can be converted into mean-field operators using Eq. 3.3 and the density matrix taken from the DFT calculation ρ_{DFT}, which defines the expectation values of any $\hat{a}_\tau^\dagger \hat{a}_{\tau'}$ term. The $DFT_{Self\ Interaction}$ is also added to the mean field operator as the DFT which is subtracted from H_{DFT} because LDA does not properly exclude the interaction of an electron with itself. The Coulomb interaction is then added back in according to equations Eq. 2.2 to Eq. 2.5, and the DFT calculated radial wave functions serve as a basis within `Quanty` for determining the Slater-Condon coefficients.
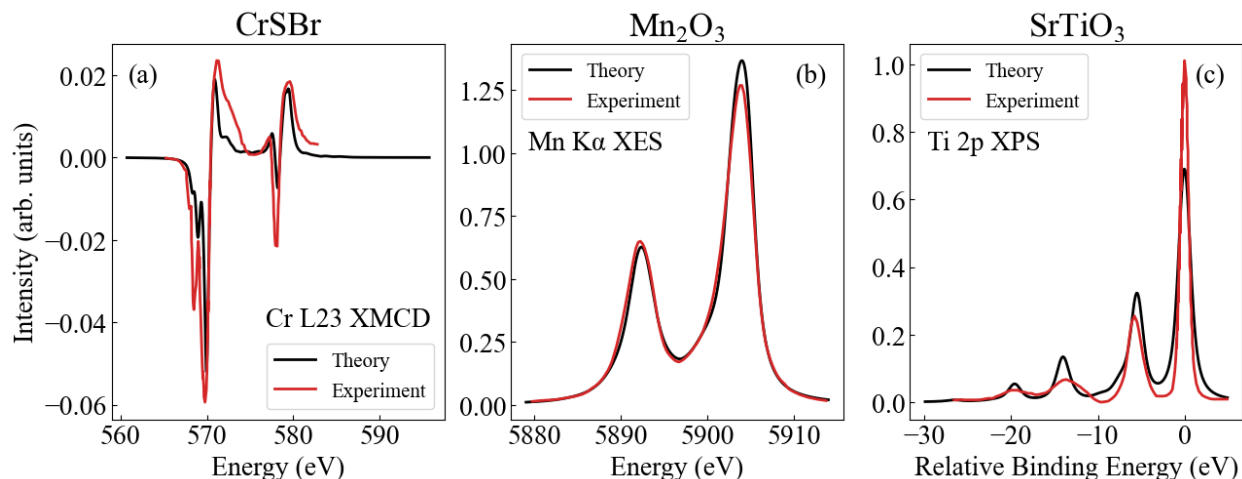
Figure 3.4: Examples of DFT + MLFT calculated spectra for three different transition metal materials with calculated spectra in black and experiment in red. Going from left to right the spectra are the (a) Cr $L_{2,3}$ XAS of CrSBr, (b) Mn Kα XES of Mn_2O_3, and (c) Ti $2p$ XPS of $SrTiO_3$. The charge transfer parameters have been optimized for fitting to experiment, but only a constant energy independent lifetime broadening is used.

The versatility of the DFT augmented approach is the same as traditional MLFT, but the massive reduction in free parameters leads to greater confidence in fits to experiment. Examples of spectra calculated using this pipeline are shown in Figure 3.4 for 3 different transition metal systems (CrSBr, Mn_2O_3, and $SrTiO_3$) and 3 different spectra (XMCD, XES, XPS). In all cases, the ideal charge transfer parameters U_{dd} and Δ can be determined via a full parameter sweep over the remaining phase spaces and achieve relatively good agreement between theory and experiment. Often, determining the best fit parameters of a general MLFT problem is done by using past work on similar systems as a starting point and then by manually changing individual parameters until a satisfactory agreement with experiment is reached [93]. While the MLFT calculations are relatively cheap compared to other methods, a full exploration of even a 4 or 5 parameter model (a highly symmetric O_h system has at a minimum 4 parameters: U_{dd}, Δ, Slater-

Condon scaling, and 10Dq) is still prohibitively expensive. However, with only two parameters, a χ^2 minimization such as the one shown in Figure 3.5 can be achieved on a modern computing cluster in approximately 24 hours. Special care needs to be taken to deal with scaling, energy shifts, and energy dependent broadening (addressed in section 2.5.2) when quantifying the difference between calculated and measured spectra, but in general this technique allows for a much more scientifically rigorous fit than was previously possible. This more *ab-initio* methodology has been successfully applied to a range of 3*d* transition metal systems and spectroscopies in published work [72, 97, 130].
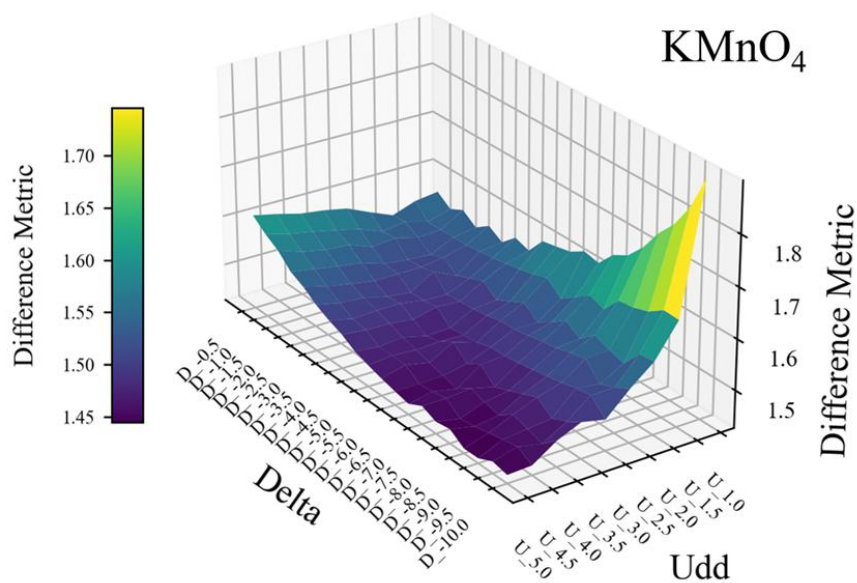
Figure 3.5: χ^2 minimization of the Kα XES for Mn in KMnO4 performed by sweeping over a range of U_{dd} and Δ values.

The idea of DFT based *ab-initio* methods for determining free parameters in MLFT is quite recent, with most new work focusing on providing interfaces between codes [119, 120, 131] or determining orbital-dependent Slater-Condon scaling factors [132]. However, one promising new avenue is the use of DFT + Dynamical Mean Field Theory (DMFT) [130] which

maps the interacting lattice problem onto a single-site impurity embedded in a self-consistent electron bath. This impurity model helps recapture some of the continuum excitations which are lost in a purely discrete model, see figure 1 from Lüder *et al.* [130]. While this approach similarly has free parameters and double counting corrections, it is a promising avenue for improved *ab-initio* MLFT calculations.

Chapter 4 Core-to-Core X-ray Emission Spectra from Wannier Based Multiplet Ligand Field Theory

Recent advances using Density Functional Theory (DFT) to augment Multiplet Ligand Field Theory (MLFT) have led to ab-initio calculations of many formerly empirical parameters. This development makes MLFT more predictive instead of interpretive, thus improving its value for studies of highly correlated 3d, 4d, and f-electron systems. Synchrotron time is always at a premium, and tools that provide predictive capabilities have clear value when it comes to planning studies. Here, we develop a DFT + MLFT based approach for core-to-core Kα x-ray emission spectra (XES) and evaluate its performance for a range of transition metal systems. We find good agreement between theory and experiment, as well as the ability to capture key spectral trends related to spin and oxidation state. We also discuss limitations of the model in the context of the remaining free parameters and suggest directions forward.

4.1   Introduction

The qualitative connection between ground state electronic structure and macroscopic physical properties of molecules and condensed phases has been evident since the earliest treatments based on the Fermi-Dirac distribution [1], Bloch waves [2], and the quantum mechanical treatment of chemical bonding [3]. However, given the nature of currently available

probes, an accurate description of excited-state electronic structure is often necessary for a quantitative connection between theory and experiment. This is especially apparent for core shell spectroscopies, such as electron energy loss spectroscopy (EELS) [4], x-ray photoelectron spectroscopy (XPS) [5], and x-ray absorption spectroscopy (XAS) (including x-ray absorption fine structure, XAFS), non-resonant x-ray emission spectroscopy (XES), and resonant inelastic x-ray scattering (RIXS) [6]. Therefore, the accurate simulation of these probes has long been a core goal of the theoretical condensed matter and chemistry communities [7, 8]. The ability to reliably predict these core-shell spectroscopies has clear scientific benefits.

To address this need, many theoretical and computational approaches for core shell spectroscopy have been developed [9], including those based on time-dependent density functional theory (TDDFT), [10], many-body perturbation theory in the form of the Bethe-Salpeter equation [11, 12], multiple scattering methods [13], quantum chemistry based methods [5, 14, 15], and the multiplet ligand field theory (MLFT) approach which we adopt here [7, 16-18]. With comparatively lower computation cost, the application of MLFT to highly correlated open-shell materials finds good agreement with a variety of x-ray spectroscopies, e.g., XAS [19], XES [20, 21], XPS [22], and RIXS [23, 24]. MLFT relies on exact diagonalization of the Hamiltonian for small clusters, making it well suited for describing local properties such as the previously mentioned excitonic spectra. The major drawback of conventional treatments of MLFT comes from the many free parameters that are used in fitting calculated spectra to experiment, limiting its predictive value and interpretation.

However, recent developments utilizing Wannier functions allow *ab-initio* DFT calculations to replace most of the free parameters related to solid state effects [16]. This process is laid out in Figure 1, where the modified Slater-Condon parameters, tight-binding Hamiltonian

71

(H^{TB}), and some charge-transfer terms are extracted from DFT calculations. This greatly simplifies the adjustable phase space of the model, allowing for a much more predictive approach to MLFT [25-28]. Although DFT + MLFT has been successfully used to simulate XAS, XPS, and RIXS, its application to core-to-core (CTC) XES has, as far as we are aware, been unexplored. Even in the context of traditional MLFT the only validated tool for CTC-XES is CTM4XAS [18], which still is subject to a large empirical parameter space. It should be noted that these tools have developed alongside rapidly improving experimental capabilities. New x-ray free electron laser (XFEL) facilities have led to an increase in femtosecond resolved dynamics of charge-transfer and spin-crossover transitions observed in CTC-XES [29-31] which is critical for characterizing molecular and bonding phenomena in $3d$ transition metal complexes. An increasing number of *in-operando* Lithium-ion battery studies rely on the Kβ XES of $3d$ transition metals for studying correlations between the magnetic moment and charge state [32, 33]. Better addressing the forward problem not only improves the interpretation of spectral characteristics but provides a useful method of screening potential studies. This can be as simple as bolstering beam-time applications to the generation of large data sets for use in machine learning [34-36]. Achieving this also lays the groundwork for improved predictive tools for photon-in photon-out techniques, given their shared dependence on the de-excitation process.
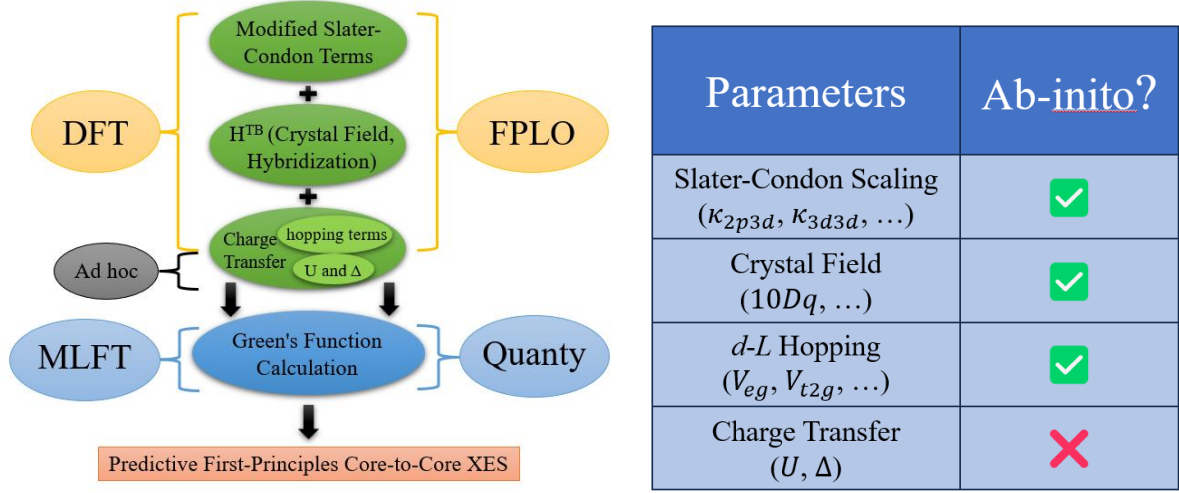
Figure 1: (Left) Schematic representation of the theoretical workflow with the left column corresponding to the method being used, the center column corresponding to the associated components calculated using said theory method, and the right column corresponding to the software carrying out the calculation at that step. (Right) Checklist of which parameters are calculated from first principles. DFT is used to extract *ab-initio* values for many traditionally empirical parameters, leaving only the charge transfer terms which must be set *ad-hoc*. These are all combined within the MLFT framework, as implemented with the Quanty code, and then used to calculate the Green's function and resulting spectrum of the target system.

In this work we present the nuances of the calculation for CTC-XES within MLFT and validate the performance of this ab-initio technique across a range of 3d transition metal (TM) systems. CTC-XES is an ideal application of DFT + MLFT for two reasons: 1), it requires charge transfer to accurately represent the system in the presence of the core-hole, meaning the hopping terms from the Wannier step are critical; and 2) the transition from intermediate to final state is charge neutral and only involves deep core levels, making it fall confidently under the

umbrella of a "perturbed atomic system" [7]. These together make it a superior direct test of DFT + MLFT compared to other techniques like XAS, XPS, and RIXS.

To this end, we will focus on DFT + MLFT for Kα ($2p \rightarrow 1s$) XES of 3d transition metals. The choice of emission line is appropriate for a validation of the approach in correlated systems. First, MLFT is fundamentally a perturbation theory, and as such, we aim to validate the leading order of environmental perturbation. This condition is justified by the weak coupling between the $2p$ states and the ligand-level electronic structure. The locality of Kα XES has also previously been contrasted to the more extended nature of XAFS, with the observation that Kα spectra can have generally simpler sensitivity to atomically-derived observables such as oxidation state [37]. This suggests that CTC-XES is only sensitive to local symmetry through Coulomb exchange coupling, unlike valence-to-core (VTC) XES or XAS where the optical excitation essentially probes the single particle density of states near the Fermi-level and is thus sensitive to the coordination symmetry. Second, the collection of $3d$ TM systems studied includes some materials with strongly localized valence-level electrons where MLFT is natural, and some systems with strong covalency where empirical parameters in MLFT typically take unexpected, if not unphysical, values to obtain numerical agreement with experiment. Again, the point here is to challenge the leading-order calculation of deep core-to-core XES via DFT + MLFT.

This paper is organized as follows: In section II, we summarize the theory of nonresonant-XES and the details of the DFT + MLFT framework as well as methods used to reduce the number of free parameters down to only two. The details of the codes being used are documented elsewhere [38, 39], but example input files are provided in SI-I. In section III, we present results, discuss the validity of the approximations used, and compare calculated spectra

with experimental spectra for a range of transition metal compounds. We examine performance across spin-state, environmental symmetry, and oxidation. Finally, in section IV, we explore the remaining two-dimensional phase space, discuss systematic drawbacks, and propose future directions for this framework.

4.2   Theoretical Formalism

A. XES Theory

The creation of a non-resonant diagram line in x-ray fluorescence is illustrated in Figure 2. In core-to-core XES, a core electron absorbs a high energy photon, leaving a deep core-hole behind and ejecting a photoelectron. After a few fs, the core-hole is filled by a less tightly bound (shallower) electron, and a photon is emitted, leaving the system in a final state with either a semi-core or valence level hole. When studied with modest energy resolution, the resulting x-ray fluorescence is commonly used for elemental identification [40]. On the other hand, following the synchrotron community convention, the same radiation is termed x-ray emission when studied with energy resolution comparable to intrinsic broadening. Such XES experiments provide information about the element specific chemical and electronic environment, often including sensitivity to oxidation and spin state of the species of interest [6].

Absorption   **Emission**
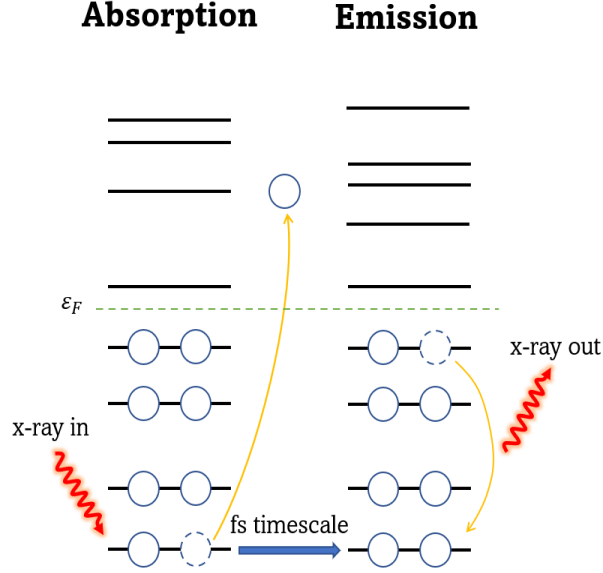
Figure 2: Schematic of the non-resonant x-ray fluorescence process. Going from left to right, an x-ray (red wiggling line) is absorbed by a core electron (solid blue circle), which is subsequently ejected from the system into the continuum. A short time later a less tightly bound electron decays into the hole (dashed blue circle) left behind by the deep core electron, emitting an x-ray to preserve energy.

The complete photon-in, photon-out process can be described by the Kramers-Heisenberg formula [7, 41],

$$\frac{d\sigma(\omega_1,\omega_2)}{d\omega_1 d\omega_2} \propto \sum_F \left| \sum_M \frac{\langle F|\hat{T}_2|M\rangle\langle M|\hat{T}_1|I\rangle}{E_I+\omega_1-E_M+i\Gamma_M/2} \right|^2 \frac{(\Gamma_F/2\pi)}{(E_I-E_F+\omega_1-\omega_2)^2+\Gamma_F^2/4}, \quad (1)$$

where $|I\rangle, |M\rangle, |F\rangle$ are initial, intermediate, and final N-electron many-body states, with corresponding energies E_I, E_M, E_F. The broadenings Γ_M, Γ_F, are due to the lifetimes of the intermediate and final states, respectively, and $\hat{T}_1, \hat{T}_2$, are dipole transition operators. The terms ω_1 and ω_2 are the energies of the incoming and outgoing photons, respectively, making $\omega_1 - \omega_2$ the energy transferred to the system. For nonresonant XES, the spectral shape is independent of

the incoming photon energy. In this case, the photoelectron can be neglected and the spectrum is proportional to the integral over incoming energy ω_1 [7]. If the lifetime broadening Γ_m is assumed constant, the integration simplifies to,

$$\frac{d\sigma_{XES}(\omega_2)}{d\omega_2} \propto \sum_f \left| \sum_m \frac{\langle f|\hat{T}_2|m\rangle\langle m|\hat{s}|I\rangle}{E_f - E_m - \omega_2 + i(\Gamma_m + \Gamma_f)/2} \right|^2 (\Gamma_m + \Gamma_f)/2\pi. \quad (2)$$

Here the states $|m\rangle, |f\rangle$ are N - 1 electron many-body states which do not include the photoelectron, and the $\hat{T}_1$ dipole transition operator has been replaced with the $1s$ annihilation operator $\hat{s}$. No polarization term is included in $\hat{T}_1$ because the continuum final state of the photoelectron is inconsequential. It should be noted that while we are focusing on the case of Kα XES for the sake of being explicit, the approach described here is generalizable to any core-to-core XES. A detailed derivation for going from Eq. (1) to Eq.(2) is given in chapter 8 of de Groot and Kotani [7]. For Kα XES, the lifetime broadenings Γ_m and Γ_f are approximately constant and are equal to the core-hole broadenings of the $1s$ and $2p$ shells (Γ_s and Γ_p), and $\hat{T}_2 = \sum_{s,p}(\vec{\epsilon}\cdot\vec{r})\hat{s}^\dagger\hat{p}$ is limited to the dipole transition operator connecting the six $2p$ fermionic modes to the two $1s$ fermionic modes. Eq. (2) considers all intermediate states which connect the final and initial states and is referred to here as *the two-step approach*.

Eq. (2) is commonly used when discussing nonresonant XES [21]; however, another possible approximation is to take the XES equivalent of the final-state rule used in VTC-XES [42] and XAS [7, 26]. In this case, the sum over intermediate states in Eq. (2) is assumed to be dominated by the ground state in the presence of the deep core-hole $|i'\rangle$ [43], which gives,

$$\frac{d\sigma_{XES}^{K\alpha}(\omega_2)}{d\omega_2} \propto \sum_f \left| \frac{\langle f|\hat{T}_2|i'\rangle}{E_f - E_{i'} - \omega_2 + i(\Gamma_s + \Gamma_p)/2} \right|^2 (\Gamma_s + \Gamma_p)/2\pi. \quad (3)$$

This approximation simplifies the problem considerably, as it requires only a single sum over the final states and will henceforth be referred to as the *one-step approach*. A full comparison between the two approaches will be explored in section IV.A. This can also be reformulated using a one-body Green's function formalism as shown in supplemental information section SI-II. Indeed, the Green's function formalism is used in Quanty for calculating the spectrum object.

B. Multiplet Ligand Field Theory

For the calculations here we use an MLFT Hamiltonian which is the sum of an atomic contribution and a tight binding Hamiltonian, $H = H^{atom} + H^{TB}$. The atomic Hamiltonian accounts for the deep-core $(1s, 2p)$ states as well as many-body Coulomb interactions U_{ijkl} between core and d states, and between individual d states. The tight-binding Hamiltonian H^{TB} describes the single particle energies of the d and ligand states, as well as hopping between them. These two terms are given by

$$H^{atom} = \varepsilon_s \sum_s \hat{c}_s^\dagger \hat{c}_s + \varepsilon_p \sum_p \hat{c}_p^\dagger \hat{c}_p + \sum_{d_1 d_2 d_3 d_4} U_{d_1 d_2 d_3 d_4} \hat{c}_{d_1}^\dagger \hat{c}_{d_2}^\dagger \hat{c}_{d_3} \hat{c}_{d4} +$$

$$\sum_{d_1 d_2 p_1 p_2} U_{d_1 p_1 d_2 p_2} \hat{c}_{d_1}^\dagger \hat{c}_{p_1}^\dagger \hat{c}_{d_2} \hat{c}_{p_2} + \sum_{d_1 d_2 s_1 s_2} U_{d_1 s_1 d_2 s_2} \hat{c}_{d_1}^\dagger \hat{c}_{s_1}^\dagger \hat{c}_{d_2} \hat{c}_{s_2} + \sum_{p_1 p_2} h^{SO}_{p_1 p_2} \hat{c}_{p_1}^\dagger \hat{c}_{p_2} +$$

$$\sum_{d_1 d_2} h^{SO}_{d_1 d_2} \hat{c}_{d_1}^\dagger \hat{c}_{d_2}, \quad (4)$$

$$H^{TB} = \varepsilon_d \sum_d \hat{c}_d^\dagger \hat{c}_d + \varepsilon_L \sum_L \hat{c}_L^\dagger \hat{c}_L + \sum_{\gamma \gamma'} V^{LF}_{\gamma \gamma'} \hat{c}_\gamma^\dagger \hat{c}_{\gamma'}. \quad (5)$$

In these equations, the indices s and p indicate a sum over the $1s$ or $2p$ states of the absorbing metal atom, d a sum over absorber $3d$ states, and γ a sum over the $3d$ and ligand states. The ε_s, ε_p, ε_d, and ε_L terms are the centroids of the single-particle energies for the corresponding shells, U_{ijkl} are the Coulomb matrix elements, and $V^{LF}_{\gamma\gamma}$ (taken from the DFT tight binding Hamiltonian) encompasses the crystal field as well as couplings between the $3d$ and ligand states. Finally, h^{SO}

is the single-particle spin orbit coupling Hamiltonian $h^{SO} = \vec{l} \cdot \vec{s}$. The U_{ijkl} Coulomb terms are parameterized by the Slater-Condon F and G parameters corresponding to direct and exchange Coulomb interactions, as well as the many-body average screened Coulomb interactions U_{dd}, U_{pd}, and U_{sd} which encompass the spherically symmetric contribution to the multipole expansion [7]. It should be noted that for the case of Kα XES the terms U_{pd} and U_{sd} refer to the average interactions between the $2p, 3d$ and $1s, 3d$ orbitals respectively. In the case of highly anisotropic (layered) systems, it may become important to account for the difference in couplings on an orbital by orbital level [44]. However, given that the anisotropy of our systems is weak compared to that of layered compounds we expect that any error introduced by averaging will be negligible. Finally, the charge transfer energy Δ defines the energy required to transfer one electron from the ligand to the metal. The Slater-Condon parameters are also obtained from the radial wave functions of the DFT calculation, so that the only remaining free parameters are the many-body charge-transfer energy Δ and the many-body average screened Coulomb interactions U_{dd}, U_{pd}, and U_{sd}.

These four free parameters are used to set the centroids of each shell according to the ligand field equations (see supplemental information section SI-III). Using the definitions of the ground state energy, a single, and double charge transfer, we can solve for $\varepsilon_s, \varepsilon_p, \varepsilon_d$, and ε_L. For the intermediate state this gives

$$\varepsilon_s = -n_d U_{sd}, \quad (6)$$

$$\varepsilon_d = (2\Delta n_L - n_d^2 U_{dd} + n_d(U_{dd} - 2n_L U_{dd}) - 4n_L U_{sd})/(2(n_d + n_L)), \quad (7)$$

$$\varepsilon_L = n_d(-2\Delta + U_{dd} + n_d U_{dd} + 4U_{sd})/(2(n_d + n_L)), \quad (8)$$

where n_d and n_L are the number of $3d$ electrons and number of ligand electron respectively. Note that centroids given by Eq. (6-8) will change for the initial (no core-hole) and final state ($2p$ core-hole). More details on origin of the ligand field equation can be found in [45], [46], and all ligand field equations for the XES process can be found in the supplemental information section SI-III.

4.3   Methods

A. Computational

In this work we use the full-potential local-orbital electronic structure code FPLO [39] to calculate the tight binding Hamiltonian and the radial wavefunctions necessary for the Slater-Condon *F* and *G* terms. The code Quanty [38] was used for the subsequent solution of the MLFT Hamiltonian and for the construction of the spectrum [16]. The interface between FPLO and Quanty was built by Heinze and Haverkort [45] following the framework developed by Haverkort et al. [16]. We used FPLO version 14.00-49-x96_64, with the Perdew-Wang 92 exchange correlation functional. For additional information about the details of the DFT calculation please refer to supplemental information section SI-VI.

Using band structure and density of states as a guide, the energy window of the down-projection of the Wannier functions was tailored to the TM-$3d$ and ligand-$2p$ orbitals following the procedure described in [47]. It should be emphasized that the Wannier functions calculated within FPLO are not maximally localized. The fact that we use a tight binding Hamiltonian then requires that, along with a localization procedure that reduces the number of overall terms in the Hamiltonian, the Wannier functions are chosen such that they reproduce both the band energies

and the orbital character of the bands. The details of this step are explained in reference [48]. The DFT mean-field Coulomb interaction between the $3d$ electrons is subtracted from the tight-binding Hamiltonian to prevent double counting; this is accounted for later with the U_{dd}, U_{pd}, U_{sd}, and Δ free parameters. Only $2p$-$3d$ exchange Slater-Condon parameters are considered in the Kα XES calculation, neglecting the weak $1s$-$3d$ Coulomb exchange terms. Additionally, it is well known that U_{pd} and U_{sd} are close numerically, and are usually 0.5 eV – 2.0 eV larger than U_{dd} [46]. Thus, we use the relations $U_{pd}/U_{dd} = 1.15$ and $U_{sd}/U_{dd} = 1.20$. Even though the ideal ratio will depend on the compound, this approximation will just result in the U_{dd} values being slightly off compared to the optimal value (on the order of 0.1 eV). For XES we expect that the more important constraint is that the U_{pd} and U_{sd} values are similar, given that they represent the influence of the core-hole on charge transfer when going between the intermediate and final states. After this, we are left with only 2 free parameters: U_{dd} and Δ, making it reasonable to do a full exploration of the remaining adjustable parameter space for each system. For most materials, the values of U_{dd} and Δ were determined by doing a grid search from 1 eV to 10 eV in 0.5 eV steps and we chose the spectrum whose features appeared to agree best with experiment. The two exceptions to this are NiO, which was taken from prior work using the same DFT + MLFT pipeline applied to XAS [16, 38], and PbCrO4 which required searching negative Δ values as explained in section IV.D. When considering charge transfer it is common to limit the number of accessible configurations (e.g. $3d^N$, $3d^{N+1} \underline{L}^1$, $3d^{N+2} \underline{L}^2$, …) to simplify the calculation. However, we opted to include all possible configurations (up to $3d^{10}$) for every system. This came at an increased computational cost but with the advantage of a more accurate and consistent procedure.

It is important to compare the theory with known trends in Kα XES. As an example we test the commonly asserted linear relationship between the Kα$_1$ full width half-maximum (FWHM) and the number of unpaired $3d$ electrons [49]. Mulliken population analysis is often used for determining the $3d$ unpaired occupation [50], but this can yield unphysical results for diffuse systems. Instead, we calculate the expectation value of the S^2 operator acting on the intermediate ground state wavefunction, which is consistent with the established MLFT framework. From this it is trivial to solve the equation,

$$S(S + 1) = \langle \hat{S}^2 \rangle; n_{unpaired\ 3d} = 2S, \quad (9)$$

and hence extract the number of unpaired $3d$ electrons for the system.

B. Experimental

MnO, Mn$_2$O$_3$, MnO$_2$, and CrCl$_2$ samples were prepared from greater than 97% reagent grade stock (Sigma Aldrich). All Mn samples were prepared by pressing a 1:1 mass mixture of powder sample and hexagonal boron nitride (BN) into a 13-mm diameter pellet before being encased in a polyimide pouch. The air and moisture sensitive CrCl$_2$ sample was prepared by sealing powder in a quartz tube (0.01 mm wall thickness), in a nitrogen glovebox.

The XES spectra for these samples were collected using the laboratory-based spectrometer described in detail in Jahrman, et al., [51]. Briefly, using a conventional x-ray tube (Varex VF80, Pd-Anode) operated at 100 W electron beam power (35 kV, 2 mA) samples were illuminated for 1.5 hours and 14 hours for the Mn samples and CrCl$_2$ samples respectively, insuring at least 10,000 counts at the Kα$_1$ peak for all spectra. Additional Cr$_2$O$_3$ and PbCrO$_4$ experimental spectra are from Jahrman, et al., [52] and the NiO spectra is digitized from Kawai, et al. [53].

C. Data Analysis

To compare spectral features quantitatively between experiment and theory and across samples, we have extracted the $K\alpha_1$ FWHMs, $K\alpha_2$ FWHMs, and $K\alpha_1$:$K\alpha_2$ integral ratios. $K\alpha$ XES is complicated by the presence of shoulders and additional multiplet features within $K\alpha_1$ and $K\alpha_2$ peaks, usually making it necessary to use more than two peak functions (Lorentzian or Voigt) to achieve the most accurate fit to a spectrum [54]. Therefore, to extract the $K\alpha$-FWHM parameters, we have used linear interpolation between data points which lie on either side of the half-maximum crossing points following Lafuerza et al., [20]. For the $K\alpha_1$:$K\alpha_2$ integral intensity ratio, individual peaks must be extracted from the overall spectra to accurately measure their relative areas. This is done using two to four Voigt functions to achieve an approximate line shape, from which we extract integral intensities. The fitting procedure follows Jabua [55] and Voigt fits for all compounds are presented in the supplemental information section SI-V.

Unless otherwise stated, all spectra have been integral normalized and shifted to align the maximum of $K\alpha_1$ at zero. Also, all calculated spectra are broadened using lifetime values in Campbell and Papp [56], which are reported for each main peak in Table 1. A 1.0 eV Gaussian broadening for experimental resolution was applied to all spectra except that of MnF_2, where 0.5 eV was used due to the higher resolution of the spectrometer used in that experiment [54]. Additional information about the extraction of the FWHM and how the spectra were broadened can be found in supplemental information section SI-V.

4.4   Results and Discussion

This section is organized as follows. In IV.A we address the validity of the one-step approach compared to the two-step approach and demonstrate that they produce nearly identical

results. All subsequent calculations use the one-step approach which greatly reduces computational costs. In IV.B we compare theory and experiment for complete spectra and address the limitations of our approach by system-specific discussions. In IV.C we compare theory and experiment for a few spectral parametrizations, including the FWHM of the two peaks, and the $K\alpha_1$:$K\alpha_2$ intensity ratio. We also show how a key trend involving the $K\alpha_1$ FWHM and number of unpaired $3d$ electrons is well reproduced by theory. Finally, in IV.D we address the remaining model limitations and discuss possible methods for overcoming them.

A. One-Step Approach versus Two-step Approach

The question naturally arises about the equality (or inequality) of the one-step and two-step methods. There is little experimental work on this question. Glatzel, et al., [57] compared the Mn Kβ XES of $^{55}Fe_2O_3$ undergoing electron orbital capture from the $1s$ shell with that of MnO excited by high energy x-rays. Distinct differences between the two spectra were observed, and it was proposed that multiple intermediate states need to be considered for a complete description of the process. While this suggests that the simplified process described by Eq. (3) may be insufficient for Kβ XES, the approximation has not been tested extensively, and not for Kα XES. However, if the simplified approach (only considering the lowest energy intermediate state) is indeed justified, then the greater theoretical complexity and much higher computational cost of the full excitation/de-excitation calculation can be avoided.

To address this question in detail, we compare the one-step and two-step approaches in Figure 3, where the left panel shows the energy transfer plane for NiO and $PbCrO_4$. Both approaches are calculated using the same DFT + MLFT cluster model in accordance with the procedure laid out in section III.A. The horizontal axis (excitation energy) corresponds to the 1s

XPS and is the result of annihilating as 1s electron. The non-resonant XES corresponds to the diagonal line through the energy transfer versus excitation energy plane, which incorporates the decay from all of the 1s XPS final states to the accessible 2p hole XES final states. By integrating out the ω_1 dependence, which is equivalent to integrating along the diagonal through the plane ($\omega_1 - \varepsilon_{corehole} = \omega_1 - \omega_2$)we obtain the two-step nonresonant XES as given by Eq. (2).. The right panel of Figure 3 compares the two approaches, and we note that there is little difference between them. This is intriguing as prior work on XPS calculated using the DFT + MLFT cluster model has been shown to perform poorly compared to techniques such as DFT + Dynamical Mean Field Theory (DMFT) because it lacks non-local relaxation effects which occur in response to the core-hole [58]. We expect that this is because the CTC-XES signal only involves electron transfer between core states and is therefore only weakly sensitive to such long-ranged effects. While the same DFT step (a few hours computation time on a modern CPU) is used for both approaches, the MLFT portion of the two-step approach requires 10 to 100 times more computational time than for the one-step approach. Given the excellent agreement between the two approaches, we use the one-step approach for all subsequent calculations.
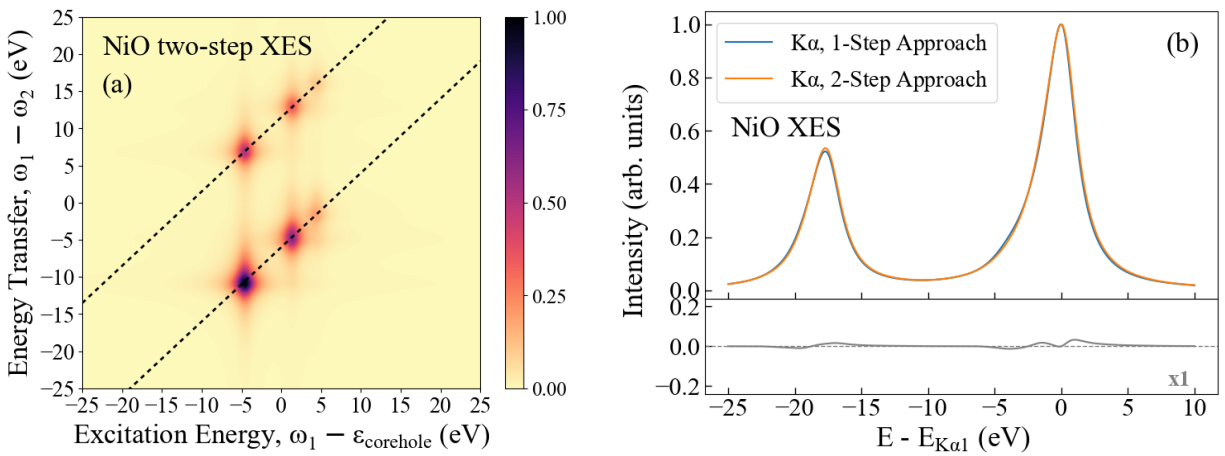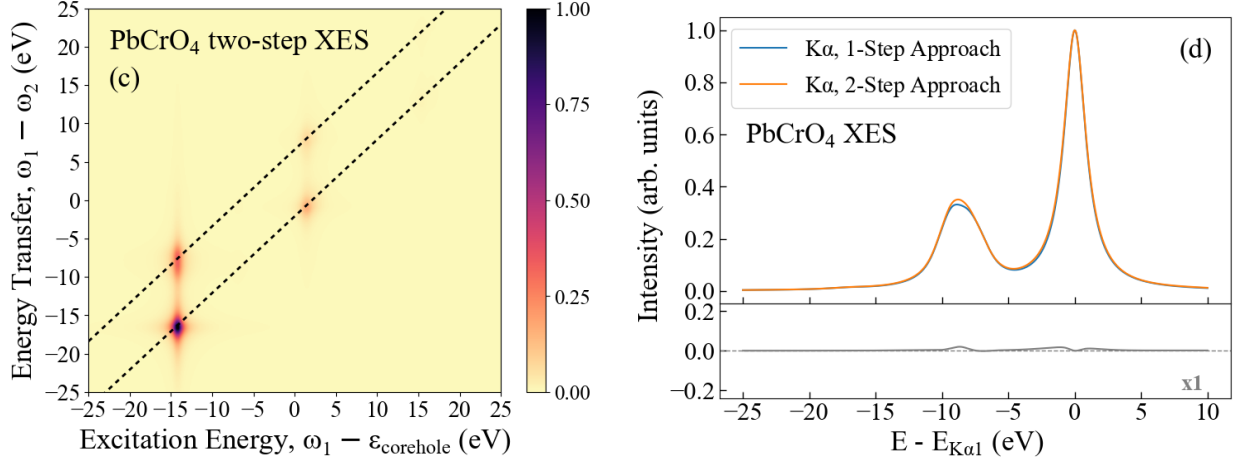
Figure 3: Calculated results of the one-step and two-step approaches for transition metal systems NiO (a, b) and PbCrO$_4$ (c, d). (Left) Two-step XES plane calculated from Eq (1). The two dashed lines in subplots (a) and (c) demonstrate how the intermediate states with different excitation energies all line up along a line with slope 1 (constant Emission Energy). By integrating along this line, we calculate the nonresonant XES as it is described by Eq. (2). (Right) Calculations of the one-step approach (blue) compared to those of the two-step approach (orange), with differences between the two approaches also shown (grey).

B. Comparison Between Theory and Experiment (Full Spectra)

Below we present a full spectral comparison between the calculated and experimental spectra for 8 different transition metal compounds. We briefly discuss the general strengths and weaknesses of the results and conclude by addressing a few interesting features of individual spectra.

Calculation Parameters

|	$F2_{dd}$	$F4_{dd}$	$G1_{pd}$	$G3_{pd}$	$F2_{pd}$	ζ_{2p}	ζ_{3d}	Δ	U_{dd}	U_{pd}	U_{sd}	$\Gamma_{K\alpha_1}$	$\Gamma_{K\alpha_2}$
NiO	11.704	7.230	5.154	2.929	6.929	11.510	0.081	4.700	7.300	8.500	8.760	2.060	2.510
$CrCl_2$	7.856	4.805	3.019	1.710	4.318	5.670	0.050	6.500	4.500	5.220	5.400	1.650	2.090
Cr_2O_3	8.531	5.246	3.216	1.822	4.585	5.670	0.050	5.500	5.500	6.380	6.600	1.650	2.090
$PbCrO_4$	8.203	5.031	3.116	1.766	4.451	5.670	0.050	-8.000	2.000	2.320	2.400	1.650	2.090
MnF_2	9.575	5.906	3.877	2.199	5.388	6.846	0.053	6.000	3.000	3.480	3.600	1.710	2.320
MnO	9.649	5.954	3.898	2.211	5.415	6.846	0.053	8.500	7.000	8.120	8.400	1.710	2.320
Mn_2O_3	9.658	5.960	3.900	2.213	5.419	6.846	0.053	6.000	4.000	4.640	4.800	1.710	2.320
MnO_2	9.722	6.003	3.920	2.224	5.444	6.846	0.053	5.000	3.000	3.480	3.600	1.710	2.320

Table 1: The Slater-Condon, the spin-orbit splitting terms ζ, charge-transfer Δ and U_{dd}, and lifetime broadening terms for each material, all in units of eV.

The Slater-Condon, charge-transfer, spin-orbit coupling, and broadening parameters for each material are presented in Table 1. Of the eight materials considered, NiO and MnO are both well studied Mott insulators, and are commonly used as standard test beds for investigating highly correlated materials [59]. Both have rock-salt crystal structures and are thus highly symmetric with perfect octahedral coordination, simplifying their treatment. In contrast, MnF_2, MnO_2, Cr_2O_3, and $CrCl_2$ all have single site, distorted octahedral coordination. Mn_2O_3 is also distorted octahedral but has two unique Mn sites which must be independently considered before being averaged together. Finally, $PbCrO_4$ has a distorted tetrahedral symmetry, the lowest symmetry system being studied, in addition to being the only $3d^0$ system (nominally no $3d$ electrons).
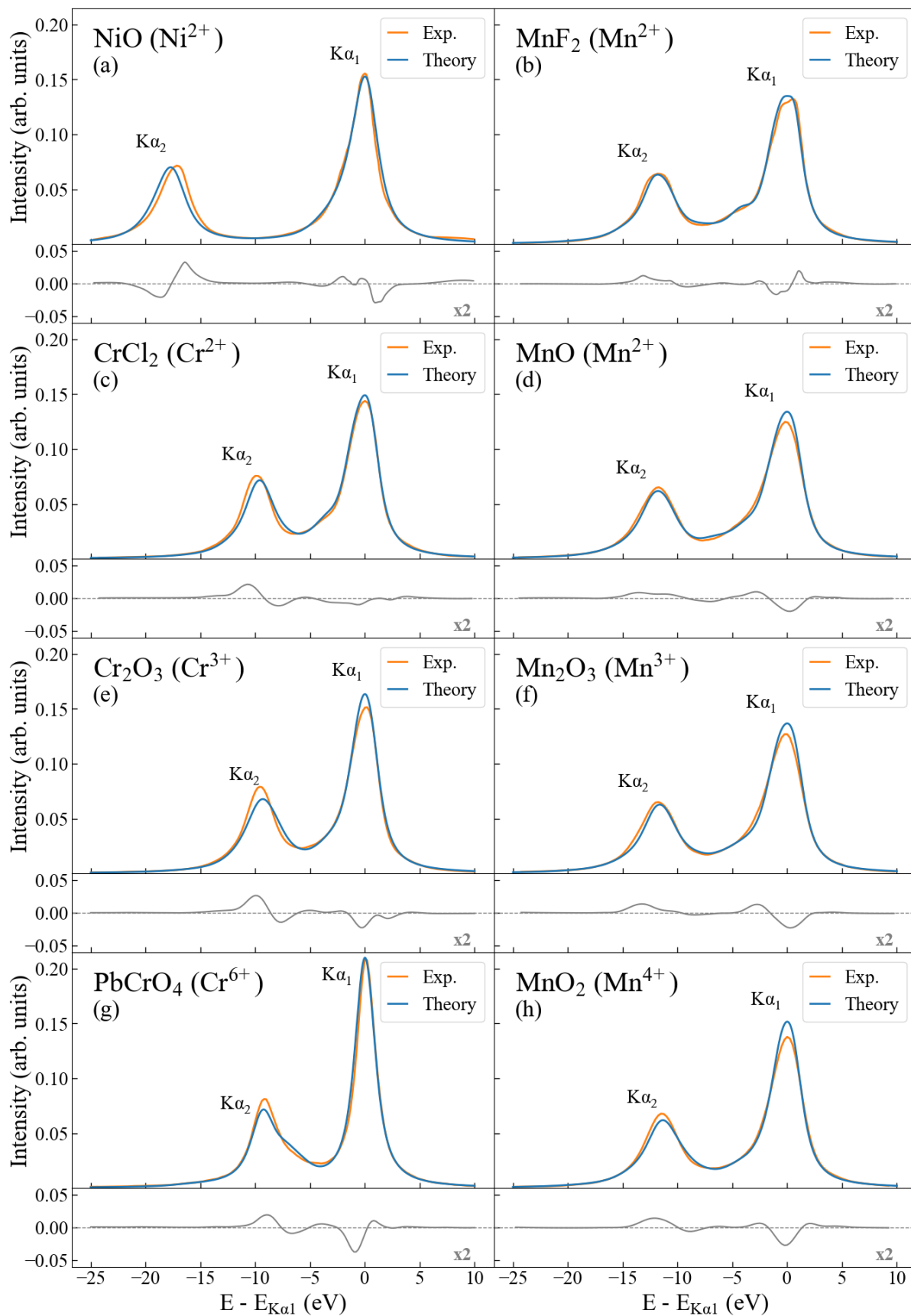
Figure 4: Theoretical (blue) and experimental (orange) Kα XES for NiO (a), MnF_2 (b), $CrCl_2$ (c), MnO (d), Cr_2O_3 (e), Mn_2O_3 (f), $PbCrO_4$ (g), and MnO_2 (h). Difference curves (gray) show experiment minus theory and are shown in the lower panel of each subplot. All theory spectra were calculated following the one-step approach laid out in Eq. (3) and have been shifted so that the $Kα_1$ peaks align with experiment.

The calculated and experimental spectra for all materials are presented in Figure 4. For most of the materials studied we observe good agreement between theory and experiment, at the same level or higher compared to other DFT + MLFT calculations [25, 26, 60] and alternative *ab-initio* techniques such as CI [61] or Discrete-Variational (DV) Xα [62]. The remaining spectral discrepancies can be discussed in terms of line shape differences or small disagreements in peak-to-peak splitting.

While the overall line shapes are in good agreement, there is a systematic trend of the $Kα_1$ peaks being too narrow (under-broadened), the $Kα_2$ peaks being too wide (over-broadened), and both peaks exhibiting slightly inaccurate asymmetries. One possible explanation for these discrepancies is that the modified Slater-Condon terms are incorrect, leading to inaccurate exchange terms between the $2p$ and $3d$ states and thus adversely affecting the multiplet splittings. However, this would affect the $Kα_1$ and $Kα_2$ states roughly equally and therefore can be ruled out. It is tempting to attribute the broadening issue entirely to errors in the core-hole lifetime values, since the overall agreement can be improved significantly by allowing these lifetimes to vary (Figure SI-V 3). However, to achieve best fits this leads to unphysical cases in which the $Kα_2$ broadenings are comparable to the $Kα_1$ broadenings, which is not possible due to Coster-Kronig decay [63]. Allowing the broadening to vary from tabulated values also causes a

deviation of theory from experiment in the high energy tails of Kα₁ (Figure SI-V 4), which together with the previous point make broadening alone unlikely to be the culprit.

With these explanations being ruled out, the error in line shape is more likely due to DFT's tendency to estimate too large a coupling between the $3d$ and ligand states. The off-diagonal coupling terms of the H^{TB} indirectly modulates the strength of the exchange interaction between the $3d$ and $2p$ levels by controlling the configuration of the $3d$ shell, as well as directly modulating the energies of the valence level states. Reducing these off-diagonal coupling terms would influence multiple factors including the relative multiplet splittings and the position of any low binding energy Kα₁ satellites that sit near the Kα₂ peak. Future work is needed to further explore this issue, with one possibility being the use of LDA + U which could help better localize the $3d$ electrons. Finally, we note that other work has shown how more advanced MLFT models that incorporate separate Slater-Condon couplings between the various crystal field split valence states can affect the broadening of the $2p_{1/2}$ and $2p_{3/2}$ levels [17].

The peak-to-peak splitting is dominated by the relativistic $2p$ spin-orbit splitting, parameterized by the coupling term ζ_{2p}, which separates emission from the $2p_{3/2}$ and $2p_{1/2}$ levels. This spin-orbit coupling is a largely intrinsic property and is not expected to change significantly when going from an atomic to solid-state system [64]. The errors in the calculated peak-to-peak splittings are of order a few tenths of an eV, with NiO being an outlier with a peak splitting error of ~1 eV. Although subtle changes in the Slater-Condon and charge transfer terms may explain some of the error and result in peak-to-peak splitting variations on the order of half an eV, the multiple interaction terms in the Hamiltonian make it difficult to pinpoint a single source of error. This discrepancy is also noted in empirical MLFT calculations performed by Glatzel [49].

Turning now to some intriguing features of the individual spectra, MnF_2 exhibits an asymmetric doublet feature in the $K\alpha_1$ as can be seen in Figure 5. This doublet splitting is approximately 1 eV and can only be seen with high resolution instruments [54]. This feature is well documented [65], and is a result of large exchange interaction allowing individual multiplet peaks to be resolved. While this same doublet feature is seen in the theory, the relative intensities of the multiplet peaks are slightly off compared to the experimental ones, causing the overall peak to broaden together into a flatter peak shape. However, this demonstrates how even in a spectroscopy with objectively simple line shapes, individual multiplet peaks can still be interpreted for the role they play [49] in much the same way as in XPS [5, 66] or RIXS [23].
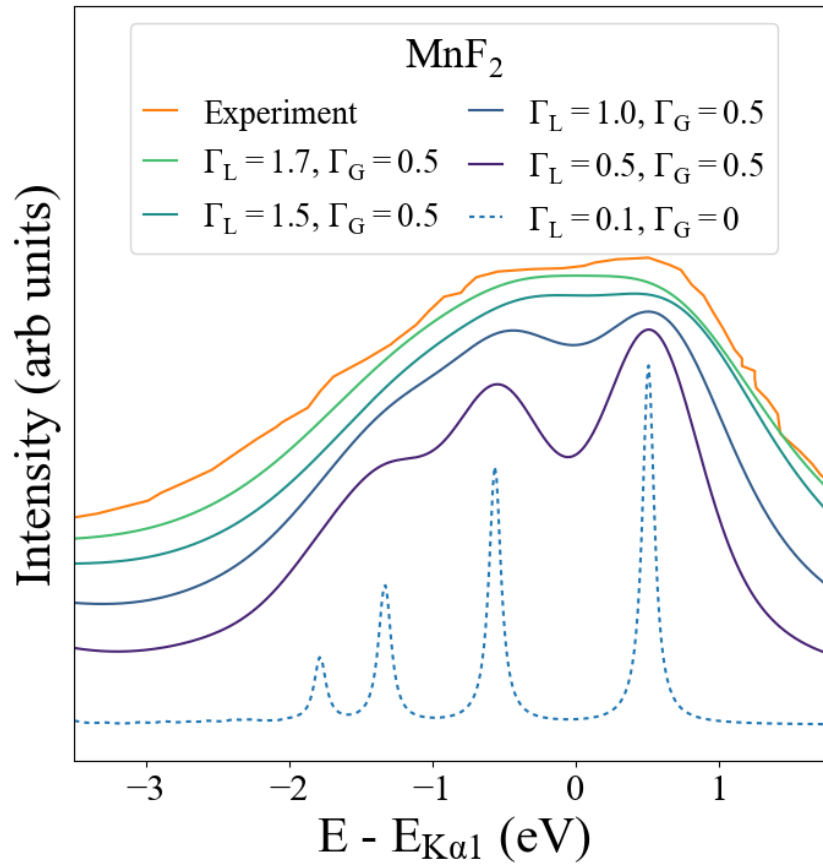
Figure 5: MnF_2 experiment compared to theory for various lifetime (0.1-1.7 eV) and experimental broadening values (0-0.5 eV). The broadening scheme for each of these calculated spectra follows that described in section SI-V. This demonstrates how the multiplet doublet that is visible in the experimental $K\alpha_1$ peak is also present in the theoretical results. However, this doublet becomes obscured by the broadening.

Shifting from the details of fine spectral features to full spectral trends across compounds, to demonstrate a potential application we chose to reproduce a key result from a 2018 study by Jahrman et al. [52] which identified nonresonant XES as a promising analytical method for determining the ratio of Cr(VI) to Cr(III) in chemically challenging matrices, such as plastics. Standard wet chemical methods are susceptible to species interconversion and incomplete extraction, which has the potential to systematically underestimate the mass fraction of Cr(VI) [67, 68]. However, the $K\alpha$ XES spectra for Cr(III) and Cr(VI) are distinct enough to allow for a linear combination to be fit to an unknown composition ratio. In Figure 6 we show that we can reproduce experimentally observed differences between the Cr(III) to Cr(VI) $K\alpha$ XES using Cr_2O_3 and $PbCrO_4$, as is shown from the residuals in grey. The most notable difference is the high peaked, narrow $K\alpha_1$ signal of Cr(VI), which is a consequence of the 6+ formal oxidation state, leading to a distinct difference in the FWHM and intensities of the $K\alpha_1$ peaks.
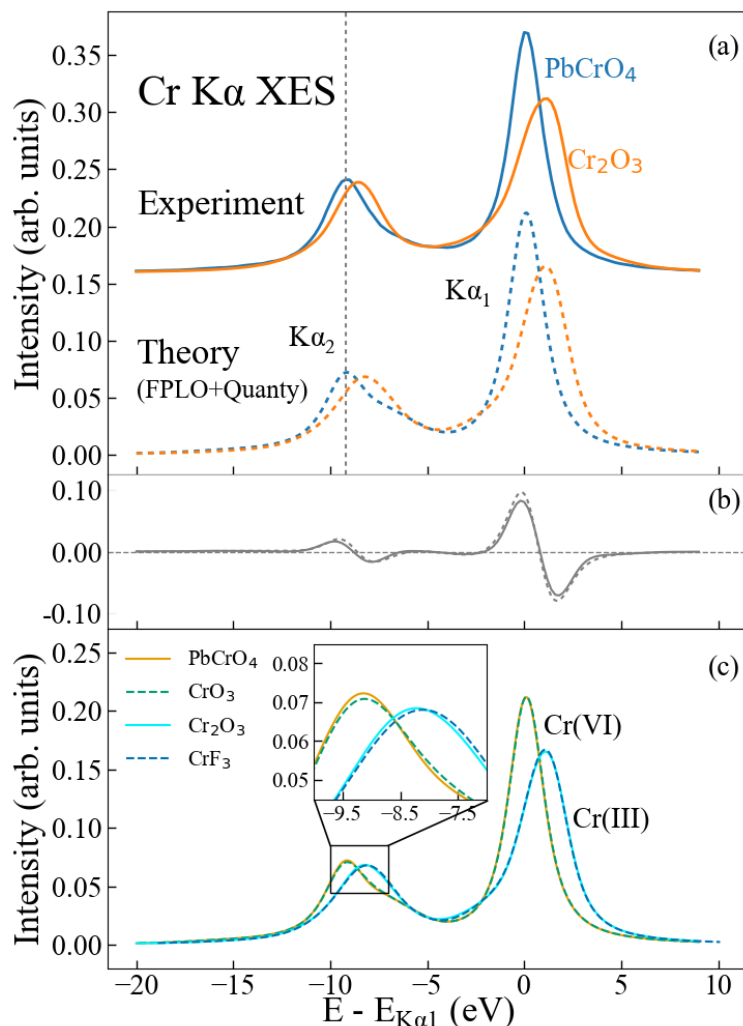
Figure 6: (a) Experimental (solid) and theory (dashed) spectra for Cr_2O_3 and $PbCrO_4$. The $K\alpha_1$ peak of the calculated $PbCrO_4$ (Cr(VI)) spectrum is shifted to 0 eV and the $K\alpha_1$ peak of the calculated Cr_2O_3 (Cr(III)) spectrum is shifted to match the splitting between the experimental spectra. (b) Difference curves for Cr(VI) experiment – Cr(III) experiment (solid) and Cr(VI) theory – Cr(III) theory (dashed). (c) Theoretical XES spectra for two Cr(III) compounds (CrF_3 and Cr_2O_3) and two Cr(VI) compounds (Cr_2O_3 and $PbCrO_4$). The inset in subplot (c) shows an enlarged view of the spectra between -10 eV and -7 eV, demonstrating that while the spectra of Cr compounds with the same oxidation state are very similar, they are not identical.

This distinction between Cr_2O_3 and $PbCrO_4$ Kα XES was demonstrated by Jahrman et al. [52] to be constant across Cr(III) and Cr(VI) materials. We found that this observation also held true for our calculated spectra, as demonstrated in the bottom of Figure 6. Both of the Cr(VI) compounds are tetragonally coordinated with oxygen and the Cr(III) compounds are octahedrally coordinated with fluorine and oxygen respectively. We note that the simulated Kα XES spectra are relatively insensitive to the particular compound, and are instead sensitive to the nominal oxidation state and environmental symmetry, again agreeing with trend observed in experiment by Jahrman et al. [52].

C. Comparison Between Experiment and Theory (Spectral Characteristics)

Neglecting interactions, the Kα1:Kα2 integral ratio is naively expected to be 2:1 due to the 4:2 ratio of occupancy of the $2p_{3/2}$ and $2p_{1/2}$ shells. However, the ratio is generally skewed by mixing between these states due to Coulomb interactions between the $2p$ core-hole and $3d$ electrons[66]. In the top panel of Figure 7 we compare theory and experiment. The deviation from the 2:1 ratio is most clear for $CrCl_2$, MnO and Mn_2O_3, each of which have strong shoulders on the lower energy side of Kα1. We note that the extracted ratio is highly dependent on the quality of the Voigt fits that are used to deconvolve the Kα1 and Kα2 peaks (Figure SI-IV 1). The scatter plot in Figure 8 (a) shows the extent of correlation between theory and experiment.

The FWHM of the peaks are a common metric for characterizing the Kα XES [49, 53, 55], even though the presence of many distributed multiplet features can impede its easy

interpretation. As with the $K\alpha_1{:}K\alpha_2$ ratio there is generally good correlation between theory and experiment; see also the bottom panel of Figure 7 and Figure 8 (b). The strongest outlier is the $PbCrO_4$ $K\alpha_2$ FWHM. This, as well $PbCrO_4$'s low $K\alpha_1{:}K\alpha_2$ ratio, can be attributed to a combination of the $2p$, $3d$ Coulomb exchange interaction and valence level hybridization. These issues will be discussed in greater detail in section IV.D, where we address the limitations of the model.
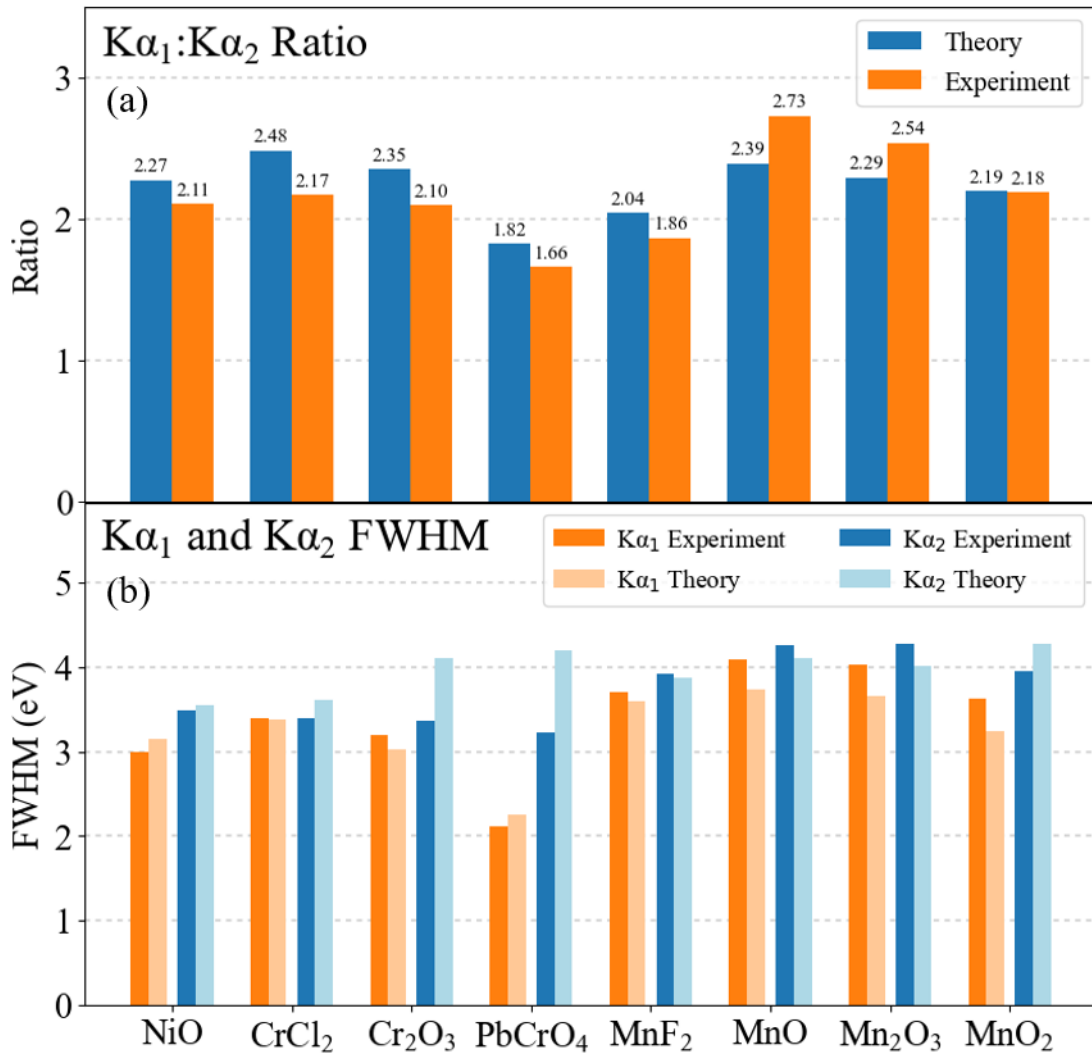
Figure 7: Comparison of theory and experiment for (a) Kα₁:Kα₂ integral ratio and (b) FWHM for the various compounds. The FWHM values were calculated according to the procedure in Figure SI-V 1.
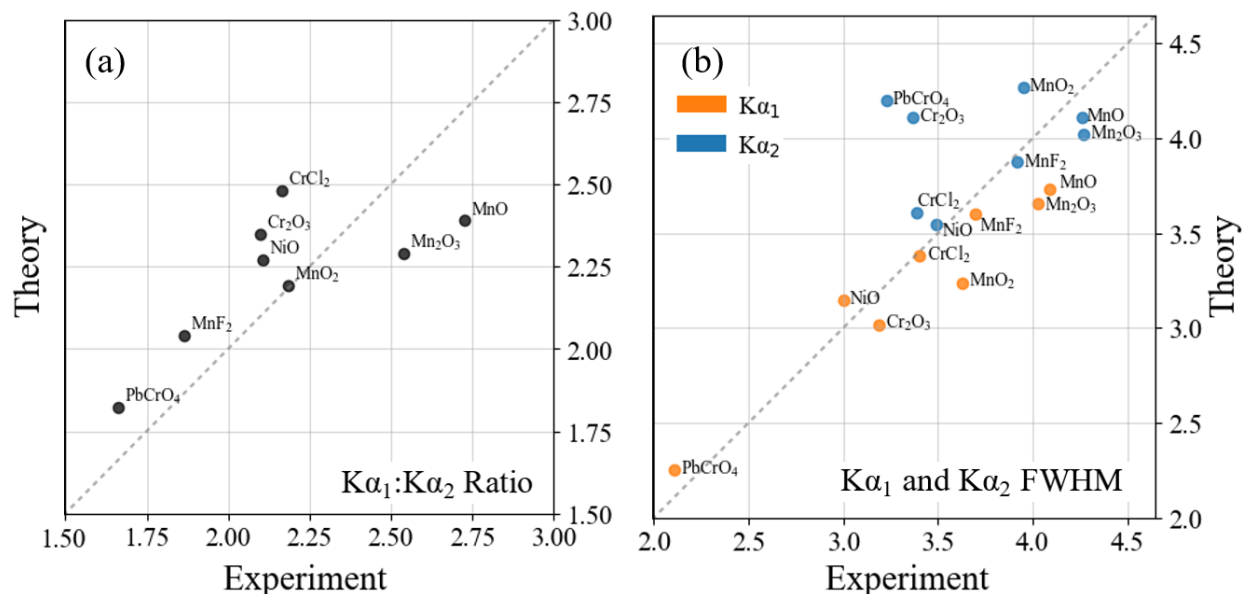
Figure 8: Trendlines between theory and experiment values for (a) the Kα₁:Kα₂ integral ratio and (b) the FWHM of Kα₁ and Kα₂. The values plotted are the same as those for the bar charts in Figure 7.

Using the FWHM values extracted from the calculated spectra, we can now explore an often-stated rule of multiplet theory that Kα₁ linewidth is directly proportional to the exchange interaction between the $2p$ and $3d$ orbitals, G_{pd}^1 and G_{pd}^3 [6]. This will allow us to test a known experimental trend across a set of compounds and confirm an important caveat first raised by Kawai [50]. Specifically, the charge-transfer state in the presence of the core-hole will necessarily influence the Kα₁ FWHM because the number of unpaired $3d$ electrons will change in response to the core-hole potential. Determining whether the theory follows the established FWHM trend provides an important litmus test, as the same charge-transfer parameters U_{dd} and

Δ which determine the fits to experiment also determine the number of unpaired 3d electrons in the intermediate state.

This dependence on the core-hole $n_{unpaired\ 3d}$ is the origin of the similarity between the Kα XES of compounds such as MnO and Mn_2O_3 [49], and FeO and Fe_2O_3 [50], with their nearly identical metal ion spin states even though they have different classical oxidation. The derivation for the linear relationship between the Kα_1 FWHM and the number of unpaired *3d* electrons relies on the use of a free ion model [69] and has a number of key assumptions, most notably that the orbital angular momentum of the *3d* states is quenched ($J = S$), simplifying the coupling between the final state *2p* hole and the valence shell [49]. As such, this linear trend is expected to be more of a general rule, rather than a hard and fast law.
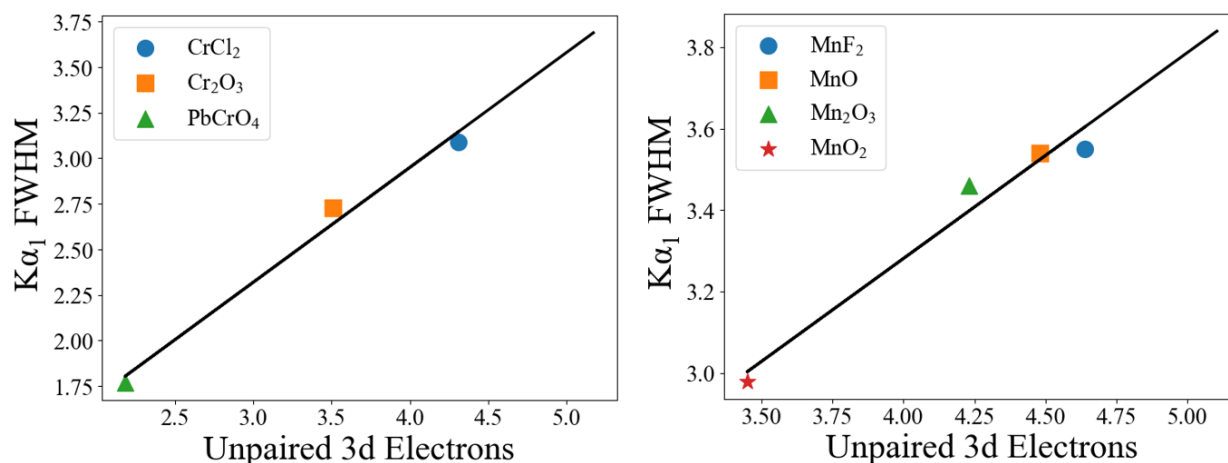
Figure 9: Kα_1 FWHM vs Number of Unpaired 3d Electrons for Cr (left) and Mn (right). Reported values of FWHM are calculated from theorical results broadened with lifetime values reported in Table 1. Both series exhibit the expected linear trend. FWHM values were calculated according to the procedure laid out in Figure SI-V 1.

$3d$ Orbital Occupations and Kα_1 FWHMs

	Nominal # of 3d Electrons	$\langle n_d \rangle$	$\langle S^2 \rangle$	# of Unpaired 3d Electrons	Kα_1 FWHM (only lifetime broadening)
NiO	8.00	9.03	0.79	1.04	2.76
CrCl$_2$	4.00	4.88	6.81	4.31	3.09
Cr$_2$O$_3$	3.00	4.35	4.83	3.51	2.73
PbCrO$_4$	0.00	5.43	2.28	2.18	1.77
MnF$_2$	5.00	5.38	7.71	4.64	3.55
MnO	5.00	5.50	7.25	4.48	3.54
Mn$_2$O$_3$	4.00	4.90	6.59	4.23	3.46
MnO$_2$	3.00	4.68	5.18	3.66	2.98

Table 2: Expectation values for the n_d number operator and S^2 operator, both calculated over the 3d fermionic modes. The number of unpaired 3d electrons (calculated from Eq. (9)) in the presence of a core-hole, the Kα_1 FWHM (calculated from theory), and the nominal number of total 3d electrons are also reported. S^2 expectation values are reported in units of $\hbar^2$ and Kα_1 FWHM are reported in units of eV.

The number of unpaired $3d$ electrons in the presence of the core-hole and the Kα_1 FWHM values are reported in Table 2 and are plotted in Figure 9 for the Cr and Mn series. As addressed earlier, PbCrO$_4$ is nominally a d^0 system. However, when hybridization with the ligand orbitals is considered, the ground state occupation's expectation value becomes approximately 1, which increases to approximately 2 when considering the effect of charge-transfer in the presence of the core-hole. The expected linear relationship is only observed when considering these multiconfigurational effects, confirming Kawai's findings that they are necessary for accurately representing the excited magnetic state of the system [50].

D. Effect of Δ and U_{dd} on the spectrum, and limitations of MLFT

As noted above a long-term goal of this research program is a fully *ab-initio*, predictive treatment of Kα XES with no adjustable parameters. Here, the traditional MLFT parameter space has been reduced to only two dimensions; however, the spectra are still quite sensitive to Δ and U_{dd}. The interplay of the tuning parameters for charge transfer and Coulomb interactions adds complexity to the spectra, making it difficult to isolate the origin of certain spectral features. However, the reduced parameter space still simplifies the process of fitting theory to experiment and allows more detailed exploration than previously possible.
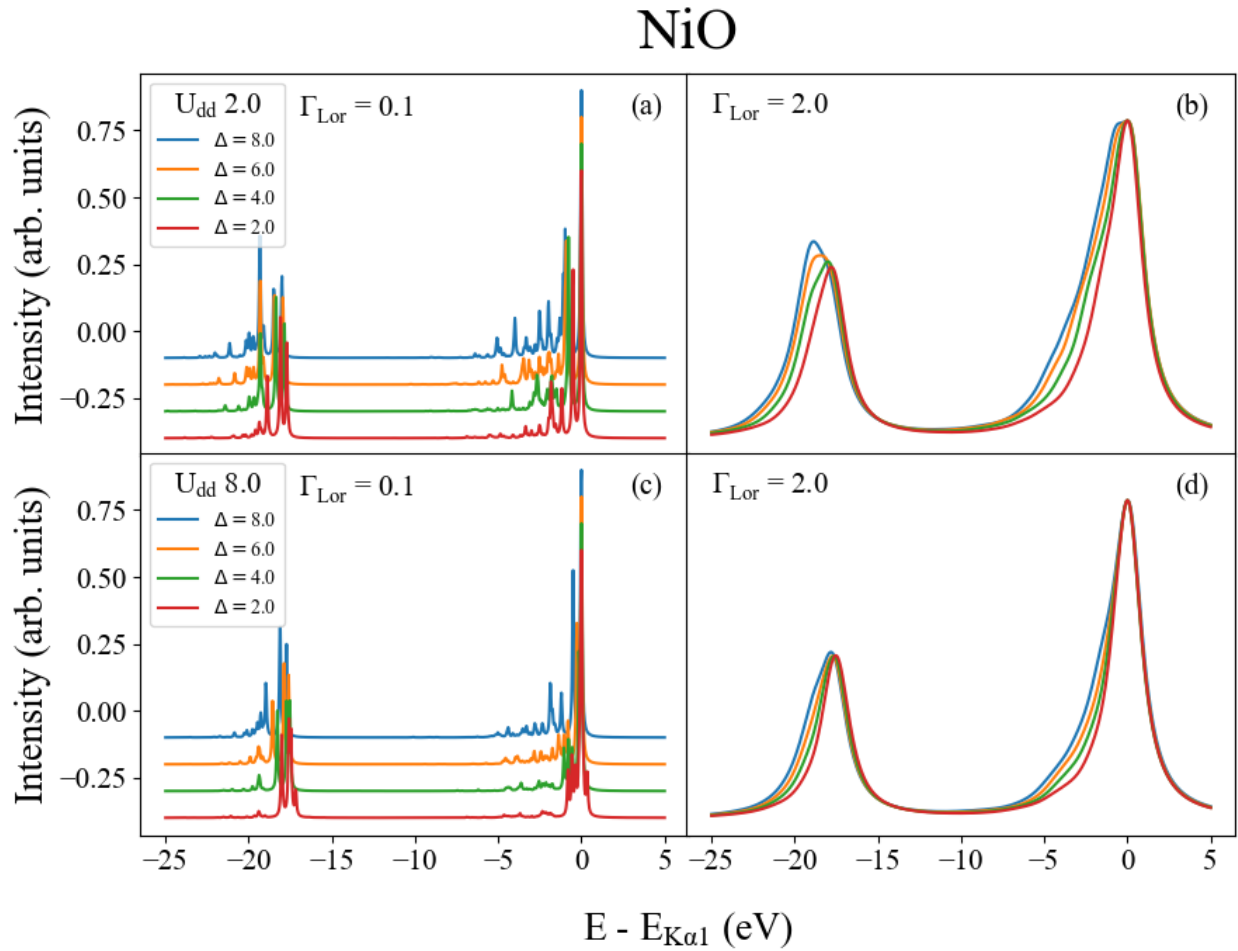
Figure 10: Parameter space exploration of NiO for a range of Δ values (2.0, 4.0, 6.0, and 8.0 eV) U_{dd} values of 2.0 eV (a, b) and 8.0 eV (c, d). The left panels have Lorentzian broadening of only $\Gamma_{Lor} = 0.1$ eV while the right panels have $\Gamma_{Lor} = 2.0$ eV.

In Figure 10 we investigate the effect of U_{dd} and Δ on DFT + MLFT calculations for NiO. Scaling Δ has the effect of widening the distance between the d and ligand centroids, thereby increasing the energy of the gap between occupied and unoccupied valence states. This is the origin of the increase in multiplet peak splitting with Δ as seen in Figure 10 and results in low-energy tails in the broadened spectra in the right column. Ideally these can be dealt with by fitting to the features which do appear in experimental spectra (additional shoulders or asymmetry), but this is not a trivial task as even within this reduced parameter space different unique choices of U_{dd} and Δ can still produce similar spectra, making the correct parameter choice ambiguous.
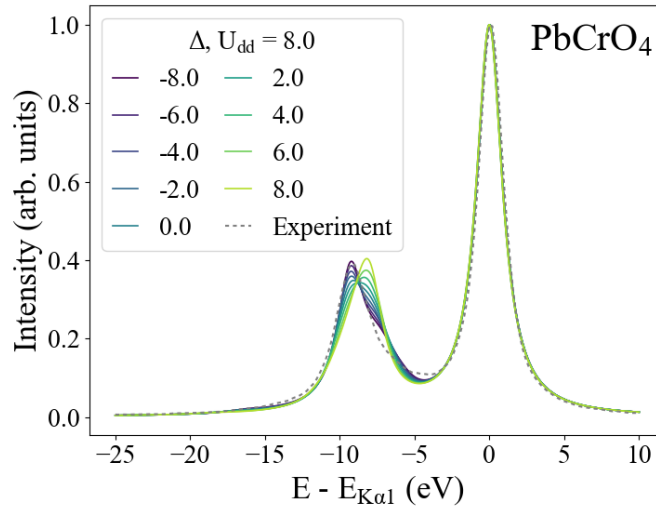

Figure 11: PbCrO$_4$ spectra for $U_{dd} = 8$ and $-8 \leq \Delta \leq 8$. The experimental spectrum is shown as a grey dashed line for reference.

The extremes of the DFT + MLFT model are well demonstrated by $PbCrO_4$. The Cr in $PbCrO_4$ has nominally zero d electrons, with $20!/(10!)^2 \sim 180,000$ possible electron configurations, making this the most computationally expensive calculation of all the materials in this manuscript. By scanning over Δ, as shown in Figure 11, it becomes clear that the double peak feature underneath $K\alpha_2$ is modulated by the charge-transfer energy while the $K\alpha_1$ is entirely insensitive to changes in Δ. In non-DFT augmented MLFT, negative values of Δ are uncommon but do occur for highly oxidized systems with more covalent character [70]. The lack of sensitivity of $K\alpha_1$ to Δ is surprising, given that number of unpaired $3d$ electrons is also modulated by Δ. As Δ increases (and U_{dd} is held constant), the splitting between the d and ligand levels increases and the lowest energy valence states have less d character, leading to a decrease in both the total number of $3d$ electrons and the number of unpaired $3d$ electrons in the intermediate ground state. This would appear to contradict the earlier conclusion about the relationship between the number of unpaired $3d$ electrons and the $K\alpha_1$ FWHM. However, the best fit between experiment and theory for $PbCrO_4$ (which depended entirely on variability in $K\alpha_2$) also resulted in a Δ value which gave the appropriate number of unpaired $3d$ electrons.

4.5   Conclusion

We have demonstrated that a DFT + MLFT approach based on the Quanty + FPLO framework can achieve a nearly first principles calculation of $K\alpha$ CTC-XES for $3d$ TM systems, with only two remaining undetermined coefficients. In so doing, we have provided a detailed guide for such *ab-initio* calculations and demonstrated a simplifying approximation for calculating XES in terms of the one-step versus two-step approach. Future work should involve

further validation of the one-step approach given the potential it has for strongly decreasing the computational effort required. Additionally, we have successfully reproduced qualitative and quantitative trends in Kα spectra with regards to oxidation and spin state. The use of only deep core levels in CTC-XES simplifies the dependence of the spectrum on these features, making it clear that the charge transfer state and crystal field effects are well reproduced by the DFT + MLFT approach. In particular, we were able to demonstrate the direct correlation between the FWHM and oxidation state, which has been well documented experimentally, has not before been validated by purely theoretical calculations. The overall satisfactory agreement between the experimental spectra with the nearly *ab-initio* calculations indicate that this technique could be immediately applicable to predictive tasks.

There are several directions for future work: 1) It would be valuable to extend this DFT + MLFT approach to other highly correlated materials such as lanthanide and actinide systems with open f shells, or other emission lines such as Kβ XES which would have even more sensitivity to the local environment due to the stronger coupling between $3p$ and $3d$ orbitals. This ties into 2) the need for a more complete picture of the domain in which DFT + MLFT approaches are suitable. Charge neutral spectroscopies such as XAS and RIXS have already been shown to be well reproduced by the same types of cluster model we use here [17, 26, 28], but in XPS the cluster model does not seem to sufficiently capture the non-local screening response to the core-hole [58, 71]. Our work implies that the non-local screening is less of a concern for Kα XES due to its deep core-to-core nature, but this may not hold for higher energy emission lines. Future work should be focused on investigating the divide between charge-neutral and non-charge-neutral spectroscopies and characterizing the regime in which DFT + MLFT techniques are accurate. 3) Improvements to the theoretical techniques are also possible. For example,

future work could consider constrained DFT calculations that include a 1s core-hole. This would provide a more accurate picture of the valence level couplings in the intermediate state which could be used to address the non-local screening issue. The current DFT framework could also be adjusted to account for the different Coulomb couplings between the core and valence levels according to their spatial extents as done by Krüger [44]. Finally, and with the highest fundamental impact, 4) future work should focus on the elimination of the remaining free parameters. Constrained DFT may offer another avenue for calculating both Δ and U_{dd} [72] using frozen orbitals [73]. Further developments of DFT + DMFT techniques [27] would provide a better representation of the hybridization between the ligand and transition metal ions. The use of multiple experimental spectra that contain sufficiently independent information could be used to constrain or entirely remove the free parameters through simultaneous fitting. In general, there should be a strong focus on the development of accurate methods for calculating charge-transfer parameters U_{dd} and Δ given that they are the only remaining roadblocks to the goal of a fully *ab-initio* theory.

Acknowledgements

Citations

1. Fermi, E., *Sulla quantizzazione del gas perfetto monoatomico.* Rendiconti Lincei, 1926. **3**: p. 145-149.
2. Bloch, F., *Über die Quantenmechanik der Elektronen in Kristallgittern.* Zeitschrift für Physik, 1929. **52**(7): p. 555-600.
3. Pauling, L., *The Nature of the Chemical Bond and the Structure of Molecules and Crystals*. 1960.
4. Keast, V.J., *Application of EELS in Materials Science.* Materials Characterization, 2012. **73**: p. 1-7.
5. Bagus, P.S., E.S. Ilton, and C.J. Nelin, *The interpretation of XPS spectra: Insights into materials properties.* Surface Science Reports, 2013. **68**(2): p. 273-304.
6. Glatzel, P. and U. Bergmann, *High resolution 1s core hole X-ray spectroscopy in 3d transition metal complexes—electronic and structural information.* Coordination Chemistry Reviews, 2005. **249**(1): p. 65-95.
7. Frank de Groot, A.K., *Core Level Spectroscopy of Solids*. 1 ed. 2008, Boca Raton: Taylor & Francis Group.
8. Cohen, A.J., P. Mori-Sánchez, and W. Yang, *Challenges for Density Functional Theory.* Chemical Reviews, 2012. **112**(1): p. 289-320.
9. De Groot, F.M.F., et al., *2p x-ray absorption spectroscopy of 3d transition metal systems.* Journal of Electron Spectroscopy and Related Phenomena, 2021. **249**: p. 147061.
10. Blaha, P., et al., *WIEN2k: An APW+lo program for calculating the properties of solids.* The Journal of Chemical Physics, 2020. **152**(7): p. 074101.
11. Vinson, J., et al., *Bethe-Salpeter equation calculations of core excitation spectra.* Physical Review B, 2011. **83**(11): p. 115106.
12. Vorwerk, C., et al., *Bethe–Salpeter equation for absorption and scattering spectroscopy: implementation in the exciting code.* Electronic Structure, 2019. **1**(3): p. 037001.
13. Ankudinov, A.L., et al., *Real-space multiple-scattering calculation and interpretation of x-ray-absorption near-edge structure.* Physical Review B, 1998. **58**(12): p. 7565-7576.
14. Bagus, P.S., et al., *Mechanisms responsible for chemical shifts of core-level binding energies and their relationship to chemical bonding.* Journal of Electron Spectroscopy and Related Phenomena, 1999. **100**(1): p. 215-236.
15. Vila, F.D., et al., *Equation-of-Motion Coupled-Cluster Cumulant Green's Function for Excited States and X-ray Spectra.* Frontiers in Chemistry, 2021. **9**: p. 734945.
16. Haverkort, M.W., M. Zwierzycki, and O.K. Andersen, *Multiplet ligand-field theory using Wannier orbitals.* Physical Review B, 2012. **85**(16): p. 165113.
17. Krüger, P., *First-Principles Calculation of Ligand Field Parameters for L-Edge Spectra of Transition Metal Sites of Arbitrary Symmetry.* Symmetry, 2023. **15**(2): p. 472.

18.   Ikeno, H., et al., *Multiplet calculations of L2,3 x-ray absorption near-edge structures for 3d transition-metal compounds.* Journal of Physics: Condensed Matter, 2009. **21**(10): p. 104208.

19.   Abu-Samak, M., et al., *Electronic structure and energy gaps evaluation of perovskite manganite single crystals using XES and XAS spectroscopy.* Journal of Electron Spectroscopy and Related Phenomena, 2021. **250**: p. 147084.

20.   Lafuerza, S., et al., *Chemical Sensitivity of Kβ and Kα X-ray Emission from a Systematic Investigation of Iron Compounds.* Inorganic Chemistry, 2020. **59**(17): p. 12518-12535.

21.   Fazinić, S., et al., *Chemical sensitivity of the Kα X-ray emission of Ti and Cr compounds induced by 2 MeV protons.* Spectrochimica Acta Part B: Atomic Spectroscopy, 2022. **195**: p. 106506.

22.   Miedema, P.S., et al., *Iron 1s X-ray photoemission of Fe2O3.* Journal of Electron Spectroscopy and Related Phenomena, 2015. **203**: p. 8-13.

23.   Zimmermann, P., M.O.J.Y. Hunault, and F.M.F. de Groot, *1s2p RIXS Calculations for 3d Transition Metal Ions in Octahedral Symmetry.* Journal of Spectroscopy, 2018. **2018**: p. 50.

24.   Zimmermann, P., et al., *Quanty4RIXS: a program for crystal field multiplet calculations of RIXS and RIXS–MCD spectra usingQuanty.* Journal of Synchrotron Radiation, 2018. **25**(3): p. 899-905.

25.   Hasan, M.N., et al., *Re-Dichalcogenides: Resolving Conflicts of Their Structure–Property Relationship.* Advanced Physics Research, 2022. **1**(1): p. 2200010.

26.   Gorelov, E., et al., *MLFT approach with p-d hybridization for ab initio simulations of the pre-edge XANES.* Radiation Physics and Chemistry, 2020. **175**: p. 108105.

27.   Lüder, J., et al., *Theory of L-edge spectroscopy of strongly correlated systems.* Physical Review B, 2017. **96**(24): p. 245131.

28.   Agrestini, S., et al., *Long-range interactions in the effective low-energy Hamiltonian of Sr2IrO4: A core-to-core resonant inelastic x-ray scattering study.* Physical Review B, 2017. **95**(20): p. 205123.

29.   Zhang, W., et al., *Tracking excited-state charge and spin dynamics in iron coordination complexes.* Nature, 2014. **509**(7500): p. 345-348.

30.   Alonso-Mori, R., et al., *Femtosecond electronic structure response to high intensity XFEL pulses probed by iron X-ray emission spectroscopy.* Scientific Reports, 2020. **10**(1): p. 16837.

31.   Khakhulin, D., et al. *Ultrafast X-ray Photochemistry at European XFEL: Capabilities of the Femtosecond X-ray Experiments (FXE) Instrument.* Applied Sciences, 2020. **10**, DOI: 10.3390/app10030995.

32.   Simonelli, L., et al., *High resolution x-ray absorption and emission spectroscopy of LixCoO2 single crystals as a function delithiation.* Journal of Physics: Condensed Matter, 2017. **29**(10): p. 105702.

33.   Simonelli, L., et al., *Role of Manganese in Lithium- and Manganese-Rich Layered Oxides Cathodes.* The Journal of Physical Chemistry Letters, 2019. **10**(12): p. 3359-3368.

34.   Tetef, S., N. Govind, and G.T. Seidler, *Unsupervised machine learning for unbiased chemical classification in X-ray absorption spectroscopy and X-ray emission spectroscopy.* Physical Chemistry Chemical Physics, 2021. **23**(41): p. 23586-23601.

35. Timoshenko, J., et al., *Supervised Machine-Learning-Based Determination of Three-Dimensional Structure of Metallic Nanoparticles.* The Journal of Physical Chemistry Letters, 2017. **8**(20): p. 5091-5098.

36. Chen, Y., et al., *Database of ab initio L-edge X-ray absorption near edge structure.* Scientific Data, 2021. **8**(1): p. 153.

37. Holden, W.M., G.T. Seidler, and S. Cheah, *Sulfur Speciation in Biochars by Very High Resolution Benchtop Kα X-ray Emission Spectroscopy.* The Journal of Physical Chemistry A, 2018. **122**(23): p. 5153-5161.

38. Haverkort, M. *Quanty - a quantum many body scripting language.* 2022; Available from: https://quanty.org/.

39. Koepernik, K. and H. Eschrig, *Full-potential nonorthogonal local-orbital minimum-basis band-structure scheme, version 14.00-49 [https://www.FPLO.de].* Physical Review B, 1999. **59**(3): p. 1743-1757.

40. Marguí, E., I. Queralt, and E. de Almeida, *X-ray fluorescence spectrometry for environmental analysis: Basic principles, instrumentation, applications and recent trends.* Chemosphere, 2022. **303**: p. 135006.

41. Kramers, H.A. and W. Heisenberg, *Über die Streuung von Strahlung durch Atome.* Zeitschrift für Physik, 1925. **31**(1): p. 681-708.

42. Mortensen, D.R., et al., *Benchmark results and theoretical treatments for valence-to-core x-ray emission spectroscopy in transition metal compounds.* Physical Review B, 2017. **96**(12): p. 125136.

43. Roychoudhury, S., et al., *Changes in polarization dictate necessary approximations for modeling electronic deexcitation intensity: Application to x-ray emission.* Physical Review B, 2022. **106**(7): p. 075133.

44. Krüger, P., *Ab initio calculation of ligand field multiplet parameters for transition metal L-edge spectra.* Radiation Physics and Chemistry, 2020. **175**: p. 108051.

45. Heinze, S., *Material Specific Simulations of Many-Body Electron Dynamics*, in *Combined Faculty of Natural Sciences and Mathematics*. 2021, Heidelberg University: Heidelberg.

46. Ballhausen, C., *Introduction to ligand field theory*. McGraw-Hill Series in Advanced Chemistry. 1962.

47. Koepernik, K., et al., *Symmetry Conserving Maximally Projected Wannier Functions.* Physical Review B, 2021. **107**(23): p. 235135.

48. Eschrig, H. and K. Koepernik, *Tight-binding models for the iron-based superconductors.* Physical Review B, 2009. **80**(10): p. 104503.

49. Glatzel, P., *Thesis: X-Ray Fluorescence Emission Following K Capture and 1s Photoionization of Mn and Fe in Various Chemical Environments*, in *Department of Physics*. 2001, University of Hamburg. p. 137.

50. Kawai, J., et al., *Charge-transfer effect on the linewidth of Fe Kα x-ray fluorescence spectra.* Physical Review B, 1994. **50**(16): p. 11347-11354.

51. Jahrman, E.P., et al., *An improved laboratory-based x-ray absorption fine structure and x-ray emission spectrometer for analytical applications in materials chemistry research.* Review of Scientific Instruments, 2019. **90**(2): p. 024106.

52. Jahrman, E.P., G.T. Seidler, and J.R. Sieber, *Determination of Hexavalent Chromium Fractions in Plastics Using Laboratory-Based, High-Resolution X-ray Emission Spectroscopy.* Analytical Chemistry, 2018. **90**(11): p. 6587-6593.

53.   Kawai, J., M. Ohta, and T. Konishi, *Chemical Effects in High-Resolution Nickel Kα X-Ray Fluorescence Spectra.* Analytical Sciences, 2005. **21**(7): p. 865-868.

54.   Jabua, M., et al., *Kα X-ray emission in manganese compounds.* Spectrochimica Acta Part B: Atomic Spectroscopy, 2016. **121**: p. 11-17.

55.   Jabua, M., *Ultimate Resolution X-ray Spectroscopy of Chemical-Effects in Manganese Compounds*, in *Mathematics and Natural Science*. 2016, Unversity of Cologne.

56.   Campbell, J.L. and T. Papp, *WIDTHS OF THE ATOMIC K–N7 LEVELS.* Atomic Data and Nuclear Data Tables, 2001. **77**(1): p. 1-56.

57.   Glatzel, P., et al., *Influence of the core hole on K beta emission following photoionization or orbital electron capture: A comparison using MnO and (Fe2O3)-Fe-55.* Physical Review B, 2001. **64**(4): p. 045109.

58.   Ghiasi, M., et al., *Charge-transfer effect in hard x-ray $1s$ and $2p$ photoemission spectra: LDA + DMFT and cluster-model analysis.* Physical Review B, 2019. **100**(7): p. 075146.

59.   Moskvin, A.S., *DFT, L(S)DA, LDA+U, LDA+DMFT, …, whether we do approach to a proper description of optical response for strongly correlated systems?* Optics and Spectroscopy, 2016. **121**(4): p. 467-477.

60.   Su, S.-Q., et al., *Quenching and Restoration of Orbital Angular Momentum through a Dynamic Bond in a Cobalt(II) Complex.* Journal of the American Chemical Society, 2020. **142**(26): p. 11434-11441.

61.   Maganas, D., S. DeBeer, and F. Neese, *A Restricted Open Configuration Interaction with Singles Method To Calculate Valence-to-Core Resonant X-ray Emission Spectra: A Case Study.* Inorganic Chemistry, 2017. **56**(19): p. 11819-11836.

62.   Adachi, H., *Theoretical analysis of X-ray and electron spectra by DV-Xα method*, in *Advances in Quantum Chemistry*. 2000, Academic Press. p. 1-29.

63.   Nyholm, R., et al., *Auger and Coster-Kronig broadening effects in the 2p and 3p photoelectron spectra from the metals 22Ti-30Zn.* Journal of Physics F: Metal Physics, 1981. **11**(8): p. 1727.

64.   Bagus, P.S., et al., *Analysis of the Fe 2p XPS for hematite α Fe2O3: Consequences of covalent bonding and orbital splittings on multiplet splittings.* The Journal of Chemical Physics, 2020. **152**(1): p. 014704.

65.   Pessa, V.M., *Multiplet splitting of manganese core p-levels in MnF2.* Journal of Physics C: Solid State Physics, 1975. **8**(11): p. 1769.

66.   Bagus, P.S., et al., *Combined multiplet theory and experiment for the Fe 2p and 3p XPS of FeO and Fe2O3.* The Journal of Chemical Physics, 2021. **154**(9): p. 094709.

67.   Malherbe, J., et al., *Evaluation of Hexavalent Chromium Extraction Method EPA Method 3060A for Soils Using XANES Spectroscopy.* Environmental Science & Technology, 2011. **45**(24): p. 10492-10500.

68.   Unceta, N., et al., *Chromium speciation in solid matrices and regulation: a review.* Analytical and Bioanalytical Chemistry, 2010. **397**(3): p. 1097-1111.

69.   Armin Meisel, G.L., Rudiger Zsargan, *X-ray Spectra and Chemical Binding (Springer Series in Chemical Physics).* 1st ed. Spring Series in Chemical Physics. Vol. 37. 1989: Springer.

70.   Choudhury, D., et al., *Anomalous charge and negative-charge-transfer insulating state in cuprate chain compound KCuO2.* Physical Review B, 2015. **92**(20): p. 201108.

71.   Bagus, P.S., C.R. Brundle, and E.S. Ilton, *A rigorous non-empirical theoretical analysis of the 2p XPS of NiO: Is it necessary to invoke nonlocal screening?* Journal of Electroanalytical Chemistry, 2020. **875**: p. 114135.

72.   Kaduk, B., T. Kowalczyk, and T. Van Voorhis, *Constrained Density Functional Theory.* Chemical Reviews, 2012. **112**(1): p. 321-370.

73.   Ratcliff, L.E., et al., *Toward Fast and Accurate Evaluation of Charge On-Site Energies and Transfer Integrals in Supramolecular Architectures Using Linear Constrained Density Functional Theory (CDFT)-Based Methods.* Journal of Chemical Theory and Computation, 2015. **11**(5): p. 2077-2086.

4.6   Supplemental Information

Note that the full, unedited supplemental information can be found with the published work. Sections of the supplemental information that are already addressed in earlier chapters have been removed for clarity and to avoid redundancy.

4.6.1   Quanty and FPLO Input Files

The input required for running the $CrCl_2$ Kα XES example can be found at

https://github.com/Seidler-Lab/CrCl2KaXES_Example. This contains three input files that when

combined create the entire pipeline for the calculation of $CrCl_2$. All of these are modified from

tutorials taken from the Quanty website [1]. The pipeline demonstrated here is characteristic of

how the calculation was performed for all other materials unless otherwise mentioned.

4.6.2   Green's Function Formalism

The formalism motivated here can be readily used to test the relevance of multiple

intermediate states. Eq. 1 in the manuscript is often expressed in terms of an effective one

particle Green's functions [2], and we will do so here as well. The two-step approach relies on the use of a third order Green's function,

$$\mathcal{G}(\omega_1, \omega_2) = \langle i| \hat{s}^\dagger \frac{1}{\omega_1 - i\frac{\Gamma_s}{2} - H_1} \hat{p}^\dagger \hat{s} \frac{1}{\omega_1 - \omega_2 - i\frac{\Gamma_p}{2} - H_2} \hat{s}^\dagger \hat{p} \frac{1}{\omega_1 - i\frac{\Gamma_s}{2} - H_1} \hat{s} |i\rangle. \quad \text{SII (1)}$$

where for Kα XES the $\hat{s}$ annihilation operator acting on the $1s$ state (initial → intermediate) and T_{sp} is the dipole transition operator between the $2p$ and $1s$ states (intermediate → final). We do not include the $\vec{\epsilon} \cdot \vec{r}$ term with the understanding that all polarization directions must be considered for an isotropic spectrum. In SII Eq. 1, H_1 and H_2 correspond to the Hamiltonians of the systems with a $1s$ core-hole and $2p$ core-hole respectively, with i being the set of ground state wavefunctions which come from solving the eigenstates of the initial state Hamiltonian. The response function has arguments ω_1 and ω_2 which are defined the same way that they are in Eq. 1, corresponding to incident energy and emission energy, respectively. Making the same approximation that was made when going from Eq. 1 to Eq. 2, SII Eq 1. can be rewritten using a one-step approach with a first order Green's function,

$$\mathcal{G}(\omega_2) = \langle i'| \hat{p}^\dagger \hat{s} \frac{1}{\omega_2 - i\frac{\Gamma}{2} - H} \hat{s}^\dagger \hat{p} |i'\rangle, \quad (2)$$

where now the i' states describe the intermediate ground state in the presence of the $1s$ core-hole.

4.6.3 Voigt Fits
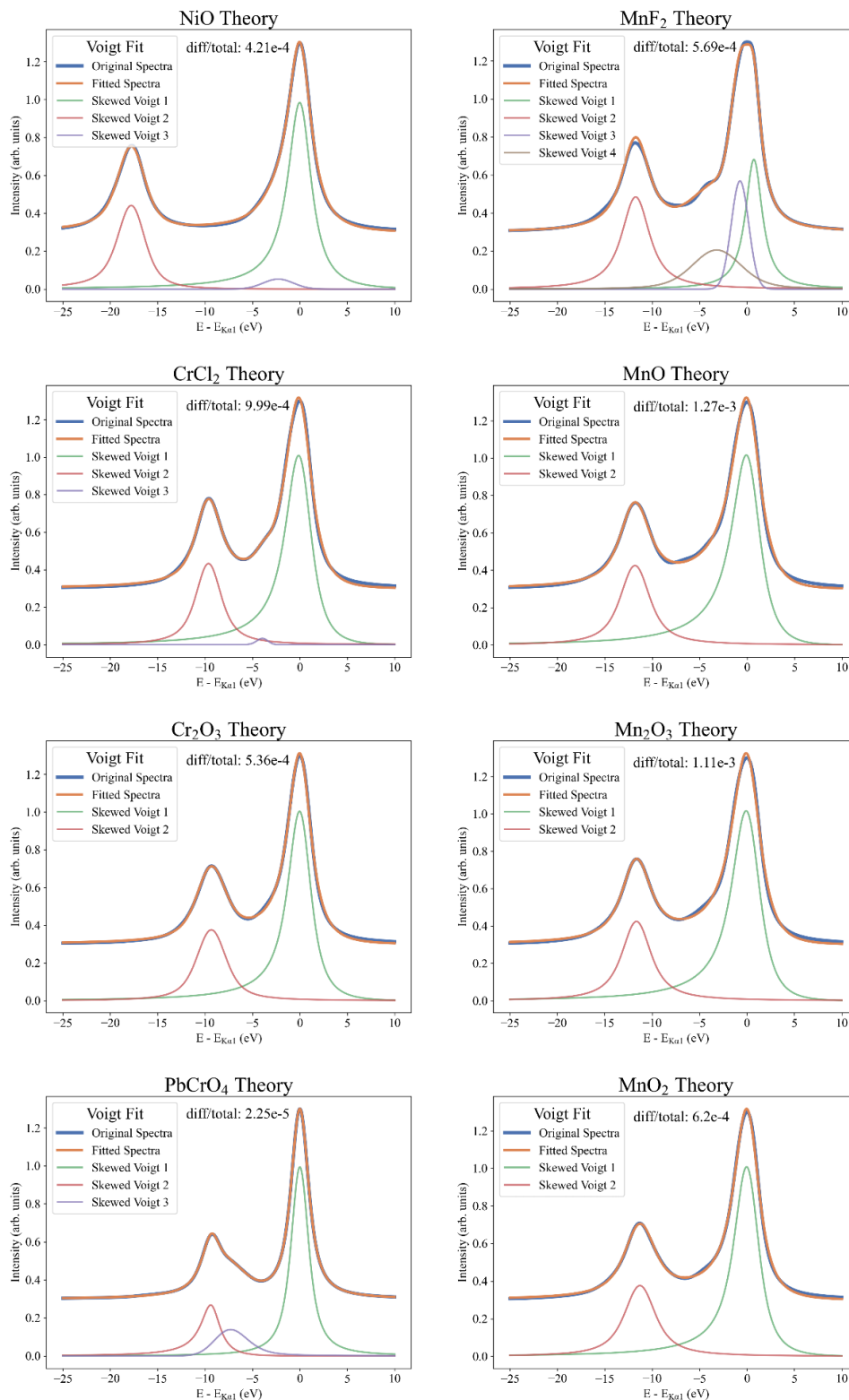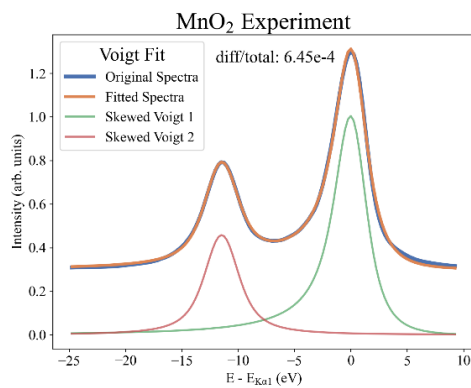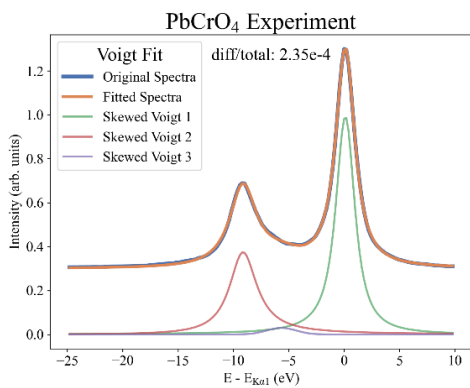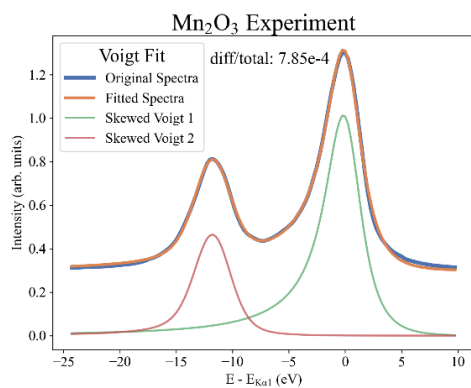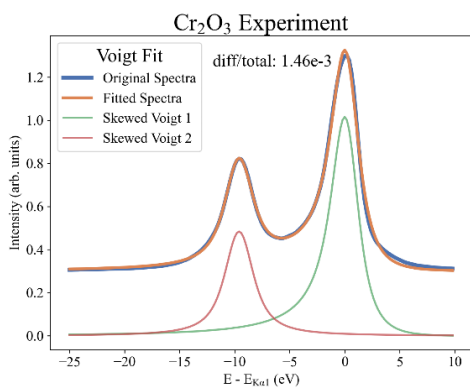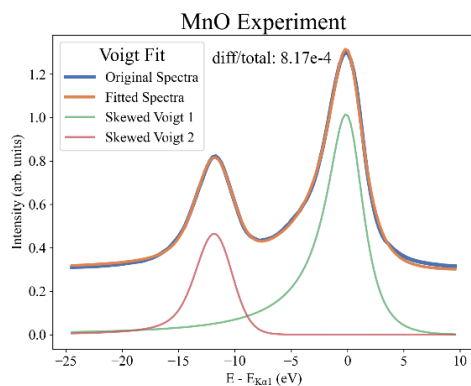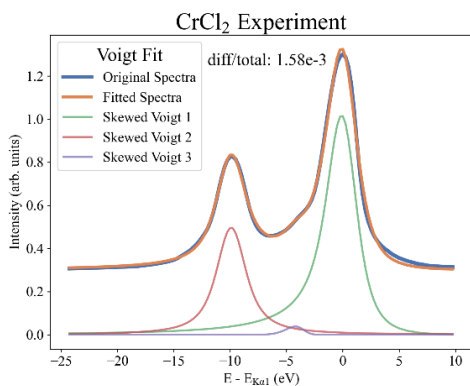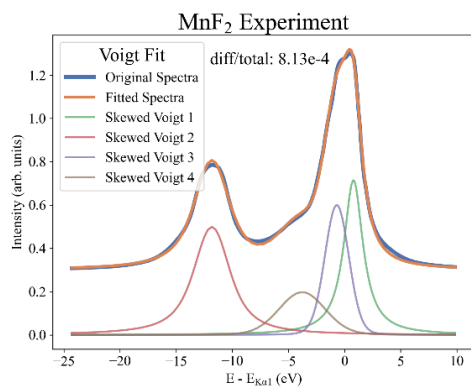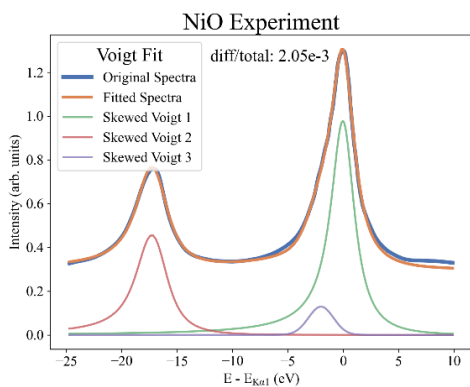
Figure SI-IV 1: Skewed Voigt fits comprised of 2, 3, or 4 individual peaks for both calculated and experimental spectra. The number of individual functions used for a particular material were the same for calculated and experiment. The diff/total parameter relates to the integrated absolute difference divided by the total area under the curve and gives some measure of how "good" the Voigt fit is.

4.6.4   FWHM Calculation and Broadening Schemes
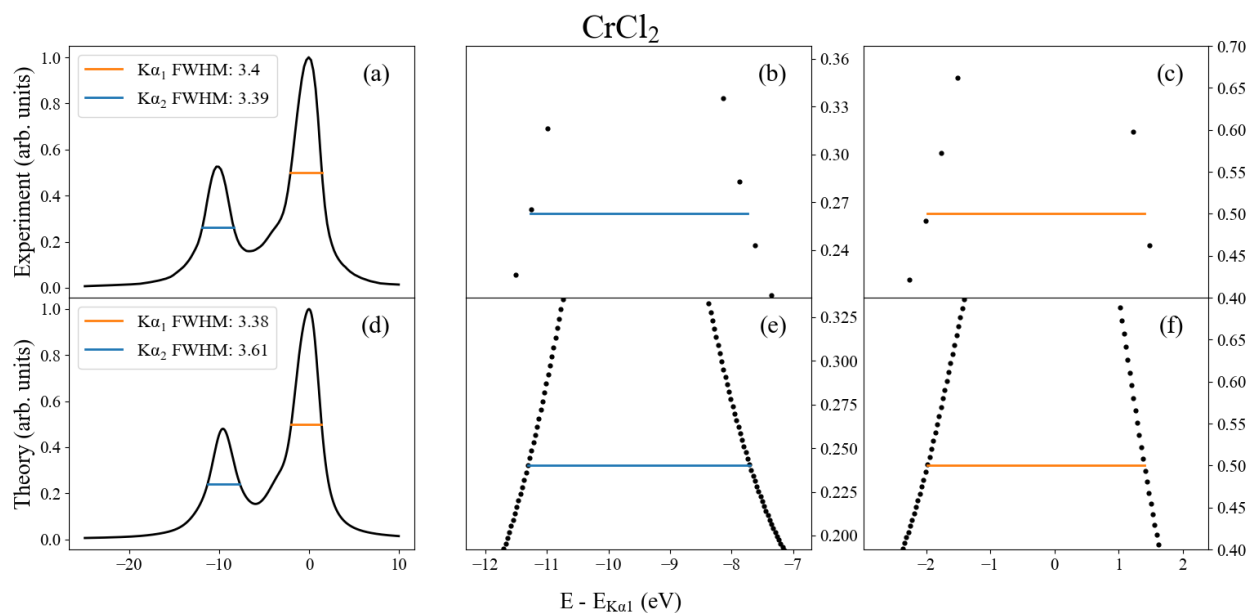
Figure SI-V 1: Depiction of how the FWHM values were calculated for the $K\alpha_1$ and $K\alpha_2$ peaks. The experimental spectrum is shown on the top (a, b, c) and the theoretical spectrum is shown on the bottom (d, e, f). The horizontal lines demonstrate how the full width at half maximum is reported for the $K\alpha_1$ (orange) and $K\alpha2$ (blue) peaks. The center column (b and e) shows a

zoomed in view of the $K\alpha_2$ peak and the right column (c and f) shows a zoomed in view of the $K\alpha_1$ peak. The FWHM is calculated via linear interpolation between data points, which provides a more accurate measure of the true FWHM for spectra with fewer data points.
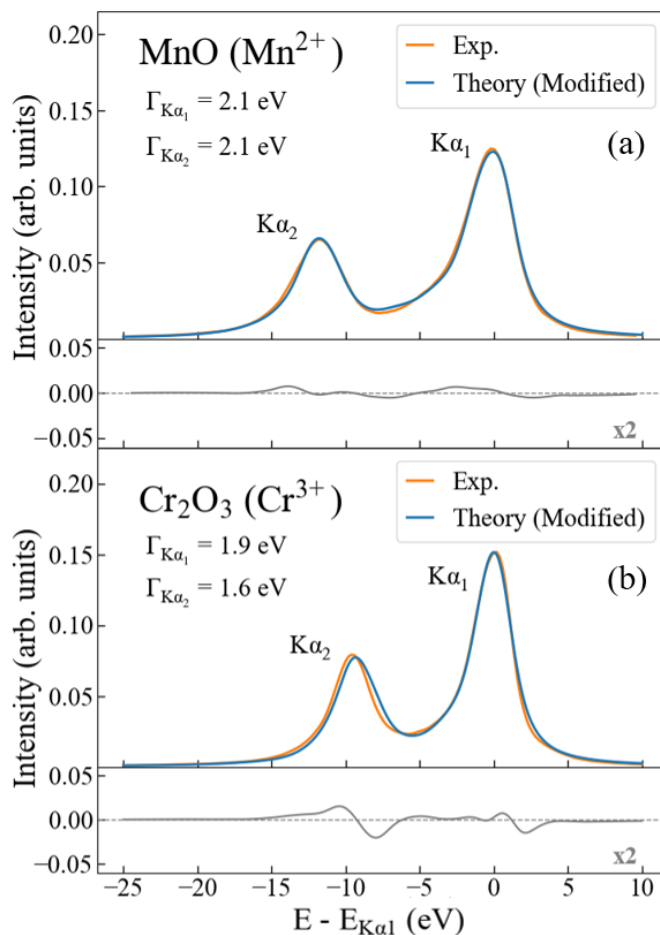
Figure SI-V 3: Modified theoretical and experimental $K\alpha$ for (a) MnO and (b) Cr_2O_3. The theoretical spectra have been modified by changing the lifetime broadening values for better overall agreement between theory and experiment. To original lifetime broadening values can be found in Table 1.
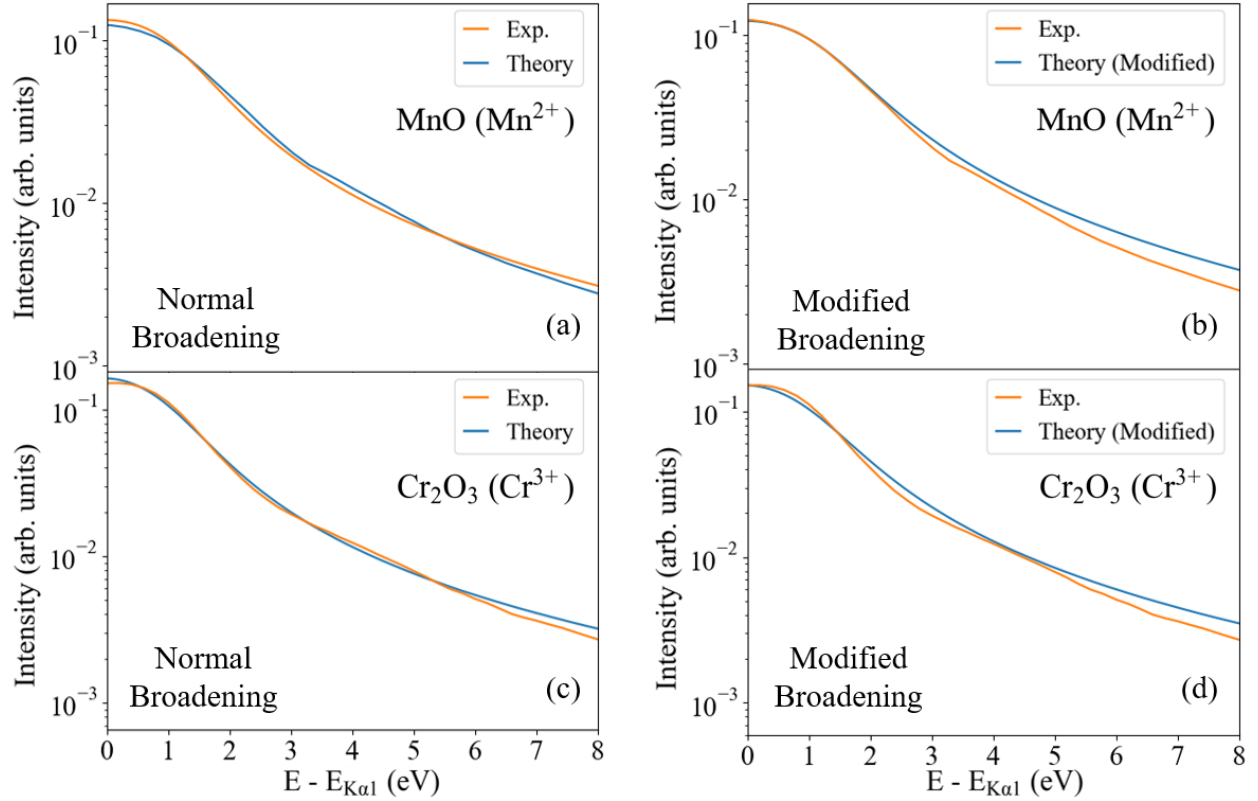
Figure SI-V 4: A zoomed in comparison of the theory and experiment for MnO (a, b) and Cr_2O_3 (c, d) with normal (a, c) and modified (b, d) broadening. The plots with modified broadening show that the larger lifetime broadenings on the $K\alpha_1$ high binding energy side diverge from the experimental line shape for both compounds.

4.6.5   Details of the DFT and Wannier Calculations

The LDA calculation was performed using the FPLO software. FPLO uses an atomic like basis, with fixed radial wave functions as described in references [3, 4]. These radial wavefunctions were used for calculating the Slater-Condon parameters following the standard formulas for the F and G terms [5]. The DFT parameters used for most materials were a 20x20x20 Monkhorst-Pack k-mesh and a density convergence parameter of 10^{-10} Å^{-3}. All

materials were carefully checked for convergence before moving on to the Wannier downfolding. More information about the default values used within FPLO can be found in the user manual [6]. The Perdue Wang 92 functional was used to perform the LDA calculation [7], and no spin was included in the DFT step. Given that the goal of this work is to reproduce local effects on deep core orbitals, within the DFT step all systems were treated as paramagnetic with no magnetic coupling between sites. All spin state effects are a result of terms included in the MLFT step. The experimental unit cells for all materials were taken from the crystallographic open database [8, 9].
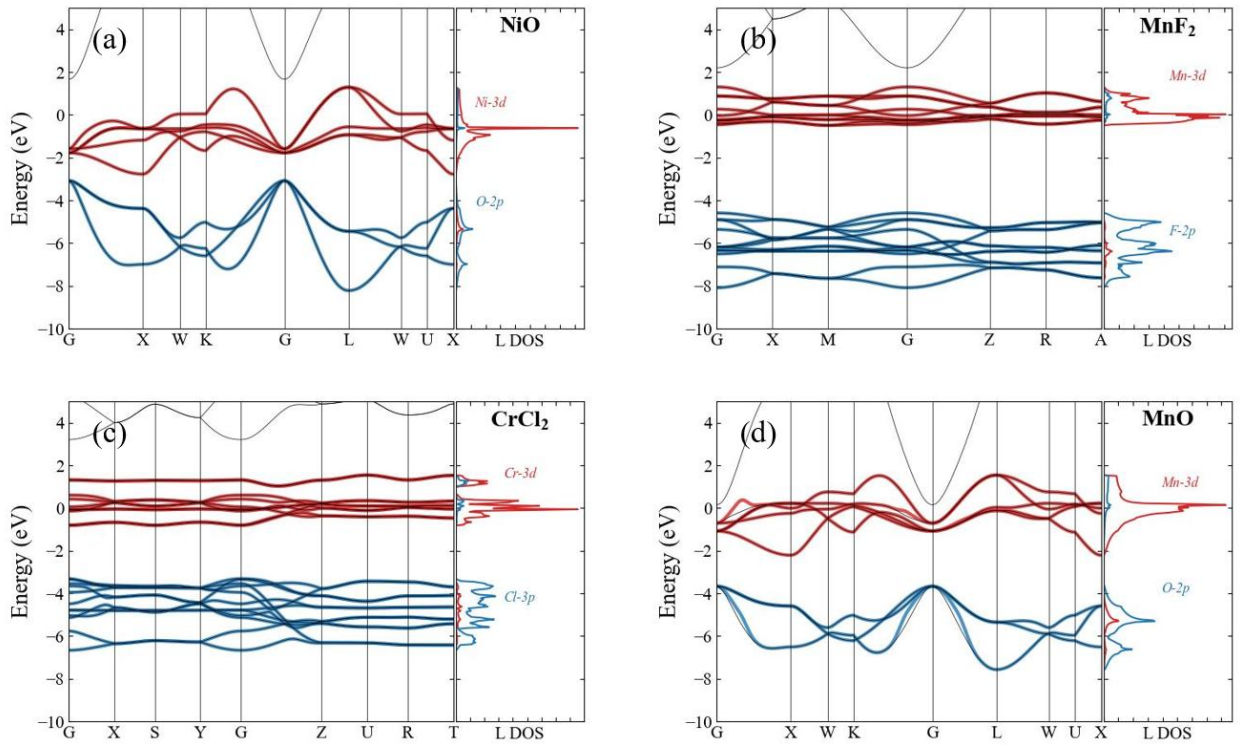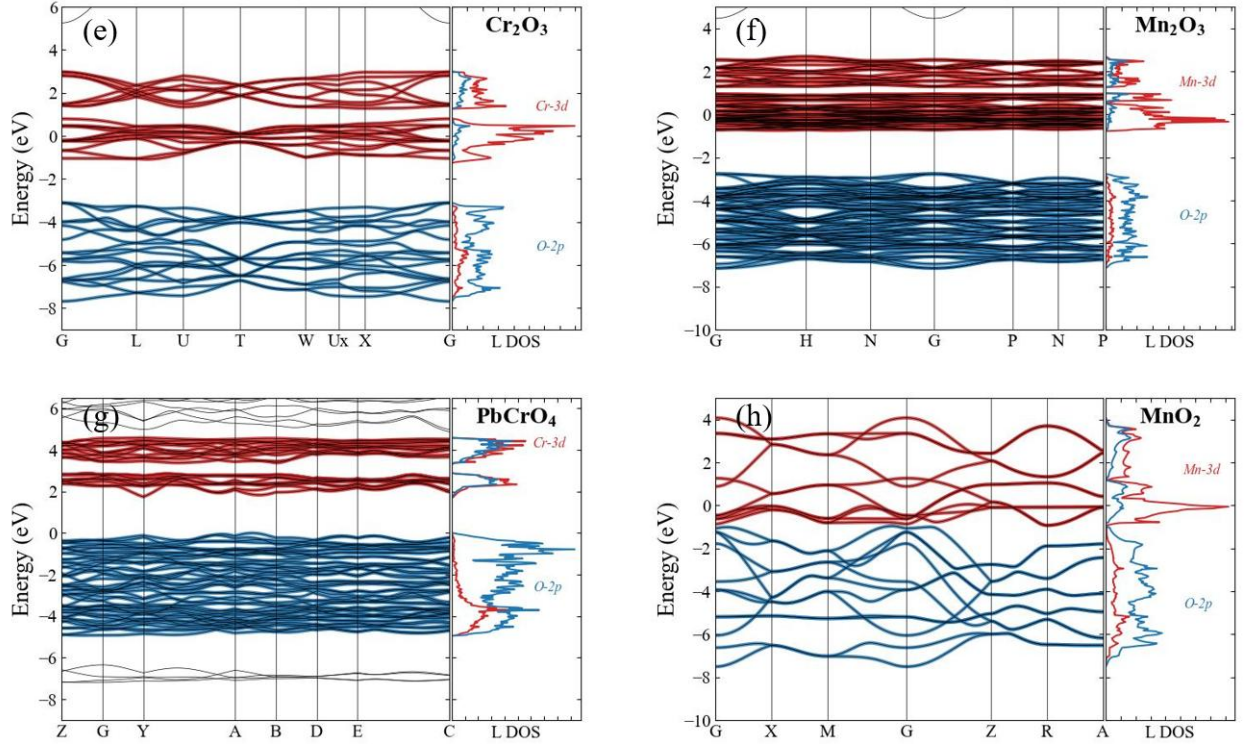
Figure SI-VI 1: Comparison of the band-structure and Wannier bands for NiO (a), MnF$_2$ (b), CrCl$_2$ (c), MnO (d), Cr$_2$O$_3$ (e), Mn$_2$O$_3$ (f), PbCrO$_4$ (g), and MnO$_2$ (h). Within each subplot, (left) the band structure is shown in thin gray lines and the Wannier bands are shown in thick colored lines for the TM 3d (red) and Ligand 2p (blue). In most cases only a single line is visible, indicating that the two band-structures are fully overlapping. (Right) the projected density of states for the Wannier orbitals.

The result of the Wannier down projection is shown in Figure SI-VI 1, where the Wannier bands are plotted over the band structure of each material. The Tight Binding Hamiltonian (H^{TB}) that is created from Wannier downfolded orbitals is block tri-diagonalized. The inclusion of only a single ligand block was sufficient to converge all compounds, resulting in a 20x20 single particle H^{TB} made up of 10 transition metal 3d states and 10 ligand d states. We emphasize here

that while the ligands do indeed have $2p$ valence shells, the 10 ligand d states come from a linear combination of all the $2p$ orbitals in the cluster ($6 \times 6 = 36$ for octahedral and $6 \times 4 = 24$ for tetrahedral). The ligand orbitals in H^{TB} are formed from symmetry considerations so that they all have the same rotational properties as the transitional metal d states. We note that for systems that are less oxidized, such as NiO and MnO, the V_{eg} and V_{t2g} coupling terms are smaller than the various lower symmetry coupling terms for more highly oxidized systems such as $PbCrO_4$ and MnO_2. This is expected, as the coupling terms tend to increase for more covalent systems, indicating that the higher oxidation states result in a greater sharing of electrons between the transition metal and ligands. There does not exist a review of hoping/hybridization and crystal field terms for a range of compounds, but for well-studied high symmetry systems such as NiO and MnO, our 10Dq, V_{eg}, and V_{t2g} parameters agree well with literature [10, 11].

1. Haverkort, M. *Quanty - a quantum many body scripting language*. 2022; Available from: https://quanty.org/.
2. Kas, J.J., et al., *Real-space Green's function approach to resonant inelastic x-ray scattering.* Physical Review B, 2011. **83**(23).
3. Koepernik, K. and H. Eschrig, *Full-potential nonorthogonal local-orbital minimum-basis band-structure scheme, version 14.00-49 [*https://www.FPLO.de*].* Physical Review B, 1999. **59**(3): p. 1743-1757.
4. M. Richter, K.K., and H. Eschrig, *Condensed Matter Physics in the Prime of the 21st Century*. 43rd Karpacz Winter School of Theoretical Physics. 2008, Poland.
5. Frank de Groot, A.K., *Core Level Spectroscopy of Solids*. 1 ed. 2008, Boca Raton: Taylor & Francis Group.
6. Richter, M. *FPLO*. 2023; Available from: https://www.fplo.de/.
7. Perdew, J.P. and Y. Wang, *Accurate and simple analytic representation of the electron-gas correlation energy.* Physical Review B, 1992. **45**(23): p. 13244-13249.
8. Vaitkus, A., A. Merkys, and S. Gražulis, *Validation of the Crystallography Open Database using the Crystallographic Information Framework.* Journal of Applied Crystallography, 2021. **54**(2): p. 661-672.
9. Merkys, A., et al., *Graph isomorphism-based algorithm for cross-checking chemical and crystallographic descriptions.* Journal of Cheminformatics, 2023. **15**(1): p. 25.
10. Haverkort, M.W., M. Zwierzycki, and O.K. Andersen, *Multiplet ligand-field theory using Wannier orbitals.* Physical Review B, 2012. **85**(16): p. 165113.
11. Ogasawara, K., et al., *Relativistic cluster calculation of ligand-field multiplet effects on cation $L_{2,3}$ x-ray-absorption edges of $SrTiO_3$ NiO, and CaF_2.* Physical Review B, 2001. **64**(11): p. 115413.

Chapter 5 Prediction and Measurement of Resonant and Nonresonant Shake Effects in the Core-level X-ray Emission Spectra of $3d^0$ Transition Metal Compounds

Shake effects, resulting from sudden core potential changes during photoexcitation, are well known in x-ray photoelectron spectroscopy (XPS) and often produce satellite peaks due to many-body excitations. It has been thought, however, that they are negligible in core-to-core x-ray emission spectroscopy (CTC-XES), where the difference in core-hole potentials upon radiative decay are rather small. We demonstrate that shake effects are significant in Kα XES from 3d transition metal systems with nominally zero valence electrons. We show that valence level shake satellites are amplified via interference due to a resonance between the $2p_{3/2}$-hole (Kα₁) plus valence level shake state, and the $2p_{1/2}$-hole (Kα₂) state. Additionally, while the Kα₂ shake satellite is indeed predicted to be weak, we observe it experimentally, providing further independent verification of our model. The prediction includes a detailed analysis of 2p to 1s Kα XES using density functional theory (DFT)-augmented multiplet ligand field theory (MLFT).

TOC GRAPHIC
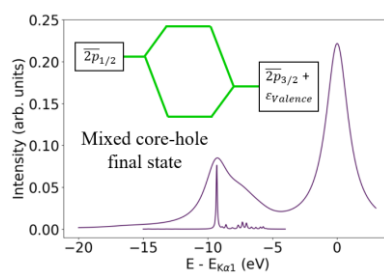
KEYWORDS: Multiplet Ligand Field Theory, Shake Excitations, X-ray Emission Spectroscopy,

Resonance

In x-ray spectroscopy, the creation of a core-hole can cause various secondary excitations due to the sudden change in potential. These co-called shake effects have strong contributions to experimental spectra, producing satellites that can carry important information about configuration interactions [1-3], ligand environment [4-5] and magnetic state [6-8]. For example, shake effects must be included in calculations for $3d$ transition metal or $4f$ lanthanide and $5f$ actinide systems to accurately describe back-donation and charge-transfer processes [9-10]. It is precisely the strongly correlated behavior of these systems which makes them useful both in the context of application [11-15] and as testbeds for advancing theoretical models which seek to capture important many-body physics [10, 16-18].

Shake effects are observed most strongly in x-ray photoelectron spectroscopy (XPS) [9, 19] where collective excitations accrue because the change in core-hole potential leaves the outer shell electrons in a state that is no longer an eigenstate of the system, i.e., the spectroscopy is comparing an initial state with no core-hole to a final state with a core-hole. Similar effects can occur in x-ray absorption spectroscopy (XAS) [20], resonant inelastic x-ray scattering (RIXS) [21], and valence-to-core (VTC)-XES [22], but shake effects in core-to-core (CTC)-XES are relatively unexplored. As discussed by in Martin, et al., [23] the shake-up satellites in CTC-XES are expected to be weak, as the process involves a neutral transition of one core-hole to another (*e.g.* $1s$ core-hole to $2p$ core-hole in Kα XES), causing only a small change in the potential felt by the valence electrons. This is in contrast to XPS, where the transition leaves the absorbing atom ionized. The difference is especially prominent in $3d$ transition metal complexes, where shake satellites in XPS are substantial, while CTC-XES spectra are dominated by either spin-orbit splitting [24] or spin dependent atomic multiplet effects [25].

However, here we report a shake-up effect which appears when the splitting of the XES final state core-hole levels is resonant with a valence level excitation, resulting in a strong magnification of the shake-up satellite. Similar resonant shake processes have been observed in XPS and help explain the dual broadening of the $2p_{1/2}$-hole final state [26]. The origin of this resonant shake effect is similar in scope to the well-known $L_2L_3M_{45}$ Coster-Kronig effect [27] where the lifetime of the $2p_{1/2}$-hole state is made significantly shorter than the corresponding $2p_{3/2}$-hole lifetime due to additional decay channels for the $2p_{3/2}$-hole final state [28].

In this Letter we present a combined theoretical and experimental study of shake excitations in CTC-XES and demonstrate the conditions under which they become important for $3d$ transition metal systems. We calculate the Kα XES using a first principles DFT + MLFT formalism [29-30] and validate against experimental results to show both the resonant shake-up effect and also the much weaker shake-up effect without resonant enhancement.

Our MLFT cluster model is built from crystal field and charge transfer perturbations to the atomic Hamiltonian [10]. The full Hamiltonian H in Eq. 1 is a combination of single particle (H_{SP} in Eq. 2) and many-body (H_C in Eq. 3) terms

$$H = H_{SP} + H_C \quad (1)$$

$$H_{SP} = \epsilon_{1/2} n_{1/2} + \epsilon_{3/2} n_{3/2} + \sum_b \epsilon_b n_b + \sum_a \epsilon_a n_a \quad (2)$$

$$H_C = \sum_{v_1 v_2 c_1 c_2} U_{v_1 c_1 v_2 c_2} \hat{a}^\dagger_{v_1} \hat{a}^\dagger_{c_1} \hat{a}_{v_2} \hat{a}_{c_2} \quad (3)$$

where ϵ is the single particle energy and n is the occupation of the level, 1/2 and 3/2 refer to the $2p_{1/2}$ and $2p_{3/2}$ levels, and b and a correspond to the bonding and antibonding levels. H_C gives a particle conserving Coulomb interaction which couples the core (c) and metal centered

valence levels (v), causing the spin-orbit split core orbitals to become mixed [31-32]. H_{SP} defines a single particle basis that is useful for discussing the valence level excitations, while H_C provides the many-body intra-atomic coupling. In the final state, the $2p$ core levels have 5 electrons total, where the character of the final state is determined by which spin-orbit split level the hole resides in. For $3d$ transition metal systems the valence levels are broken into 10 d orbitals and 10 ligand orbitals, which have total occupations of n_d and 10 respectively. The choice of using a 10 orbital ligand shell comes from the orthogonalized representation of the ligand orbitals in regular MLFT cluster approaches [29].
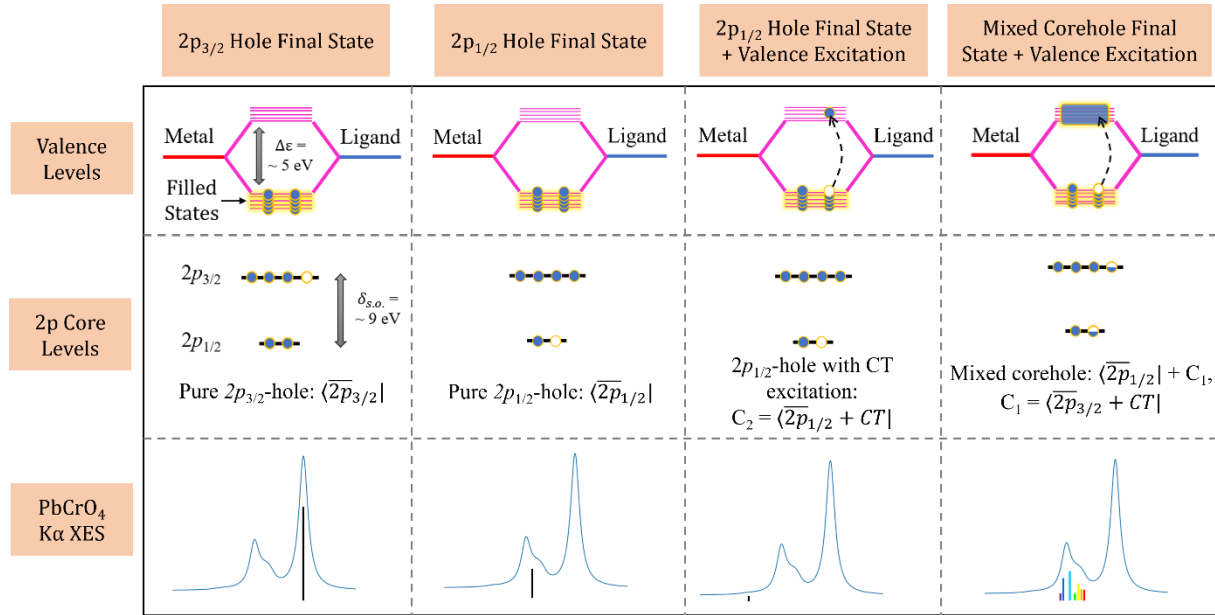
Figure 1: Valence (top) and core (middle) configurations of the relevant final states in Kα XES of a d^0 system, along with the corresponding emission lines (bottom) shown as sticks. Each column shows a different final state electron configuration. For reference, the spectrum of the d^0 material PbCrO₄ is also shown (bottom).

The focus on d^0 systems is twofold. First, they are the most highly oxidized (ex: Cr(VI) from PbCrO$_4$) state for a metal, which results in a more covalent bonding scheme, giving a large splitting between the bonding and antibonding levels [10, 23]. Second, the energy distribution of the states after a charge transfer shake excitation (effectively a d^1 system) is much narrower than for a system that starts with more d electrons. As we will see later, having a relatively tight, localized shake satellite at the right energy is what will allow the corresponding final states to meaningfully impact the spectrum.

Figure 1 shows diagrams (top, middle) representing the various final states involved in this resonance for a d^0 system such as PbCrO$_4$, as well as the corresponding emission lines (bottom, sticks). The pure $2p_{3/2}$-hole and $2p_{1/2}$-hole states are given by the first and second columns of Figure 1 where no valence level (shake-up) excitation takes place. The third column shows a $2p_{1/2}$-hole plus charge transfer (CT) shake-up final state (denoted C$_2$) with no final state resonances or interference. Finally, the fourth column shows a mixed $2p$ final state where a valence level shake excitation allows a $2p_{3/2}$-hole + CT (C$_1$) final state to become degenerate in energy with the purely $2p_{1/2}$-hole final state.

In general, the overlap between the valence component of the wavefunction for the $1s$ core-hole and $2p_{3/2}$-hole + CT states will be very weak [23]. However, when the $2p$ core-hole state has a sufficient mix of $2p_{1/2}$-hole and $2p_{3/2}$-hole character then the weak $2p_{3/2}$-hole + CT final state becomes magnified by cross term which includes the large overlap between the purely $2p_{1/2}$ core-hole state and $1s$ core-hole state, $i.e.$,

$$\left|\langle\alpha|\hat{T}|\overline{1s}\rangle\right|^2 = a_1^2\left|\langle\overline{2p}_{1/2}|\hat{T}|\overline{1s}\rangle\right|^2 + 2a_1a_2\langle\overline{2p}_{1/2}|\hat{T}|\overline{1s}\rangle\langle C_1|\hat{T}|\overline{1s}\rangle + a_2^2\left|\langle C_1|\hat{T}|\overline{1s}\rangle\right|^2 \quad (4)$$

where $|\alpha\rangle$ is a mixed $2p_{1/2}$-hole and C_1 final state and a_1 and a_2 are coefficients determining the relative $2p_{1/2}$-hole and C_1 character of the final state. In the third column of Figure 1 we see that this resonance phenomenon is missing from the purely $2p_{1/2}$-hole + CT (C_2) final state because it also has weak overlap between the valence wavefunction and the $1s$ core-hole valence wavefunction, but no multiplicative factor to amplify it.

To illustrate these effects and serve as a quantitative test of theory, we measured the Kα XES from the transition metals species in Cr metal, Cr_2O_3, $PbCrO_4$, $SrTiO_3$, $KMnO_4$, V_2O_3, VO_2, and V_2O_5. All samples were 97% or higher purity from commercial vendors. The $KMnO_4$ samples were prepared by sealing powder in thin-walled quartz capillary holders to limit air exposure [33]. All other samples were prepared with a 1:1 mass mixture of paraffin wax and powder.

XES of the V and Ti materials was measured with an easyXES150 spectrometer (easyXAFS LLC). For Mn and Cr materials, XES spectra was collected on a laboratory based spectrometer described in Jahrman, *et al.* [34] with a 100W x-ray source and Pd anode. For all compounds measurement times were chosen to get ~10,000 or more total counts at the peak of the Kα_1 line. For the Cr compounds special care was taken to achieve excellent counting statistics with ~100,000 total counts at the peak of the Kα_1 line. All samples were carefully monitored for beam damage over the course of the measurement time. We used 0.25 eV energy steps in the region of the spectral features and wider, 1-eV steps outside that range to define background levels. A narrow entrance slit (0.25 mm for the half-meter Rowland circle, easyXES150, and 1 mm for the 1-meter Rowland circle) was used to reduce source size broadening.

Our calculations use the DFT + MLFT cluster model approach detailed in Haverkort *et al.* [29], which has been demonstrated to perform well for $3d$ transition metal systems [35]. The computational details are described elsewhere [30] and only summarized here. The DFT step is used to create a tight binding (TB) Hamiltonian H^{TB} which describes the local environment in the context of the crystal field split levels and charge transfer between a central metal ion and neighboring ligands [36]. This is accomplished by a symmetry restricted Wannier projection onto the bands near the Fermi level which encodes information about the hybridization between the orbitals involved in bonding [18, 29]. This approach successfully replaces many of the empirical parameters in traditional MLFT [18, 29-30], but DFT does not correctly reproduce the many-body Coulomb interactions which are necessary for an accurate approximation of charge transfer dynamics. To overcome this problem, two remaining free parameters U_{dd} and Δ are used to account for the average screened d-d Coulomb interaction and the energy difference between the $d^n L$ and $d^{(n+1)}\overline{L}$ states respectively. As in previous work, we approximate the Coulomb interaction between core and valence levels, U_{pd} and U_{sd}, by assuming proportionality to U_{dd}, which makes it feasible to fully explore the remaining parameter space [30].

Reduced Slater-Condon parameters were also extracted from the DFT radial wavefunctions for $1s$, $2p$, and $3d$ orbitals, while spin-orbit couplings are taken from atomic calculations using Cowan's code [37-39]. All calculated spectra were Lorentzian broadened with core-hole lifetime values taken from Ref [40], and a 1.0 eV to 1.2 eV Gaussian broadening was applied to match experimental resolution. The experimental spectra were not all measured at the same instrument, the high binding energy side of the Kα₁ was used to tune the Gaussian broadening to ensure a consistent broadening scheme. Additional details for this broadening procedure as well as parameters for the DFT step including functionals, k-point grids, and

convergence parameters can be found in the supporting information of Ref [30]. All calculated

spectra were checked for convergence with respect to the energy window of the Wannier

projection, density, total energy, k-mesh and were fit according to a 0.5 eV grid search of U_{dd}

and Δ. Further details are briefly summarized in supporting information section SI-IV.
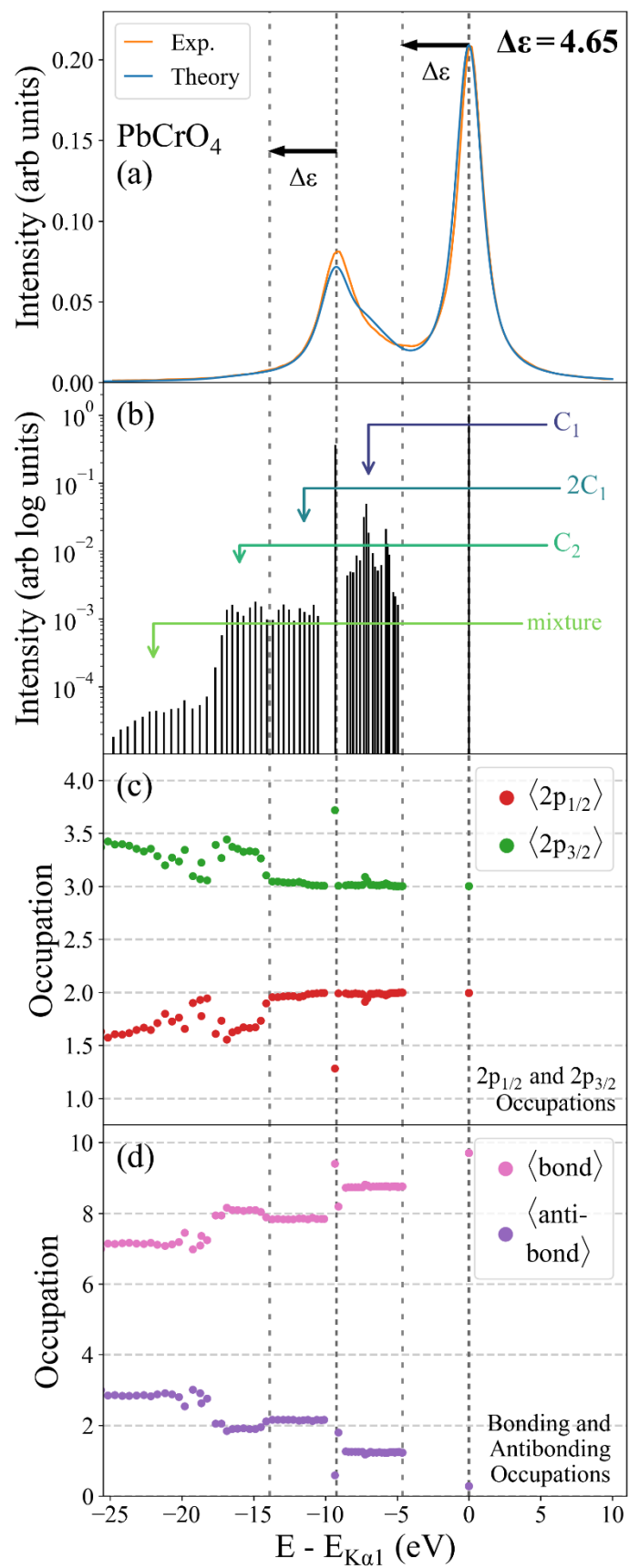
Figure 2: Spectra and final state character analysis for PbCrO4. (a) Broadened theory and experimental Kα XES spectra. Parameters for calculated spectra are reported in Table 1. (b) Calculated intensities and energies of individual transitions. The regimes labeled by C_1 and C_2 are consistent with their earlier definitions. $2C_1$ refers to CT satellites of double valence electron excitations, and "mixture" simply means that the low energy regime below approximately -18 eV has contributions from multiple many-body final states. (c) and (d) Expectation of the number operators for the core and valence orbitals respectively for each of the final states.

Moving to results, in Figure 2 we show the calculated spectra and orbital occupations for a choice of $\Delta = -8.0$ eV which creates a valence level gap $\Delta\varepsilon \sim 4.65$ eV. Beginning with Figure 2(a) which compares calculated and experimental spectra for PbCrO4 we see that the theory agrees quite well overall, with the high energy tail of the Cr $K\alpha_2$ peak being qualitatively reproduced. The calculated spectrum is nearly perfect in the vicinity of the $K\alpha_1$ and low binding energy side of the $K\alpha_2$ as expected, but the C_1 shake satellite is slightly too strong compared to experiment. This makes sense, as we are using a discrete number of valence states in our cluster model, limiting the number of possible final states with many-body shake excitations. A more accurate agreement could likely be achieved with DFT + DMFT or a similar technique which takes into account the continuous band nature of the valence states, thereby producing a broader satellite peak [41].

From Figure 2(b) and 2(c) we see that final states that have at least a little $2p_{1/2}$-hole character (around ~7.5 eV below $K\alpha_1$) have meaningful intensity contribution, which agrees with the resonance condition from Eq. 4. It is important to highlight that many of the mixed final states are weighted more heavily towards $2p_{3/2}$-hole character, which is a product of the ratio between the number of $2p_{3/2}$ states and $2p_{1/2}$ states, *i.e.* 4:2. This ratio can be modified by many-

body interactions, but the $2p_{3/2}$ contribution to the spectrum is generally larger. In Figure 2(d) we note that the first final states roughly 5 eV below the main Kα_1 peak have a roughly one electron shift in occupation between the bonding and antibonding orbitals, which is consistent with the single-particle final states in column 4 of Figure 1. The occupation of the final states as a function of Δ is shown in Figure S4 and we note that the trend in the valence level splitting and core orbital occupation is consistent with the single particle picture from Figure 1 where the states that have highly mixed $2p$-hole character are those for which the $2p_{3/2}$-hole + CT and $2p_{1/2}$-hole are nearly degenerate.
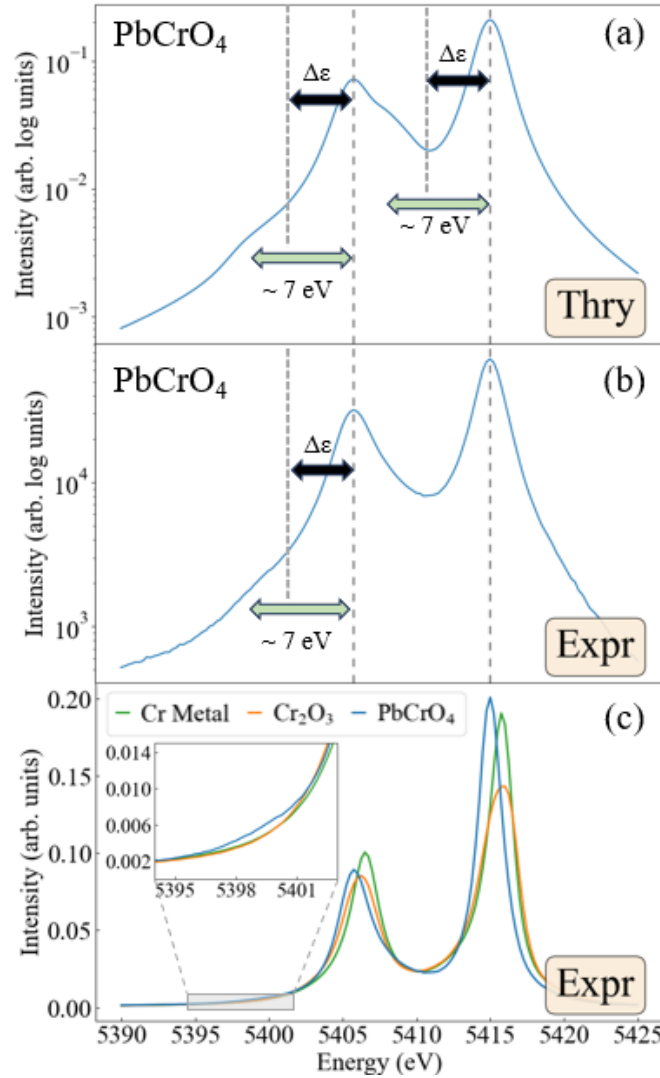
Figure 3: (a) Calculated spectra for PbCrO4 plotted with log intensity. The Kα2 satellite peak is roughly 7 eV below the main Kα2 line. (b) Experimental spectra for PbCrO4. (c) Experimental spectra for bulk Cr metal ($3d^4 4s^2$), Cr2O3 ($3d^3$), and PbCrO4 ($3d^0$).

The MLFT results as shown in Figure 2 predict a very weak nonresonant Kα2 satellite peak corresponding to the C_2 states in the region between 5396 eV and 5401 eV. We investigate this in Figure 3 and present what we believe is its first observation, giving additional independent evidence for our description of shake effects in CTC-XES. From the calculated PbCrO4 spectra in Figure 3(a) (note the logarithmic scale) we predict that the Kα2 satellite should have ~1% the intensity of the main Kα1 peak and will be ~7 eV below the main Kα2 peak (the same energy difference as for the Kα1 satellite). In Figure 3(b) we show a highly averaged experimental spectrum for the Kα XES of the PbCrO4 sample, and indeed we observe a weak but noticeable Kα2 satellite peak. In Figure 3(c) we return to a linear scale and show the PbCrO4 result together with spectra for Cr metal and Cr2O3, for which the equivalent shake satellites are suppressed as discussed earlier. There is a broad satellite feature below the Kα2 peak of the PbCrO4 spectra which is not present in the other two Cr materials.

Looking for other examples of these phenomenon in d^0 compounds, the calculated and experimental spectra for the d^0 KMnO4, V2O5, and SrTiO3 are presented in Figure 4, where we see good agreement. The MLFT parameters for the calculated spectra are presented in Table 1 and the DFT derived TB Hamiltonians are presented in supporting information section SI-II.

	$F2_{dd}$	$F4_{dd}$	$G1_{pd}$	$G3_{pd}$	$F2_{pd}$	ζ_{2p}	ζ_{3d}	Δ	U_{dd}	U_{pd}	U_{sd}	$\Gamma_{K\alpha_1}$	$\Gamma_{K\alpha_2}$	Γ_G	$\Delta\epsilon$
SrTiO3	7.679	4.741	2.633	1.490	3.874	3.780	0.020	5.000	5.500	4.640	4.800	1.55	1.95	1.2	5.95
V2O5	8.258	5.093	3.038	1.721	4.368	4.650	0.030	0.000	4.000	4.640	4.800	1.59	2.0	1.2	3.08
PbCrO4	8.203	5.031	3.116	1.766	4.451	5.670	0.050	-8.000	2.000	2.320	2.400	1.65	2.09	1.0	4.65
KMnO4	9.528	5.876	3.864	2.192	5.370	6.846	0.053	-9.000	5.000	5.800	6.000	1.72	2.32	1.0	5.10

Table 1: The Slater-Condon, spin-orbit splitting, charge transfer, broadening parameters, and minimum bonding-antibonding splitting Δε for all calculated materials. All values are reported in eV.
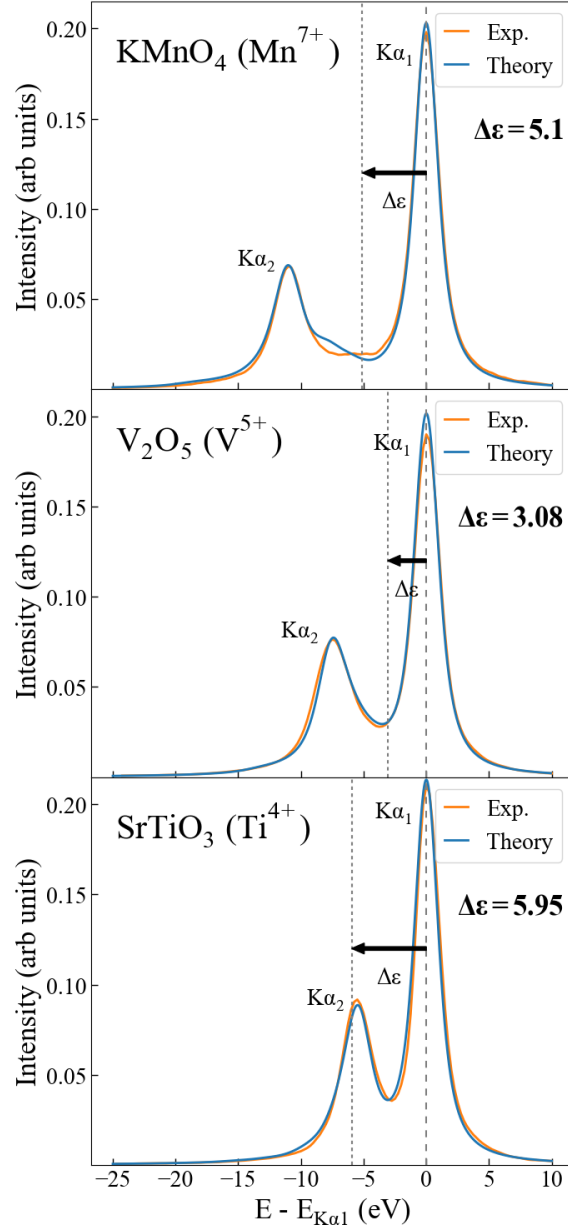
Figure 4: Comparison between experiment (orange) and theory (blue) for $KMnO_4$, V_2O_5, and $SrTiO_3$. All parameters for the calculated spectra are reported in Table 1.

The spectra with the strongest resonance features are clearly $PbCrO_4$ and $KMnO_4$ which are also the two most highly oxidized of the d^0 systems presented, and the two cases with the most negative Δ values. While negative charge transfer energies are rare, they have been previously identified [42] as a sign of strong covalence, which is supported by the large coupling between the $3d$ and ligand blocks. In the case of $PbCrO_4$ there is a strong satellite on the high binding energy side of the $K\alpha_2$ peak at roughly -7.5 eV below the $K\alpha_1$ peak, leading to very pronounced asymmetry. For $KMnO_4$ the resonance peak is also roughly at -7.0 eV, but the larger spin-orbit splitting leads to the two main peaks staying relatively symmetric and instead there is some filling of spectral intensity in the region between $K\alpha_1$ and $K\alpha_2$.

For V_2O_5 we found that achieving best fit with experiment required scaling the coupling parameters between the $3d$ and Ligand blocks of the TB Hamiltonian, as we demonstrate in Figure S3. This puts the resonance peak just slightly higher in energy (at roughly -6.5 eV) compared to the main $K\alpha_2$. Compared to previous semi-empirical calculations such as those by Bocquet *et al.* [9], our average unreduced coupling parameters agree well with the values they find. However, they do not account for crystal field effects, which are of order 0.8 eV, or configuration dependence in the coupling, which is on the order of 1.4 eV, implying that the local environment around the V is not well approximated by the O_h point group that they assume. Further details are given in the supporting information section SI-I.

Finally, $SrTiO_3$ was the only material that did not require a negative or small Δ when fitting to experiment. While the line shape of the $K\alpha_2$ is in slight disagreement with experiment,

with an overestimated asymmetry, the width of the peak is in good agreement with experiment. This supports conclusions from earlier studies by Bagus et al [26] which demonstrate that a similar coupling to shake phenomenon produce mixed $2p_{1/2}$-hole + C_1 states in the XPS of $SrTiO_3$, explaining the anomalously large broadening within the $K\alpha_2$ peak. The resonance peak is at roughly -6 eV, nearly exactly on top of the $K\alpha_2$ peak. This comes from a combination of the fact that $SrTiO_3$ has the strongest $3d$-Ligand coupling of the materials studied in this work, consistent with a positive Δ. Our values for $3d$-Ligand coupling, U_{dd} and Δ similarly agree well with previous work by Bocquet *et al.* [9], where in this case the point group of the first shell around the Ti is perfectly O_h.

In summary, we have demonstrated how a coincidence of energy splitting between deep core spin-orbit split orbitals and valence level bonding-antibonding orbitals results in strong shake satellites underneath the $K\alpha_2$ peak. The resonant shake effects manifest as broad satellites near the main $K\alpha_2$ peak and appear as an asymmetry in its line shape. They are strongest for highly oxidized systems, showing that the line shape of the $K\alpha_2$ peak is often closely connected to metal ionicity or metal-ligand covalency. In particular, the position of the resonance satellite is influenced by the coupling between the metal valence and ligand orbitals. Our picture of the resonant shake effect is further supported by the prediction and first observation of a nonresonant shake satellite at the corresponding energy below the $K\alpha_2$ peak in $PbCrO_4$.

Future work is needed to achieve a better understanding the characteristics of the valence level excitation in these d^0 materials and a search for similar core-valence energy difference coincidences in other systems beyond the 3d row. From techniques such as RIXS, shake-up satellites have been used to study similar charge transfer excitations between bonding and antibonding orbitals, which allows for detailed study of the symmetry of the various orbitals

involved in bonding [43]. Similar studies applied to d^0 systems would be a next step in exploring the properties of these resonant shake features, especially when comparing d^0 systems with different local symmetries (ex: $SrTiO_3$ with O_h and $PbCrO_4$ with T_d).

Finally, other techniques like High Energy Resolution Fluorescence Detection (HERFD) have been used to measure x-ray absorption spectrums through the emission from decays into deep core levels [44]. By using a judicious choice of a cut through the RIXS plane, this technique can provide an XAS spectrum which is only dependent on the final state core-hole lifetime. This is often much longer and leads to less lifetime broadening and a sharper XAS spectrum. The specific energy range of emission spectrum that should be used to perform the HERFD measurement is not always obvious, and it is possible that a study of Kα detected HERFD which uses different parts of the Kα spectrum to perform the same measurement may produce spectra with different broadenings, in accordance with the lifetimes of the final states being probed.

ACKNOWLEDGMENTS

5.1 Citations

1. Ehrman, J. N.; Shumilov, K.; Jenkins, A. J.; Kasper, J. M.; Vitova, T.; Batista, E. R.; Yang, P.; Li, X., Unveiling Hidden Shake-up Features in the Uranyl M4-Edge Spectrum. *JACS Au* **2024**, *4*, 1134-1141.

2. Polly, R.; Schacherl, B.; Rothe, J.; Vitova, T., Relativistic Multiconfigurational Ab Initio Calculation of Uranyl 3d4f Resonant Inelastic X-Ray Scattering. *Inorganic Chemistry* **2021**, *60*, 18764-18776.

3. Bagus, P. S.; Nelin, C. J.; Brundle, C. R.; Crist, B. V.; Lahiri, N.; Rosso, K. M., Origin of the Complex Main and Satellite Features in Fe 2p Xps of Fe2o3. *Physical Chemistry Chemical Physics* **2022**, *24*, 4562-4575.

4. Stetina, T. F.; Kasper, J. M.; Li, X., Modeling L2,3-Edge X-Ray Absorption Spectroscopy with Linear Response Exact Two-Component Relativistic Time-Dependent Density Functional Theory. *The Journal of Chemical Physics* **2019**, *150*, 234103.

5. Bagus, P. S.; Ilton, E. S.; Nelin, C. J., The Interpretation of Xps Spectra: Insights into Materials Properties. *Surface Science Reports* **2013**, *68*, 273-304.

6. Calandra, M.; Rueff, J. P.; Gougoussis, C.; Céolin, D.; Gorgoi, M.; Benedetti, S.; Torelli, P.; Shukla, A.; Chandesris, D.; Brouder, C., K-Edge X-Ray Absorption Spectra in Transition-Metal Oxides Beyond the Single-Particle Approximation: Shake-up Many-Body Effects. *Physical Review B* **2012**, *86*, 165102.

7. Sassi, M.; Pearce, C. I.; Bagus, P. S.; Arenholz, E.; Rosso, K. M., First-Principles Fe L2,3-Edge and O K-Edge Xanes and Xmcd Spectra for Iron Oxides. *The Journal of Physical Chemistry A* **2017**, *121*, 7613-7618.

8. Ikeno, H., First-Principles Analysis of X-Ray Magnetic Circular Dichroism for Transition Metal Complex Oxides. *Journal of Applied Physics* **2016**, *120*, 142104.

9. Bocquet, A. E.; Mizokawa, T.; Morikawa, K.; Fujimori, A.; Barman, S. R.; Maiti, K.; Sarma, D. D.; Tokura, Y.; Onoda, M., Electronic Structure of Early 3d-Transition-Metal Oxides by Analysis of the 2p Core-Level Photoemission Spectra. *Physical Review B* **1996**, *53*, 1161-1170.

10. Groot, F. d.; Kotani, A., *Core Level Spectroscopy of Solids*, 1 ed.; Taylor & Francis Group: Boca Raton, 2008.

11. Zhang, M., et al., Pushing the Limit of 3d Transition Metal-Based Layered Oxides That Use Both Cation and Anion Redox for Energy Storage. *Nature Reviews Materials* **2022**, *7*, 522-540.

12. Abakumov, A. M.; Fedotov, S. S.; Antipov, E. V.; Tarascon, J.-M., Solid State Chemistry for Developing Better Metal-Ion Batteries. *Nature Communications* **2020**, *11*, 4976.

13. Vogiatzis, K. D.; Polynski, M. V.; Kirkland, J. K.; Townsend, J.; Hashemi, A.; Liu, C.; Pidko, E. A., Computational Approach to Molecular Catalysis by 3d Transition Metals: Challenges and Opportunities. *Chemical Reviews* **2019**, *119*, 2453-2523.

14. Ping, J.; Jia, H., The 3d Transition Metal Single Atom Catalysis for Prominent Adsorption Performance Towards Cr(Vi) a First Principle Study. *arXiv [physics.chem-ph]* **2022**.

15. Ghosh, A., et al., Exotic Magnetic and Electronic Properties of Layered Cri3 Single Crystals under High Pressure. *Physical Review B* **2022**, *105*, L081104.

16. Vladimir, A.; Yuri, I., *Electronic Structure of Strongly Correlated Materials*; Springer, 2010.

17. Acioli, P. H., Review of Quantum Monte Carlo Methods and Their Applications. *Journal of Molecular Structure: THEOCHEM* **1997**, *394*, 75-85.

18. Schött, J. Theoretical and Computational Studies of Strongly Correlated Electron Systems Dynamical Mean Field Theory, X-Ray Absorption Spectroscopy and Analytical Continuation. Uppsala University, 2018.

19. Brisk, M. A.; Baker, A. D., Shake-up Satellites in X-Ray Photoelectron Spectroscopy. *Journal of Electron Spectroscopy and Related Phenomena* **1975**, *7*, 197-213.

20. Krüger, P.; Natoli, C. R., X-Ray Absorption Spectra at the Ca L_2,3 Edge Calculated within Multichannel Multiple Scattering Theory. *Physical Review B* **2004**, *70*, 245120.

21. Van Stappen, C.; Van Kuiken, B. E.; Mörtel, M.; Ruotsalainen, K. O.; Maganas, D.; Khusniyarov, M. M.; DeBeer, S., Correlating Valence and 2p3d Rixs Spectroscopies: A Ligand-Field Study of Spin-Crossover Iron(Ii). *Inorganic Chemistry* **2024**, *63*, 7386-7400.

22. Zhang, Y.; Mukamel, S.; Khalil, M.; Govind, N., Simulating Valence-to-Core X-Ray Emission Spectroscopy of Transition Metal Complexes with Time-Dependent Density Functional Theory. *Journal of Chemical Theory and Computation* **2015**, *11*, 5804-5809.

23. Martin, R. L.; Kowalczyk, S. P.; Shirley, D. A., The Relation between Satellite Peaks in X-Ray Emission and X-Ray Photoemission Spectra. *The Journal of Chemical Physics* **1978**, *68*, 3829-3836.

24. Lafuerza, S.; Carlantuono, A.; Retegan, M.; Glatzel, P., Chemical Sensitivity of Kβ and Kα X-Ray Emission from a Systematic Investigation of Iron Compounds. *Inorganic Chemistry* **2020**, *59*, 12518-12535.

25. Glatzel, P.; Bergmann, U., High Resolution 1s Core-hole X-Ray Spectroscopy in 3d Transition Metal Complexes—Electronic and Structural Information. *Coordination Chemistry Reviews* **2005**, *249*, 65-95.

26. Bagus, P. S.; Nelin, C. J.; Brundle, C. R.; Chambers, S. A., A New Mechanism for Xps Line Broadening: The 2p-Xps of Ti(Iv). *The Journal of Physical Chemistry C* **2019**, *123*, 7705-7716.

27. Coster, D.; L. Kronig, R. D., New Type of Auger Effect and Its Influence on the X-Ray Spectrum. *Physica* **1935**, *2*, 13-24.

28. Nyholm, R.; Martensson, N.; Lebugle, A.; Axelsson, U., Auger and Coster-Kronig Broadening Effects in the 2p and 3p Photoelectron Spectra from the Metals 22ti-30zn. *Journal of Physics F: Metal Physics* **1981**, *11*, 1727.

29. Haverkort, M. W.; Zwierzycki, M.; Andersen, O. K., Multiplet Ligand-Field Theory Using Wannier Orbitals. *Physical Review B* **2012**, *85*, 165113.

30. Cardot, C. A.; Kas, J. J.; Abramson, J. E.; Rehr, J. J.; Seidler, G. T., Core-to-Core X-Ray Emission Spectra from Wannier Based Multiplet Ligand Field Theory. *Journal of Electron Spectroscopy and Related Phenomena* **2024**, *270*, 147419.

31. Nesvizhskii, A. I. Theory and Interpretation of L-Shell X-Ray Absorption Spectra. University of Washington, 2001.

32. Laskowski, R.; Blaha, P., Understanding the L_2,3 X-Ray Absorption Spectra of Early 3d Transition Elements. *Physical Review B* **2010**, *82*, 205104.

33. Dhakal, D., et al., The Evolution of Solvation Symmetry and Composition in Zn Halide Aqueous Solutions from Dilute to Extreme Concentrations. *Physical Chemistry Chemical Physics* **2023**, *25*, 22650-22661.

34. Bi, W. C.; Jahrman, E.; Seidler, G.; Wang, J. C.; Gao, G. H.; Wu, G. M.; Atif, M.; AlSalhi, M.; Cao, G. Z., Tailoring Energy and Power Density through Controlling the Concentration of Oxygen Vacancies in V2o5/Pedot Nanocable-Based Supercapacitors. *Acs Applied Materials & Interfaces* **2019**, *11*, 16647-16655.

35. Huzan, M. S.; Burrow, T. G.; Fix, M.; Breitner, F. A.; Chong, S. K.; Bencok, P.; Aramini, M.; Jesche, A.; Baker, M. L., Quantifying the Influence of 3d–4s Mixing on Linearly Coordinated Metal-Ions by L2,3-Edge Xas and Xmcd. *Chemical Science* **2024**, *15*, 2433-2442.

36. Koepernik, K.; Eschrig, H., Full-Potential Nonorthogonal Local-Orbital Minimum-Basis Band-Structure Scheme. *Physical Review B* **1999**, *59*, 1743-1757.

37. Kramida, A., Cowan Code: 50 Years of Growing Impact on Atomic Physics. *Atoms* **2019**, *7*.

38. Cowan, R. D., *The Theory of Atomic Structure and Spectra*, 1 ed., 1981.

39. Dallera, C.; Gusmerolil, R. Missing 1.1. https://www.esrf.fr/computing/scientific/MISSING/ (accessed 05/14/2024).

40. Campbell, J. L.; Papp, T., Widths of the Atomic K-N7 Levels. *Atomic Data and Nuclear Data Tables* **2001**, *77*, 1-56.

41. Kotliar, G.; Savrasov, S. Y.; Haule, K.; Oudovenko, V. S.; Parcollet, O.; Marianetti, C. A., Electronic Structure Calculations with Dynamical Mean-Field Theory. *Reviews of Modern Physics* **2006**, *78*, 865-951.

42. Choudhury, D., et al., Anomalous Charge and Negative-Charge-Transfer Insulating State in Cuprate Chain Compound Kcuo2. *Physical Review B* **2015**, *92*, 201108.

43. Döring, G.; Sternemann, C.; Kaprolat, A.; Mattila, A.; Hämäläinen, K.; Schülke, W., Shake-up Valence Excitations in Cuo by Resonant Inelastic X-Ray Scattering. *Physical Review B* **2004**, *70*, 085115.

44. Zasimov, P.; Amidani, L.; Retegan, M.; Walter, O.; Caciuffo, R.; Kvashnina, K. O., Herfd-Xanes and Rixs Study on the Electronic Structure of Trivalent Lanthanides across a Series of Isostructural Compounds. *Inorganic Chemistry* **2022**, *61*, 1817-1830.

5.2 Supplemental Information

Note that the full, unedited supplemental information can be found with the published work.

Sections of the supplemental information that are already addressed in earlier chapters have been

removed for clarity and to avoid redundancy.

I. Vanadium Results
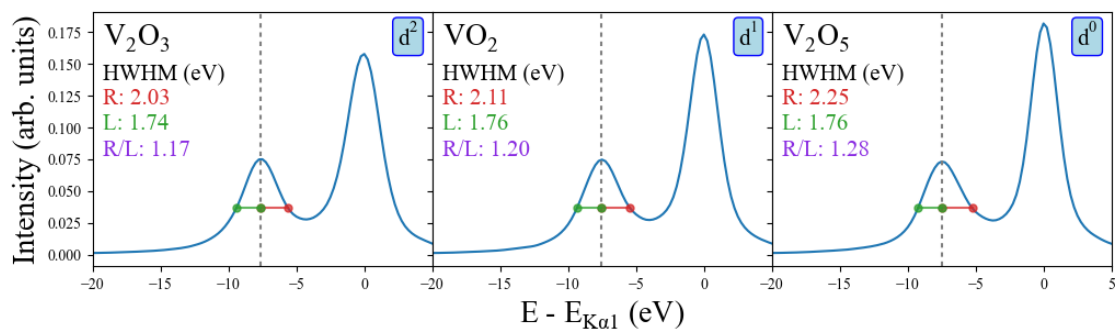
Figure S1: Experimental Kα XES for (left) V_2O_3, (middle) VO_2, and (right) V_2O_5.

In Figure S1 we present the experimental Kα spectra for a series of vanadium compound going from d^2 to d^0, where we have taken the ratio of the right and left halfwidth at half max (HWHM) of the $K\alpha_2$ peak as a rough method of quantifying the peak asymmetry. The $K\alpha_2$ R/L ratio grows monotonically as the vanadium becomes more oxidized, which corresponds to the shake satellites from the $K\alpha_1$ peak becoming stronger as the $2p_{3/2}$-hole + CT final state energy gets closer to the purely $2p_{1/2}$-hole finale state. This trend is in agreement with previous work for Ti by Kawai *et al*. [1] and demonstrates how the turn on of the resonance feature can be modulated as a function of oxidation state.
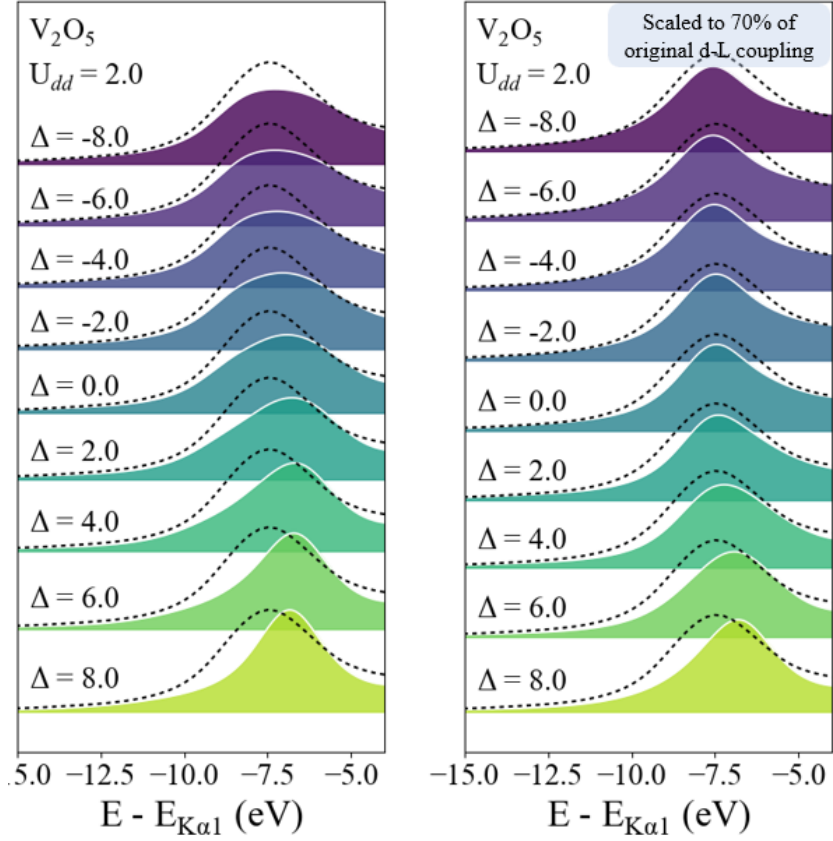
Figure S2: The Kα$_2$ peak of calculated spectra for V_2O_5 as a function of Δ, with a constant U_{dd} of 2.0 eV. (left) The calculated spectra using the *ab-initio* TB Hamiltonian which is produced from DFT. (right) The same calculated spectra but with the coupling parameters between the 3*d* and Ligand blocks scaled to 70% of their *ab-initio* values. The dashed lines in both subplots are the experimental spectra for V_2O_5.

The 3*d* - Ligand coupling is normally taken *ab-initio* from the TB Hamiltonian constructed via a down projection of Wannier states onto the metal 3*d* and Ligand 2*p* states. The *ad-hoc* modification to the TB Hamiltonian required to get good agreement with experiment implies that the LDA step overestimates the valence hybridization coupling for V_2O_5, which has been known to be notoriously difficult properly simulate due to its highly correlated nature [2]. We have tried a GGA functional and the inclusion of different orbitals (V 4*s* and V 4*p*) in the down

projections step, but we have not observed any change in coupling that would explain the roughly 70% reduction required to achieve best fit with experiment. Future work should explore the potential origin of this reduction. Specifically, we expect that a more realistic description of the valence orbitals may be required, either by moving beyond discrete orbital representations with DMFT [3], or by using a higher level post Hartree-Fock methods to better capture the many-body dynamics in the valence orbitals [4].

II.   DFT TB Hamiltonians

The tight binding Hamiltonians (H^{TB}) for $KMnO_4$, $PbCrO_4$, V_2O_5, and $SrTiO_3$ are shown in Figure S3. The number of crystal field and charge transfer parameters are symmetry constrained by the local environment around each transition metal ion. This can be seen most clearly when comparing the number of non-zero terms in the H^{TB} from $SrTiO_3$ with perfect O_h local symmetry and V_2O_5, with C_s local symmetry. The DFT calculation does not include spin, and all spin effects come from terms added to H^{TB} during the MLFT portion of the calculation, as described in Ref [5].

Figure S3: DFT derived tight binding Hamiltonians for KMnO₄, PbCrO₄, V₂O₅, and SrTiO₃. For each compound the 3*d* block is shown in red, the ligand *d* block is shown in blue, and the coupling terms between them are shown in pink.

III. Final State Occupations
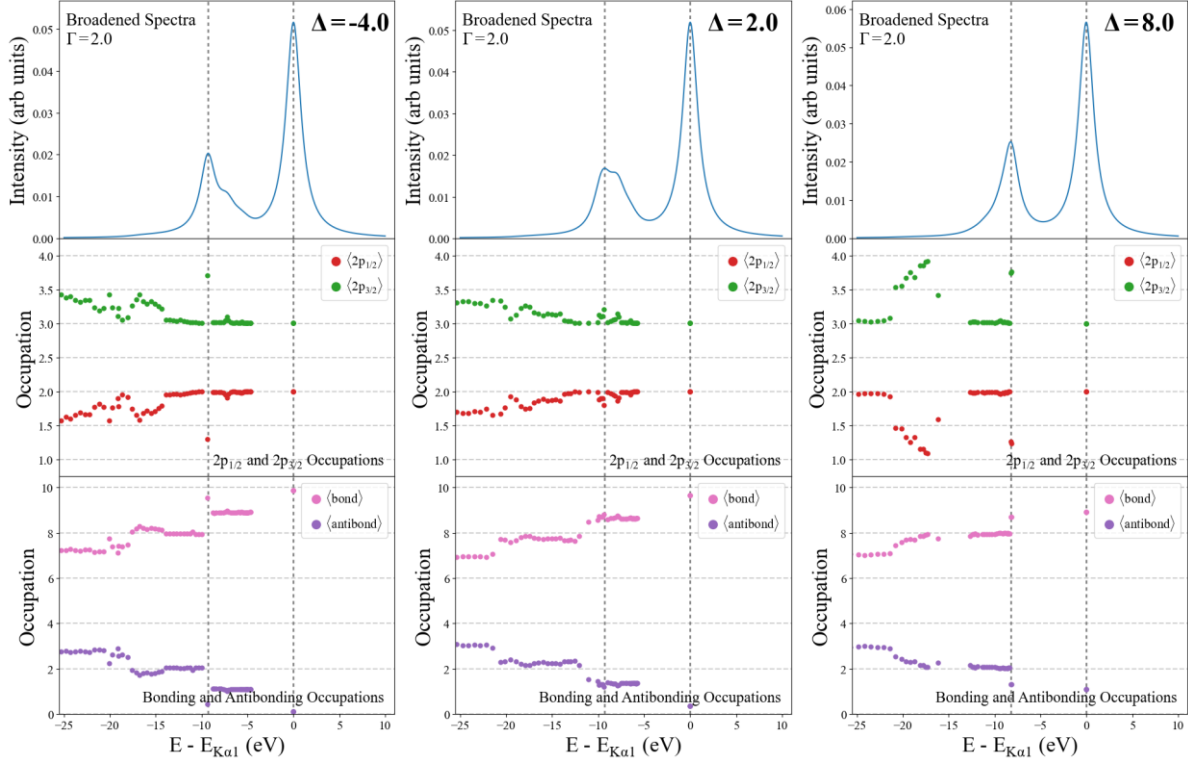
Figure S4: Final state character analysis of $PbCrO_4$. The top row shows broadened spectra calculated with $U_{dd} = 2.0$ eV, $\Delta = -4.0, 2.0$, and 8.0 eV, and a constant Lorentzian broadening of 2.0 eV FWHM. The middle and bottom rows are the expectation of the number operators for the core and valence level respectively.

The condition of maximal mixing of the final state character is reached near $\Delta = 2.0$, where the final states in the vicinity of the $K\alpha_2$ are all strongly mixed in $2p$-hole character and the bonding-antibonding splitting matches the ~9.0 eV spin-orbit splitting. For $\Delta = -4.0$ and 2.0, the first final states lower in energy than the main $K\alpha_1$ peak have a transition of roughly 1 electron from the bonding to antibonding orbitals. This is consistent with the mixed single-particle final state picture described in column 4 of Figure 1 and makes it clear that the satellite spectra features are dominated by charge transfer effects. We note that for all d^0 materials

studied the shake features are entirely dependent on the presence of the ligand coupling. In fact, without ligand coupling, traditional MFLT approach produces a simple two-peak spectra that is devoid of multiplet effects, because the oxidized metal d shell has no way to recover the electrons it has lost in bonding. We also note that while the single-particle derived bonding and anti-bonding orbitals (bottom row of Figure S4) are not perfect eigenstates of the full many-body Hamiltonian which includes d-d Coulomb interactions, the trend of the occupations still agrees with what we expect from model in Figure 1 of the main text, with the $2p_{3/2}$-hole + CT final states having a corresponding transfer of electron occupation from bonding to anti-bonding orbitals.

IV.   Multiplicity Analysis

In some cases, there is a connection between the multiplicity of the overall system in the final state and the satellite features which are observed. This is strongly observed in Kβ XES, where the Kβ' shoulder is directly tied to multiplet effects from the Coulomb exchange splitting between the $3p$ and $3d$ levels [6]. The effect is often used to directly infer the high-spin or low-spin character of the valence orbital [7]. The approximate values we list here are for $3d$ transition metals. The spin-orbit splitting of the $3p$ levels and $3d$ levels are small, approximately 1 eV and 0.05 eV respectively, and the final states can be interpreted in terms of the singlet, doublet, triplet, etc … multiplicities, as has been done in Guo *et al.* [8]. Comparatively, the Coulomb exchange (G Slater-Condon terms) between the $3p$ and $3d$ levels is much larger (on the order of 15 eV) and therefore a distinct splitting in the final state energies is observed when the unpaired *3p* spin is aligned (ex: triplet) or opposed (ex: singlet) with the $3d$ spins [7,9]. This is shown explicitly in the thesis of Pieter Glatzel in figures 16 and 17 [6]. It should be noted that the $3p$ to $1s$

transition is dipole mediated, which means that the multiplicity of the state is conserved, and the final states have the same multiplicity as the intermediate state that they originate from.

In Kα XES however, the $2p$ core level spin-orbit splitting is much stronger (on the order of 10 eV) and the exchange between the $2p$ and $3d$ levels is about 5x weaker (approximately 3 eV). This means that Kα spectra is instead dominated by the $2p$ spin-orbit splitting while the individual L_3 and L_2 peak shapes are the product of multiplet effects. This distinction between the role of spin in the Kα and Kβ emission lines is highlighted by an example Cu(2+) system in an O_h local environment shown in Figure S6. The spectra originate from triplet and singlet intermediate states shown in S6 e) and S6 f). In S6 b) we see that the Kβ' peak has a strong 'spin anti-aligned' character, which comes from the higher energy final state (and thus lower energy of emission) when the unpaired core electron is the opposite spin of the unpaired valence electron. This comes directly from the Coulomb exchange [10].
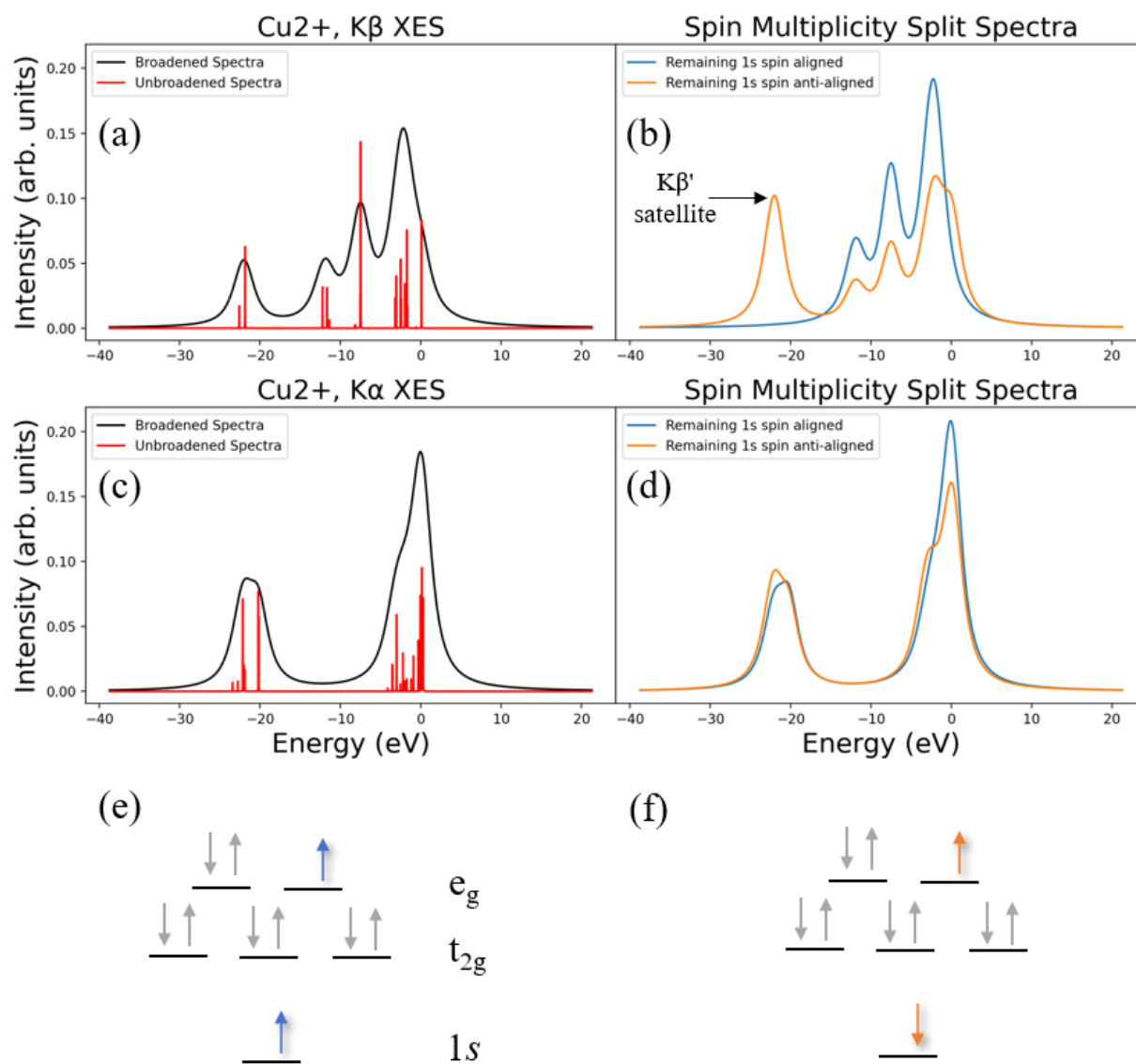
Figure S6: Subplots (a, b) show the calculated Kβ XES for a Cu(2+) system, $n_d = 9$. Subplot (a) shows the broadened (black) and unbroadened (red) calculated from summing over all ground states in the presence of the $1s$ core-hole. Subplots (c, d) show the corresponding Kα XES from the same system. Subplots (e, f) show the triplet and singlet states respectively. Notably, the Kβ' satellite near -23 eV in subplot (b) comes from the singlet ground state due to the Coulomb exchange between the $3p$ and $3d$ orbitals. This calculation is only meant to highlight the behavior

of the emission with regards to the spin of the intermediate state and not to be directly compared with experiment.

It is worth considering if the charge-transfer satellites that we observe in d^0 systems are spin-mediated in a similar fashion. However, the nature of the full bonding orbital and empty anti-bonding orbital immediately leads us to see that all the valence electrons are trivially spin-paired, at least in the lowest energy intermediate state. The $1s$ ionized intermediate state is a doublet, and even though quartet and higher multiplicities are accessible (due to the sudden approximation from the creation of the core-hole [11]) they do not contribute meaningfully to the intensity of our spectra. For more information, please see the discussion comparing the "one-step" and "two-step" methods for calculating XES in our previous work [5]. At least in the discrete orbital approach implemented within MLFT which has 10 d fermionic modes and 10 Ligand fermionic modes, this behavior a general property of all d^0 systems, and the shake satellites are entirely dominated by the charge transfer mechanism between the $3d$ and Ligand orbitals.
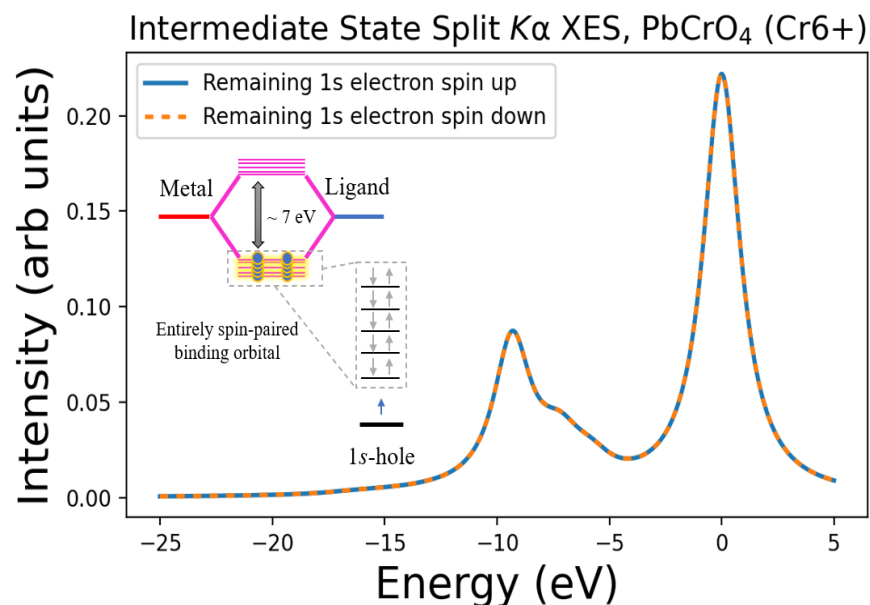
Figure S7: The calculated Kα XES of Cr in PbCrO$_4$ using the spin-up and spin-down intermediate states. The two spectra are identical and have the same multiplicity.

Citations

1. Kawai, J.; Konishi, T.; Shimohara, A.; Gohshi, Y., High Resolution Titanium Kalpha X-Ray Fluorescence Spectra. *Spectrochimica Acta* **1994**, *49B*, 725-738.
2. Jovanović, A.; Dobrota, A. S.; Rafailović, L. D.; Mentus, S. V.; Pašti, I. A.; Johansson, B.; Skorodumova, N. V., Structural and Electronic Properties of V2o5 and Their Tuning by Doping with 3d Elements – Modelling Using the Dft+U Method and Dispersion Correction. *Physical Chemistry Chemical Physics* **2018**, *20*, 13934-13943.
3. Georges, A.; Kotliar, G.; Krauth, W.; Rozenberg, M. J., Dynamical Mean-Field Theory of Strongly Correlated Fermion Systems and the Limit of Infinite Dimensions. *Reviews of Modern Physics* **1996**, *68*, 13-125.
4. Townsend, J.; Kirkland, J. K.; Vogiatzis, K. D., Chapter 3 - Post-Hartree-Fock Methods: Configuration Interaction, Many-Body Perturbation Theory, Coupled-Cluster Theory. In *Mathematical Physics in Theoretical Chemistry*, Blinder, S. M.; House, J. E., Eds. Elsevier: 2019; pp 63-117.
5. Cardot, C. A.; Kas, J. J.; Abramson, J. E.; Rehr, J. J.; Seidler, G. T., Core-to-Core X-Ray Emission Spectra from Wannier Based Multiplet Ligand Field Theory. *Journal of Electron Spectroscopy and Related Phenomena* **2024**, *270*, 147419.
6. Glatzel, P. Thesis: X-Ray Fluorescence Emission Following K Capture and 1s Photoionization of Mn and Fe in Various Chemical Environments. Dissertation, University of Hamburg, 2001.

7.   Lafuerza, S.; Carlantuono, A.; Retegan, M.; Glatzel, P., Chemical Sensitivity of Kβ and Kα X-Ray Emission from a Systematic Investigation of Iron Compounds. *Inorganic Chemistry* **2020**, *59*, 12518-12535.

8.   Guo, M.; Braun, A.; Sokaras, D.; Kroll, T., Iron Kβ X-Ray Emission Spectroscopy: The Origin of Spectral Features from Atomic to Molecular Systems Using Multi-Configurational Calculations. *The Journal of Physical Chemistry A* **2024**, *128*, 1260-1273.

9.   Glatzel, P.; Bergmann, U.; de Groot, F. M. F.; Cramer, S. P., Influence of the Core Hole on K Beta Emission Following Photoionization or Orbital Electron Capture: A Comparison Using Mno and (Fe2o3)-Fe-55. *Physical Review B* **2001**, *64*, 045109.

10.   Slater, J. C., *Quantum Theory of Atomic Structure*, 1st ed.; McGraw-Hill, 1960.

11.   Åberg, T., Theory of X-Ray Satellites. *Physical Review* **1967**, *156*, 35-41.

Chapter 6 X-ray Emission Spectropolarimetry of Single Crystal Cu and Ni systems

Polarization dependence has historically seen extensive use in x-ray spectroscopy to determine magnetic and local geometric properties, but more broadly as a way to gain extra sensitivity to the electronic structure at the level of individual magnetic orbitals. This is often done in the context of x-ray absorption through techniques like x-ray magnetic circular dichroism or x-ray linear dichroism, but it has seen little application to x-ray emission. Here we explore the information contained in the polarized emission of two 3d transition metal systems across both core-to-core and valence-to-core emission lines. We demonstrate how the Rowland circle geometry can be used as a sepctropolarimeter, and apply it to the XES of LiVCuO₄ and DyNiC₂. From this we explore how the polarized XES provides a reflection of the occupied density of states at the valence level, either as a second order effect through Coulomb exchange (CtC-XES) or by direct transitions (VtC-XES). Finally, we highlight how the individually polarized dipole emission spectra can be extracted from an orthogonal suite of directed emission

spectra, allowing for polarized measurements at high Bragg angle with lower experimental broadening.

6.1   Introduction

Many functional materials, such as superconducting cuprates, layered perovskites, and quasi-1D materials, exhibit anisotropic electronic and chemical environments [1–3]. This makes them ideal candidates for polarization-sensitive x-ray techniques, which exploit dipole selection rules to resolve direction-dependent electronic features [4]. Polarized XAS, in particular, has become a standard technique in studying the magnetic, orbital, and local electronic anisotropy. It is the backbone to many polarized spectroscopy techniques such as x-ray magnetic circular dichroism (XMCD) [5, 6], x-ray magnetic linear dichroism (XMLD) [7], angle-resolved photoemission spectroscopy (ARPES) [8–12], and resonant inelastic x-ray scattering (RIXS) [13–17].

X-ray emission spectroscopy (XES) is a versatile, element-specific probe that is well suited to a wide range of sample environments, including liquids, powders, single crystals, and even under *in situ* or *operando* conditions. The technique is ideal for characterizing the occupied density of states, providing insight into valence-level electronic structure, oxidation states, covalency, and chemical bonding [18, 19]. Because XES exclusively probes occupied orbitals, it can be paired with x-ray absorption spectroscopy (XAS), which probes unoccupied orbitals, to create a powerful complementary framework for understanding electronic and chemical structure [20–22].

In contrast, polarized non-resonant XES has seen little study due to the difficulty involved in measuring the polarization of a photon from low brilliance sources, i.e. fluorescence. Studies by Drager̈ and Czolbe [23, 24] showed there were polarization effects in XES which reflected the *m*-resolved density of states, but these developments were hampered due to optical constraints and

detector efficiency. Later, Bergmann and co-workers [25] demonstrated how electronic anisotropy from different ligand species can produce a polarization dependence in the ligand-coupled $K\beta''$ peak of Mn VtC-XES from $[Rh(en)_3][Mn(N)(CN)_5]\cdot H_2O$ single crystals.

To further investigate the application of polarized XES, we present two case studies on single crystal systems, $LiVCuO_4$ and $DyNiC_2$. $LiVCuO_4$ is a low-dimensional cuprate with strong orbital ordering from crystal field effects [26, 27] and $DyNiC_2$ is an electronically quasi-one-dimensional rare-earth inter-metallic carbide [28, 29]. Similar to other rare-earth nickel carbides such as $SmNiC_2$, the quasi one-dimensionality of $DyNiC_2$ arises from its Ni chain structures, which drive anisotropic electronic behavior along the chain direction [30]. We directly measure polarized XES using a spectropolarimeter design similar to the one developed by Dräger *et al.* [31] but with improved energy resolution, and indirectly by a new technique to extract the polarized spectra from a set of linearly independent, unpolarized XES spectra. We employ multiplet and real space Green's function calculations to help interpret the electronic structure information from polarized CtC- and VtC-XES techniques. From the lineshape and energy shifts of the polarized x-ray emission, we can infer the occupational configuration of the valence electrons to a similar extent as can be achieved with x-ray linear dichroism (XLD) or ARPES studies [32–35].

6.1.1   Manuscript Overview

The manuscript proceeds as follows. Section 2 describes the relevant terminology, a framework of XES and corresponding toy model, and the single crystal systems we study. In Section 3 we describe the experimental and computational methods. Special attention will be paid to the experimental setup and data processing to confirm that we perform a comparison of different polarizations on a consistent energy scale. In Section 4 we present a polarization analysis of the

CtC Kβ XES and VtC-XES for both materials. Finally, in Section 5 we summarize our results and conclude.

6.2 Background

6.2.1 X-ray Emission Spectroscopy

X-ray emission is the fine energy resolution study of the fluorescence given off when an atom radiatively decays to fill a core hole left behind from an absorption event [18]. Core-to-core (CtC) Kβ XES involves filling a $1s$ core hole from the $3p$ orbital. CtC Kβ XES has two main spectral features: K$\beta_{1,3}$ and Kβ'. The K$\beta_{1,3}$ is defined by transitions from the spin-orbit split $3p_{1/2}$ or $3p_{3/2}$ orbitals filling the $1s$ hole. The Kβ' satellite line originates from the exchange interaction between the $3p$ core hole and unpaired $3d$ electrons in the valence shell. The strength of the satellite is strongly dependent on the $3d$ spin state, growing for higher spin systems [18].

When the transition is from the valence levels, which have a mix of $3d$ and ligand character, to $1s$ core hole the process is known as a valence-to-core (VtC) transition. $3d$ TMs VtC-XES also has two main spectral features; a main K$\beta_{2,5}$ spectral region coming from molecular orbitals with metal $3d$, metal $4p$, metal $4s$, and ligand $2p$ character, and a Kβ'' satellite from ligand $2s$ electrons filling the metal $1s$ hole. As such VtC-XES is highly depend on local environment with the K$\beta_{2,5}$ peak changing due to bonding and $3d$ electron configuration and the Kβ'' peak energy and intensity being dependent on ligand speciation and bond length [36].

6.2.2 Polarization Dependence

Terminology

Here we introduce and define the terminology for directed and polarized spectra. Spectra measured at high Bragg angle will contain approximately equal contributions from in-plane (p) and out-of-plane (s) polarizations, and are referred to as *unpolarized*. Spectra measured at low Bragg angle will be dominated by the out-of-plane polarization, and we call these *partially polarized*. Further details will be provided in Section 3.1.

A key note is that both of these are considered *directed* spectra, where the specified axis refers to the direction of photon propagation, denoted as I_x, I_y, or I_z. However, the *partially polarized* spectra are dominated by a specific polarization component that is perpendicular to the propagation direction, and are therefore denoted with both the polarization axis and propagation axis specified (ex: σ_x, I_z). In contrast, *polarized* spectra refer to emission resulting from a dipole transition along a specific axis, denoted purely as σ_x, σ_y, or σ_z. All polarized spectra presented in this work are either extracted from experiment following Section 3.4.3 or directly calculated from theory. The terminology is summarized in Table 1.

Term	Definition
Unpolarized	High Bragg Angle
Partially Polarized	Low Bragg Angle
σ_x	x-polarized spectrum
σ_y	y-polarized spectrum
σ_z	z-polarized spectrum
I_x	x-directed spectrum

I_y	y-directed spectrum
I_z	z-directed spectrum

Table 1: Terminology and symbol definitions used in this work.

Polarized Dipole Components

The x-ray emission intensity from a given initial state i is expressed in Eq. 1. The total spectrum comes from the sum over Fermi's golden rule for all final states f [37]. The energy $\hbar\omega$ is the energy of the radiation, m is the mass of the electron, $\vec{r}$ is the spatial coordinate vector, and $\vec{k}$ ($|\vec{k}| = 2\pi/\lambda$) is the propagation vector of the photon [37–39]. The orientation of the emitted radiation is entirely described by $\vec{k}$ and the polarization unit vector $\hat{\epsilon}$, which is orthogonal to $\vec{k}$.

$$\sigma = \frac{\omega e^2}{hm^2c^3} \sum_f \left| \langle f | \exp(i\vec{k} \cdot \vec{r}) \, \hat{\epsilon} \cdot \vec{r} | i \rangle \right|^2$$
$$\times \, \delta(E_f - E_i + \hbar\omega) \tag{1}$$

If we approximate the wavelength of the photon, λ, to be much larger than the size of the 1s shell, $\lambda \gg r$, we arrive at the dipole approximation in Eq. 2. The dipole transition operator is given by $\sum_\alpha \hat{\epsilon}_\alpha \cdot \vec{r}$. The isotropic spectrum is equivalent to taking the average of the trace of the polarization tensor.

$$\sigma^{\mathbf{dip}} \propto \sum_f |\langle f| \sum_\alpha \hat{\epsilon}_\alpha \cdot \vec{r} |i\rangle |^2 \delta(E_f - E_i + \hbar\omega)$$
$$\propto \sum_f |\langle f| \epsilon_x \hat{x} + \epsilon_y \hat{y} + \epsilon_z \hat{z} |i\rangle|^2 \, \delta(E_f - E_i + \hbar\omega)$$
$$= \sigma_x + \sigma_y + \sigma_z \tag{2}$$

We refer to the observables σ_x, σ_y, and σ_z as the polarized spectra. They represent the emission intensity as a function of energy for a dipole transition along a given axis, and they are the quantity

that polarization analysis of a single-crystal XES study seeks to determine. For information about how the radiation pattern of dipole (and higher order) transitions, please refer to Supplemental Information section A. The dipole selection rules restrict transitions to be between orbitals that are related by $\Delta l = \pm 1$, which follows from the fact that the position operators x, y, and z transform as components of a spherical tensor of rank 1 and thus only connect states whose angular momenta differ by one unit [40].

The spectrum corresponding to a photon with wave vector $\vec{k}$ will have a polarization perpendicular to the direction of propagation [41]. The intensity of the emitted photon is symmetric azimuthally about the dipole transition moment axis, which means that the measured emission along a given axis is composed of an equal mixing of the two signals with polarization perpendicular to the direction of propagation. The system of equations which gives the unpolarized intensity measured from a photon propagating in a given direction (I_x, I_y, and I_z) is shown in Eq. 3, where σ_x, σ_y, and σ_z correspond to the spectra from the x, y, and z dipole transition operators respectively.

$$\vec{I}_{\text{dir}} = \begin{bmatrix} I_x \\ I_y \\ I_z \end{bmatrix} \propto \frac{1}{2} \begin{bmatrix} 0 & 1 & 1 \\ 1 & 0 & 1 \\ 1 & 1 & 0 \end{bmatrix} \begin{bmatrix} \sigma_x \\ \sigma_y \\ \sigma_z \end{bmatrix}$$

(3)

6.2.3 Toy Model of CtC-XES

Local anisotropy is often reflected in the (projected) electronic density of states of the valence shell of metal ions. For the purpose of demonstrating the origin of polarization effects in CtC-XES, we investigate how anisotropy in the valence level electron configuration is transferred to other levels via the electron-electron Coulomb interaction. This will be crucially instructive for demonstrating how the electron configuration can be inferred from the polarized CtC-XES of real systems, as we will see in section 4.

We consider a toy system of one d electron and one p electron, fixing the d electron to be spin down in the d_{xy} orbital. The choice of d_{xy} for this example is arbitrary, but in a real system will be determined by valence level splitting from crystal field effects. The Coulomb Hamiltonian is given in second quantization in Eq 4a, where $\tau = \sigma,m,l,n$ denotes the spin and orbital degrees of freedom. The two particle Coulomb operator between the p and d orbitals can be split into spherical ($\Theta^k[\tau_1\tau_2\tau_3\tau_4]$) and radial ($R^k[\tau_1\tau_2\tau_3\tau_4]$) components (Eq. 4b), and further split into the 'direct' ($H_{Fpd}^{(0)}$, $H_{Fpd}^{(2)}$) and 'exchange' ($H_{Gpd}^{(1)}$, $H_{Gpd}^{(3)}$) terms (Eq. 4c) [42]. The Slater-Condon F and G terms are usually determined by the overlap of the radial wave functions, but in this toy Hamiltonian we just set $R^k = [F_{pd}^0, G_{pd}^1, F_{pd}^2, G_{pd}^3] = [1.2, 8.0, 9.0, 5.0]$ to approximate the interaction between the $3p$ and $3d$ orbitals in the final state of a Kβ XES process.

$$H_{\text{toy}}^C = \sum_{\tau_1\tau_2\tau_3\tau_4} U_{\tau_1\tau_2\tau_3\tau_4}\, a_{\tau_1}^\dagger a_{\tau_2}^\dagger a_{\tau_4} a_{\tau_3} \tag{4a}$$

$$
\begin{aligned}
U_{\tau_1\tau_2\tau_3\tau_4} &= -\frac{1}{2}\delta_{\sigma_1,\sigma_3}\delta_{\sigma_2,\sigma_4} \sum_{k=0}^{\infty} \frac{4\pi}{2k+1} \\
&\times \langle Y_{m_1}^{(l_1)}| Y_{m_1-m_3}^{(k)} |Y_{m_3}^{(l_3)}\rangle \langle Y_{m_4}^{(l_4)}| Y_{m_4-m_2}^{(k)} |Y_{m_2}^{(l_2)}\rangle \\
&\times R^k[\tau_1\tau_2\tau_3\tau_4] \\
&= -\frac{1}{2}\delta_{\sigma_1,\sigma_3}\delta_{\sigma_2,\sigma_4} \sum_{k=0}^{\infty} \frac{4\pi}{2k+1} \\
&\times \Theta^k[\tau_1\tau_2\tau_3\tau_4] \times R^k[\tau_1\tau_2\tau_3\tau_4]
\end{aligned}
\tag{4b}
$$

$$
\begin{aligned}
H_{\text{toy}}^C &= -2\pi \sum_{\tau_1\tau_2\tau_3\tau_4} \left(\Theta^0 F_{pd}^0 + \frac{1}{3}\Theta^1 G_{pd}^1 \right. \\
&\left. + \frac{1}{5}\Theta^2 F_{pd}^2 + \frac{1}{7}\Theta^3 G_{pd}^3 \right) a_{\tau_1}^\dagger a_{\tau_2}^\dagger a_{\tau_4} a_{\tau_3} \\
&= H_{Fpd}^{(0)} + H_{Gpd}^{(1)} + H_{Fpd}^{(2)} + H_{Gpd}^{(3)}
\end{aligned}
\tag{4c}
$$

Table 2 shows the contributions to the total energy $\langle H_{toy}^C \rangle$ for different p, d configurations. These were calculated using the many-body second quantization code Quanty to encode the toy Hamiltonian [43]. The direct terms $H_{Fpd}^{(0)}$ and $H_{Fpd}^{(2)}$ are always non-zero, with the $H_{Fpd}^{(0)}$ term corresponding to a
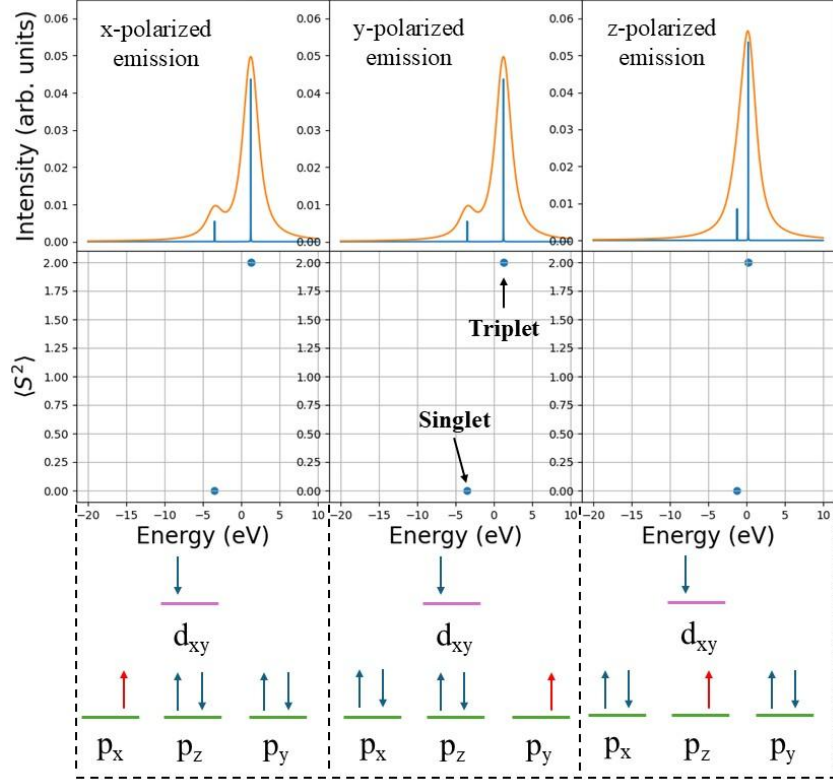
Figure 1: The polarized dipole $p \rightarrow s$ emission spectra and final states of our toy system described by Eq. 4. Only final state configurations with a spin down electron in the d_{xy} orbital are calculated. The top row shows the spectra for different dipole transition operators (x, y, and z). The middle row shows the expectation value of the total system $\langle S^2 \rangle$ operator for the final states. The last row shows the singlet configuration corresponding to the p core hole created by each of the dipole transition operators
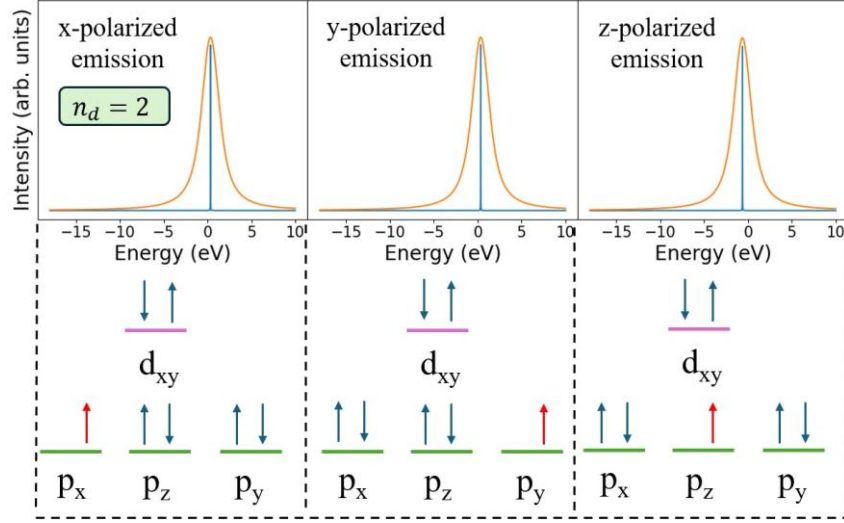
Figure 2: The polarized dipole $p \rightarrow s$ emission spectra for a final state described by Eq. 4, but with two electrons pinned into the same d_{xy} orbital. The top row shows the emission spectra for each polarization and the bottom row shows the singlet configuration of each final state.

d-Orbital	d-Spin	p-Orbital	p-Spin	Spin Aligned?	$\langle H^C_{\mathbf{toy}} \rangle$	$\langle H^{(0)}_{Fpd} \rangle$	$\langle H^{(2)}_{Fpd} \rangle$	$\langle H^{(1)}_{Gpd} \rangle$	$\langle H^{(3)}_{Gpd} \rangle$
d_{xy}	down	p_x	down	yes	-0.885	0.748	0.457	-1.600	-0.490
d_{xy}	down	p_x	up	no	1.205	0.748	0.457	0.000	0.000
d_{xy}	down	p_y	down	yes	-0.885	0.748	0.457	-1.600	-0.490
d_{xy}	down	p_y	up	no	1.205	0.748	0.457	0.000	0.000
d_{xy}	down	p_z	down	yes	-0.473	0.748	-0.914	0.000	-0.306
d_{xy}	down	p_z	up	no	-0.167	0.748	-0.914	0.000	0.000

Table 2: Table of Coulombic d-orbital and p-orbital interactions for a system with one d electron constrained in the spin down d_{xy} fermionic mode and one p electron.

spherically symmetric constant contribution and the $H_{Fpd}^{(2)}$ changing signs and magnitude according to whether the occupied orbitals have overlapping symmetry. This behavior is effectively an inter-orbital Hund's rule [44]; when the d and p electrons have overlapping symmetry (ex: d_{xy} and p_x) the energy of that configuration is raised compared to when their symmetries do not overlap (ex: d_{xy} and p_z).

The exchange terms $H_{Gpd}^{(1)}$ and $H_{Gpd}^{(3)}$ come from the fermionic behavior of electrons which energetically split spin-aligned configurations from spin-opposed. Hund's principle of maximum multiplicity leads to systems with aligned spins having lower energy than when spins are opposed. The exchange terms behave similarly to the direct terms in that the magnitude of the interaction is larger when the symmetries of the two occupied orbitals are overlapping, but the contribution to the total energy is always negative. The behavior of the exchange Coulomb terms is what gives sensitivity to spin in CtC-XES, where for example the Kβ' peak changes depending on whether a system is in a high spin or low spin configuration [18].

We demonstrate how this behavior in Fig. 1 combines with the difference in Coulomb interaction based on symmetry overlap to give polarized spectra. Starting from an initial state with six p electrons and an s core hole, we use the x, y, and z dipole transition operators to control where the unpaired electron in the p orbital ends up in the final state. The final state is constrained to have the single d electron in the d_{xy} orbital, meaning that our final states are analogous to the six rows shown in Table 2 (up to an overall shift). Note that the peak corresponding to a spin-aligned (triplet) final state is higher energy then the spin-opposed (singlet) peak. This is because the emission energy is equal to the difference in energies between the initial and final states.

Quanty was used to calculate the $p \rightarrow s$ polarized dipole emission spectra. The first row in Fig. 1 shows x, y, and z polarized emission spectra. We note that the x and y polarized emission are identical with a large splitting between the singlet and triplet states, while the z polarized emission has a much smaller splitting. An important note is that because we are neglecting spin-orbit splitting in this toy model the multiplicity of the entire system $\langle S^2 \rangle$ is a good quantum number, and it allows us to distinguish the configurations as seen in the second row. The singlet configuration for each final state is shown in the last row. For more information about the quantitative behavior of the splitting between the singlet and triplet states we refer readers to the theory discussion in Lafuerza et $al.$ [19]. The splitting between these configurations is the same mechanism that underpins the spin-dependence of the Kβ' peak in $3p \rightarrow 1s$ XES. The behavior of this toy system highlights a key result, namely that the intensity and position of the Kβ' in polarized emission can be a reflection of orbital occupation as well as the spin state.

A simpler, but equally useful result comes from adding a second electron into the d_{xy} orbital, see Fig. 2. The addition of a second electron takes the system from a spin-1/2 to spin-0 configuration and removes the split singlet-triplet behavior. While the final states of the non-degenerate polarizations will still experience an overall shift in energy, the effective anisotropy in the spectra becomes much weaker.

The toy model here is simple, but the results are generic. We have demonstrated how the polarized emission of CtC-XES is sensitive to the occupation of the valence orbitals via the Coulomb exchange interaction. Consequently, any symmetry breaking perturbations (crystal field, charge transfer) will also be reflected in the spectra. This is distinct from the polarization sensitivity

observed in absorption techniques like $L_{2,3}$ XLD or XMCD, where the electron transitions from p into d provide a direct probe of the unoccupied density of states in the presence of a core hole.

6.2.4   Crystal Systems

We study two transition metal compounds: $LiVCuO_4$ and $DyNiC_2$. Both materials are studied at room temperature. The crystal structure of $LiVCuO_4$ [26] is shown in Fig. 3. CuO_4 ladders run through the *ab* plane, and have a nearly perfect square planar bond orientation with a small rhomboidal distortion, giving the Cu-O cluster a point group of D_{2h}. The Cu(II) ion leaves the system with $n_d = 9$. The crystal field splitting for the local cluster around the Cu leaves a single unpaired *d*-electron and a spin-1/2 system [45].

The $DyNiC_2$ structure is shown in Fig. 4 and has a structure of alternating Ni-C and Dy sheets in the *bc*-plane [46]. The local Ni-C cluster is a strongly distorted square planar structure with a point group C_{2v}. The Ni(II) ion has $n_d = 8$. Low-symmetry clusters, like $DyNiC_2$, experience spin-quenching when the crystal field split levels all lose their degeneracy [47], hence the $n_d = 8$ configuration here is fully spin-paired, leading to a spin-0 system.

Both systems have orthorhombic unit cells and therefore the crystal axes are orthogonal. For describing the direction of propagation and polarization of the x-ray emission we will use the x, y, z coordinate convention with the obvious mapping to the a, b, c crystal axes.
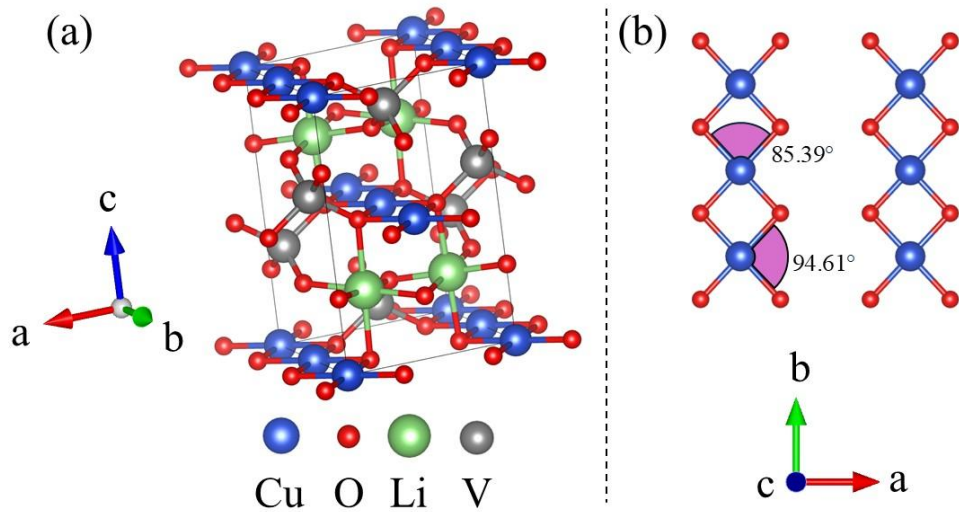
Figure 3: (a) LiVCuO₄ crystal structure. (b) Face down view on the a-b plane of square planar Cu-O chains.

6.3 Methods

6.3.1 Experimental Setup

All XES measurements were performed at room temperature on a laboratory spectrometer described in Jahrman et al. [48], using a 100W x-ray source with a Pd anode, 10-cm diameter spherically bent crystal analyzer (SBCA), and an Amptek X-123 silicon drift detector on a 1-m Rowland circle. The x-ray tube was held at 2.8 mA current and 35 kV accelerating potential. A 1-mm entrance slit and a mask that covers the outer 30 mm on either side of the SBCA were used to reduce the experimental broadening. Measurements were made with 0.25 eV steps around the features of interest and 1 eV steps outside this region for background determination. Each spectrum was collected over multiple scans, with the specific number of scans chosen to obtain a total of at least 10,000 counts for the $K\beta_{1,3}$ peak and $\sim$1000 counts for the $K\beta_{2,5}$ peak. The first and last few scans were compared and showed no evidence of beam damage.

As shown in Fig. 5, two spectrometer geometries were used to obtain the unpolarized and partially polarized XES measurements, using high and low Bragg angles, respectively. Specific Bragg angles are shown in Table 3. All SBCA were used in symmetric reflection geometries. The experimental broadening is ∼3-eV greater for the low Bragg angle geometry compared to the high Bragg angle, shown for reference spectra in Fig. 6, due to source size and Johann error broadening being worse for smaller Bragg angles [49–51].

Polarization control was achieved by exploiting the difference in reflectivity of emission from photons polarized perpendicular (s-polarized) versus parallel (p-polarized) to the reflection plane, see Fig. 7. The reflectivity of these two polarizations is calculated with Fresnel's equations [52] using the index of refraction for Si or Ge at x-ray energies. This gives a ratio of emission reflecting off
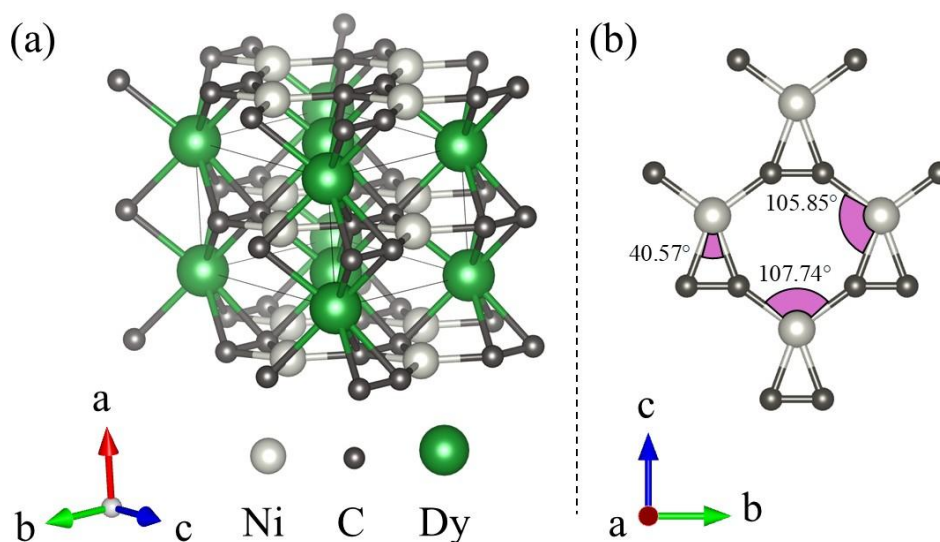
Figure 4: (a) DyNiC$_2$ crystal structure. (b) Face down view on the b-c plane of distorted square planar Ni-C chains.

the SBCA with polarization parallel (R_p) versus perpendicular (R_s) to the Rowland plane of ~0.2 for low Bragg angles and ~0.85 for high Bragg angles. Therefore using the spectrometer at low Bragg angles achieves selection of x-rays that are primarily polarized perpendicular to the Rowland plane, meaning that we detect a partially polarized spectra. By orienting the emitting sample with a chosen crystallographic axis perpendicular to the Rowland plane the partially polarized spectra show the transition intensity along the specific axis.

6.3.2   Samples and Sample Orientation

Photographs of the two samples are shown in Fig. 8 (a) and (b). Both samples are plate-like having 4-mm to 8-mm spatial extent in their planar directions and are thinner (~1-mm) in the perpendicular direction. The $LiVCuO_4$ crystal was grown from $LiVO_3$ flux cooled by 0.1K/hour from ~880K as described in Grams *et al.* [53]. Single crystal X-ray diffraction was performed to confirm the structure and to orient the crystal. The $DyNiC_2$ crystal was grown and characterized following the procedure described in Roman *et al.* [28]. The crystal was synthesized using pure elements and the floating zone technique. It was oriented with Laue method and then characterized by scanning electron microscopy, powder x-ray diffraction to confirm crystal growth and homogeneity.

The samples were oriented in the spectrometer on a custom 3D printed mount for each measurement so one crystallographic axis is perpendicular to the Rowland plane and another is 15 degrees from the emission direction. An example of this mounting is given in Fig.8 (c). The 15 degree offset allows for a much higher count rate with a small correctable loss of directionality along the in-plane crystal axis, discussed in Section 3.4.3. Reference Cu and Ni foils that were

used during the calibration process were procured from ESPI metals being 99.995% elementally pure.
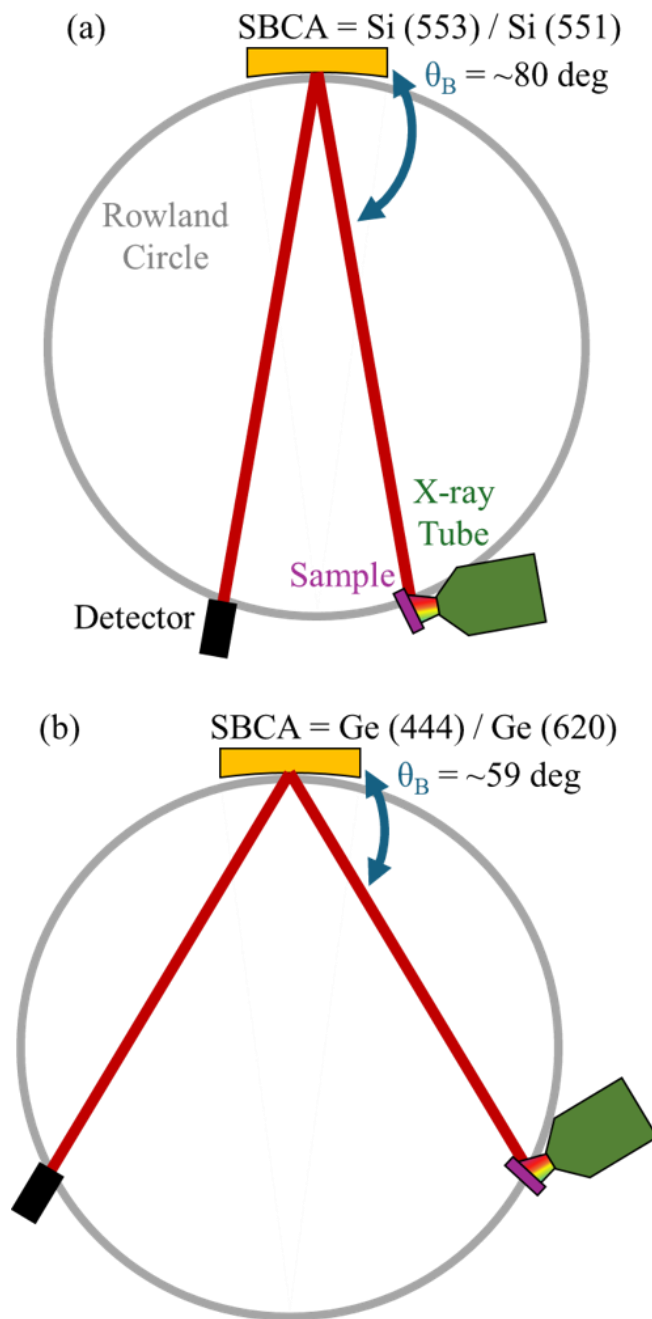
Figure 5: Rowland Circle geometry for unpolarized, (a), and partially polarized, (b), CtC and VtC Kβ XES measurements. For each geometry the first SBCA is for Cu measurements and the second is for Ni measurements.
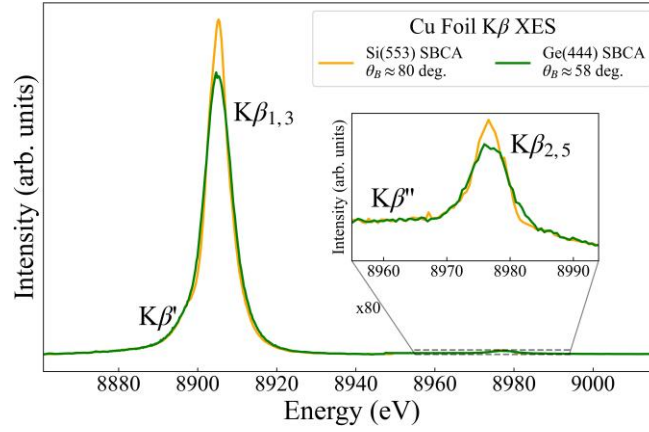
Figure 6: Cu foil Kβ x-ray emission spectra taken at high (orange) and low (green) Bragg angle.
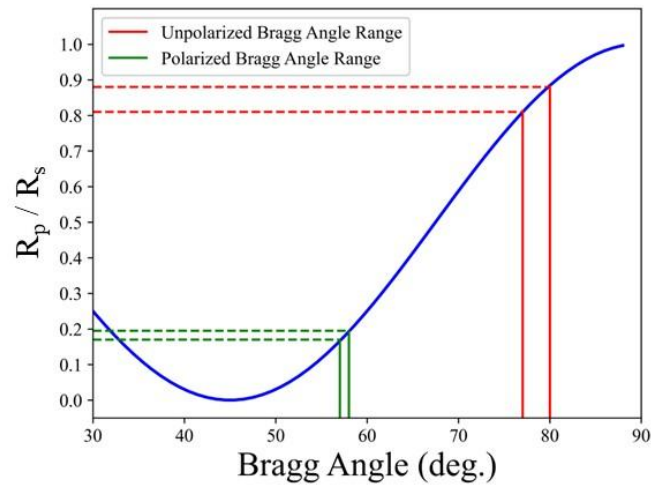
Figure 7: The calculated ratio of reflectance of x-rays with polarization parallel to the Rowland plane (R_p) verse perpendicular to the Rowland plane (R_s) as a function of Bragg angle for the SBCA. The minimum and maximum Bragg angles for the unpolarized (red) and partially polarized (green) XES spectra are marked.
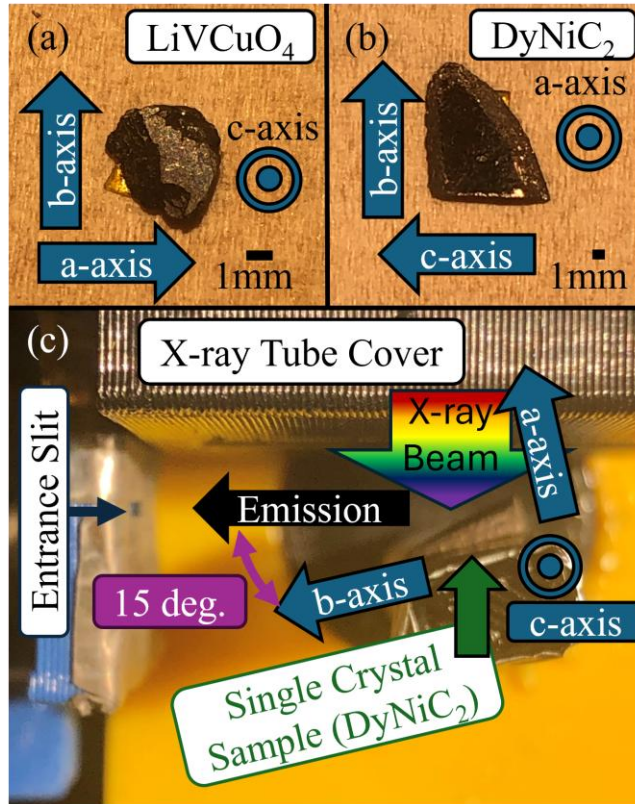
Figure 8: (a) LiVCuO$_4$ single crystal sample. (b) DyNiC$_2$ single crystal sample. (c) DyNiC$_2$ sample shown positioned in the spectrometer sample environment for z-polarized, y-directed (σ_z, I$_y$) XES spectra.

Emission		Spectrometer		
Emission Line	Polarized	SBCA	θ_B (deg.)	Pol. Factor

Cu Kβ	No	Si (553)	80	0.88
Cu Kβ	Partial	Ge (444)	58	0.19
Cu VtC	No	Si (553)	78	0.84
Cu VtC	Partial	Ge (444)	58	0.19
Ni Kβ	No	Si (551)	81	0.91
Ni Kβ	Partial	Ge (620)	57	0.17
Ni VtC	No	Si (551)	80	0.88
Ni VtC	Partial	Ge (620)	57	0.17

Table 3: Emission line, polarization classification, analyzer, Bragg angle, and polarization factor (R_p/R_s) for all studies presented in this work. See Fig. 5 for graphical representations.

6.3.3 VtC-XES Computational Details

To calculate the VtC-XES and the *l,m* projected density of states (DOS) we use the real-space Green's function code FEFF10 [54] which calculates a single-particle Green's function where many-body interactions are approximated via the LDA exchange-correlation potential. This is sufficient for valence level spectroscopies due to the more delocalized nature of the orbitals involved in bonding, and has been demonstrated to perform similarly to time-dependent DFT approaches for VtC-XES [55]. The *x*, *y*, and *z* polarizations are calculated using the POLARIZATION card and we include both electric dipole and quadrupole transitions with the MULTIPOLE card. While the main contribution to the VtC-XES of 3*d* transition metals comes from the *p* DOS from the dipole transition, roughly 10% of the intensity can come from quadrupole

transitions from the *s* and *d* DOS, as demonstrated in Mortensen *et al.* [56] and in Supplemental Information section B.

The potentials and densities were calculated with the self-consistent field (SCF) approach and an SCF radius of 5.0 A around the emitting atom and the spectra were calculated with a full multiple˚ scattering (FMS) radius of 7.0 A. The XES was calculated using the standard practice of omitting˚ the core hole in accordance with the final state rule. The lifetime broadening from the core hole is already included within FEFF spectra, and a 1.0 eV FWHM Gaussian broadening was convolved with the spectra for comparison with experiment. Spectra were energy shifted independently to align with experiment, which is necessary to account for limitations from the muffin-tin potentials used within FEFF [56]. An extended version of the FEFF code was use to calculate the real spherical harmonic projected density of states, which can be directly compared to the *x*, *y*, *z* polarized spectra.

6.3.4   Data Processing Procedure

CtC-XES

The CtC Kβ spectra were processed by first averaging all spectra for one sample orientation. A background subtraction calculated from the first and last 5 eV of the spectrum was applied, followed by an integral normalization over the background subtracted spectrum. A unique Bragg angle correction is
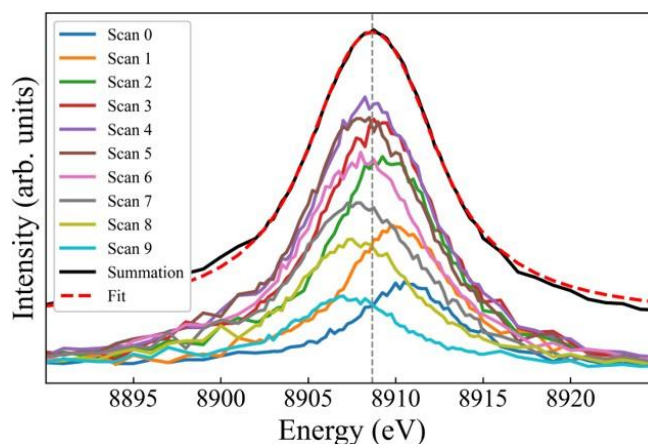
Figure 9: Kβ XES scans of the LiVCuO$_4$ single crystal sample as it is stepped across the entrance slit and the summation of these scans. A vertical gray dashed line marks the center position of the K$\beta_{1,3}$ peak, found by a fit to the summation. This energy is used to apply a Bragg angle correction to the sample spectra, positioning it correctly in energy relative to a Cu foil reference spectra.

applied to the spectrum to position it in energy relative to a foil reference spectra. This is necessary because of the sensitivity of the energy scale to the sample position's relative to the entrance slit when the sample is not large enough to fully illuminate the entrance slit, a limitation that is related to the issue addressed in Abramson et al. [57]. Following that work, we find that summing a series of alignment scans as the sample steps across the entrance slit creates an effectively-large sample spectrum that fully illuminates the entrance slit. This set of scans can be used to finely calibrate the energy scale for the final measurement with a stationary, small sample - see Fig. 9. The calibration procedure involves comparing the resulting effectively-large sample spectrum's and the normalized, background subtracted spectrum's K$\beta_{1,3}$ energy to find the Bragg angle offset that corrects for the actual illumination of the entrance slit. This step is followed by the usual Bragg angle correction applied equally to all reference and sample spectra to align the Cu and Ni foil

reference $K\beta_{1,3}$ energy with their published, standard values. This process aligns both the partially polarized and unpolarized spectra on the same energy scale for comparison.

VtC-XES

VtC-XES spectra were processed by summing all scans for one orientation then subtracting a constant background calculated by averaging the highest 5 eV of data. This was followed by normalization of the VtC region with the integral of the $K\beta_{1,3}$ and $K\beta'$ features to bring the VtC spectra to a consistent molar scale [58]. The Bragg angle corrections determined by the CtC $K\beta$ XES are similarly applied to the VtC-XES.

Polarized Spectra Extraction

X-ray emission propagating in a particular direction (ex: z) is a combination of emission from predominantly dipole transitions in the plane perpendicular to this direction of propagation (x and y). For the Rowland circle spectrometer, the direction of propagation is towards the SBCA, and the two polarizations which can reach the detector are orthogonal to the propagation direction: in the Rowland plane (p) and perpendicular to the Rowland plane (s). The ratio of s and p polarizations which reach the detector depend on the Bragg angle, laid out in Fig. 7 and Table 3. Due to the 15 degree difference between crystallographic axis and emission direction in the Rowland plane (Section 2.4) the p-polarization has contribution from polarized spectra along two crystallographic axis while s-polarization is only from the polarized spectra of the out of plane axis, example shown in 8(c).

By measuring the emission spectra from a sample along three linearly independent directions, a system of equations is created where each directed spectra is an linear combination of the underlying polarized spectra. The relationship between measured intensities and the

underlying polarized emission along the x-, y-, and z- directions is given in Eq. 5. The linear combination coefficients, A, have a geometric component due to the 15 degree difference between crystallographic axis and emission direction in the Rowland plane (Section 2.4) and a reflectivity component due to the R_p/R_s ratio of the Rowland circle geometry. A in Eq. 5b is given for DyNiC$_2$ with the second row matching the sample orientation shown in Fig. 8(c). With A being known, we extract the polarized spectra by matrix inversion.

At high Bragg angle, R_p/R_s is ~0.85, requiring the extraction procedure of Eq. 5 to infer the polarized spectra from the measured unpolarized directional spectra. At low Bragg angle R_p/R_s is ~0.2 which heavily favors the out of plane polarization. Performing the dipole extraction on the measured partially polarized directional spectra changes the integral intensity by ~5 percent, meaning that the measured partially polarized directional spectra are approximately equal to the polarized spectra. An important note here is that this extraction procedure will only be exact for dipole transition spectra. Because the spectra we study in this work are all highly dipole dominated (see Figures 13 and 14), we will only consider the previously mentioned extraction procedure.

$$\begin{bmatrix} I_x \\ I_y \\ I_z \end{bmatrix} = A \begin{bmatrix} \sigma_x \\ \sigma_y \\ \sigma_z \end{bmatrix} \tag{5a}$$

$$A = \begin{bmatrix} R_p \sin 15° & R_s & R_p \cos 15° \\ R_p \cos 15° & R_p \sin 15° & R_s \\ R_s & R_p \cos 15° & R_p \cos 15° \end{bmatrix} \tag{5b}$$

6.4   Results and Discussion

6.4.1   CtC-XES

We expect core-to-core transitions to demonstrate relatively weak polarization sensitivity given that local environmental effects are only reflected through a coupling between the core hole and

valence level, as we discussed in Section 2.3. The size of the effect is demonstrated through experimental spectra in Fig. 10. The left and right columns show the $K\beta$ emission from $LiVCuO_4$ and $DyNiC_2$ respectively. The top (a, b) row shows the unpolarized spectra and the bottom (c, d) row shows the extracted polarized spectra along the crystallographic directions using the procedure laid out in Section 3.4.3.

While the overall anisotropic signals in both CtC $K\beta$ spectra are weak, one key observation is the polarization dependence of the $K\beta$' feature. The spin-1/2 Cu in $LiVCuO_4$ shows a significant difference between the σ_z spectrum and the σ_x/σ_y spectra. This, along with knowledge of the crystal
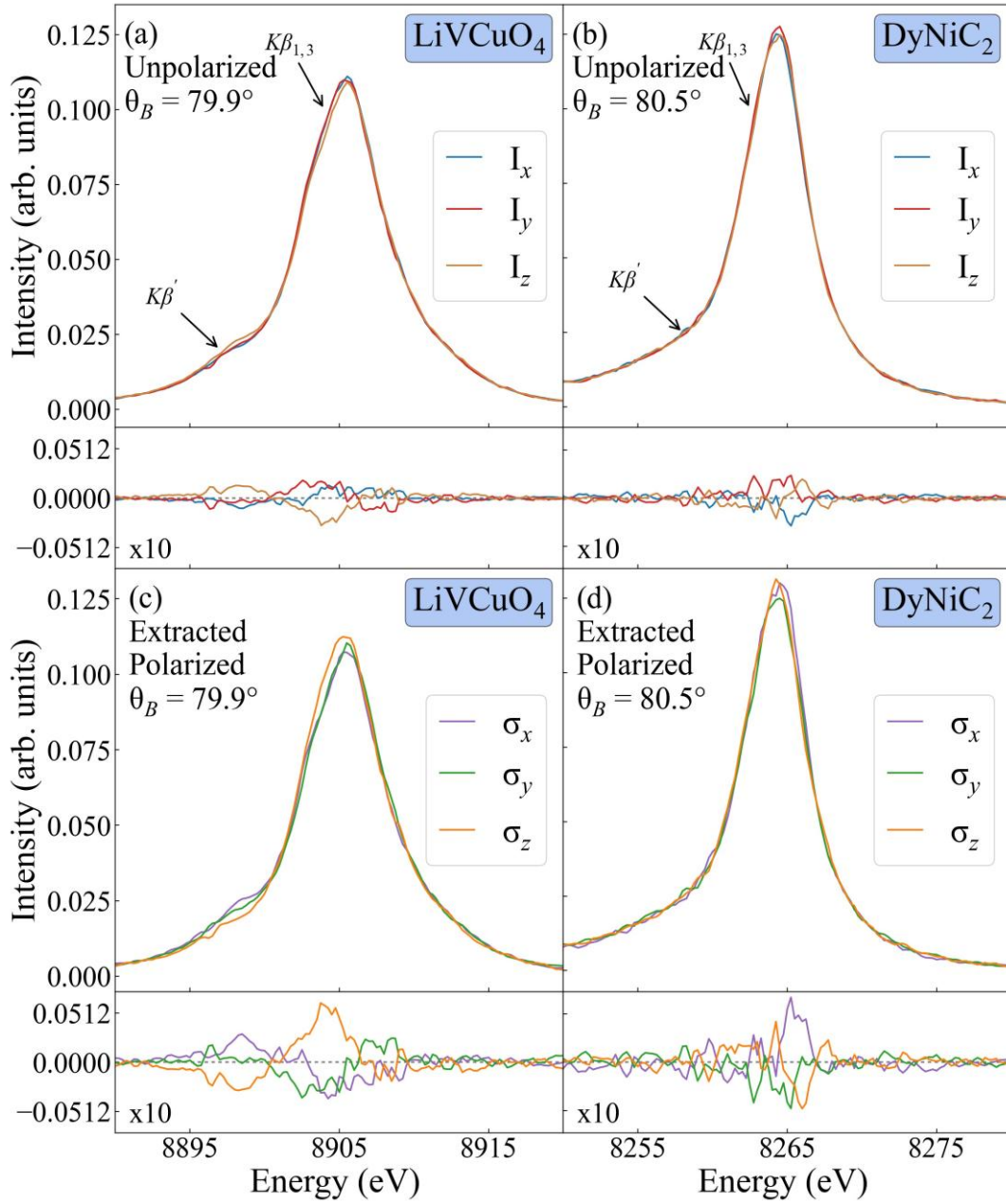
Figure 10: (left) LiVCuO$_4$ Cu and (right) DyNiC$_2$ Ni Kβ CtC-XES. (a, b) Unpolarized emission at high Bragg angle from radiation propagating along the x (blue), y (red), and z (brown) directions. (c, d) polarized spectra extracted from the directional spectra in (a, b) with polarizations along the x (purple), y (green), and z (orange) directions. Difference curves are shown at the bottom of each

subplot and are calculated by subtracting the average spectra from each curve. Note the polarization dependence in the Kβ' feature for LiVCuO$_4$.

field symmetry from the C$_{2v}$ Cu cluster, allows us to determine that the unpaired electron and thus the single $3d$ hole lies in the d_{xy} orbital (using the crystal axes as a basis).

When the polarization vector is in the xy-plane, the interaction between the newly unpaired $3p$ electron and the unpaired $3d_{xy}$ electron produces an energy difference between the spin-aligned (triplet) and spin-opposed (singlet) configurations, leading to a more prominent Kβ' satellite. Conversely, when the polarization vector of the emission is along the z-axis, the symmetry of the core hole and the unpaired valence electron do not match and the interaction is weaker, leading to a less prominent Kβ' feature and a larger Kβ main peak for the z-polarized spectra in Fig. 10 (c). These energy shifts of the Kβ' peak are qualitatively consistent with the behavior observed in the toy model and Figure 1, reinforcing our underlying physical interpretation.

The Ni in the DyNiC$_2$ system is spin-0 and therefore produces no Kβ' feature. The absence of a singlet-triplet splitting interaction limits the anisotropic signal to small changes in the energy and intensity of the K$\beta_{1,3}$ main peak. This is similar to what we observe in Fig. 2 of the toy model, where having a spin-0 valence suppresses anisotropy in the polarized spectra. The overall weak polarization dependence of the main K$\beta_{1,3}$ is not unexpected given it is a second-order property transferred to the core level through the core-valence Coulomb interaction.

6.4.2 VtC-XES

The Cu and Ni VtC emission from LiVCuO$_4$ and DyNiC$_2$ are shown in Fig. 11. Unpolarized (high Bragg angle) and partially polarized (low Bragg angle) are shown in subplots (a, b) and (c, d) respectively. The extracted polarization spectra in subplots (e, f) are calculated from combinations

of the directional spectra, as described in the system of equations given in Section 3.4.3. The theory spectra in subplots (g, h) are calculated according to Section 3.3, and follow the exact same extraction procedure for the purpose of comparison.

The directed emission spectra (a, b) show weakly anisotropic behavior, which is expected given that they are averages of two polarization contributions. The partially polarized spectra in (c, d) qualitatively match with the polarized spectra (e, f) and the calculated polarized spectra (g, h). They show clear polarization differences, such as the ability to distinguish which polarized spectra are most contributing to the $K\beta''$ ligand peak or $K\beta_{2,5}$ feature, indicating the usefulness of these spectropolarimeter measurements. But the ~20 percent contribution of in-plane polarized spectra, Fig. 7, and the lower resolution, Fig. 6, for the partially polarized measurements restricts its quantitative analysis.

For $LiVCuO_4$ the nearly square planar CuO_4 structure means the Cu-O bonds lie in the xy-plane. This geometry means that the Cu d_{z^2} orbital lacks suitable ligand orbitals to form σ bonds, leading to reduced electron density along the z-axis and, consequently, weaker z-polarized (σ_z) emission compared to the x and y polarizations. The unpolarized I_z emission in (a) is therefore stronger than the I_x and I_y signals, as it averages over stronger in-plane transitions. Similarly, the partially polarized and extracted polarized spectra in (c) and (e) show suppressed σ_z contributions, while σ_x and σ_y remain strong and nearly identical due to the symmetry of the in-plane bonding environment. This also accounts for the presence of the $K\beta''$ ligand peak at 8958 eV in both σ_x and σ_y.

For $DyNiC_2$, the distorted planar structure leads to highly anisotropic emission, with the σ_y spectrum being the strongest, followed by σ_z, and then σ_x, which is the weakest due to the absence of a Ni–C bond along the x-direction. This is analogous to the lack of Cu-O bonding along the z-

axis in LiVCuO$_4$. The distortion of the NiC$_4$ cluster results in non-equivalent σ_y and σ_z spectra. The differences are consistent with the Ni–C bond angles in the bc-plane: an average of $42.78°$ relative to the
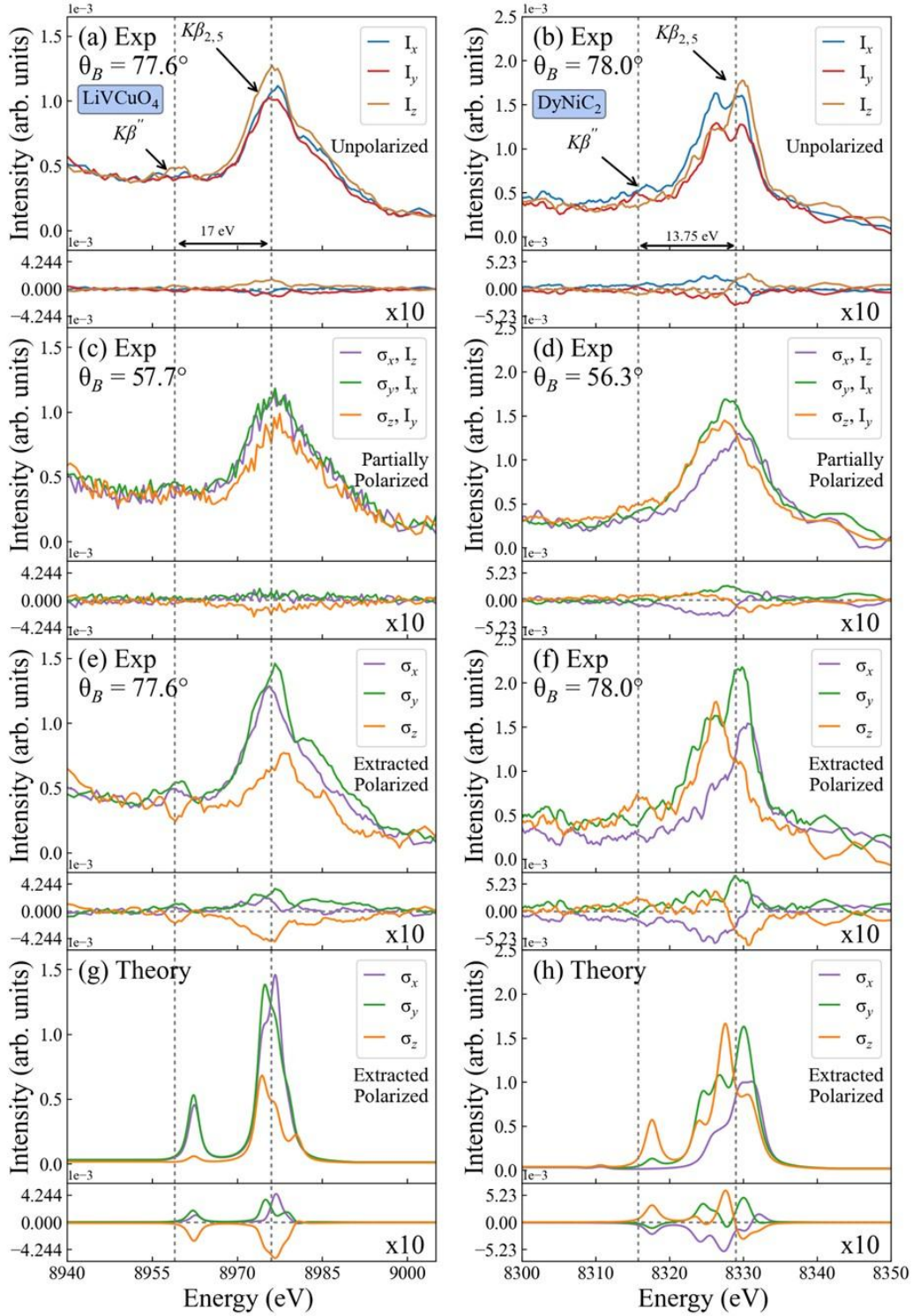
Figure 11: (left) LiVCuO$_4$ Cu and (right) DyNiC$_2$ Ni VtC-XES. Difference curves are shown below each subplot where the difference is taken relative to the averaged (isotropic) spectrum. (a, b)

Measured unpolarized emission from radiation propagating along the *x*, *y*, and *z* directions as defined by the coordinate systems in Section 2.4. (c, d) Measured partially polarized emission, where each spectrum is dominated by a single polarization axis, albeit with poorer energy resolution. (e, f) Extracted polarized spectra. (g, h) Calculated polarized emission, including both electric dipole and quadrupole components.

b/*y*-axis and 37.08° relative to the *c*/*z*-axis. This slight compression along the *z*-axis manifests in the spectra as a ~3 eV energy shift of the σ_z K$\beta_{2,5}$ emission peak compared to the σ_y one, and a more intense C ligand peak at 8316 eV in the *z*-polarization.

In both DyNiC$_2$ and LiVCuO4, the $K\beta''$ satellite is relatively weak compared to the main $K\beta_{2,5}$ peak, a trend attributable to the long metal–ligand bond distances—1.96 $A°$ for Ni–C bonds in DyNiC$_2$ and 2.14 $A°$ for Cu–O bonds in LiVCuO4 [36]. This reduces the hybridization between the ligand 2*s* and metal valence orbitals, thereby suppressing the weak $K\beta''$ feature. Additionally, the $K\beta''$–$K\beta_{2,5}$ energy separation is roughly 5 eV greater in LiVCuO$_4$ than in DyNiC$_2$, reflecting the difference in 2*s* binding energies between O and C ligands [59].

The extracted polarization spectra in subplots (e, f) match well with the calculated polarized spectra in subplots (g, h), and their residuals. However, one important difference between the calculated and extracted is that the position of the calculated $K\beta''$ peak is too low in energy by about 2 eV compared to experiment. This is likely due to limitations imposed by the use of muffin-tin potentials within the FEFF code to approximate the scattering potential, which tend to underestimate the anisotropy of the electron density in the interstitial regions. As a result, the hybridization between the transition metal 3*d* and ligand 2*p* states may be overestimated, artificially shifting the energy position of the $K\beta''$ peak.

6.4.3 Future Directions

The spectropolarimetry to directly measure the polarized spectra (low Bragg angle) suffered as a analytical measurement from low resolution and only partial polarization sensitivity. Both factors can be greatly improved upon by working in an asymmetric Rowland configuration [60], allowing for a selection of reflection geometry with near 45 degree Bragg angle for perfect polarization sensitivity with emission incident perpendicular to the SBCA face reducing one of two main broadening mechanisms, Johann error [49]. If the spectropolarimetry measurements were performed with the optimally polarized asymmetric Rowland geometry and with micro-focused synchrotron radiation the other main broadening mechanism, source size error, could be eliminated resulting in a direct, high-fidelity measurement of polarized spectra.

An additional benefit of performing the direct polarized measurements at a synchrotron source is the increased flux which allows for resolving weaker spectral features such as quadrupole transitions, which depend on both the direction of propagation and the polarization axis, adding an extra layer of complexity. Because quadrupole transitions are much weaker than the dominant dipole transitions (see Supplemental Information B), their detection requires careful analysis of intensity variations with crystal orientation. Lower experimental broadening and increased flux would make it significantly easier to isolate and identify these subtle features.

6.5 Conclusion

We have shown that the anisotropy observed in the polarized CtC and VtC-XES emission spectra reflects the local asymmetry around the $3d$ transition metal in single crystal systems. The polarized emission along a specific crystallographic direction is obtained directly via partially polarized measurements using single crystal spectropolarimetry and indirectly with a new technique to

extract polarized spectra from unpolarized emission. The polarized emission provided information about the symmetry of the local electronic structure, allowing us to determine the anisotropic distribution of the occupied magnetic orbitals. By combining these results with a polarized absorption study, such as an XLD analysis of the Cu and Ni K-edges, our findings could be further corroborated by looking for a polarization dependent pre-edge feature. In this way, combining both absorption and emission techniques would provide a more complete understanding of the orbital anisotropy and would help disentangle the full anisotropic electronic structure of complex materials.

The CtC Kβ features showed clear polarization dependence for Cu in LiVCuO$_4$, which can be attributed to the spin-1/2 nature of Cu^{2+}. This allows for Coulomb coupling between the 3p and 3d orbitals. The emission weight shifts toward the Kβ' feature when the polarization is in the ligand plane and toward the K$\beta_{1,3}$ feature when it is perpendicular to the plane. In contrast, DyNiC$_2$ contains Ni^{2+} in a spin-0 configuration, and its CtC spectrum showed little to no polarization dependence. This contrasting behavior is consistent with predictions from a simple toy model.

In the VtC region, both systems exhibited strong polarization effects. The Kβ'' and K$\beta_{2,5}$ features became more intense when the polarization aligned with metal-ligand bond directions, consistent with expectations based on orbital occupation. Additionally, the Kβ'' peak entirely disappeared for out of-plane polarizations, further emphasizing the directional nature of the metal-ligand bonding. These trends were qualitatively reproduced by FEFF calculations, reinforcing the interpretation that VtC XES is sensitive to directional bonding and orbital interactions [55].

Overall, these results establish polarization-resolved XES as a tool for probing anisotropic electronic environments in transition metal systems. This technique provides access to subtle variations in the character of the occupied orbitals, which could be leveraged in future studies to

resolve weak quadrupole transitions and characterize ligand field asymmetry. Just as conventional XES complements conventional XAS by probing the occupied density of states, polarized XES serves as a natural complement to polarized XAS, offering a more complete picture of directionally resolved electronic structure.

Acknowledgments

6.6   Appendix

6.6.1   Directional and Polarization Dependence of Emitted Radiation

The radiation pattern of any dipole or quadrupole transition element between two hydrogenic orbitals can be calculated by directly integrating the matrix elements from Eq 2 (dipole) and Eq 6 (quadrupole) for an arbitrary $\vec{k}$. The propagation vector $\vec{k}$ and polarization vector $\vec{\epsilon}$ are given in

Eq 7, where δ is the angle $\vec{\epsilon}$ makes in the plane perpendicular to $\vec{k}$ which will be integrated out. This follows the same convention established in [38].

$$\sigma^{\text{quad}} \propto \sum_f \left| \left\langle f \left| (\hat{\epsilon} \cdot \vec{r})(\vec{k} \cdot \vec{r}) \right| i \right\rangle \right|^2 \delta(E_f - E_i + \hbar\omega)$$

(6)

$$\vec{k}(\theta, \phi) = \begin{bmatrix} \sin\theta\cos\phi \\ \sin\theta\sin\phi \\ \cos\theta \end{bmatrix}$$

(7a)

$$\vec{\epsilon}(\theta, \phi, \delta) = \begin{bmatrix} \cos\theta\cos\phi\cos\delta - \sin\phi\sin\delta \\ \cos\theta\sin\phi\cos\delta - \cos\omega\sin\delta \\ -\sin\theta\cos\delta \end{bmatrix}$$

(7b)

For example, the angular component of a dipole transition from a p_z orbital to a s orbital is written out in Eq 8, where θ, ϕ, and δ are as defined in equation 7, and ρ and ω are dummy variables used for evaluating the matrix element. The matrix element ends up simply as $\langle s| \vec{\epsilon} \cdot \vec{r} | p_z \rangle \propto \sin\theta$, and the radiation pattern is given by $(\sin\theta)^2$, as is shown in Fig. 12 (a). We also show examples for the $p_x \rightarrow s$, $d_{z2} \rightarrow s$, and $d_{xy} \rightarrow s$. The surface of the radiation pattern gives a qualitative measure of how much radiation is emitted in a particular direction from a given dipole transition element.

Given the generalized definitions of $\vec{k}$ and $\vec{\epsilon}$, it's possible to invert them and derive the 'polarization' pattern for a fixed polarization direction and a propagation vector integrated over a plane (δ), which of course produces the exact same patterns but with a different interpretation.

$$\langle s| \vec{\epsilon} \cdot \vec{r} |p_z\rangle = \left[\int_0^{2\pi} \int_0^{2\pi} \int_0^{\pi} \right.$$

$$\left((\cos\theta\cos\phi\cos\delta - \sin\phi\sin\delta)\sin\rho\cos\omega \right)$$

$$\left((\cos\theta\sin\phi\cos\delta - \cos\omega\sin\delta)\sin\rho\sin\omega \right)$$

$$\left((-\sin\theta\cos\delta)\cos\rho \right)(\sin\rho\cos\rho)\, d\rho\, d\omega\, d\delta \Bigg]$$

$$\propto \sin\theta \tag{8}$$

6.6.2 Additional FEFF calculations

X-ray emission is often interpreted as a reflection of the occupied density of states [18, 19, 61] in the presence of a core hole. We see this represented in figures 13 and 14 which show how the polarized VtC-XES in subplot (a) matches up almost exactly with the p-projected DOS in subplot (c). We also note that the quadrupole contribution shown in subplot (b) is relatively weak, with it making up only 10% and 3% of the total spectral intensity for $LiVCuO_4$ and $DyNiC_2$ respectively. This supports the approximation made when extracting the polarizations from the directional spectra. The main contribution to the quadrupole transition is the *d*-projected DOS which is much larger (in units of electron/eV) than the p-DOS. The overall weak contribution to the total spectra is due to the additional $\vec{k}$ term in the quadrupole matrix element and the small overlap between the metal $3d$ orbital and $1s$ orbital.
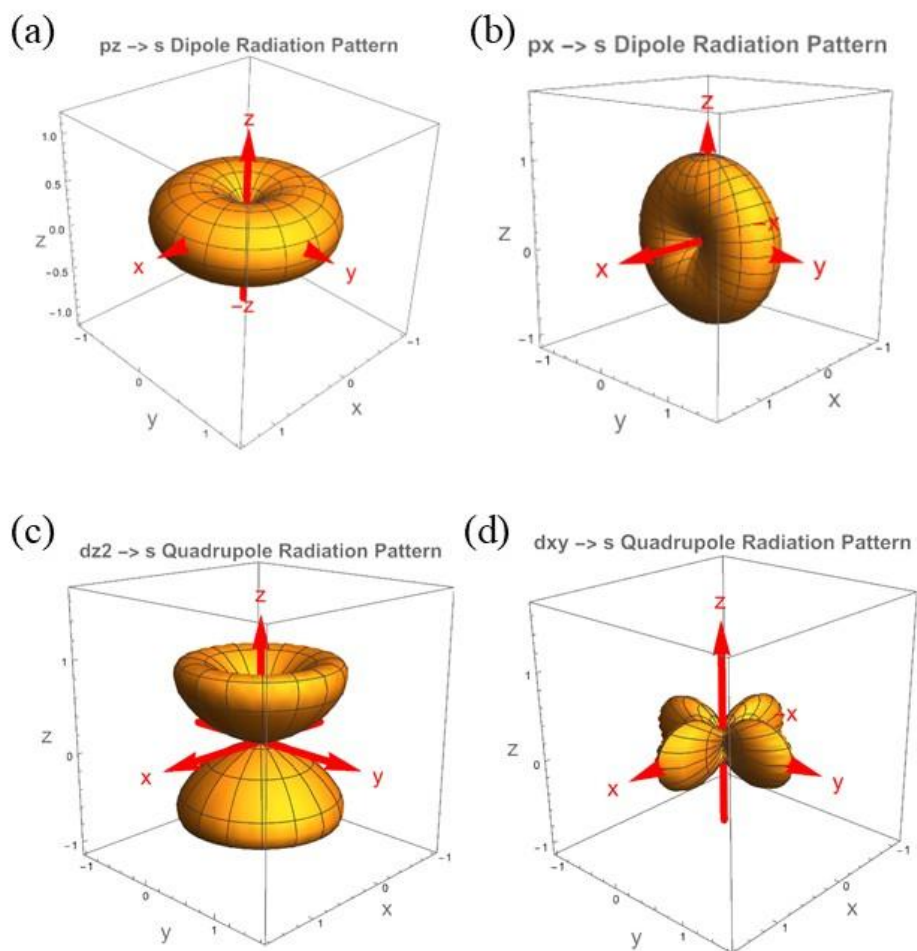
Figure 12: Radiation pattern of dipole and quadrupole transitions between different l, m orbitals. (a) and (b) show dipole transitions from the p_z and p_x to s orbitals respectively while (c) and (d) show quadrupole transition from the d_{z2} and d_{xy} to s orbitals. The shape of the radiation patterns are equivalent to oscillating charges with spatial distributions that are consistent with the lobes of positive and negative phases from each atomic orbital.
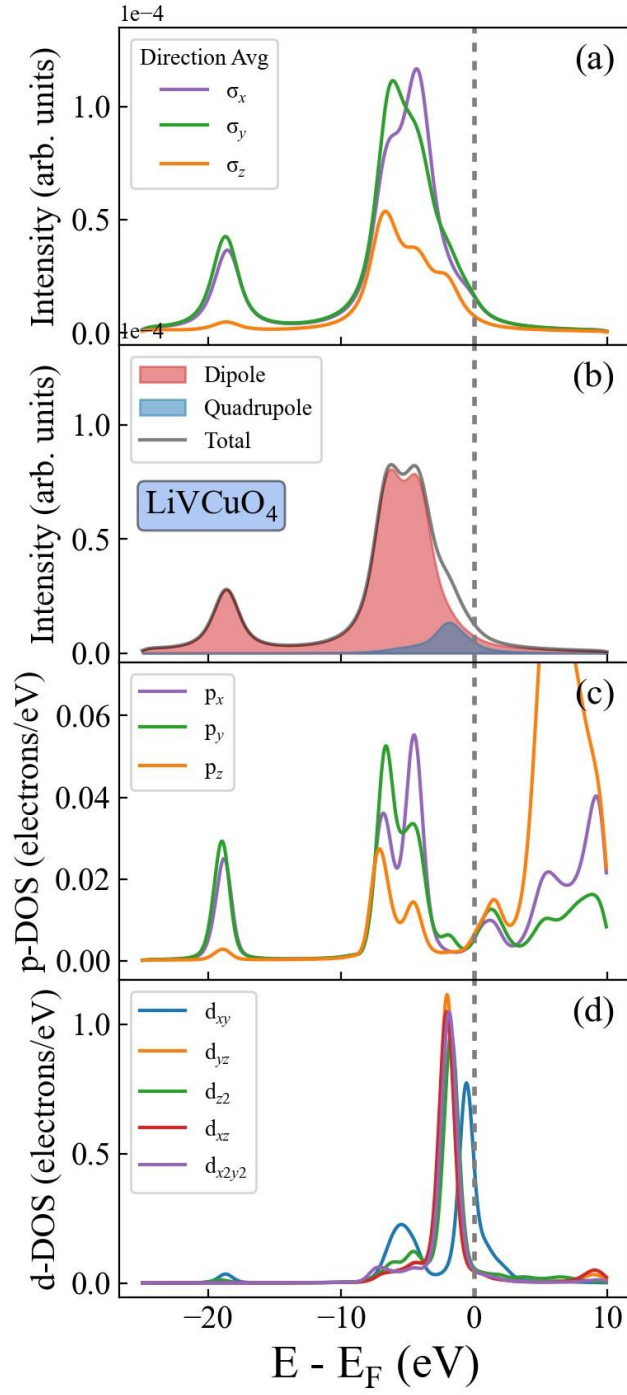
Figure 13: FEFF calculated Cu VtC spectra and DOS from LiVCuO$_4$. (a) Polarized x-ray emission with the quadrupole component averaged over directions perpendicular to the polarization axes.

(b) Isotropic emission separated into dipole (red) and quadrupole (blue) components. (c) The p-projected density of states. (d) The d-projected density of states.
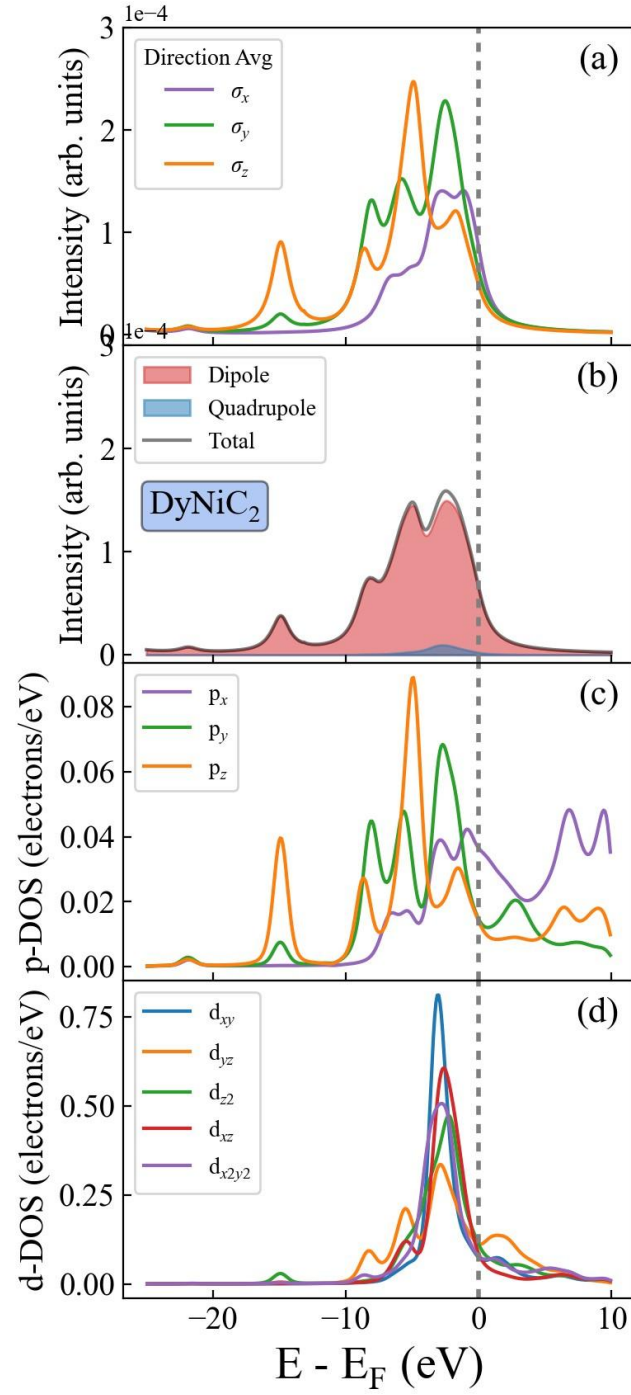
Figure 14: FEFF calculated Ni VtC spectra and DOS from $DyNiC_2$. (a) Polarized x-ray emission with the quadrupole component averaged over directions perpendicular to the polarization axes. (b) Isotropic emission separated into dipole (red) and quadrupole (blue) components. (c) The p-projected density of states. (d) The d-projected density of states.

6.7   Citations

1. H. A. Evans, L. Mao, R. Seshadri, and A. K. Cheetham. Layered double perovskites. *Annual Review of Materials Research*, 51:351–380, 2021.
2. Faran Zhou, Kyle Hwangbo, Qi Zhang, Chong Wang, Lingnan Shen, Jiawei Zhang, Qianni Jiang, Alfred Zong, Yifan Su, Marc Zajac, Youngjun Ahn, Donald A. Walko, Richard D. Schaller, Jiun-Haw Chu, Nuh Gedik, Xiaodong Xu, Di Xiao, and Haidan Wen. Dynamical criticality of spin-shear coupling in van der Waals antiferromagnets. *Nature Communications*, 13(1), 11 2022.
3. J. Schlappa, K. Wohlfeld, K. J. Zhou, M. Mourigal, M. W. Haverkort, V. N. Strocov, C. Monney, T. Hunt, J. Stahler, H. M. Ronnow, et al. Spin–orbital separation in the quasi-one-dimensional¨ mott insulator sr_2cuo_3. *Nature*, 485(7396):82–85, 2012.
4. S.H. Southworth, D.W. Lindle, R. Mayer, and P.L. Cowan. Anisotropy of polarized x-ray emission from molecules. *Physical Review Letters*, 67(1):1098–1101, 1991.
5. J. Stohr. X-ray magnetic circular dichroism spectroscopy of transition metal thin films.¨ *Journal of Electron Spectroscopy and Related Phenomena*, 75:253–272, 1995.
6. Gerrit Van Der Laan and Adriana I. Figueroa. X-ray magnetic circular dichroism—A versatile tool to study magnetism. *Coordination Chemistry Reviews*, 277-278:95–129, 2014.
7. E. Heppell, F. Maccherozzi, L. S. I. Veiga, S. Langridge, G. Van Der Laan, T. Hesjedal, and D. Backes. Handle on the antiferromagnetic spin structure of NiO using a ferromagnetic adlayer. *Physical Review Materials*, 9(1):4408, 2025.
8. Jonathan A. Sobota, Yu He, and Zhi-Xun Shen. Angle-resolved photoemission studies of quantum materials. *Reviews of Modern Physics*, 93(2):5006, 2021.
9. Elliott Rosenberg, Jonathan M. DeStefano, Yucheng Guo, Ji Seop Oh, Makoto Hashimoto, Donghui Lu, Robert J. Birgeneau, Yongbin Lee, Liqin Ke, Ming Yi, and Jiun-Haw Chu. Uniaxial ferromagnetism in the kagome metal TbV6Sn6. *Physical Review B*, 106(11):5139, 2022.
10. Derek Bergner, Tai Kong, Ping Ai, Daniel Eilbott, Claudia Fatuzzo, Samuel Ciocys, Nicholas Dale, Conrad Stansbury, Drew W. Latzke, Everardo Molina, Ryan Reno, Robert J. Cava, Alessandra Lanzara, and Claudia Ojeda-Aristizabal. Polarization dependent photoemission as a probe of the magnetic ground state in the van der Waals ferromagnet VI3. *Applied Physics Letters*, 121(18):3104, 2022.
11. M. C. Falub, M. Shi, P. R. Willmott, J. Krempasky, S. G. Chiuzbaian, K. Hricovini, and L. Patthey. Polarization-dependent angle-resolved photoemission spectroscopy study of La1xSrxMnO3. *Physical Review B*, 72(5):4444, 2005.
12. T Hajiri, R Niwa, T Ito, M Matsunami, B H Min, S Kimura, and Y S Kwon. Polarization dependent three-dimensional angle-resolved photoemission study on LiFeAs. *Journal of Physics Conference Series*, 391:012125, 2012.

13. Luuk J. P. Ament, Michel Van Veenendaal, Thomas P. Devereaux, John P. Hill, and Jeroen Van Den Brink. Resonant inelastic x-ray scattering studies of elementary excitations. *Reviews of Modern Physics*, 83(2):705–767, 2011.

14. C. Ulrich, L. J. P. Ament, G. Ghiringhelli, L. Braicovich, M. Moretti Sala, N. Pezzotta, T. Schmitt, G. Khaliullin, J. Van Den Brink, H. Roth, T. Lorenz, and B. Keimer. Momentum dependence of orbital excitations in Mott-Insulating titanates. *Physical Review Letters*, 103(10):7205, 2009.

15. Yoshihisa Harada, Kozo Okada, Ritsuko Eguchi, Akio Kotani, Hidenori Takagi, Tomoyuki Takeuchi, and Shik Shin. Unique identification of Zhang-Rice singlet excitation in Sr2CuO2Cl. *Physical Review B, Condensed matter*, 66(16):5104, 2002.

16. M Moretti Sala, V Bisogni, C Aruta, G Balestrino, H Berger, N B Brookes, G M De Luca, D Di Castro, M Grioni, M Guarise, P G Medaglia, F Miletto Granozio, M Minola, P Perna, M Radovic, M Salluzzo, T Schmitt, K J Zhou, L Braicovich, and G Ghiringhelli. Energy and symmetry of dd excitations in undoped layered cuprates measured by Cu L3 resonant inelastic x-ray scattering. *New Journal of Physics*, 13(4):043026, 2011.

17. Michel Van Veenendaal. Polarization dependence ofL- andM-Edge resonant inelastic X-Ray scattering in Transition-Metal compounds. *Physical Review Letters*, 96(11):7404, 2006.

18. Pieter Glatzel and Uwe Bergmann. High resolution 1s core hole X-ray spectroscopy in 3d transition metal complexes—electronic and structural information. *Coordination Chemistry Reviews*, 249(1-2):65–95, 2004.

19. Sara Lafuerza, Andrea Carlantuono, Marius Retegan, and Pieter Glatzel. Chemical Sensitivity of Kβ and Kα X-ray Emission from a Systematic Investigation of Iron Compounds. *Inorganic Chemistry*, 59(17):12518–12535, 2020.

20. Joanna Kowalska and Serena DeBeer. The role of x-ray spectroscopy in understanding the geometric and electronic structure of nitrogenase. *Biochimica et Biophysica Acta (BBA) - Molecular Cell Research*, 1853(6):1406–1415, 2015.

21. Abiram Krishnan, Dong-Chan Lee, Ian Slagle, Sumaiyatul Ahsan, Samantha Mitra, Ethan Read, and Faisal M. Alamgir. Monitoring redox processes in lithium-ion batteries by laboratory-scale operando x-ray emission spectroscopy. *ACS Applied Materials & Interfaces*, 16(13):16096– 16105, 2024.

22. Filippo Giordanino, Elisa Borfecchia, Kirill A. Lomachenko, Andrea Lazzarini, Giovanni Agostini, Erik Gallo, Alexander V. Soldatov, Pablo Beato, Silvia Bordiga, and Carlo Lamberti. Interaction of nh3 with cu-ssz-13 catalyst: A complementary ftir, xanes, and xes study. *The Journal of Physical Chemistry Letters*, 5(9):1552–1559, 2014.

23. G. Drager and O. Brummer. Polarized X-Ray emission spectra of single crystals.¨ *physica status solidi (b)*, 124(1):11–28, 1984.

24. W. Czolbe, U. Dick, G. Drager, and K. Fischer.¨ The electronic structure of single crystal YBa2Cu3O7–δ studied by polarized Cu Kβ2,5 X-ray emission. *physica status solidi (b)*, 174(1):91–98, 1992.

25. U. Bergmann, J. Bendix, P. Glatzel, H. B. Gray, and S. P. Cramer. Anisotropic valence→core x-ray fluorescence from a [Rh(en)3][Mn(N)(CN)5]·H2O single crystal: Experimental results and density functional calculations. *The Journal of Chemical Physics*, 116(5):2011–2015, 2002.

26. Satoshi Nishimoto, Stefan-Ludwig Drechsler, Roman Kuzian, Johannes Richter, Ji˘ri Malek,´ Miriam Schmitt, Jeroen Van Den Brink, and Helge Rosner. The strength of frustration and quantum fluctuations in LiVCuO4. *EPL (Europhysics Letters)*, 98(3):37007, 5 2012.

27. Hsiao-Yu Huang, Nikolay A. Bogdanov, Liudmila Siurakshina, Peter Fulde, Jeroen Van Den Brink, and Liviu Hozoi. Ab initio calculation of d-d excitations in quasi-one-dimensional Cu d9 correlated materials. *Physical Review B*, 84(23), 12 2011.

28. Marta Roman, Maria Fritthum, Berthold Stoger, Devashibhai T. Adroja, and Herwig Michor.¨ Charge density wave and crystalline electric field effects inTmNiC2. *Physical Review B*, 107(12), 3 2023.

29. Hiroyuki Maeda, Ryusuke Kondo, and Yoshio Nogami. Multiple charge density waves compete in ternary rare-earth nickel carbides, RNiC2(R:Y,Dy. *Physical Review B.*, 100(10), 9 2019.

30. Jae Nyeong Kim, Changhoon Lee, and Ji-Hoon Shim. Chemical and hydrostatic pressure effect on charge density waves of SmNiC2. *New Journal of Physics*, 15(12):123018, 12 2013.

31. G. Drager and O. Brummer.¨ X-ray spectroscopic investigation of beryllium by polarized K emission valence bands. *physica status solidi (b)*, 78(2):729–735, 1976.

32. P. D. C. King, S. McKeown Walker, A. Tamai, A. De La Torre, T. Eknapakul, P. Buaphet, S.-k. Mo, W. Meevasana, M. S. Bahramy, and F. Baumberger. Quasiparticle dynamics and spin–orbital texture of the SrTiO3 two-dimensional electron gas. *Nature Communications*, 5(1), 2 2014.

33. Yang Wang and Maciej Dendzik. Recent progress in angle-resolved photoemission spectroscopy. *Measurement Science and Technology*, 35(4):042002, 12 2023.

34. D. J. Huang, W. B. Wu, G. Y. Guo, H. J. Lin, T. Y. Hou, C. F. Chang, C. T. Chen, A. Fujimori, T. Kimura, H. B. Huang, A. Tanaka, and T. Jo. Orbital ordering in La0.5 Sr1.5 Mn O4 studied by soft X-ray Linear Dichroism. *Physical Review Letters*, 92(8), 2 2004.

35. W.B. Wu, D.J. Huang, G.Y. Guo, H.-j. Lin, T.Y. Hou, C.F. Chang, C.T. Chen, A. Fujimori, T. Kimura, H.B. Huang, A. Tanaka, and T. Jo. Orbital polarization of LaSrMnO4 studied by soft X-ray linear dichroism. *Journal of Electron Spectroscopy and Related Phenomena*, 137140:641–645, 4 2004.

36. U Bergmann, CR Horne, TJ Collins, JM Workman, and SP Cramer. Chemical dependence of interatomic x-ray transition energies and intensities–a study of mn kβ and kβ2, 5 spectra. *Chemical physics letters*, 302(1-2):119–124, 1999.

37. Frank De Groot and Akio Kotani. *Core Level Spectroscopy of Solids*. CRC Press, 1st edition, 2008.

38. R. Laihia, K. Kokko, W. Hergert, and J. A. Leiro. K-emission spectra of Zn, ZnS, and ZnSe within dipole and quadrupole approximations. *Physical Review B, Condensed matter*, 58(3):1272–1278, 1998.

39. H. Ogasawara, K. Fukui, and M. Matsubara. Polarization dependence of X-ray emission spectroscopy. *Journal of Electron Spectroscopy and Related Phenomena*, 136(1-2):161–166, 2004.

40. J. J. Sakurai and Jim Napolitano. *Modern Quantum Mechanics*. Cambridge University Press, 3rd edition, 2020.

41. David J. Griffiths. *Introduction to Electrodynamics*. Cambridge University Press, 4th edition, 2017.

42. John Clarke Slater. *Quantum Theory of Atomic Structure*. McGraw-Hill, 1st edition, 1960.

43. M. W. Haverkort, M. Zwierzycki, and O. K. Andersen. Multiplet ligand-field theory using Wannier orbitals. *Physical Review B*, 85(16):5113, 2012.

44. Y. Sajeev, M. Sindelka, and N. Moiseyev. Hund's multiplicity rule: From atoms to quantum dots. *The Journal of Chemical Physics*, 128(6):1101, 2008.

45. Hiroshi Watanabe. *Operator methods in ligand field theory*. Prentice-Hall, 1st edition, 1966.

46. W. Jeitschko and M.H. Gerss. Ternary carbides of the rare earth and iron group metals with CeCoC2- and CeNiC2-type structure. *Journal of the Less Common Metals*, 116(1):147–157, 2 1986.

47. Gianfranco Pacchioni and Piercarlo Fantucci. Spin states and quenching of magnetism in naked and carbonylated nickel clusters. *Chemical Physics Letters*, 134(5):407–412, 1987.

48. Evan P. Jahrman, William M. Holden, Alexander S. Ditter, Devon R. Mortensen, Gerald T. Seidler, Timothy T. Fister, Stosh A. Kozimor, Louis F. J. Piper, Jatinkumar Rana, Neil C. Hyatt, and Martin C. Stennett. An improved laboratory-based x-ray absorption fine structure and xray emission spectrometer for analytical applications in materials chemistry research. *Review of Scientific Instruments*, 90(2):024106, 2019.

49. Yeu Chen, Anthony J. Gironda, Yaxin Shen, Andre D. Taylor, and Gerald T. Seidler.´ A ray tracing survey of asymmetric operation of the x-ray rowland circle using spherically bent crystal analyzers. *J. Anal. At. Spectrom.*, 40:836–847, 2025.

50. Uwe Bergmann and Stephen P. Cramer. High-resolution large-acceptance analyzer for x-ray fluorescence and Raman spectroscopy. In Albert T. Macrander, Andreas K. Freund, Tetsuya Ishikawa, and Dennis M. Mills, editors, *Crystal and Multilayer Optics*, volume 3448, pages 198 – 209. International Society for Optics and Photonics, SPIE, 1998.

51. Mauro Rovezzi, Christophe Lapras, Alain Manceau, Pieter Glatzel, and Roberto Verbeni. High energy-resolution x-ray spectroscopy at ultra-high dilution with spherically bent crystal analyzers of 0.5 m radius. *Review of Scientific Instruments*, 88(1):013108, 01 2017.

52. Eugene Hecht. *Optics*. Pearson, 5th edition, 2016.

53. Christoph P. Grams, Severin Kopatz, Daniel Bruning, Sebastian Biesenkamp, Petra Becker,¨ Ladislav Bohaty, Thomas Lorenz, and Joachim Hemberger. Evidence for polarized nanoregions´ from the domain dynamics in multiferroic LiCuVO4. *Scientific Reports*, 9(1), 3 2019.

54. J. J. Kas, F. D. Vila, C. D. Pemmaraju, T. S. Tan, and J. J. Rehr. Advanced calculations of X-ray spectroscopies with FEFF10 and Corvus. *Journal of Synchrotron Radiation*, 28(6):1801–1810, 2021.

55. Evan P. Jahrman, William M. Holden, Niranjan Govind, Joshua J. Kas, Jatinkumar Rana, Louis F. J. Piper, Carrie Siu, M. Stanley Whittingham, Timothy T. Fister, and Gerald T. Seidler. Valence-to-core X-ray emission spectroscopy of vanadium oxide and lithiated vanadyl phosphate materials. *Journal of Materials Chemistry A*, 8(32):16332–16344, 2020.

56. D. R. Mortensen, G. T. Seidler, Joshua J. Kas, Niranjan Govind, Craig P. Schwartz, Sri Pemmaraju, and David G. Prendergast. Benchmark results and theoretical treatments for valenceto-core x-ray emission spectroscopy in transition metal compounds. *Physical Review B*, 96(12):125136, 2017.

57. Jared E. Abramson, Nancy M. Avalos, Agathe L. M. Bourchy, Sarah A. Saslow, and Gerald T. Seidler. An exploration of benchtop X-ray emission spectroscopy for precise characterization of the sulfur redox state in cementitious materials. *X-Ray Spectrometry*, 51(2):151–162, 2021.

58. Diwash Dhakal, Darren M. Driscoll, Niranjan Govind, Andrew G. Stack, Nikhil Rampal, Gregory Schenter, Christopher J. Mundy, Timothy T. Fister, John L. Fulton, Mahalingam Balasubramanian, and Gerald T. Seidler. The evolution of solvation symmetry and composition in Zn halide aqueous solutions from dilute to extreme concentrations. *Physical Chemistry Chemical Physics*, 25(34):22650–22661, 2023.

59. Luis Miaja-Avila, Galen C. O'Neil, Young Il Joe, Kelsey M. Morgan, Joseph W. Fowler, William B. Doriese, Brianna Ganly, Deyu Lu, Bruce Ravel, Daniel S. Swetz, and Joel N. Ullom. Valence-to-core X-ray emission spectroscopy of titanium compounds using energy dispersive detectors. *X-Ray Spectrometry*, 50(1):9–20, 2020.

60. Anthony J. Gironda, Jared E. Abramson, Yeu Chen, Mikhail Solovyev, George E. Sterbinsky, and Gerald T. Seidler. Asymmetric Rowland circle geometries for spherically bent crystal analyzers in laboratory and synchrotron applications. *Journal of Analytical Atomic Spectrometry*, 39(5):1375– 1387, 2024.

61. Samantha Tetef, Niranjan Govind, and Gerald T. Seidler. Unsupervised machine learning for unbiased chemical classification in X-ray absorption spectroscopy and X-ray emission spectroscopy. *Physical Chemistry Chemical Physics*, 23(41):23586–23601, 2021.

Chapter 7 Conclusion

7.1   Summary of Results

Starting with a precursor DFT calculation, the traditional theoretical technique of MLFT has been improved to become a much strong predictive tool. This brings MLFT closer to state-of-the-art quantum chemistry techniques while maintaining the intuition and simplicity of a model Hamiltonian approach. Here this improved DFT+MLFT technique has been applied to x-ray emission for the first time and has been demonstrated to perform well across multiple highly correlated $3d$ transition metal systems. Specifically, the theory was validated by assessing how it treated charge transfer effects in the presence of a core-hole, and it was demonstrated that the model was consistent with the expected experimental behavior across oxidations states.

These results led directly to a second project which addressed a previously undiscovered resonant shake effect in the Kα XES of $3d^0$ materials. Here I proposed a model that allowed for mixing between core-holes in the two $2p$ spin-orbit split levels when the energy splitting between them matched a valence level bonding to antibonding transition. This model was later validated by using it to predict a second shake excitation on the tail of the Kα_2 peak, which was experimentally confirmed. This was only possible due to the constrained phase space achieved through the DFT + MLFT approach, and is the first example that this author is aware of the MLFT technique being used for predictive studies instead of interpretive ones.

In parallel with these theoretical advancements in Kα XES, I also contributed to the development of a reliable experimental method for polarized X-ray emission spectroscopy. Specifically, I have used MLFT and real space Green's function theory to build a framework for disentangling complex polarization-dependent spectral features in CtC and VtC XES. This work

explores how the polarized XES can be directly linked to specific features in the occupied density of states, enabling deeper insight into orbital-level electronic structure and crystal field effects. While a robust experimental geometry was established to enable polarized measurements, the strength of this work lies in showing how polarization-resolved spectra can be predicted, understood, and used as a spatially sensitive probe of local geometric and chemical features.

7.2   Future Outlook

One particularly promising framework for continually improving the DFT + MLFT approach is the addition of dynamical mean field theory (DMFT) to the pipeline. This will help better capture many-body screening effects and is especially relevant for systems with strong hybridization, where the perturbed ionic model breaks down. A DFT + DMFT + MLFT approach would allow for a more faithful treatment of charge transfer behavior while retaining the interpretability of the ligand field basis. While DMFT does not address the question of the remaining free parameters (in fact it introduced a new double-counting correction parameter), it may also provide an avenue to include more nonlocal Coulombic interactions through an impurity model than includes retarded interactions or GW+DMFT, allowing screening from nearby metal sites.

From an experimental perspective, substantial gains can also be made in the spectropolarimetry measurement of polarized XES. The current low-Bragg-angle geometry suffers from limited resolution and incomplete polarization selectivity, limiting its ability to serve as a high-fidelity validation tool for theory. These limitations can be overcome by adopting an asymmetric Rowland geometry with a high Bragg angle near 45°, which would both maximize polarization contrast and reduce Johann broadening. Additionally, performing these

measurements at a micro-focused synchrotron beamline would reduce the source size

broadening, resulting in much sharper spectral features. Such an experimental setup would not

only allow for clearer validation of theoretical models but also make it possible to detect weak

transitions, such as quadrupole features.

Chapter 8 Appendix

8.1 Non-zero dipole matrix elements

Here I provide a series of tables that show which combinations of atomic orbitals have non-zero dipole matrix elements. Each element in a table is either 0, indicating that there is no non-zero dipole matrix elements, or x, y, or z, which indicates the specific dipole operator that connects those two orbitals. Ex: The x dipole operator connects the p_y and d_{xy} orbitals, meaning that $\langle p_y|x|d_{xy}\rangle \neq 0$.

Dipole Matrix Elements

Table 1: Non-zero dipole matrix elements for s and p orbitals

	p_y	p_z	p_x
s	y	z	x

Table 2: Non-zero dipole matrix elements for p and d orbitals

	d_{xy}	d_{yz}	d_{z^2}	d_{xz}	$d_{x^2y^2}$
p_y	x	z	y	0	y
p_z	0	y	z	x	0
p_x	y	0	x	z	x

Table 3: Non-zero dipole matrix elements for d and f orbitals

	$f_{y(3x^2-y^2)}$	f_{xyz}	f_{yz^2}	f_{z^3}	f_{xz^2}	$f_{z(x^2-y^2)}$	$f_{x(x^2-3y^2)}$
d_{xy}	x	z	x	0	y	0	y
d_{yz}	0	x	z	y	0	y	0
d_{z^2}	0	0	y	z	x	0	0
d_{xz}	0	y	0	x	z	x	0
$d_{x^2y^2}$	y	0	y	0	x	z	x

8.2   DFT + MLFT Script Pipeline

Preface

All of the scripts used in this automation pipeline are adapted from the ones provided by Maurits Haverkort at the bi-annual Heidelberg workshops, and can be found on the Quanty website (https://www.quanty.org/workshop/heidelberg/october_2022/programme). For users looking to learn more about the technical side of the DFT + MLFT pipeline, please consult the Quanty documentation and the accompanying manuscript [74]. All of the code discussed in this pipeline along with example templates is available on Github at

https://github.com/CharlesCardot/ElectronicStructureAutomation/tree/release/1.0.0. The two major FPLO and one major Quanty input files are included at the end of this appendix for reference.

Pipeline Details

Over the course of my PhD I have worked to automate the DFT + MLFT calculation pipeline through a combination of BASH and python scripts that make "smart" choices of certain parameters in the FPLO and Quanty input files. These choices are usually designed to get a "good enough" result for fast comparisons but are not meant to be truly converged (e.g. with respect to k-grid in FPLO) or publication ready. This pipeline is laid out in Figure B1. The script begins by looping over a directory of compounds (*materials*), each folder in *materials* is named using the compound formula (ex: NiO), and contains two files: (ex: *NiO.cif* and *NiO.inp*). The first is a crystallographic information file which can be acquired from most materials databases (ex: Materials Project [133], Crystallography Open Database [126]). The second is a series of

custom inputs that specify a few of the run parameters, which orbitals to include in the Wannier down-projection, and the number of ligand atoms in the local cluster around the central atom. The majority of the "automation" comes from setting up the DFT calculation for a given material and making sure that the Wannier orbitals provide a reasonable agreement with the real band structure and can be trusted to create the tight binding Hamiltonian.

The upper block in Figure B1 shows the major steps in the pipeline. Once a user has customized the *materials* directory to include every system they want to calculate, the *execute_all.sh* loops over every compound and generates a working directory for it, with copies of the FPLO and Quanty input files. The *.cif* and *.inp* are used by *write_0.py* to create the input for the first FPLO band structure calculation, *0_RunNAMEFPLO.Quanty*. While the file name has the *.Quanty* ending, this is only because Quanty uses Lua as a scripting language when creating a Quanty input file. This means that any *.Quanty* script can also be used for defining variables, functions, or i/o tasks as needed by the user. In this case, it is simply doing the job of generating the FPLO input from a list of variables, which specify details like the output directory (ex: DFT), real-space grid, k-grid, lattice constants, Wyckoff positions, and the exchange-correlation potential. Once the calculation has converged, a *check_simple_cs.py* script is called to make sure that only one Wyckoff position for the specified $3d$ TM is present and that the calculation has properly converged. Finally, *write_1.py* is used to edit *1_RunNAMEFPLO_WF.Quanty* which controls the Wannier component of the DFT calculation. The main output of this is a list of single-particle overlap energies between the transition metal $3d$ orbitals and the p orbitals of any neighboring ligands.
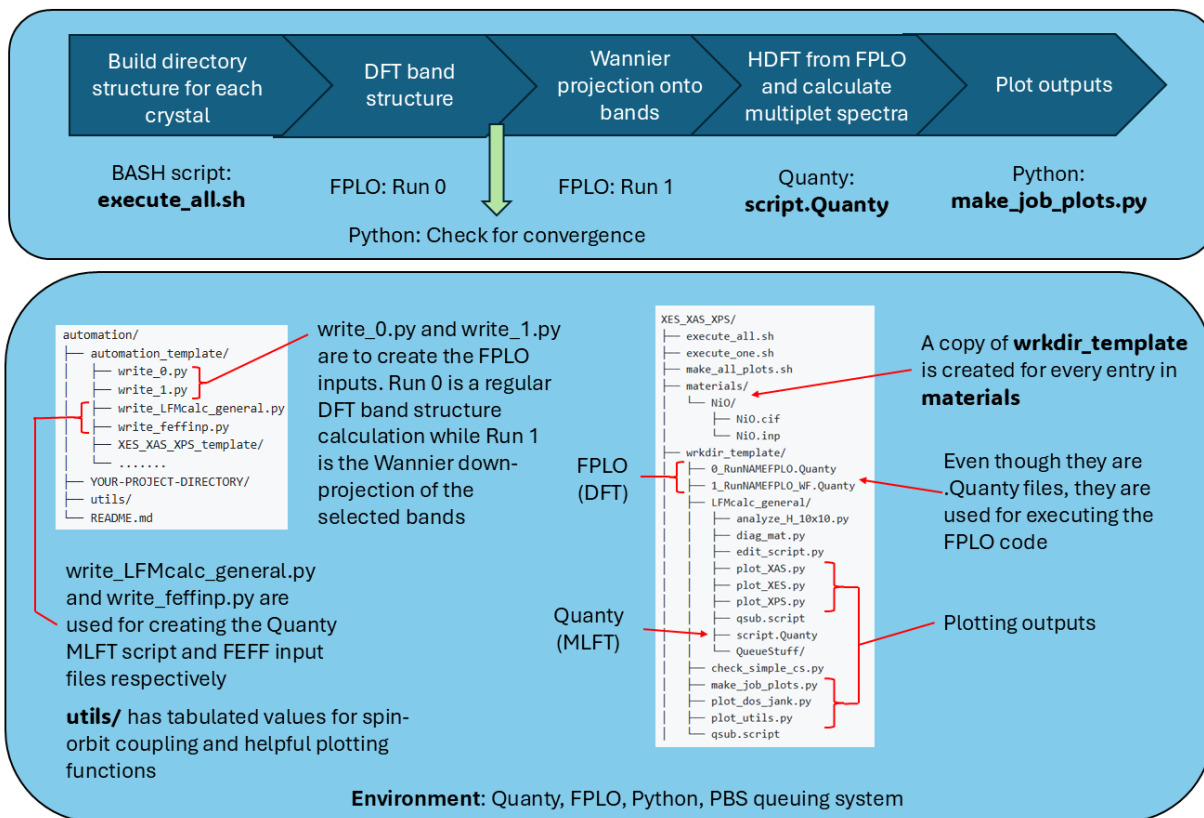
Figure B1: Diagram of the automation workflow for calculating the 2*p* XAS, XES, and XPS of an arbitrary 3*d* transition metal crystal structure. BASH scripts take care of directory setup, python scripts fill out input files using the .cif and .inp for each material, and FPLO and Quanty calculate the DFT and MLFT components of the pipeline respectively.

This list (along with some symmetry operations to condense the matrix) is used to create the tight binding Hamiltonian HDFT within *script.Quanty*. Examples and more detailed explanations of the functions within Quanty are laid out in section 5 of Ackermann *et al.* [74], but I will briefly describe what is happening in the *script.Quanty* file. The raw terminal output of the DFT calculation is piped into *out.wan*, which can be directly read into Quanty using *FileReadDresdenFPLO*. A tight-binding (TB) object is generated from this output, and a cluster of atoms is created by taking a radius around some [x, y, z] position. The single-particle energies

from the TB object are then mapped onto the atoms in the cluster to create *HDFTLarge*, which can be converted into a block band diagonal format and truncated to include only 2 blocks ("NTri", 2.)

The *Index* and *NFermi* variables are helpers to establish the fermionic size of the system. For a 3*d* TM coupled to a 10x10 ligand block, with holes in the 2*p* and 1*s* orbitals, this equates to an *NFermi* = 10 + 10 + 6 + 2 = 28. The *Index* is a hashmap that allows one to quickly access the indices corresponding to each orbital. The density matrix *rho_d* is calculated to perform a double counting correction later in the script. From lines 82-103 the various Slater-Condon operators are defined which will later be added to the Hamiltonian. Note that the operators are all 'rotated' using *YtoZtriple*, which just transforms the basis from spherical harmonics to cubic harmonics. This has the advantage of being more computationally efficient because the basis is no longer complex, and more intuitive for users when dealing with linear polarizations. The radial wavefunctions are read in from the DFT calculation in lines 123-129, which are immediately used to extract *F* and *G* Slater-Condon integrals from the radial wavefunctions. One example is on line 234 where the double-counting corrected *HDFT* is calculated and the 3*d*-3*d* block is written out for convenience and later analysis. From line 243-271 additional operators are defined, mostly for the purpose of analyzing the characteristics of wavefunctions by taking expectation values of these operators. The *ldots* operators on lines 249 and 250, however, are used to add spin-orbit interaction to the *HDFT* Hamiltonian.

The XES, XAS, and XPS transition operators are defined on lines 277-379. The XES and XAS operators are explicitly transitions of an electron between two orbitals, involving both a creation and annihilation operator. Because we are only dealing with a discrete basis of states, and we are not interested in the behavior of the photoelectron, the XPS transition operator can be

approximated by adding the spectra obtaining from annihilating each electron in the 2*p* shell. Now that all the operators and their coefficients have been defined, the full MLFT Hamiltonian for each state can be built (lines 385-439). The *OperatorSetTrace* function uses the charge-transfer equations from section 2.4 to shift the centroids of any orbitals which are partially occupied. The lowest energy *Npsi* eigenstates of the non-ionized Hamiltonian (*GS_Hamiltonian*) are determined on line 466, and there is some logic on lines 502-523 to make sure that *Npsi* is large enough so that all thermally accessible states are found. The same thing is done for the system in the presence of a 1*s* core-hole (*s_hole_Hamiltonian*).

The actual spectra are calculated by the *CreateSpectra* function which evaluates the matrix element from every ground eigenstate to every accessible final state from the *p_hole_Hamiltonian*. The thermal cutoff is enforced through Fermi-Dirac statistics (ex: line 594). The dipole transition operators for each cartesian polarization are used to generate the individual polarized spectra, which are later combined to make a single isotropic spectrum and broadened before being written out to a file. The general procedure is the same for XAS, XES, and XPS, but the starting Hamiltonian for XES already includes as 1*s* core-hole (as addressed in 4.4 A) so it requires a different loop over the "initial" wavefunctions. The main computational time comes from determining the ground states of the starting Hamiltonians and evaluating the individual matrix elements using the *CreateSpectra* function. As addressed in Ackermann *et al.* [74], the Lanczos method is used to determine the response function and find the lowest N eigenstates, which dramatically improves the computational cost of the calculation compared to exact diagonalization.

0_RunFPLONAME.Quanty

```
 1. -- This script runs FPLO to create an LDA calculation of NAME
 2.
 3. -- The name of the program and version
 4. FPLO  = "fplo14.00-49-x86_64"
 5. FEdit = "fedit14.00-49-x86_64"
 6.
 7. directoryname = "DFT"
 8.
 9. -- create the directory where the calculation should be stored
10. os.execute("if [ ! -d \""..directoryname.."\" ]; then mkdir "..directoryname.."; fi")
11.
12. -- we use the -p option of FPLO to run it in a scripting mode
13. -- here the script to setup the calculation
14. FEditMenuOptions = [[
15. # go to symmetry menu
16. @+@
17. # title
18. @c@NAME
19. # enter spacegroup select box - SPACEGROUP
20. @s@
21. @SPACEGROUP@
22. @x@
23. # structure type - crystal
24. @t@
25. @c@
26. @x@
27. # lenth units - angstroem
28. @u@
29. @a@
30. @x@
31. # lattice constants;
32. @l@ LATTICECONSTANTS
33. # set axis angles
34. @a@ AXISANGLES
35. # setup Wyckoff positions
36. @n@WYCHKOFF_NUMBER
37. # Now, give list of ALL !!! Wyckoff positions.
38. WYCHKOFF_POSITIONS
39. #
40. # NOW CALL UPDATE, NEVER FORGET THIS!!!
41. #
42. @+@
43. # leave symmetry menu
44. @x@
45. # back in main menu
46. # This was the symmetry setup, and now we follow our advise to create
47. # the default =.in input by using the REBUILD-action.
48. # (The space before the 'e' opens the alternative menu bar.)
49. @ e@
50. # now we have the default input, and are still in the main menu
51.
52. # Set the number of k-points
53. @k@ 10 10 10
```

```
 54. # Set the xc-potential version
 55. # first enter select box
 56. @v@
 57. # select via search
 58. !Perdew Wang 92!
 59. # leave select box, go back to main menu
 60. @x@
 61.
 62. # Set the relativistic mode:
 63. @r@
 64. # Select by search, please note that the parentheses indicating the hotkey
 65. # are not considered in search mode.
 66. # (Have a look at the select box interactively.)
 67. !scalar relativistic!
 68. # leave select box
 69. @x@
 70. # Set number of iterations
 71. @n@ 100
 72.
 73.
 74. # last action must be
 75. @q@
 76. ]]
 77.
 78. -- The first run to selfconsistency.
 79. -- Copy the string above to an input file
 80. file = io.open(directoryname.."/=.pipe", "w")
 81. file:write(FEditMenuOptions)
 82. file:close()
 83. -- run FEdit
 84. os.execute("cd "..directoryname.."; "..FEdit.." -p "..FPLO.." -pipe <=.pipe 2>+log 1>
out.fedit")
 85. -- run FPLO
 86.
 87.
 88. os.execute("cd "..directoryname.."; "..FPLO.." 2>>+log 1 | tee out.scflow")
 89.
 90. -- Next we increase the number of k-points and numerical accuracy
 91. FEditMenuOptionsMorekPoints = [[
 92. # Set the number of k-points
 93. K-POINTS
 94. # Set the accuracy of density
 95. @a@ 1.e-10
 96. # Set the accuracy of Etot
 97. @a@ 1.e-10
 98.
 99. # Set options:
100. @-@
101. # save the basis orbitals to disk
102. !PLOT_BASIS!+
103. #leave menu
104. @x@
105. # Set number of iterations
106. @n@ 100
107.
108.
```

```
109. # last action must be
110. @q@
111. ]]
112.
113. -- write the above string to a file
114. file = io.open(directoryname.."/=.pipekmesh", "w")
115. file:write(FEditMenuOptionsMorekPoints)
116. file:close()
117. -- run FEdit
118. os.execute("cd "..directoryname.."; ".."FEdit.." -p "..FPLO.." -pipe <=.pipekmesh 2>+log 1>
out.feditkmesh")
119. -- run FPLO
120. os.execute("cd "..directoryname.."; ".."FPLO.." 2>>+log 1 | tee out.scf")
121.
122. -- calculate bands
123. FEditMenuOptionsBand = [[
124. @ b@
125.   @b@+
126.   @w@+
127. @x@
128. @q@";
129. ]]
130.
131. -- copy the string to a file
132. file = io.open(directoryname.."/=.pipeband", "w")
133. file:write(FEditMenuOptionsBand)
134. file:close()
135. -- run FEDIT
136. os.execute("cd "..directoryname.."; ".."FEdit.." -p "..FPLO.." -pipe <=.pipeband 2>+log 1>
out.feditband")
137. -- run FPLO
138. os.execute("cd "..directoryname.."; ".."FPLO.." 2>>+log 1 | tee out.band")
139.
```

1_RunFPLONAME_WF.Quanty

```
1.  -- This script  downfold the solution of a DFT calculation for NAME to
2.  -- a basis of TM_ELEMENT-TM_VALENCE and LIGAND_ELEMENT-LIGAND_VALENCE orbitals, hopefully
3.
4.  -- The name of the program and version
5.  FPLO  = "fplo14.00-49-x86_64"
6.  FEdit = "fedit14.00-49-x86_64"
7.
8.  directoryname = "DFT"
9.
10.
11. -- define the =.wandef file to calculate the Wannier functions
12. WanDef=[[doit
13.
14. ---- real space grid for pictures of WFs ---------------------
15.
16. WF_grid_basis conv
17. WF_grid_directions
18. 2 0 0
```

205

```
19. 0 2 0
20. 0 0 2
21. WF_grid_subdivision  1 1 1
22.
23. -------------------------------------------------
24. ham_cutoff 18
25. -- the thresholds need to be 0, otherwise the result is symmetry braking
26. -- the z^2 orbital has different values for the same hopping from the x^2-y^2 orbital
27. -- cutting them by value leads to a different behaviour of the z^2 from the x^2-y^2 orbital
28. -- and by hybridization the pz will be different from the px/py or the dxy from the dxz/dyz
29. WF_ham_threshold 0
30. WF_coeff_threshold 0
31. WF_write_coeff_stats on
32. ham_write_t_stats on
33.
34. ----- ham export grid --------
35.
36. k_grid_basis prim
37. k_grid_directions
38. 1 0 0
39. 0 1 0
40. 0 0 1
41. k_grid_subdivision  1 1 1
42. k_grid_incl_periodic_points off
43.
44. ]]
45.
46. --Wandefs for the TM_ELEMENT atoms
47. for i=TM_START,TM_END do
48. WanDef = WanDef..[[
49. wandef
50. on
51.     name TM_ELEMENT_]]..i..[[_3dxy
52.     emin EMIN
53.     emax EMAX
54.     de 2.0
55.     contrib
56.        site ]]..i..[[
57.        difvec 0 0 0
58.        xaxis 1 0 0
59.        zaxis 0 0 1
60.        orb 3d-2
61.        fac    1
62. wandef
63. on
64.     name TM_ELEMENT_]]..i..[[_3dyz
65.     emin EMIN
66.     emax EMAX
67.     de 2.0
68.     contrib
69.        site ]]..i..[[
70.        difvec 0 0 0
71.        xaxis 1 0 0
72.        zaxis 0 0 1
73.        orb 3d-1
74.        fac    1
```

```
 75. wandef
 76. on
 77.    name TM_ELEMENT_]]..i..[[_3dz2
 78.    emin EMIN
 79.    emax EMAX
 80.    de 2.0
 81.    contrib
 82.       site ]]..i..[[
 83.       difvec 0 0 0
 84.       xaxis 1 0 0
 85.       zaxis 0 0 1
 86.       orb 3d+0
 87.       fac    1
 88. wandef
 89. on
 90.    name TM_ELEMENT_]]..i..[[_3dxz
 91.    emin EMIN
 92.    emax EMAX
 93.    de 2.0
 94.    contrib
 95.       site ]]..i..[[
 96.       difvec 0 0 0
 97.       xaxis 1 0 0
 98.       zaxis 0 0 1
 99.       orb 3d+1
100.       fac    1
101. wandef
102. on
103.    name TM_ELEMENT_]]..i..[[_3dx2-y2
104.    emin EMIN
105.    emax EMAX
106.    de 2.0
107.    contrib
108.       site ]]..i..[[
109.       difvec 0 0 0
110.       xaxis 1 0 0
111.       zaxis 0 0 1
112.       orb 3d+2
113.       fac    1
114. ]]
115. end
116.
117.
118. -- Wandefs for the LIGAND_ELEMENT Atoms
119. for i=LIGAND_START,LIGAND_END do
120. WanDef = WanDef..[[
121. wandef
122. on
123.    name LIGAND_ELEMENT_]]..i..[[_LIGAND_VALENCEy
124.    emin EMIN
125.    emax EMAX
126.    de 2.0
127.    contrib
128.       site ]]..i..[[
129.       difvec 0 0 0
130.       xaxis 1 0 0
```

```
131.       zaxis 0 0 1
132.       orb LIGAND_VALENCE-1
133.       fac     1
134. wandef
135. on
136.    name LIGAND_ELEMENT_]]..i..[[_LIGAND_VALENCEz
137.    emin EMIN
138.    emax EMAX
139.    de 2.0
140.    contrib
141.       site ]]..i..[[
142.       difvec 0 0 0
143.       xaxis 1 0 0
144.       zaxis 0 0 1
145.       orb LIGAND_VALENCE+0
146.       fac     1
147. wandef
148. on
149.    name LIGAND_ELEMENT_]]..i..[[_LIGAND_VALENCEx
150.    emin EMIN
151.    emax EMAX
152.    de 2.0
153.    contrib
154.       site ]]..i..[[
155.       difvec 0 0 0
156.       xaxis 1 0 0
157.       zaxis 0 0 1
158.       orb LIGAND_VALENCE+1
159.       fac     1
160. ]]
161. end
162.
163. -- write to file
164. file = io.open(directoryname.."/=.wandef", "w")
165. file:write(WanDef)
166. file:close()
167. -- run FPLO
168. os.execute("cd "..directoryname.."; "..FPLO.." 2>>+log 1 | tee out.wandef")
169. -- rerun FPLO, needed for Wannier functions.
170. os.execute("cd "..directoryname.."; "..FPLO.." 2>>+log 1 | tee out.wan")
171.
```

script.Quanty

```
1. -- Material:
2. -- Date:
3. -- Author: Charles Cardot
4.
5. -- read the output of FPLO
6. print("--Read FPLO output--\n")
7. FPLOOut = FileReadDresdenFPLO("DFT_PATH/out.wan")
8.
```

```lua
 9. function print_HDFT(O)
10.     local m = OperatorToMatrix(O)
11.     m = Matrix.ToUserdata(Chop(m,1e-3))
12.      local headers = {"dxy", "dxy", "dyz", "dyz", "dz^2", "dz^2", "dxz", "dxz", "dx2y2", "dx2y2"}
13.     local output = ""
14.     for i, str in ipairs(headers) do
15.         output = output .. str
16.         if i < #headers then
17.             output = output .. string.rep(" ", 9 - #str)
18.         end
19.     end
20.      print("      " .. output)
21.     print(Matrix.Sub(m, {1,20},{1,20}))
22. end
23.
24.
25. -- from the DFT output we can create a tight binding Hamiltonian
26. print("--Create the Tight Binding Hamiltonian--\n")
27. print("Create the tight binding Hamiltonian for the crystal\n")
28. TB = TightBindingDefFromDresdenFPLO(FPLOOut)
29.
30. -- Sorts cluster so that the TM atom comes first
31. ClusterTmp = FindAllAtomsInsideSphere(TB.Atoms,TB.Cell,{TM_FPLO_XYZ},TM_CLUSTER_RADIUS)
32. print("\n Temp Cluster")
33. print(ClusterTmp)
34. Cluster = {}
35.     for key, atom in pairs(ClusterTmp) do
36.         if atom[1] == "TM_ELEMENT" then
37.             Cluster[1] = Copy(atom)
38.             break
39.         end
40.     end
41.     for key, atom in pairs(ClusterTmp) do
42.         if atom[1] ~= "TM_ELEMENT" then
43.             Cluster[#Cluster + 1] = Copy(atom)
44.         end
45.     end
46.     ClusterTmp = nil
47. print("\n Cluster Sorted")
48. print(Cluster)
49.
50. HDFTLarge, ClusterTB = CreateClusterHamiltonian(TB, {"open", Cluster},  {{"AddSpin",true}})
51.
52. -- NTri = 2 grabs the 3d-3d block and first ligand-ligand block,
53. -- giving a total single particle basis of size 20
54. tri, T2 = BlockBandDiagonalize(OperatorToMatrix(HDFTLarge), 10, {{"NTri", 2}})
55.
56. HDFT = Rotate(HDFTLarge, T2)
57. print_HDFT(HDFT)
58. print(HDFT.NF)
59. ----------------------------------------------------------------------------------------
60. --Now we want to add the TM_ELEMENT 2p and 1s shell to the system
61. --New index object (first argument is a list of all orbitals, the second argument groups the
two Ni orbitals)
```

```
 62. Index, NFermi =
CreateAtomicIndicesDict({"TM_ELEMENT_3d","Ligand_d","TM_ELEMENT_2p","TM_ELEMENT_1s"},
{{"TM_ELEMENT",{"TM_ELEMENT_2p","TM_ELEMENT_3d","TM_ELEMENT_1s"}}})
 63. HDFT.NF = NFermi
 64. print(HDFT.NF)
 65. print("The indices of the system are now fixed:")
 66. print(Index)
 67. print("")
 68.
 69.
 70. -- Next we need to correct for the double counting (i.e. subtract the DFT Mean-field
approximation of the Coulomb interaction)
 71. print("--Subtract the DFT Mean-field Coulomb interaction between the d electrons from the
tight-binding Hamiltonian--\n")
 72. -- calculate DFT density Matrix in order to create double counting potential
 73. print("Calculate the DFT 1-particle density matrix\n")
 74. rhoNoSpin = Chop(CalculateRho(TB))
 75. -- reduce the matrix to keep only the d shell
 76. rhoNoSpin_d = Matrix.ToTable(Matrix.Sub(rhoNoSpin,5))
 77. -- add spin
 78. rho_d = Matrix.AddSpin(rhoNoSpin_d)
 79. print(rho_d)
 80.
 81. -- create the Coulomb operator on a basis of tesseral Harmonics
 82. print("Create the Coulomb operator for the d-shell\n")
 83. OppF0 =
Rotate(NewOperator("U",10,Index["TM_ELEMENT_3d_Up"],Index["TM_ELEMENT_3d_Dn"],{1,0,0}),YtoZMatrix({"
d"}))
 84. OppF2 =
Rotate(NewOperator("U",10,Index["TM_ELEMENT_3d_Up"],Index["TM_ELEMENT_3d_Dn"],{0,1,0}),YtoZMatrix({"
d"}))
 85. OppF4 =
Rotate(NewOperator("U",10,Index["TM_ELEMENT_3d_Up"],Index["TM_ELEMENT_3d_Dn"],{0,0,1}),YtoZMatrix({"
d"}))
 86.
 87. YtoZtriple = YtoZMatrix({"TM_ELEMENT_3d","Ligand_d","TM_ELEMENT_2p","TM_ELEMENT_1s"})
 88.
 89. print("Create the Coulomb operator for the s-shell\n")
 90. OppF0sd = Rotate(NewOperator("U", NFermi, Index["TM_ELEMENT_1s_Up"],Index["TM_ELEMENT_1s_Dn"],
Index["TM_ELEMENT_3d_Up"],Index["TM_ELEMENT_3d_Dn"], {1}, {0}),YtoZtriple)
 91. OppG2sd = Rotate(NewOperator("U", NFermi, Index["TM_ELEMENT_1s_Up"],Index["TM_ELEMENT_1s_Dn"],
Index["TM_ELEMENT_3d_Up"],Index["TM_ELEMENT_3d_Dn"], {0}, {1}),YtoZtriple)
 92.
 93. print("Create the Coulomb operator between the p- and d-shell\n")
 94. OppUpdF0 = Rotate(NewOperator("U", NFermi, Index["TM_ELEMENT_2p_Up"],Index["TM_ELEMENT_2p_Dn"],
Index["TM_ELEMENT_3d_Up"],Index["TM_ELEMENT_3d_Dn"], {1,0}, {0,0}),YtoZtriple)
 95. OppUpdF2 = Rotate(NewOperator("U", NFermi, Index["TM_ELEMENT_2p_Up"],Index["TM_ELEMENT_2p_Dn"],
Index["TM_ELEMENT_3d_Up"],Index["TM_ELEMENT_3d_Dn"], {0,1}, {0,0}),YtoZtriple)
 96. OppUpdG1 = Rotate(NewOperator("U", NFermi, Index["TM_ELEMENT_2p_Up"],Index["TM_ELEMENT_2p_Dn"],
Index["TM_ELEMENT_3d_Up"],Index["TM_ELEMENT_3d_Dn"], {0,0}, {1,0}),YtoZtriple)
 97. OppUpdG3 = Rotate(NewOperator("U", NFermi, Index["TM_ELEMENT_2p_Up"],Index["TM_ELEMENT_2p_Dn"],
Index["TM_ELEMENT_3d_Up"],Index["TM_ELEMENT_3d_Dn"], {0,0}, {0,1}),YtoZtriple)
 98.
 99. -- create the Hartree-Fock mean-field approximation that needs to be substracted from the DFT
results
```

```
100. print("Create the Coulomb operator for the d-shell using the mean-field approximation (needs
the DFT density)\n")
101. OppF0MFDFT = Chop(MeanFieldOperator(OppF0,rho_d,{{"AddDFTSelfInteraction",true}}))
102. OppF2MFDFT = Chop(MeanFieldOperator(OppF2,rho_d,{{"AddDFTSelfInteraction",true}}))
103. OppF4MFDFT = Chop(MeanFieldOperator(OppF4,rho_d,{{"AddDFTSelfInteraction",true}}))
104.
105. -- change the dimension of the Coulomb operator the work on a space that includes both the d
and the ligand orbitals
106. --The operators acting on the d- and p-shell furthermore need to be rotated
107. OppF0.NF = NFermi
108. OppF2.NF = NFermi
109. OppF4.NF = NFermi
110. OppF0MFDFT.NF = NFermi
111. OppF2MFDFT.NF = NFermi
112. OppF4MFDFT.NF = NFermi
113.
114.
115. -- set parameters
116. print("--Set the parameters--\n")
117. nd = NUMBER_OF_D
118. Delta = DDDD
119. Udd = UUUU
120. Upd = 1.2*Udd -- based on rule of thumb, see Table II from
https://journals.aps.org/prb/abstract/10.1103/PhysRevB.85.165113
121. Usd = 1.3*Udd
122. --The slater integrals are calculated using the radial functions generated by FPLO, which can
be read within Quanty:
123. correlatedRadialFunctionss = ReadFPLOBasisFunctions({"1s"},"DFT_PATH/+fcor.TM_NUMBER.1")
124. correlatedRadialFunctionsp = ReadFPLOBasisFunctions({"2p"},"DFT_PATH/+fcor.TM_NUMBER.1")
125. correlatedRadialFunctionsd = ReadFPLOBasisFunctions({"3d"},"DFT_PATH/+fval.TM_NUMBER.1")
126. --The radial functions are saved in two different files, but we need them in the same object:
127.
correlatedRadialFunctions={correlatedRadialFunctionss[1],correlatedRadialFunctionsp[1],correlatedRad
ialFunctionsd[1]}
128. --Now the slater integrals can be calculated
129. slaterIntegrals = GetSlaterIntegrals({"1s","2p","3d"},correlatedRadialFunctions)
130.
131. --The resulting object can then be evaluated at the position of interest:
132. scale = 1.0
133. F0ddtemp = slaterIntegrals["3d 3d 3d 3d"][0] * EnergyUnits.Ha.value*scale
134. F2dd = slaterIntegrals["3d 3d 3d 3d"][2] * EnergyUnits.Ha.value*scale
135. F4dd = slaterIntegrals["3d 3d 3d 3d"][4] * EnergyUnits.Ha.value*scale
136. F0dd    = Udd+(F2dd+F4dd)*2/63
137. F0pdtemp = slaterIntegrals["3d 2p 3d 2p"][0] * EnergyUnits.Ha.value*scale
138. F2pd    =  slaterIntegrals["3d 2p 3d 2p"][2] * EnergyUnits.Ha.value*scale
139. G1pd    =  slaterIntegrals["2p 3d 3d 2p"][1] * EnergyUnits.Ha.value*scale
140. G3pd    =  slaterIntegrals["2p 3d 3d 2p"][3] * EnergyUnits.Ha.value*scale
141. F0pd    = Upd + (1/15)*G1pd + (3/70)*G3pd
142. F0sdtemp = slaterIntegrals["3d 1s 3d 1s"][0] * EnergyUnits.Ha.value*scale
143. G2sd    =  slaterIntegrals["1s 3d 3d 1s"][2] * EnergyUnits.Ha.value*scale
144. F0sd    = Usd
145.
146. -- Magnetic Field
147. Bz = 0.1 * EnergyUnits.Tesla.value
148.
149. -- Exchange Field
```

```
150. mag_moment_dir = TM_MAG_DIR
151. H_mag = TM_H_MAG -- (eV)
152. Hx = H_mag * mag_moment_dir[1]
153. Hy = H_mag * mag_moment_dir[2]
154. Hz = H_mag * mag_moment_dir[3]
155.
156. -- Spin orbit
157. zeta_3d =  TM_ZETA_3D
158. zeta_2p =  TM_ZETA_2P
159.
160.
161. --------------------------------------------------------------------
162. -- Writing out run parameters
163. --------------------------------------------------------------------
164. print("Parameters:")
165. print("nd = "..nd)
166. print("Delta fit to exp = "..Delta.." eV")
167. print("Udd fit to exp= "..Udd.." eV")
168. print("Upd fit to exp = "..Upd.." eV")
169. print("Usd fit to exp = "..Usd.." eV")
170. print("Bz = "..Bz.." eV")
171. print("Hx = "..Hx.." eV")
172. print("Hy = "..Hy.." eV")
173. print("Hz = "..Hz.." eV")
174. print("zeta_3d = "..zeta_3d.." eV")
175. print("zeta_2p = "..zeta_2p.." eV")
176. print("")
177.
178. print("Slater integrals computed from DFT radial wavefunctions:")
179. print("F0sd ab initio = "..F0sdtemp.." eV")
180. print("F0dd ab initio = "..F0ddtemp.." eV")
181. print("F2dd = "..F2dd.." eV")
182. print("F4dd = "..F4dd.." eV")
183. print("F0pd ab initio = "..F0pdtemp.." eV")
184. print("F2pd = "..F2pd.." eV")
185. print("G1pd = "..G1pd.." eV")
186. print("G3pd = "..G3pd.." eV")
187. print("G2sd = "..G2sd.." eV")
188. print("")
189.
190. print("Monopole like Slater integrals (from U):")
191. print("F0dd fit to exp = "..F0dd.." eV")
192. print("F0pd fit to exp = "..F0pd.." eV")
193. print("F0sd fit to exp = "..F0sd.." eV")
194. print("")
195.
196. function table.val_to_str ( v )
197.   if "string" == type( v ) then
198.     v = string.gsub( v, "\n", "\\n" )
199.     if string.match( string.gsub(v,"[^'\"]",""), '^"+$' ) then
200.       return "'" .. v .. "'"
201.     end
202.     return '"' .. string.gsub(v,'"', '\\"' ) .. '"'
203.   else
204.     return "table" == type( v ) and table.tostring( v ) or
205.       tostring( v )
```

```lua
206.      end
207. end
208.
209. function table.key_to_str ( k )
210.    if "string" == type( k ) and string.match( k, "^[_%a][_%a%d]*$" ) then
211.       return k
212.    else
213.       return "[" .. table.val_to_str( k ) .. "]"
214.    end
215. end
216.
217. function table.tostring( tbl )
218.    local result, done = {}, {}
219.    for k, v in ipairs( tbl ) do
220.       table.insert( result, table.val_to_str( v ) )
221.       done[ k ] = true
222.    end
223.    for k, v in pairs( tbl ) do
224.       if not done[ k ] then
225.          table.insert( result,
226.             table.key_to_str( k ) .. "=" .. table.val_to_str( v ) )
227.       end
228.    end
229.    return "{" .. table.concat( result, "," ) .. "}"
230. end
231.
232.
233.
234. HDFT_temp = OperatorToMatrix(HDFT - F0dd * OppF0MFDFT - F2dd * OppF2MFDFT - F4dd * OppF4MFDFT)
235. HDFT_temp = Matrix.Sub(HDFT_temp, {1,10},{1,10})
236. file = io.open("H_10x10.dat", "w")
237. file:write(table.tostring(HDFT_temp))
238. file:close()
239. ----------------------------------------------------------------------
240.
241. print("--Define some additional operators--\n")
242.
243. OppSx    = Rotate(NewOperator("Sx",
NFermi,Index["TM_ELEMENT_3d_Up"],Index["TM_ELEMENT_3d_Dn"]),YtoZtriple)
244. OppSy    = Rotate(NewOperator("Sy",
NFermi,Index["TM_ELEMENT_3d_Up"],Index["TM_ELEMENT_3d_Dn"]),YtoZtriple)
245. OppSz    = Rotate(NewOperator("Sz",
NFermi,Index["TM_ELEMENT_3d_Up"],Index["TM_ELEMENT_3d_Dn"]),YtoZtriple)
246. OppLz    = Rotate(NewOperator("Lz",
NFermi,Index["TM_ELEMENT_3d_Up"],Index["TM_ELEMENT_3d_Dn"]),YtoZtriple)
247. OppJz    = Rotate(NewOperator("Jz",
NFermi,Index["TM_ELEMENT_3d_Up"],Index["TM_ELEMENT_3d_Dn"]),YtoZtriple)
248.
249. Oppldots_3d =
Rotate(NewOperator("ldots",NFermi,Index["TM_ELEMENT_3d_Up"],Index["TM_ELEMENT_3d_Dn"]),YtoZtriple)
250. Oppldots_2p =
Rotate(NewOperator("ldots",NFermi,Index["TM_ELEMENT_2p_Up"],Index["TM_ELEMENT_2p_Dn"]),YtoZtriple)
251.
252. OppSsqr  = Rotate(NewOperator("Ssqr",
NFermi,Index["TM_ELEMENT_3d_Up"],Index["TM_ELEMENT_3d_Dn"]),YtoZtriple)
```

```
253. OppLsqr   = Rotate(NewOperator("Lsqr",
NFermi,Index["TM_ELEMENT_3d_Up"],Index["TM_ELEMENT_3d_Dn"]),YtoZtriple)
254. OppJsqr   = Rotate(NewOperator("Jsqr",
NFermi,Index["TM_ELEMENT_3d_Up"],Index["TM_ELEMENT_3d_Dn"]),YtoZtriple)
255.
256. OppN_TM_ELEMENT      = NewOperator("Number",NFermi,Index["TM_ELEMENT"], Index["TM_ELEMENT"],
{1,1,1,1,1,1,1,1,1,1,1,1,1,1,1,1,1,1})
257. OppN_Ligand          = NewOperator("Number",NFermi,Index["Ligand_d"], Index["Ligand_d"],
{1,1,1,1,1,1,1,1,1,1})
258.
259. OppN_TM_ELEMENT_yz   = NewOperator("Number",NFermi,{2,3}, {2,3}, {1,1})
260. OppN_TM_ELEMENT_xz   = NewOperator("Number",NFermi,{6,7}, {6,7}, {1,1})
261. OppN_TM_ELEMENT_xy   = NewOperator("Number",NFermi,{0,1}, {0,1}, {1,1})
262. OppN_TM_ELEMENT_x2y2 = NewOperator("Number",NFermi,{8,9}, {8,9}, {1,1})
263. OppN_TM_ELEMENT_z2   = NewOperator("Number",NFermi,{4,5}, {4,5}, {1,1})
264.
265. OppN_TM_ELEMENT_3dUp =
NewOperator("Number",NFermi,Index["TM_ELEMENT_3d_Up"],Index["TM_ELEMENT_3d_Up"],{1,1,1,1,1})
266. OppN_TM_ELEMENT_3dDn =
NewOperator("Number",NFermi,Index["TM_ELEMENT_3d_Dn"],Index["TM_ELEMENT_3d_Dn"],{1,1,1,1,1})
267.
268. OppN_TM_ELEMENT_eg  = OppN_TM_ELEMENT_x2y2 + OppN_TM_ELEMENT_z2
269. OppN_TM_ELEMENT_t2g = OppN_TM_ELEMENT_yz + OppN_TM_ELEMENT_xz + OppN_TM_ELEMENT_xy
270.
271. OppD = OppN_TM_ELEMENT_eg + OppN_TM_ELEMENT_t2g
272.
273.
274. -- XES 2p->1s dipole transition
275. t=math.sqrt(1/2)
276. Akm = {{1,-1,t},{1, 1,-t}}
277. TXESx = Rotate(NewOperator("CF", NFermi, Index["TM_ELEMENT_1s_Up"], Index["TM_ELEMENT_1s_Dn"],
Index["TM_ELEMENT_2p_Up"], Index["TM_ELEMENT_2p_Dn"], Akm), YtoZtriple)
278. Akm = {{1,-1,t*I},{1, 1,t*I}}
279. TXESy = Rotate(NewOperator("CF", NFermi, Index["TM_ELEMENT_1s_Up"], Index["TM_ELEMENT_1s_Dn"],
Index["TM_ELEMENT_2p_Up"], Index["TM_ELEMENT_2p_Dn"], Akm), YtoZtriple)
280. Akm = {{1,0,1}}
281. TXESz = Rotate(NewOperator("CF", NFermi, Index["TM_ELEMENT_1s_Up"], Index["TM_ELEMENT_1s_Dn"],
Index["TM_ELEMENT_2p_Up"], Index["TM_ELEMENT_2p_Dn"], Akm), YtoZtriple)
282.
283. TXESr = t*(TXESx - I * TXESy)
284. TXESl =-t*(TXESx + I * TXESy)
285.
286. -- we can remove zero's from the dipole operator by chopping it
287. TXESx.Chop()
288. TXESy.Chop()
289. TXESz.Chop()
290. TXESr.Chop()
291. TXESl.Chop()
292.
293.
294. -- XAS 2p->3d dipole transition
295. t=math.sqrt(1/2)
296. Akm = {{1,-1,t},{1, 1,-t}}
297. TXASx = Rotate(NewOperator("CF", NFermi, Index["TM_ELEMENT_3d_Up"], Index["TM_ELEMENT_3d_Dn"],
Index["TM_ELEMENT_2p_Up"], Index["TM_ELEMENT_2p_Dn"], Akm), YtoZtriple)
298. Akm = {{1,-1,t*I},{1, 1,t*I}}
```

```
299. TXASy = Rotate(NewOperator("CF", NFermi, Index["TM_ELEMENT_3d_Up"], Index["TM_ELEMENT_3d_Dn"],
     Index["TM_ELEMENT_2p_Up"], Index["TM_ELEMENT_2p_Dn"], Akm), YtoZtriple)
300. Akm = {{1,0,1}}
301. TXASz = Rotate(NewOperator("CF", NFermi, Index["TM_ELEMENT_3d_Up"], Index["TM_ELEMENT_3d_Dn"],
     Index["TM_ELEMENT_2p_Up"], Index["TM_ELEMENT_2p_Dn"], Akm), YtoZtriple)
302.
303. TXASr = t*(TXASx - I * TXASy)
304. TXASl =-t*(TXASx + I * TXASy)
305.
306. -- we can remove zero's from the dipole operator by chopping it
307. TXASx.Chop()
308. TXASy.Chop()
309. TXASz.Chop()
310. TXASr.Chop()
311. TXASl.Chop()
312.
313. -- L and R Polarizations, Z Propegation
314. -------------------------------------------------------------------------
315. k = {0, 0, 1}
316. ev = {0, 1, 0}
317. eh = {1, 0, 0}
318.
319. er = {t * (eh[1] - I * ev[1]),
320.       t * (eh[2] - I * ev[2]),
321.       t * (eh[3] - I * ev[3])}
322.
323. el = {-t * (eh[1] + I * ev[1]),
324.       -t * (eh[2] + I * ev[2]),
325.       -t * (eh[3] + I * ev[3])}
326.
327. TXASr_zprop = er[1] * TXASx + er[2] * TXASy + er[3] * TXASz
328. TXASl_zprop = el[1] * TXASx + el[2] * TXASy + el[3] * TXASz
329. TXASr_zprop.Chop()
330. TXASl_zprop.Chop()
331. -------------------------------------------------------------------------
332.
333. -- L and R Polarizations, Y Propegation
334. -------------------------------------------------------------------------
335. k = {0, 1, 0}
336. ev = {1, 0, 0}
337. eh = {0, 0, 1}
338.
339. er = {t * (eh[1] - I * ev[1]),
340.       t * (eh[2] - I * ev[2]),
341.       t * (eh[3] - I * ev[3])}
342.
343. el = {-t * (eh[1] + I * ev[1]),
344.       -t * (eh[2] + I * ev[2]),
345.       -t * (eh[3] + I * ev[3])}
346.
347. TXASr_yprop = er[1] * TXASx + er[2] * TXASy + er[3] * TXASz
348. TXASl_yprop = el[1] * TXASx + el[2] * TXASy + el[3] * TXASz
349. TXASr_yprop.Chop()
350. TXASl_yprop.Chop()
351. -------------------------------------------------------------------------
352.
```

```
353. -- L and R Polarizations, X Propegation
354. --------------------------------------------------------------
355. k = {1, 0, 0}
356. ev = {0, 0, 1}
357. eh = {0, 1, 0}
358.
359. er = {t * (eh[1] - I * ev[1]),
360.       t * (eh[2] - I * ev[2]),
361.       t * (eh[3] - I * ev[3])}
362.
363. el = {-t * (eh[1] + I * ev[1]),
364.       -t * (eh[2] + I * ev[2]),
365.       -t * (eh[3] + I * ev[3])}
366.
367. TXASr_xprop = er[1] * TXASx + er[2] * TXASy + er[3] * TXASz
368. TXASl_xprop = el[1] * TXASx + el[2] * TXASy + el[3] * TXASz
369. TXASr_xprop.Chop()
370. TXASl_xprop.Chop()
371. --------------------------------------------------------------
372.
373. -- defining XPS annhilation operators
374. OppAnnUp_0 = NewOperator('An', NFermi, Index["TM_ELEMENT_2p_Up"][1])
375. OppAnnUp_2 = NewOperator('An', NFermi, Index["TM_ELEMENT_2p_Up"][2])
376. OppAnnUp_4 = NewOperator('An', NFermi, Index["TM_ELEMENT_2p_Up"][3])
377. OppAnnDn_1 = NewOperator('An', NFermi, Index["TM_ELEMENT_2p_Dn"][1])
378. OppAnnDn_3 = NewOperator('An', NFermi, Index["TM_ELEMENT_2p_Dn"][2])
379. OppAnnDn_5 = NewOperator('An', NFermi, Index["TM_ELEMENT_2p_Dn"][3])
380. --------------------------------------------------------------
381.
382.
383. -- DEFINE ALL HAMILTONIANS
384. -- define the Ground State Hamiltonian
385. GS_Hamiltonian = HDFT - F0dd * OppF0MFDFT - F2dd * OppF2MFDFT - F4dd * OppF4MFDFT
386.                + F0dd * OppF0 + F2dd * OppF2 + F4dd * OppF4
387.                + Bz * (2*OppSz + OppLz) + zeta_3d * Oppldots_3d
388.
389. GS_Hamiltonian = GS_Hamiltonian + Hx * OppSx + Hy * OppSy + Hz * OppSz
390.
391. GS_Hamiltonian = GS_Hamiltonian/2
392. GS_Hamiltonian = GS_Hamiltonian + ConjugateTranspose(GS_Hamiltonian)
393.
394. edgs = (10*Delta-nd*(19+nd)*Udd/2)/(10+nd)
395. eLgs = nd*((1+nd)*Udd/2-Delta)/(10+nd)
396.
397. OperatorSetTrace(GS_Hamiltonian,edgs,Index["TM_ELEMENT_3d"])
398. OperatorSetTrace(GS_Hamiltonian,eLgs,Index["Ligand_d"])
399.
400. -- define the 1s Core Hole State Hamiltonian
401. print("--Define 1s Core Hole State Hamiltonian--\n")
402. s_hole_Hamiltonian = HDFT - F0dd * OppF0MFDFT - F2dd * OppF2MFDFT - F4dd * OppF4MFDFT
403.                    + F0dd * OppF0 + F2dd * OppF2 + F4dd * OppF4
404.                    + Bz * (2*OppSz + OppLz) + zeta_3d * Oppldots_3d
405.
406. s_hole_Hamiltonian = s_hole_Hamiltonian + Hx * OppSx + Hy * OppSy + Hz * OppSz
407.
408. s_hole_Hamiltonian = s_hole_Hamiltonian + OppF0sd * F0sd + OppG2sd * G2sd
```

```
409. s_hole_Hamiltonian = s_hole_Hamiltonian/2
410. s_hole_Hamiltonian = s_hole_Hamiltonian + ConjugateTranspose(s_hole_Hamiltonian)
411.
412. esinter       = -nd*Usd
413. edinter       = -((-20*Delta + 19*nd*Udd+nd*nd*Udd+40*Usd)/(2*(10+nd)))
414. eLinter       = nd*((1+nd)*Udd/2 - Delta + 2*Usd)/(10+nd)
415.
416. OperatorSetTrace(s_hole_Hamiltonian,esinter,Index["TM_ELEMENT_1s"])
417. OperatorSetTrace(s_hole_Hamiltonian,edinter,Index["TM_ELEMENT_3d"])
418. OperatorSetTrace(s_hole_Hamiltonian,eLinter,Index["Ligand_d"])
419.
420. -- define the Final State Hamiltonian
421. print("--Define XAS-Hamiltonian--\n")
422. p_hole_Hamiltonian = HDFT - F0dd * OppF0MFDFT - F2dd * OppF2MFDFT - F4dd * OppF4MFDFT
423.              + F0dd * OppF0 + F2dd * OppF2 + F4dd * OppF4
424.              + Bz * (2*OppSz + OppLz) + zeta_3d * Oppldots_3d
425.
426. p_hole_Hamiltonian = p_hole_Hamiltonian + Hx * OppSx + Hy * OppSy + Hz * OppSz
427.
428. p_hole_Hamiltonian = p_hole_Hamiltonian + zeta_2p * Oppldots_2p
429.              + F0pd * OppUpdF0 + F2pd * OppUpdF2 + G1pd * OppUpdG1 + G3pd * OppUpdG3
430. p_hole_Hamiltonian = p_hole_Hamiltonian/2
431. p_hole_Hamiltonian = p_hole_Hamiltonian + ConjugateTranspose(p_hole_Hamiltonian)
432.
433. epfinal       = -nd*Upd
434. edfinal       = -((-20*Delta + 19*nd*Udd + nd*nd*Udd + 120*Upd)/(2*(10 + nd)))
435. eLfinal       = nd*(-2*Delta + Udd + nd*Udd + 12*Upd)/(2*(10 + nd))
436.
437. OperatorSetTrace(p_hole_Hamiltonian,epfinal,Index["TM_ELEMENT_2p"])
438. OperatorSetTrace(p_hole_Hamiltonian,edfinal,Index["TM_ELEMENT_3d"])
439. OperatorSetTrace(p_hole_Hamiltonian,eLfinal,Index["Ligand_d"])
440.
441. print("edgs = "..edgs.." eV")
442. print("eLgs = "..eLgs.." eV")
443. print("edinter = "..edinter.." eV")
444. print("eLinter = "..eLinter.." eV")
445. print("edfinal = "..edfinal.." eV")
446. print("eLfinal = "..eLfinal.." eV")
447.
448. -------------------------------------------------------------------------------------
449. -- Collect operators to take expectation values of
450. GS_Hamiltonian.Name = "<E>"
451. s_hole_Hamiltonian.Name = "<E>"
452. p_hole_Hamiltonian.Name = "<E>"
453. OppSsqr.Name = "<S^2>"
454. OppLsqr.Name = "<L^2>"
455. OppJsqr.Name = "<J^2>"
456. OppSz.Name = "<S_z^3d>"
457. OppLz.Name = "<L_z^3d>"
458. OppJz.Name = "<J_z^3d>"
459. Oppldots_3d.Name = "<l.s>"
460. OppN_TM_ELEMENT_eg.Name = "<Neg_TM_ELEMENT>"
461. OppN_TM_ELEMENT_t2g.Name = "<Nt2g_TM_ELEMENT>"
462. OppN_TM_ELEMENT.Name = "<N_TM_ELEMENT>"
463. OppN_Ligand.Name = "<N_L>"
464. OppD = OppN_TM_ELEMENT_eg + OppN_TM_ELEMENT_t2g
```

```
465. OppD.Name = "<N_TM_ELEMENT_d>"
466.
467. OppN_TM_ELEMENT_yz.Name = "<3d_yz>"
468. OppN_TM_ELEMENT_xz.Name = "<3d_xz>"
469. OppN_TM_ELEMENT_xy.Name = "<3x_xy>"
470. OppN_TM_ELEMENT_x2y2.Name = "<3d_x2y2>"
471. OppN_TM_ELEMENT_z2.Name = "<3x_z2>"
472.
473. OppN_TM_ELEMENT_3dUp.Name = "<N_TM_ELEMENT_dUp>"
474. OppN_TM_ELEMENT_3dDn.Name = "<N_TM_ELEMENT_dDn>"
475.
476. GS_oppList={GS_Hamiltonian, OppSz, OppLz, OppJz, OppSsqr, OppLsqr, OppJsqr,
477. -- OppN_TM_ELEMENT_eg, OppN_TM_ELEMENT_t2g, OppN_TM_ELEMENT_3dUp, OppN_TM_ELEMENT_3dDn,
478. OppN_TM_ELEMENT_yz, OppN_TM_ELEMENT_xz, OppN_TM_ELEMENT_xy, OppN_TM_ELEMENT_x2y2,
OppN_TM_ELEMENT_z2,
479. OppD, OppN_TM_ELEMENT, OppN_Ligand}
480.
481. s_hole_oppList={s_hole_Hamiltonian, OppSz, OppLz, OppJz, OppSsqr, OppLsqr, OppJsqr,
482. -- OppN_TM_ELEMENT_eg, OppN_TM_ELEMENT_t2g, OppN_TM_ELEMENT_3dUp, OppN_TM_ELEMENT_3dDn,
483. OppN_TM_ELEMENT_yz, OppN_TM_ELEMENT_xz, OppN_TM_ELEMENT_xy, OppN_TM_ELEMENT_x2y2,
OppN_TM_ELEMENT_z2,
484. OppD, OppN_TM_ELEMENT, OppN_Ligand}
485. --------------------------------------------------------------------------------
486.
487. print("\n--Compute Ground State eigenstates--")
488. -- we now can create the lowest Npsi eigenstates:
489. Npsi=5
490. print("Npsi", Npsi)
491. StartRestrictions = {NFermi, 0, {DeterminantString(NFermi,Index["TM_ELEMENT_1s"]),2,2},
492. {DeterminantString(NFermi,Index["TM_ELEMENT_3d"],Index["Ligand_d"]),10+nd,10+nd},
493. {DeterminantString(NFermi,Index["TM_ELEMENT_2p"]),6,6}}
494.
495. print("\nGround State Start Restrictions")
496. print(StartRestrictions)
497.
498. GS_psilist = Eigensystem(GS_Hamiltonian, StartRestrictions, Npsi, {{'Zero',1e-c,{'Epsilon',1e-
06}})
499. GS_psilist = Chop(GS_psilist)
500.
501. -- Making sure that all thermally accessible states are included in GS_psilist
502. T = 293 * EnergyUnits.Kelvin.value
503. Egrd = GS_psilist[1]*GS_Hamiltonian*GS_psilist[1]
504. dZ = exp(-(GS_psilist[#GS_psilist] * GS_Hamiltonian * GS_psilist[#GS_psilist] - Egrd)/T)
505. print("\ndZ")
506. print(dZ)
507. while dZ > 0.01 do
508.     print("\n--Compute eigenstates--")
509.
510.     -- we now can create the lowest Npsi eigenstates:
511.     Npsi = Npsi + 4
512.     print("Npsi")
513.     print(Npsi)
514.
515.     GS_psilist = Eigensystem(GS_Hamiltonian, StartRestrictions, Npsi, {{'Zero',1e-
06},{'Epsilon',1e-06}})
516.     GS_psilist = Chop(GS_psilist)
```

218

```
517.
518.        Egrd = GS_psilist[1]*GS_Hamiltonian*GS_psilist[1]
519.        dZ = exp(-(GS_psilist[#GS_psilist] * GS_Hamiltonian * GS_psilist[#GS_psilist] - Egrd)/T)
520.
521.        print("\ndZ")
522.        print(dZ)
523. end
524.
525.
526. print("\n--Compute 1s Corehole eigenstates--")
527. -- we now can create the lowest Npsi eigenstates:
528. Npsi=5
529. print("Npsi", Npsi)
530. StartRestrictions = {NFermi, 0, {DeterminantString(NFermi,Index["TM_ELEMENT_1s"]),1,1},
531. {DeterminantString(NFermi,Index["TM_ELEMENT_3d"],Index["Ligand_d"]),10+nd,10+nd},
532. {DeterminantString(NFermi,Index["TM_ELEMENT_2p"]),6,6}}
533.
534. print("\n1s Corehole Start Restrictions")
535. print(StartRestrictions)
536.
537. s_hole_psilist = Eigensystem(s_hole_Hamiltonian, StartRestrictions, Npsi, {{'Zero',1e-06},{'Epsilon',1e-06}})
538. s_hole_psilist = Chop(s_hole_psilist)
539.
540. -- Making sure that all thermally accessible states are included in s_hole_psilist
541. T = 293 * EnergyUnits.Kelvin.value
542. Egrd = s_hole_psilist[1]*s_hole_Hamiltonian*s_hole_psilist[1]
543. dZ = exp(-(s_hole_psilist[#s_hole_psilist] * s_hole_Hamiltonian * s_hole_psilist[#s_hole_psilist] - Egrd)/T)
544. print("\ndZ")
545. print(dZ)
546. while dZ > 0.01 do
547.        print("\n--Compute eigenstates--")
548.
549.        -- we now can create the lowest Npsi eigenstates:
550.        Npsi = Npsi + 4
551.        print("Npsi")
552.        print(Npsi)
553.
554.        s_hole_psilist = Eigensystem(s_hole_Hamiltonian, StartRestrictions, Npsi, {{'Zero',1e-06},{'Epsilon',1e-06}})
555.        s_hole_psilist = Chop(s_hole_psilist)
556.
557.        Egrd = s_hole_psilist[1]*s_hole_Hamiltonian*s_hole_psilist[1]
558.        dZ = exp(-(s_hole_psilist[#s_hole_psilist] * s_hole_Hamiltonian * s_hole_psilist[#s_hole_psilist] - Egrd)/T)
559.
560.        print("\ndZ")
561.        print(dZ)
562. end
563.
564.
565. print("\n--Ground State Expectation Values--")
566. PrintExpectationValues(GS_psilist, GS_oppList,{{"ColWidth",10}})
567.
568.
```

```
569. print("\n--1s Corehole State Expectation Values--")
570. PrintExpectationValues(s_hole_psilist, s_hole_oppList,{{"ColWidth",10}})
571. ----------------------------------------------------------------------------------------
     ----------------------
572.
573. print("\n--Create the XES Spectra--\n")
574.
575. -- Constant Lorentzian Broadening --
576. -----------------------------------
577. Gamma = 0.1
578. -----------------------------------
579. ----------- For Sticks -------------
580. Emin = -50
581. Emax = 50
582. NE= 4000
583.
584. epsilon = 0.0001
585.
586. Spectra_z=0
587. Spectra_x=0
588. Spectra_y=0
589. Egrd = s_hole_psilist[1]*s_hole_Hamiltonian*s_hole_psilist[1]
590. T = 293 * EnergyUnits.Kelvin.value
591. Z = 0
592.
593. for j=1, Npsi do
594.     dZ = Complex.Re(exp(-(s_hole_psilist[j] * s_hole_Hamiltonian * s_hole_psilist[j] -
     Egrd)/T))
595.     print(dZ)
596.     if dZ < 0.01 then break end
597.     Z  = Z + dZ
598.     Spectra_z = Spectra_z + CreateSpectra(p_hole_Hamiltonian, TXESz, s_hole_psilist[j],
     {{"Emin",Emin}, {"Emax",Emax}, {"NE",NE}, {"Gamma",Gamma}, {"epsilon",epsilon}})*math.exp(-
     (s_hole_psilist[j]*s_hole_Hamiltonian*s_hole_psilist[j] - Egrd)/T)
599.     Spectra_x = Spectra_x + CreateSpectra(p_hole_Hamiltonian, TXESx, s_hole_psilist[j],
     {{"Emin",Emin}, {"Emax",Emax}, {"NE",NE}, {"Gamma",Gamma}, {"epsilon",epsilon}})*math.exp(-
     (s_hole_psilist[j]*s_hole_Hamiltonian*s_hole_psilist[j] - Egrd)/T)
600.     Spectra_y = Spectra_y + CreateSpectra(p_hole_Hamiltonian, TXESy, s_hole_psilist[j],
     {{"Emin",Emin}, {"Emax",Emax}, {"NE",NE}, {"Gamma",Gamma}, {"epsilon",epsilon}})*math.exp(-
     (s_hole_psilist[j]*s_hole_Hamiltonian*s_hole_psilist[j] - Egrd)/T)
601. end
602. Spectra_z = Spectra_z/Z
603. Spectra_x = Spectra_x/Z
604. Spectra_y = Spectra_y/Z
605.
606. XESSpectra = (Spectra_z+Spectra_x+Spectra_y)/3
607. XESSpectra.Print({{"file", "XES_sticks.dat"}})
608.
609. XESSpectra.Broaden(0, 1.9)
610. XESSpectra.Print({{"file", "XES.dat"}})
611.
612. Spectra_z.Broaden(0, 1.9)
613. Spectra_x.Broaden(0, 1.9)
614. Spectra_y.Broaden(0, 1.9)
615. Spectra_z.Print({{"file", "XES_zpol.dat"}})
616. Spectra_x.Print({{"file", "XES_xpol.dat"}})
```

```
617.  Spectra_y.Print({{"file", "XES_ypol.dat"}})
618.
619.
620.  print("\n--Create the XAS and XPS Spectra--\n")
621.
622.  -- Constant Lorentzian Broadening --
623.  -----------------------------------
624.  Gamma = 0.1
625.  -----------------------------------
626.  ----------- For Sticks -------------
627.  Emin = -50
628.  Emax = 50
629.  NE= 4000
630.
631.  epsilon = 0.00001
632.
633.  Spectra_z=0 -- Linearly Polarized along z
634.  Spectra_x=0 -- Linearly Polarized along x
635.  Spectra_y=0 -- Linearly Polarized along y
636.
637.  Spectra_r_z=0 -- Right Circularly Polarized, propegating along z
638.  Spectra_l_z=0 -- Left Circularly Polarized,  propegating along z
639.  Spectra_r_y=0 -- Right Circularly Polarized, propegating along y
640.  Spectra_l_y=0 -- Left Circularly Polarized,  propegating along y
641.  Spectra_r_x=0 -- Right Circularly Polarized, propegating along x
642.  Spectra_l_x=0 -- Left Circularly Polarized,  propegating along x
643.
644.  Spectra_0=0 -- Annhilation of electron at 0
645.  Spectra_1=0 -- Annhilation of electron at 1
646.  Spectra_2=0 -- Annhilation of electron at 2
647.  Spectra_3=0 -- Annhilation of electron at 3
648.  Spectra_4=0 -- Annhilation of electron at 4
649.  Spectra_5=0 -- Annhilation of electron at 5
650.
651.  Egrd = GS_psilist[1]*GS_Hamiltonian*GS_psilist[1]
652.  T = 293 * EnergyUnits.Kelvin.value
653.  Z = 0
654.
655.  for j=1, Npsi do
656.      dZ = Complex.Re(exp(-(GS_psilist[j] * GS_Hamiltonian * GS_psilist[j] - Egrd)/T))
657.      print(dZ)
658.      if dZ < 0.01 then break end
659.      Z  = Z + dZ
660.      Spectra_z = Spectra_z + CreateSpectra(p_hole_Hamiltonian, TXASz, GS_psilist[j],
{{"Emin",Emin}, {"Emax",Emax}, {"NE",NE}, {"Gamma",Gamma}, {"epsilon",epsilon}})*math.exp(-
(GS_psilist[j]*GS_Hamiltonian*GS_psilist[j] - Egrd)/T)
661.      Spectra_x = Spectra_x + CreateSpectra(p_hole_Hamiltonian, TXASx, GS_psilist[j],
{{"Emin",Emin}, {"Emax",Emax}, {"NE",NE}, {"Gamma",Gamma}, {"epsilon",epsilon}})*math.exp(-
(GS_psilist[j]*GS_Hamiltonian*GS_psilist[j] - Egrd)/T)
662.      Spectra_y = Spectra_y + CreateSpectra(p_hole_Hamiltonian, TXASy, GS_psilist[j],
{{"Emin",Emin}, {"Emax",Emax}, {"NE",NE}, {"Gamma",Gamma}, {"epsilon",epsilon}})*math.exp(-
(GS_psilist[j]*GS_Hamiltonian*GS_psilist[j] - Egrd)/T)
663.
664.      Spectra_r_z = Spectra_r_z + CreateSpectra(p_hole_Hamiltonian, TXASr_zprop, GS_psilist[j],
{{"Emin",Emin}, {"Emax",Emax}, {"NE",NE}, {"Gamma",Gamma}, {"epsilon",epsilon}})*math.exp(-
(GS_psilist[j]*GS_Hamiltonian*GS_psilist[j] - Egrd)/T)
```

```
665.    Spectra_l_z = Spectra_l_z + CreateSpectra(p_hole_Hamiltonian, TXASl_zprop, GS_psilist[j],
{{"Emin",Emin}, {"Emax",Emax}, {"NE",NE}, {"Gamma",Gamma}, {"epsilon",epsilon}})*math.exp(-
(GS_psilist[j]*GS_Hamiltonian*GS_psilist[j] - Egrd)/T)
666.    Spectra_r_y = Spectra_r_y + CreateSpectra(p_hole_Hamiltonian, TXASr_yprop, GS_psilist[j],
{{"Emin",Emin}, {"Emax",Emax}, {"NE",NE}, {"Gamma",Gamma}, {"epsilon",epsilon}})*math.exp(-
(GS_psilist[j]*GS_Hamiltonian*GS_psilist[j] - Egrd)/T)
667.    Spectra_l_y = Spectra_l_y + CreateSpectra(p_hole_Hamiltonian, TXASl_yprop, GS_psilist[j],
{{"Emin",Emin}, {"Emax",Emax}, {"NE",NE}, {"Gamma",Gamma}, {"epsilon",epsilon}})*math.exp(-
(GS_psilist[j]*GS_Hamiltonian*GS_psilist[j] - Egrd)/T)
668.    Spectra_r_x = Spectra_r_x + CreateSpectra(p_hole_Hamiltonian, TXASr_xprop, GS_psilist[j],
{{"Emin",Emin}, {"Emax",Emax}, {"NE",NE}, {"Gamma",Gamma}, {"epsilon",epsilon}})*math.exp(-
(GS_psilist[j]*GS_Hamiltonian*GS_psilist[j] - Egrd)/T)
669.    Spectra_l_x = Spectra_l_x + CreateSpectra(p_hole_Hamiltonian, TXASl_xprop, GS_psilist[j],
{{"Emin",Emin}, {"Emax",Emax}, {"NE",NE}, {"Gamma",Gamma}, {"epsilon",epsilon}})*math.exp(-
(GS_psilist[j]*GS_Hamiltonian*GS_psilist[j] - Egrd)/T)
670.
671.    Spectra_0 = Spectra_0 + CreateSpectra(p_hole_Hamiltonian, OppAnnUp_0, GS_psilist[j],
{{"Emin",Emin}, {"Emax",Emax}, {"NE",NE}, {"Gamma",Gamma}, {"epsilon",epsilon}})*math.exp(-
(GS_psilist[j]*GS_Hamiltonian*GS_psilist[j] - Egrd)/T)
672.    Spectra_1 = Spectra_1 + CreateSpectra(p_hole_Hamiltonian, OppAnnDn_1, GS_psilist[j],
{{"Emin",Emin}, {"Emax",Emax}, {"NE",NE}, {"Gamma",Gamma}, {"epsilon",epsilon}})*math.exp(-
(GS_psilist[j]*GS_Hamiltonian*GS_psilist[j] - Egrd)/T)
673.    Spectra_2 = Spectra_2 + CreateSpectra(p_hole_Hamiltonian, OppAnnUp_2, GS_psilist[j],
{{"Emin",Emin}, {"Emax",Emax}, {"NE",NE}, {"Gamma",Gamma}, {"epsilon",epsilon}})*math.exp(-
(GS_psilist[j]*GS_Hamiltonian*GS_psilist[j] - Egrd)/T)
674.    Spectra_3 = Spectra_3 + CreateSpectra(p_hole_Hamiltonian, OppAnnDn_3, GS_psilist[j],
{{"Emin",Emin}, {"Emax",Emax}, {"NE",NE}, {"Gamma",Gamma}, {"epsilon",epsilon}})*math.exp(-
(GS_psilist[j]*GS_Hamiltonian*GS_psilist[j] - Egrd)/T)
675.    Spectra_4 = Spectra_4 + CreateSpectra(p_hole_Hamiltonian, OppAnnUp_4, GS_psilist[j],
{{"Emin",Emin}, {"Emax",Emax}, {"NE",NE}, {"Gamma",Gamma}, {"epsilon",epsilon}})*math.exp(-
(GS_psilist[j]*GS_Hamiltonian*GS_psilist[j] - Egrd)/T)
676.    Spectra_5 = Spectra_5 + CreateSpectra(p_hole_Hamiltonian, OppAnnDn_5, GS_psilist[j],
{{"Emin",Emin}, {"Emax",Emax}, {"NE",NE}, {"Gamma",Gamma}, {"epsilon",epsilon}})*math.exp(-
(GS_psilist[j]*GS_Hamiltonian*GS_psilist[j] - Egrd)/T)
677. end
678. Spectra_z = Spectra_z/Z
679. Spectra_x = Spectra_x/Z
680. Spectra_y = Spectra_y/Z
681.
682. Spectra_r_z = Spectra_r_z/Z
683. Spectra_l_z = Spectra_l_z/Z
684. Spectra_r_y = Spectra_r_y/Z
685. Spectra_l_y = Spectra_l_y/Z
686. Spectra_r_x = Spectra_r_x/Z
687. Spectra_l_x = Spectra_l_x/Z
688.
689. XASSpectra = (Spectra_z+Spectra_x+Spectra_y)/3
690. XASSpectra.Print({{"file", "XAS_sticks.dat"}})
691.
692. XASSpectra.Broaden(0, 0.5)
693. XASSpectra.Print({{"file", "XAS.dat"}})
694.
695. Spectra_z.Print({{"file", "XAS_zpol_sticks.dat"}})
696. Spectra_x.Print({{"file", "XAS_xpol_sticks.dat"}})
697. Spectra_y.Print({{"file", "XAS_ypol_sticks.dat"}})
698.
```

```
699. Spectra_r_z.Print({{"file", "XAS_rpol_zdir_sticks.dat"}})
700. Spectra_l_z.Print({{"file", "XAS_lpol_zdir_sticks.dat"}})
701. Spectra_r_y.Print({{"file", "XAS_rpol_ydir_sticks.dat"}})
702. Spectra_l_y.Print({{"file", "XAS_lpol_ydir_sticks.dat"}})
703. Spectra_r_x.Print({{"file", "XAS_rpol_xdir_sticks.dat"}})
704. Spectra_l_x.Print({{"file", "XAS_lpol_xdir_sticks.dat"}})
705.
706. Spectra_z.Broaden(0, 0.5)
707. Spectra_x.Broaden(0, 0.5)
708. Spectra_y.Broaden(0, 0.5)
709.
710. Spectra_r_z.Broaden(0, 0.5)
711. Spectra_l_z.Broaden(0, 0.5)
712. Spectra_r_y.Broaden(0, 0.5)
713. Spectra_l_y.Broaden(0, 0.5)
714. Spectra_r_x.Broaden(0, 0.5)
715. Spectra_l_x.Broaden(0, 0.5)
716.
717. Spectra_z.Print({{"file", "XAS_zpol.dat"}})
718. Spectra_x.Print({{"file", "XAS_xpol.dat"}})
719. Spectra_y.Print({{"file", "XAS_ypol.dat"}})
720.
721. Spectra_r_z.Print({{"file", "XAS_rpol_zdir.dat"}})
722. Spectra_l_z.Print({{"file", "XAS_lpol_zdir.dat"}})
723. Spectra_r_y.Print({{"file", "XAS_rpol_ydir.dat"}})
724. Spectra_l_y.Print({{"file", "XAS_lpol_ydir.dat"}})
725. Spectra_r_x.Print({{"file", "XAS_rpol_xdir.dat"}})
726. Spectra_l_x.Print({{"file", "XAS_lpol_xdir.dat"}})
727.
728. Spectra_0 = Spectra_0 / Z
729. Spectra_1 = Spectra_1 / Z
730. Spectra_2 = Spectra_2 / Z
731. Spectra_3 = Spectra_3 / Z
732. Spectra_4 = Spectra_4 / Z
733. Spectra_5 = Spectra_5 / Z
734.
735. XPSSpectra = (Spectra_0 + Spectra_1 + Spectra_2 + Spectra_3 + Spectra_4 + Spectra_5) / 6
736. XPSSpectra.Print({{"file", "XPS_sticks.dat"}})
737.
738. XPSSpectra.Broaden(0, 0.5)
739. XPSSpectra.Print({{"file", "XPS.dat"}})
740.
741. print("Finished")
742.
```

8.3   Spin-orbit coupling parameters for 3*d* elements

The spin-orbit coupling parameters used in this thesis were calculated using the

MISSING code interface for Cowan's code. Each row lists the element, configuration, and the

associated 2*p*, 3*p*, and 3*d* spin-orbit coupling ζ parameters. For configurations with no electrons in one of these shells, the value is left as just "-". All values are in eV.

Table 1: Spin-Orbit Coupling Constants for Ti

Element	Configuration	2p	3p	3d
Ti	2p63p64s23d2	3.597	0.386	0.015
Ti	2p63p64s13d2	3.597	0.386	0.015
Ti	2p63p64s03d2	3.598	0.387	0.016
Ti	2p63p64s23d1	3.595	0.401	0.018
Ti	2p63p64s13d1	3.596	0.403	0.019
Ti	2p63p64s03d1	3.597	0.406	0.019
Ti	2p63p64s03d0	3.597	0.43	-
Ti	2p53p64s23d2	3.774	0.451	0.026
Ti	2p53p64s13d2	3.775	0.453	0.027
Ti	2p53p64s03d2	3.776	0.455	0.027
Ti	2p53p64s23d1	3.774	0.474	0.03
Ti	2p53p64s13d1	3.775	0.477	0.031
Ti	2p53p64s03d1	3.776	0.481	0.032
Ti	2p53p64s03d0	3.778	0.51	-
Ti	2p63p54s23d2	3.601	0.408	0.019
Ti	2p63p54s13d2	3.601	0.409	0.019
Ti	2p63p54s03d2	3.602	0.412	0.02
Ti	2p63p54s23d1	3.6	0.428	0.022
Ti	2p63p54s13d1	3.601	0.431	0.023
Ti	2p63p54s03d1	3.603	0.435	0.024
Ti	2p63p54s03d0	3.604	0.462	-

Table 2: Spin-Orbit Coupling Constants for V

Element	Configuration	2p	3p	3d
V	2p63p64s23d3	4.441	0.492	0.021
V	2p63p64s13d3	4.441	0.492	0.021
V	2p63p64s03d3	4.442	0.493	0.022
V	2p63p64s23d2	4.439	0.509	0.025
V	2p63p64s13d2	4.44	0.511	0.026
V	2p63p64s03d2	4.441	0.514	0.027
V	2p63p64s03d1	4.441	0.54	0.031
V	2p63p64s03d0	4.443	0.572	-
V	2p53p64s23d3	4.648	0.566	0.035
V	2p53p64s13d3	4.648	0.568	0.036
V	2p53p64s03d3	4.649	0.57	0.036
V	2p53p64s23d2	4.647	0.591	0.04
V	2p53p64s13d2	4.648	0.594	0.041
V	2p53p64s03d2	4.65	0.598	0.041
V	2p53p64s03d1	4.652	0.63	0.047
V	2p53p64s03d0	4.656	0.667	-
V	2p63p54s23d3	4.446	0.516	0.026
V	2p63p54s13d3	4.446	0.518	0.027
V	2p63p54s03d3	4.447	0.52	0.027
V	2p63p54s23d2	4.445	0.539	0.03
V	2p63p54s13d2	4.446	0.542	0.031
V	2p63p54s03d2	4.448	0.545	0.032
V	2p63p54s03d1	4.449	0.576	0.036
V	2p63p54s03d0	4.453	0.61	-

Table 3: Spin-Orbit Coupling Constants for Cr

Element	Configuration	2p	3p	3d
Cr	2p63p64s23d4	5.426	0.617	0.029
Cr	2p63p64s13d4	5.426	0.617	0.03
Cr	2p63p64s03d4	5.427	0.618	0.03
Cr	2p63p64s23d3	5.424	0.637	0.034
Cr	2p63p64s13d3	5.425	0.638	0.035
Cr	2p63p64s03d3	5.426	0.641	0.035
Cr	2p63p64s03d2	5.426	0.67	0.041
Cr	2p63p64s03d1	5.428	0.705	0.046
Cr	2p63p64s03d0	5.432	0.745	-
Cr	2p53p64s23d4	5.665	0.701	0.045
Cr	2p53p64s13d4	5.666	0.702	0.046
Cr	2p53p64s03d4	5.667	0.705	0.047

Cr	2p53p64s23d3	5.665	0.729	0.051
Cr	2p53p64s13d3	5.666	0.732	0.052
Cr	2p53p64s03d3	5.668	0.736	0.053
Cr	2p53p64s03d2	5.67	0.772	0.06
Cr	2p53p64s03d1	5.674	0.812	0.066
Cr	2p53p64s03d0	5.68	0.857	-
Cr	2p63p54s23d4	5.431	0.644	0.035
Cr	2p63p54s13d4	5.432	0.646	0.035
Cr	2p63p54s03d4	5.433	0.648	0.036
Cr	2p63p54s23d3	5.431	0.669	0.04
Cr	2p63p54s13d3	5.432	0.672	0.04
Cr	2p63p54s03d3	5.434	0.676	0.041
Cr	2p63p54s03d2	5.435	0.71	0.047
Cr	2p63p54s03d1	5.439	0.748	0.053
Cr	2p63p54s03d0	5.444	0.79	-

Table 4: Spin-Orbit Coupling Constants for Mn

Element	Configuration	2p	3p	3d
Mn	2p63p64s23d5	6.568	0.764	0.039
Mn	2p63p64s13d5	6.568	0.764	0.039
Mn	2p63p64s03d5	6.569	0.764	0.04
Mn	2p63p64s23d4	6.566	0.785	0.044
Mn	2p63p64s13d4	6.567	0.787	0.045
Mn	2p63p64s03d4	6.568	0.789	0.046
Mn	2p63p64s03d3	6.568	0.822	0.052
Mn	2p63p64s03d2	6.57	0.861	0.059
Mn	2p63p64s03d1	6.573	0.904	0.066
Mn	2p63p64s03d0	6.579	0.953	-
Mn	2p53p64s23d5	6.843	0.858	0.058
Mn	2p53p64s13d5	6.844	0.859	0.059
Mn	2p53p64s03d5	6.845	0.862	0.059
Mn	2p53p64s23d4	6.842	0.889	0.065
Mn	2p53p64s13d4	6.843	0.892	0.065
Mn	2p53p64s03d4	6.845	0.896	0.066
Mn	2p53p64s03d3	6.847	0.936	0.074
Mn	2p53p64s03d2	6.851	0.981	0.082
Mn	2p53p64s03d1	6.858	1.03	0.09
Mn	2p53p64s03d0	6.867	1.083	-
Mn	2p63p54s23d5	6.574	0.794	0.045
Mn	2p63p54s13d5	6.575	0.795	0.046
Mn	2p63p54s03d5	6.576	0.797	0.047

Mn	2p63p54s23d4	6.573	0.821	0.051
Mn	2p63p54s13d4	6.574	0.824	0.052
Mn	2p63p54s03d4	6.576	0.828	0.053
Mn	2p63p54s03d3	6.578	0.865	0.059
Mn	2p63p54s03d2	6.581	0.908	0.066
Mn	2p63p54s03d1	6.587	0.955	0.073
Mn	2p63p54s03d0	6.596	1.006	-

Table 5: Spin-Orbit Coupling Constants for Fe

Element	Configuration	2p	3p	3d
Fe	2p63p64s23d6	7.366	0.928	0.043
Fe	2p63p64s13d6	7.882	0.934	0.051
Fe	2p63p64s03d6	7.883	0.934	0.052
Fe	2p63p64s23d5	7.88	0.958	0.057
Fe	2p63p64s13d5	7.881	0.959	0.058
Fe	2p63p64s03d5	7.882	0.962	0.059
Fe	2p63p64s03d4	7.882	0.998	0.066
Fe	2p63p64s03d3	7.884	1.04	0.074
Fe	2p63p64s03d2	7.887	1.088	0.082
Fe	2p63p64s03d1	7.894	1.142	0.09
Fe	2p63p64s03d0	7.903	1.199	-
Fe	2p53p64s23d6	8.197	1.04	0.073
Fe	2p53p64s13d6	8.198	1.041	0.073
Fe	2p53p64s03d6	8.199	1.044	0.074
Fe	2p53p64s23d5	8.196	1.074	0.08
Fe	2p53p64s13d5	8.197	1.077	0.081
Fe	2p53p64s03d5	8.199	1.081	0.082
Fe	2p53p64s03d4	8.201	1.125	0.091
Fe	2p53p64s03d3	8.205	1.175	0.1
Fe	2p53p64s03d2	8.212	1.229	0.11
Fe	2p53p64s03d1	8.221	1.288	0.119
Fe	2p53p64s03d0	8.234	1.351	-
Fe	2p63p54s23d6	7.889	0.967	0.058
Fe	2p63p54s13d6	7.89	0.969	0.059
Fe	2p63p54s03d6	7.891	0.971	0.059
Fe	2p63p54s23d5	7.888	0.998	0.064
Fe	2p63p54s13d5	7.89	1.001	0.065
Fe	2p63p54s03d5	7.891	1.005	0.066
Fe	2p63p54s03d4	7.893	1.046	0.074

Fe	2p63p54s03d3	7.897	1.092	0.082
Fe	2p63p54s03d2	7.903	1.144	0.09
Fe	2p63p54s03d1	7.911	1.201	0.099
Fe	2p63p54s03d0	7.923	1.261	-

Table 6: Spin-Orbit Coupling Constants for Co

Element	Configuration	2p	3p	3d
Co	2p63p64s23d7	8.801	1.13	0.055
Co	2p63p64s13d7	9.387	1.131	0.065
Co	2p63p64s03d7	9.388	1.131	0.066
Co	2p63p64s23d6	9.384	1.157	0.072
Co	2p63p64s13d6	9.385	1.159	0.073
Co	2p63p64s03d6	9.386	1.161	0.074
Co	2p63p64s03d5	9.386	1.2	0.082
Co	2p63p64s03d4	9.388	1.247	0.091
Co	2p63p64s03d3	9.391	1.3	0.1
Co	2p63p64s03d2	9.398	1.358	0.11
Co	2p63p64s03d1	9.407	1.422	0.12
Co	2p63p64s03d0	9.42	1.49	-
Co	2p53p64s23d7	9.744	1.249	0.09
Co	2p53p64s13d7	9.745	1.25	0.091
Co	2p53p64s03d7	9.746	1.252	0.092
Co	2p53p64s23d6	9.743	1.286	0.099
Co	2p53p64s13d6	9.744	1.289	0.1
Co	2p53p64s03d6	9.746	1.293	0.101
Co	2p53p64s03d5	9.748	1.342	0.111
Co	2p53p64s03d4	9.752	1.396	0.121
Co	2p53p64s03d3	9.759	1.457	0.132
Co	2p53p64s03d2	9.769	1.522	0.144
Co	2p53p64s03d1	9.782	1.591	0.155
Co	2p53p64s03d0	9.799	1.664	-
Co	2p63p54s23d7	9.394	1.168	0.073
Co	2p63p54s13d7	9.395	1.169	0.074
Co	2p63p54s03d7	9.397	1.17	0.075
Co	2p63p54s23d6	9.393	1.201	0.08
Co	2p63p54s13d6	9.395	1.204	0.081
Co	2p63p54s03d6	9.397	1.208	0.082
Co	2p63p54s03d5	9.398	1.253	0.091
Co	2p63p54s03d4	9.402	1.304	0.1
Co	2p63p54s03d3	9.408	1.361	0.11
Co	2p63p54s03d2	9.417	1.423	0.12

Co	2p63p54s03d1	9.429	1.49	0.13
Co	2p63p54s03d0	9.445	1.561	-

Table 7: Spin-Orbit Coupling Constants for Ni

Element	Configuration	2p	3p	3d
Ni	2p63p64s23d8	10.482	1.566	0.113
Ni	2p63p64s13d8	11.099	1.356	0.082
Ni	2p63p64s03d8	11.1	1.356	0.083
Ni	2p63p64s23d7	11.096	1.385	0.09
Ni	2p63p64s13d7	11.097	1.386	0.09
Ni	2p63p64s03d7	11.098	1.389	0.091
Ni	2p63p64s03d6	11.098	1.431	0.101
Ni	2p63p64s03d5	11.1	1.482	0.111
Ni	2p63p64s03d4	11.103	1.54	0.121
Ni	2p63p64s03d3	11.11	1.605	0.133
Ni	2p63p64s03d2	11.119	1.675	0.145
Ni	2p63p64s03d1	11.132	1.75	0.156
Ni	2p63p64s03d0	11.149	1.829	-
Ni	2p53p64s23d8	11.503	1.488	0.11
Ni	2p53p64s13d8	11.504	1.489	0.111
Ni	2p53p64s03d8	11.506	1.491	0.112
Ni	2p53p64s23d7	11.502	1.529	0.12
Ni	2p53p64s13d7	11.503	1.532	0.121
Ni	2p53p64s03d7	11.505	1.536	0.122
Ni	2p53p64s03d6	11.507	1.589	0.133
Ni	2p53p64s03d5	11.511	1.649	0.145
Ni	2p53p64s03d4	11.518	1.715	0.157
Ni	2p53p64s03d3	11.528	1.786	0.17
Ni	2p53p64s03d2	11.542	1.863	0.184
Ni	2p53p64s03d1	11.559	1.944	0.197
Ni	2p53p64s03d0	11.581	2.029	-
Ni	2p63p54s23d8	11.108	1.397	0.09
Ni	2p63p54s13d8	11.109	1.397	0.091
Ni	2p63p54s03d8	11.11	1.399	0.092
Ni	2p63p54s23d7	11.106	1.433	0.099
Ni	2p63p54s13d7	11.108	1.436	0.1
Ni	2p63p54s03d7	11.11	1.44	0.101
Ni	2p63p54s03d6	11.111	1.49	0.111
Ni	2p63p54s03d5	11.115	1.546	0.121
Ni	2p63p54s03d4	11.121	1.609	0.132
Ni	2p63p54s03d3	11.13	1.677	0.144

Ni	2p63p54s03d2	11.143	1.751	0.156
Ni	2p63p54s03d1	11.159	1.829	0.168
Ni	2p63p54s03d0	11.18	1.911	-

Table 8: Spin-Orbit Coupling Constants for Cu

Element	Configuration	2p	3p	3d
Cu	2p63p64s23d9	12.376	1.96	0.154
Cu	2p63p64s13d9	13.038	1.613	0.101
Cu	2p63p64s03d9	13.039	1.613	0.102
Cu	2p63p64s23d8	13.035	1.645	0.11
Cu	2p63p64s13d8	13.036	1.646	0.111
Cu	2p63p64s03d8	13.038	1.648	0.112
Cu	2p63p64s03d7	13.037	1.695	0.123
Cu	2p63p64s03d6	13.038	1.751	0.134
Cu	2p63p64s03d5	13.042	1.814	0.146
Cu	2p63p64s03d4	13.048	1.885	0.158
Cu	2p63p64s03d3	13.058	1.961	0.172
Cu	2p63p64s03d2	13.071	2.043	0.186
Cu	2p63p64s03d1	13.089	2.13	0.2
Cu	2p63p64s03d0	13.11	2.222	-
Cu	2p53p64s23d9	13.494	1.76	0.133
Cu	2p53p64s13d9	13.495	1.761	0.134
Cu	2p53p64s03d9	13.496	1.763	0.135
Cu	2p53p64s23d8	13.492	1.804	0.144
Cu	2p53p64s13d8	13.493	1.807	0.146
Cu	2p53p64s03d8	13.496	1.812	0.147
Cu	2p53p64s03d7	13.497	1.869	0.159
Cu	2p53p64s03d6	13.501	1.935	0.172
Cu	2p53p64s03d5	13.508	2.007	0.186
Cu	2p53p64s03d4	13.518	2.085	0.201
Cu	2p53p64s03d3	13.532	2.169	0.216
Cu	2p53p64s03d2	13.55	2.258	0.232
Cu	2p53p64s03d1	13.573	2.351	0.248
Cu	2p53p64s03d0	13.6	2.449	-
Cu	2p63p54s23d9	13.048	1.658	0.111
Cu	2p63p54s13d9	13.049	1.659	0.112
Cu	2p63p54s03d9	13.051	1.66	0.113
Cu	2p63p54s23d8	13.046	1.698	0.121
Cu	2p63p54s13d8	13.048	1.701	0.122
Cu	2p63p54s03d8	13.05	1.705	0.123
Cu	2p63p54s03d7	13.052	1.759	0.134

Cu	2p63p54s03d6	13.055	1.821	0.145
Cu	2p63p54s03d5	13.061	1.889	0.158
Cu	2p63p54s03d4	13.071	1.964	0.171
Cu	2p63p54s03d3	13.084	2.044	0.185
Cu	2p63p54s03d2	13.101	2.13	0.199
Cu	2p63p54s03d1	13.122	2.22	0.213
Cu	2p63p54s03d0	13.147	2.315	-

Table 9: Spin-Orbit Coupling Constants for Zn

Element	Configuration	2p	3p	3d
Zn	2p63p64s23d10	15.224	1.906	0.123
Zn	2p63p64s13d10	15.225	1.905	0.123
Zn	2p63p64s03d10	15.226	1.904	0.124
Zn	2p63p64s23d9	15.221	1.94	0.133
Zn	2p63p64s13d9	15.222	1.941	0.134
Zn	2p63p64s03d9	15.224	1.943	0.136
Zn	2p63p64s03d8	15.223	1.994	0.147
Zn	2p63p64s03d7	15.224	2.054	0.16
Zn	2p63p64s03d6	15.228	2.123	0.173
Zn	2p63p64s03d5	15.234	2.2	0.187
Zn	2p63p64s03d4	15.244	2.283	0.202
Zn	2p63p64s03d3	15.257	2.373	0.218
Zn	2p63p64s03d2	15.275	2.468	0.235
Zn	2p63p64s03d1	15.297	2.569	0.251
Zn	2p63p64s03d0	15.325	2.675	-
Zn	2p53p64s23d10	15.735	2.068	0.16
Zn	2p53p64s13d10	15.736	2.068	0.161
Zn	2p53p64s03d10	15.738	2.07	0.162
Zn	2p53p64s23d9	15.733	2.116	0.173
Zn	2p53p64s13d9	15.735	2.119	0.174
Zn	2p53p64s03d9	15.737	2.123	0.175
Zn	2p53p64s03d8	15.739	2.186	0.189
Zn	2p53p64s03d7	15.742	2.257	0.203
Zn	2p53p64s03d6	15.749	2.336	0.219
Zn	2p53p64s03d5	15.76	2.422	0.235
Zn	2p53p64s03d4	15.774	2.513	0.252
Zn	2p53p64s03d3	15.792	2.61	0.27
Zn	2p53p64s03d2	15.815	2.712	0.288
Zn	2p53p64s03d1	15.843	2.819	0.307
Zn	2p53p64s03d0	15.876	2.931	-
Zn	2p63p54s23d10	15.236	1.954	0.134

Zn	2p63p54s13d10	15.236	1.955	0.135
Zn	2p63p54s03d10	15.238	1.956	0.137
Zn	2p63p54s23d9	15.233	1.998	0.145
Zn	2p63p54s13d9	15.235	2.001	0.147
Zn	2p63p54s03d9	15.238	2.005	0.148
Zn	2p63p54s03d8	15.239	2.063	0.16
Zn	2p63p54s03d7	15.242	2.13	0.173
Zn	2p63p54s03d6	15.249	2.205	0.187
Zn	2p63p54s03d5	15.258	2.287	0.201
Zn	2p63p54s03d4	15.271	2.375	0.217
Zn	2p63p54s03d3	15.289	2.468	0.233
Zn	2p63p54s03d2	15.31	2.568	0.25
Zn	2p63p54s03d1	15.337	2.672	0.267
Zn	2p63p54s03d0	15.368	2.78	-

Bibliography

1. Röntgen, W.C., *Ueber eine neue Art von Strahlen*. Annalen der Physik, 1898. **300**(1): p. 12-17.

2.   Bragg, W.H. and W.L. Bragg, *The reflection of X-rays by crystals*. Proceedings of the Royal Society of London. Series A, Containing Papers of a Mathematical and Physical Character, 1997. **88**(605): p. 428-438.

3.   De Broglie, L., *Recherches sur la théorie des Quanta*. Ann. Phys., 1925. **10**(3): p. 22-128.

4.   Siegbahn, M., *Spektroskopie der Röntgenstrahlen*. 1925: Springer Berlin, Heidelberg.

5.   Lytle, F., *The EXAFS family tree: a personal history of the development of extended X-ray absorption fine structure*. Journal of Synchrotron Radiation, 1999. **6**(3): p. 123-134.

6.   Einstein, A., *Über einen die Erzeugung und Verwandlung des Lichtes betreffenden heuristischen Gesichtspunkt*. Annalen der Physik, 1905. **322**(6): p. 132-148.

7.   Beer, *Bestimmung der Absorption des rothen Lichts in farbigen Flüssigkeiten*. Annalen der Physik, 1852. **162**(5): p. 78-88.

8.   Creagh, D. and J. Hubbell, *X-Ray Absorption (or Attenuation) Coefficients, ed. by A.J.C. Wilson*. 1992, Kluwer Academic Publishers , Hingham, MA.

9.   Dirac, P.A.M. and N.H.D. Bohr, *The quantum theory of the emission and absorption of radiation*. Proceedings of the Royal Society of London. Series A, Containing Papers of a Mathematical and Physical Character, 1927. **114**(767): p. 243-265.

10.   Sakurai, J.J., *Modern Quantum Mechanics*. Revised Edition ed, ed. J. Napolitano. 1994, Reading, MA: Addison-Wesley.

11.   Bunker, G., *Introduction to XAFS: A Practical Guide to X-ray Absorption Fine Structure Spectroscopy*. 2010: Cambridge University Press.

12.   Calvin, S., *XAFS for Everyone*. 2013: Taylor & Francis.

13.   Rehr, J.J. and R.C. Albers, *Theoretical approaches to x-ray absorption fine structure*. Reviews of Modern Physics, 2000. **72**(3): p. 621-654.

14.   Sayers, D.E., E.A. Stern, and F.W. Lytle, *New Technique for Investigating Noncrystalline Structures: Fourier Analysis of the Extended X-Ray---Absorption Fine Structure*. Physical Review Letters, 1971. **27**(18): p. 1204-1207.

15.   Stöhr, J., *Exploring the microscopic origin of magnetic anisotropies with X-ray magnetic circular dichroism (XMCD) spectroscopy*. Journal of Magnetism and Magnetic Materials, 1999. **200**(1): p. 470-497.

16.   Gota, S., M. Gautier-Soyer, and M. Sacchi, *Magnetic properties of ${\mathrm{Fe}}_{2}{\mathrm{O}}_{3}(0001)$ thin layers studied by soft x-ray linear dichroism*. Physical Review B, 2001. **64**(22): p. 224407.

17.   Laan, G.v.d., *Applications of soft x-ray magnetic dichroism*. Journal of Physics: Conference Series, 2013. **430**(1): p. 012127.

18.   Nordén, B., *Applications of linear Dichroism Spectroscopy*. Applied Spectroscopy Reviews, 1978. **14**(2): p. 157-248.

19.   Greczynski, G. and L. Hultman, *X-ray photoelectron spectroscopy: Towards reliable binding energy referencing*. Progress in Materials Science, 2020. **107**: p. 100591.

20.   Hedin, L. and J.D. Lee, *Sudden approximation in photoemission and beyond*. Journal of Electron Spectroscopy and Related Phenomena, 2002. **124**(2): p. 289-315.

21.   von Barth, U. and G. Grossmann, *Dynamical effects in x-ray spectra and the final-state rule*. Physical Review B, 1982. **25**(8): p. 5150-5179.

22.   Walters, D.L. and C.P. Bhalla, *Nonrelativistic Auger Rates, X-Ray Rates, and Fluorescence Yields for the $2p$ Shell*. Physical Review A, 1971. **4**(6): p. 2164-2170.

23.   Glatzel, P. and U. Bergmann, *High resolution 1s core hole X-ray spectroscopy in 3d transition metal complexes—electronic and structural information*. Coordination Chemistry Reviews, 2005. **249**(1): p. 65-95.

24.   Bhargava, A., et al., *X-ray emission spectroscopy: an effective route to extract site occupation of cations*. Physical Chemistry Chemical Physics, 2018. **20**(46): p. 28990-29000.

25.   Pollock, C.J. and S. DeBeer, *Insights into the Geometric and Electronic Structure of Transition Metal Centers from Valence-to-Core X-ray Emission Spectroscopy*. Accounts of Chemical Research, 2015. **48**(11): p. 2967-2975.

26.   Rovezzi, M. and P. Glatzel, *Hard x-ray emission spectroscopy: a powerful tool for the characterization of magnetic semiconductors*. Semiconductor Science and Technology, 2014. **29**(2): p. 023002.

27.   Gironda, A.J., et al., *Asymmetric Rowland circle geometries for spherically bent crystal analyzers in laboratory and synchrotron applications*. Journal of Analytical Atomic Spectrometry, 2024. **39**(5): p. 1375-1387.

28.   Kramers, H.A. and W. Heisenberg, *Über die Streuung von Strahlung durch Atome*. Zeitschrift für Physik, 1925. **31**(1): p. 681-708.

29.   Frank de Groot, A.K., *Core Level Spectroscopy of Solids*. 2008: Taylor & Francis Group. 512.

30.   Wu, X., et al., *Investigation of plasmon relaxation mechanisms using nonadiabatic molecular dynamics*. The Journal of Chemical Physics, 2022. **157**(21).

31.   Lafuerza, S., et al., *Chemical Sensitivity of Kβ and Kα X-ray Emission from a Systematic Investigation of Iron Compounds*. Inorganic Chemistry, 2020. **59**(17): p. 12518-12535.

32.   Roychoudhury, S., et al., *Changes in polarization dictate necessary approximations for modeling electronic deexcitation intensity: Application to x-ray emission*. Physical Review B, 2022. **106**(7): p. 075133.

33.   Nagel, D.J., *Interpretation of Valence Band X-Ray Spectra*. Advances in X-ray Analysis, 1969. **13**: p. 182-236.

34.   Helliwell, J.R., *Synchrotron X-radiation protein crystallography: instrumentation, methods and applications*. Reports on Progress in Physics, 1984. **47**(11): p. 1403.

35.   Jahrman, E.P., et al., *An improved laboratory-based x-ray absorption fine structure and x-ray emission spectrometer for analytical applications in materials chemistry research*. Review of Scientific Instruments, 2019. **90**(2).

36.   Holden, W.M., et al., *A compact dispersive refocusing Rowland circle X-ray emission spectrometer for laboratory, synchrotron, and XFEL applications*. Review of Scientific Instruments, 2017. **88**(7).

37.   Robbins, D.L., et al., *High-resolution compact Johann crystal spectrometer with the Livermore electron beam ion trap*. Review of Scientific Instruments, 2004. **75**(10): p. 3717-3719.

38. Kleymenov, E., et al., *Five-element Johann-type x-ray emission spectrometer with a single-photon-counting pixel detector*. Review of Scientific Instruments, 2011. **82**(6).

39. Bragg, W.H. and W.L. Bragg, *The reflection of X-rays by crystals*. Proceedings of the Royal Society of London. Series A, Containing Papers of a Mathematical and Physical Character, 1913. **88**(605): p. 428-438.

40. Authier, A., *Optical properties of X-rays - dynamical diffractionThis Laue centennial article has also been published in Zeitschrift fur Kristallographie [Authier (2012). Z. Kristallogr. 227, 36-51]*. Acta Crystallographica Section A, 2012. **68**(1): p. 40-56.

41. Mortensen, D.R., et al., *Benchtop Nonresonant X-ray Emission Spectroscopy: Coming Soon to Laboratories and XAS Beamlines Near You?* Journal of Physics: Conference Series, 2016. **712**(1): p. 012036.

42. Brooke, S.J. and M.R. Waterland, *Edge Modes of MoS2 via Indirect Double Resonant Raman Spectroscopy*. The Journal of Physical Chemistry C, 2022. **126**(30): p. 12592-12602.

43. Johann, H.H., *Die Erzeugung lichtstarker Röntgenspektren mit Hilfe von Konkavkristallen*. Zeitschrift für Physik, 1931. **69**(3): p. 185-206.

44. Johansson, T., *Über ein neuartiges, genau fokussierendes Röntgenspektrometer*. Zeitschrift für Physik, 1933. **82**(7): p. 507-528.

45. Chen, Y., et al., *A ray tracing survey of asymmetric operation of the X-ray Rowland circle using spherically bent crystal analyzers*. Journal of Analytical Atomic Spectrometry, 2025. **40**(3): p. 836-847.

46. Jones, R.O. and O. Gunnarsson, *The density functional formalism, its applications and prospects*. Reviews of Modern Physics, 1989. **61**(3): p. 689-746.

47. Hohenberg, P. and W. Kohn, *Inhomogeneous Electron Gas*. Physical Review, 1964. **136**(3B): p. B864-B871.

48. Kohn, W. and L.J. Sham, *Self-Consistent Equations Including Exchange and Correlation Effects*. Physical Review, 1965. **140**(4A): p. A1133-A1138.

49. Toulouse, J., *Review of approximations for the exchange-correlation energy in density-functional theory*. 2022.

50. Mardirossian, N. and M. and Head-Gordon, *Thirty years of density functional theory in computational chemistry: an overview and extensive assessment of 200 density functionals*. Molecular Physics, 2017. **115**(19): p. 2315-2372.

51. Tetef, S., N. Govind, and G.T. Seidler, *Unsupervised machine learning for unbiased chemical classification in X-ray absorption spectroscopy and X-ray emission spectroscopy*. Physical Chemistry Chemical Physics, 2021. **23**(41): p. 23586-23601.

52. DeBeer George, S., P. Brant, and E.I. Solomon, *Metal and Ligand K-Edge XAS of Organotitanium Complexes: Metal 4p and 3d Contributions to Pre-edge Intensity and Their Contributions to Bonding*. Journal of the American Chemical Society, 2005. **127**(2): p. 667-674.

53. Schirmer, J., *Review of the foundations of time-dependent density-functional theory (TDDFT)*. Physical Chemistry Chemical Physics, 2025. **27**(10): p. 4992-5005.

54. Runge, E. and E.K.U. Gross, *Density-Functional Theory for Time-Dependent Systems*. Physical Review Letters, 1984. **52**(12): p. 997-1000.

55. Valiev, M., et al., *NWChem: A comprehensive and scalable open-source solution for large scale molecular simulations*. Computer Physics Communications, 2010. **181**(9): p. 1477-1489.

56. Neese, F., *The ORCA program system*. WIREs Computational Molecular Science, 2012. **2**(1): p. 73-78.

57. Ankudinov, A.L., et al., *Real-space multiple-scattering calculation and interpretation of x-ray-absorption near-edge structure*. Physical Review B, 1998. **58**(12): p. 7565-7576.

58. Kas, J.J., et al., *Real-space Green's function approach to resonant inelastic x-ray scattering*. Physical Review B, 2011. **83**(23): p. 235114.

59. van der Veen, R.M., et al., *L-edge XANES analysis of photoexcited metal complexes in solution*. Physical Chemistry Chemical Physics, 2010. **12**(21): p. 5551-5561.

60. Mattern, B.A., et al., *Real-space Green's function calculations of Compton profiles*. Physical Review B, 2012. **85**(11): p. 115135.

61. Carbone, M.R., et al., *Machine-Learning X-Ray Absorption Spectra to Quantitative Accuracy*. Physical Review Letters, 2020. **124**(15): p. 156401.

62. Chen, Y., *High-throughput Computations of X-ray Spectroscopy and Machine Learning-assisted Chemical Environment Identification*. 2023, UC San Diego.

63. Mathew, K., et al., *High-throughput computational X-ray absorption spectroscopy*. Scientific Data, 2018. **5**(1): p. 180151.

64. Sherrill, C.D., *An Introduction to Configuration Interaction Theory*. 1995, School of Chemistry and Biochemistry, Georgia Institute of Technology.

65. Frisch, M.e., et al., *Gaussian 16*. 2016, Gaussian, Inc. Wallingford, CT.

66. Kresse, G. and J. Hafner, *Ab initio molecular dynamics for liquid metals*. Physical Review B, 1993. **47**(1): p. 558-561.

67. de Groot, F.M.F., et al., *2p x-ray absorption spectroscopy of 3d transition metal systems*. Journal of Electron Spectroscopy and Related Phenomena, 2021. **249**: p. 147061.

68. David Sherrill, C. and H.F. Schaefer, *The Configuration Interaction Method: Advances in Highly Correlated Approaches*, in *Advances in Quantum Chemistry*, P.-O. Löwdin, et al., Editors. 1999, Academic Press. p. 143-269.

69. Vila, F.D., et al., *Real-Time Coupled-Cluster Approach for the Cumulant Green's Function*. Journal of Chemical Theory and Computation, 2020. **16**(11): p. 6983-6992.

70. Bartlett, R.J., *Many-Body Perturbation Theory and Coupled Cluster Theory for Electron Correlation in Molecules*. Annual Review of Physical Chemistry, 1981. **32**(Volume 32): p. 359-401.

71. Nave, C.R. *Hund's Rules*. 2000; Available from: http://hyperphysics.phy-astr.gsu.edu/hbase/Atomic/Hund.html.

72. Cheng, X., *Multiplet computation methods for core level X-ray spectroscopy of transition metal and rare earth elements*. 2023, KTH Royal Institute of Technology.

73. Leedahl, B., et al., *Fundamental crystal field excitations in magnetic semiconductor SnO2: Mn, Fe, Co, Ni*. Physical Chemistry Chemical Physics, 2019. **21**(22): p. 11992-11998.

74. Ackermann, K., et al., *QUANTY, a quantum many-body scripting toolkit*. 2024, SciPost Physics Codebases.

75. Ghijsen, J., et al., *Electronic structure of ${\mathrm{Cu}}_{2}$O and CuO*. Physical Review B, 1988. **38**(16): p. 11322-11330.

76. Okada, K., A. Kotani, and B.T. Thole, *Charge transfer satellites and multiplet splitting in X-ray photoemission spectra of late transition metal halides*. Journal of Electron Spectroscopy and Related Phenomena, 1992. **58**(4): p. 325-343.

77. Condon, E.U. and G.H. Shortley, *The Theory of Atomic Spectra*. 1935, Cambridge, UK: Cambridge University Press.

78. Slater, J.C., *The Theory of Complex Spectra*. Physical Review, 1929. **34**(10): p. 1293-1322.

79. Condon, E.U., *The Theory of Complex Spectra*. Physical Review, 1930. **36**(7): p. 1121-1133.

80. Yükçü, S.A., et al., *Calculation of the Gaunt coefficients over real spherical harmonics*. Canadian Journal of Physics, 2025. **103**(4): p. 321-327.

81. Slater, J.C., *Quantum Theory of Atomic Structure*. Vol. Vol. 1 and 2. 1960, New York: McGraw-Hill.

82. Kramida, A., *Cowan Code: 50 Years of Growing Impact on Atomic Physics*. Atoms, 2019. **7**(3): p. 64.

83. Haverkort, M., *Spin and orbital degrees of freedom in transition metal oxides and oxide thin films studied by soft x-ray absorption spectroscopy*. 2005, Universität zu Köln.

84. Zilberberg, I.L., M.A. Milov, and G.M. Zhidomirov, *Scaling the Coulomb interaction in calculations of electron spectra of transition metal complexes*. Journal of Structural Chemistry, 1999. **40**(1): p. 1-9.

85. Glatzel, P., *X-Ray Fluorescence Emission Following K Capture and 1s Photoionization of Mn and Fe in Various Chemical Environments*. 2001, Universität Hamburg and DESY: Hamburg, Germany. p. DESY-THESIS-2001-062.

86. Kroll, T., E.I. Solomon, and F.M.F. de Groot, *Final-State Projection Method in Charge-Transfer Multiplet Calculations: An Analysis of Ti L-Edge Absorption Spectra*. The Journal of Physical Chemistry B, 2015. **119**(43): p. 13852-13858.

87. Bethe, H., *Termaufspaltung in Kristallen*. Annalen der Physik, 1929. **395**(2): p. 133-208.

88. Watanabe, H., *Operator Methods in Ligand Field Theory*. 1966, Englewood Cliffs, NJ: Prentice-Hall.

89. Pollock, C.J., et al., *Kβ Mainline X-ray Emission Spectroscopy as an Experimental Probe of Metal–Ligand Covalency*. Journal of the American Chemical Society, 2014. **136**(26): p. 9453-9463.

90. van der Laan, G., *Theory of simple spectra*. Journal of Electron Spectroscopy and Related Phenomena, 1997. **86**(1): p. 41-47.

91. Kwiatkowski, T., S. Olszewski, and A. Wierzbicki, *Cubic harmonics in Cartesian coordinates*. International Journal of Quantum Chemistry, 1977. **11**(1): p. 21-47.

92. Zaanen, J., G.A. Sawatzky, and J.W. Allen, *Band gaps and electronic structure of transition-metal compounds*. Physical Review Letters, 1985. **55**(4): p. 418-421.

93. Bocquet, A.E., et al., *Electronic structure of early 3d-transition-metal oxides by analysis of the 2p core-level photoemission spectra*. Physical Review B, 1996. **53**(3): p. 1161-1170.

94. Bocquet, A.E., et al., *Electronic structure of 3d-transition-metal compounds by analysis of the 2p core-level photoemission spectra*. Physical Review B, 1992. **46**(7): p. 3771-3784.

95. Anisimov, V. and Y. Izyumov, *Electronic Structure of Strongly Correlated Materials*. Springer Series in Solid-State Sciences. Vol. 163. 2010, Berlin, Heidelberg: Springer.

96. Heinze, S., *Material-Specific Simulations of Many-Body Electron Dynamics*. 2021, Heidelberg University: Heidelberg, Germany.

97. Haverkort, M.W., M. Zwierzycki, and O.K. Andersen, *Multiplet ligand-field theory using Wannier orbitals*. Physical Review B, 2012. **85**(16): p. 165113.

98. Ballhausen, C.J., *Introduction to Ligand Field Theory*. 1962, New York: McGraw-Hill.

99. Okada, K. and A. Kotani, *Interatomic and Intra-Atomic Configuration Interactions in Core-Level X-Ray Photoemission Spectra of Late Transition-Metal Compounds*. Journal of the Physical Society of Japan, 1992. **61**(12): p. 4619-4637.

100. Green, R.J. and G.A. Sawatzky, *Negative Charge Transfer Energy in Correlated Compounds*. Journal of the Physical Society of Japan, 2024. **93**(12): p. 121007.

101. Cardot, C.A., et al., *Core-to-core X-ray emission spectra from Wannier based multiplet ligand field theory*. Journal of Electron Spectroscopy and Related Phenomena, 2024. **270**: p. 147419.

102. Brisk, M.A. and A.D. Baker, *Shake-up satellites in X-ray photoelectron spectroscopy*. Journal of Electron Spectroscopy and Related Phenomena, 1975. **7**(3): p. 197-213.

103. Kramida, A., *A Suite of Atomic Structure Codes Originally Developed by R. D. Cowan Adapted for Windows-Based Personal Computers*. 2021, National Institute of Standards and Technology.

104. Thole, B.T., et al., *3d x-ray-absorption lines and the $3d^{9}4f^{n+1}$ multiplets of the lanthanides*. Physical Review B, 1985. **32**(8): p. 5107-5118.

105. Stavitski, E. and F.M.F. de Groot, *The CTM4XAS program for EELS and XAS spectral shape analysis of transition metal L edges*. Micron, 2010. **41**(7): p. 687-694.

106. Retegan, M., *Crispy: v0.8.0*. 2024.

107. Gusmeroli, R. and C. Dallera, *Missing 1.1: Short User Manual*. 2025, ESRF (European Synchrotron Radiation Facility).

108. Lu, Q., *How to Correctly Analyze 2p X-ray Photoelectron Spectra of 3d Transition-Metal Oxides: Pitfalls and Principles*. ACS Nano, 2024. **18**(22): p. 13973-13982.

109. Suzuki, Y., et al., *Automated estimation of materials parameter from X-ray absorption and electron energy-loss spectra with similarity measures*. npj Computational Materials, 2019. **5**(1): p. 39.

110. Hwang, I.-H., et al., *The AXEAP2 program for K[beta] X-ray emission spectra analysis using artificial intelligence*. Journal of Synchrotron Radiation, 2023. **30**(5): p. 923-933.

111. Lüder, J., *Determining electronic properties from L-edge x-ray absorption spectra of transition metal compounds with artificial neural networks*. Physical Review B, 2021. **103**(4): p. 045140.

112. Ramaker, D.E., et al., *An atomic X-ray absorption fine structure study of the influence of hydrogen chemisorption and support on the electronic structure of supported Pt particles*. Topics in Catalysis, 2000. **10**(3): p. 157-165.

113. Campbell, J.L. and T. Papp, *Atomic level widths for x-ray spectrometry*. X-Ray Spectrometry, 1995. **24**(6): p. 307-319.

114. Taguchi, M., T. Uozumi, and A. Kotani, *Theory of X-Ray Photoemission and X-Ray Emission Spectra in Mn Compounds*. Journal of the Physical Society of Japan, 1997. **66**(1): p. 247-256.

115. Zasimov, P., et al., *HERFD-XANES and RIXS Study on the Electronic Structure of Trivalent Lanthanides across a Series of Isostructural Compounds*. Inorganic Chemistry, 2022. **61**(4): p. 1817-1830.

116. Imada, S. and F.M.F. de Groot, *Geometry-dependent analysis of 2p3d- and 2p3s-partial fluorescence yield spectra for high-spin 3d5 systems*. Journal of Electron Spectroscopy and Related Phenomena, 2025. **280**: p. 147538.

117. Ikeno, H., et al., *First-principles multielectron calculations of Ni ${L}_{2,3}$ NEXAFS and ELNES for $\mathrm{Li}\mathrm{Ni}{\mathrm{O}}_{2}$ and related compounds*. Physical Review B, 2005. **72**(7): p. 075123.

118. Ikeno, H., et al., *Multiplet calculations of L2,3 x-ray absorption near-edge structures for 3d transition-metal compounds*. Journal of Physics: Condensed Matter, 2009. **21**(10): p. 104208.

119. Blaha, P., et al., *WIEN2k: An APW+lo program for calculating the properties of solids*. The Journal of Chemical Physics, 2020. **152**(7).

120. Koepernik, K. and H. Eschrig, *Full-potential nonorthogonal local-orbital minimum-basis band-structure scheme*. Physical Review B, 1999. **59**(3): p. 1743-1757.

121. Marzari, N. and D. Vanderbilt, *Maximally localized generalized Wannier functions for composite energy bands*. Physical Review B, 1997. **56**(20): p. 12847-12865.

122. Pizzi, G., et al., *Wannier90 as a community code: new features and applications*. Journal of Physics: Condensed Matter, 2020. **32**(16): p. 165902.

123. Sakuma, R., *Symmetry-adapted Wannier functions in the maximal localization procedure*. Physical Review B, 2013. **87**(23): p. 235109.

124. Perdew, J.P. and Y. Wang, *Accurate and simple analytic representation of the electron-gas correlation energy*. Physical Review B, 1992. **45**(23): p. 13244-13249.

125. Merkys, A., et al., *Graph isomorphism-based algorithm for cross-checking chemical and crystallographic descriptions*. Journal of Cheminformatics, 2023. **15**(1): p. 25.

126. Vaitkus, A., A. Merkys, and S. Grazulis, *Validation of the Crystallography Open Database using the Crystallographic Information Framework*. Journal of Applied Crystallography, 2021. **54**(2): p. 661-672.

127. Marzari, N., et al., *Maximally localized Wannier functions: Theory and applications*. Reviews of Modern Physics, 2012. **84**(4): p. 1419-1475.

128. Bischof, C.H. and X. Sun, *On Tridiagonalizing and Diagonalizing Symmetric Matrices with Repeated Eigenvalues*. SIAM Journal on Matrix Analysis and Applications, 1996. **17**(4): p. 869-885.

129. Mattuck, R.D., *A Guide to Feynman Diagrams in the Many-Body Problem*. 2nd Edition ed. 1976, New York: Dover Publications.

130. Lüder, J., et al., *Theory of L-edge spectroscopy of strongly correlated systems*. Physical Review B, 2017. **96**(24): p. 245131.

131. Thunström, P., et al., *RSPt: Relativistic Spin-Polarized Toolkit (FP-LMTO electronic structure code)*. Vol. 109. 2012: Uppsala University. 186401.

132. Krüger, P., *First-Principles Calculation of Ligand Field Parameters for L-Edge Spectra of Transition Metal Sites of Arbitrary Symmetry*. Symmetry, 2023. **15**(2): p. 472.

133. Jain, A., et al., *Commentary: The Materials Project: A materials genome approach to accelerating materials innovation*. APL Materials, 2013. **1**(1).